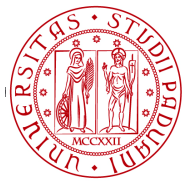

UNIVERSITÀ
DEGLI STUDI
DI PADOVA

Sede Amministrativa: UNIVERSITÀ DEGLI STUDI DI PADOVA

DIPARTIMENTO DI INGEGNERIA INDUSTRIALE

SCUOLA DI DOTTORATO DI RICERCA IN : Ingegneria Industriale

INDIRIZZO: Ingegneria Chimica, dei Materiali e Meccanica

XXVIII° CICLO

DEVELOPMENT OF NANOSTRUCTURED MEMBRANES FOR ENERGY AND ENVIRONMENTAL APPLICATIONS

Direttore della Scuola : Ch.mo Prof. Paolo Colombo

Coordinatore d'indirizzo: Ch.mo Prof. Enrico Savio

Supervisore : Ch.mo Prof. Michele Modesti

Co-supervisore : Ch.ma Prof.ssa Alessandra Lorenzetti

Co-supervisore : Dott.ssa Martina Roso

Dottorando : Carlo Boaretti

CONTENTS

RIASSUNTO

Lo scopo del seguente lavoro di tesi ha riguardato lo sviluppo di membrane nanostrutturate ottenute mediante tecniche elettroidrodinamiche (electrospinning/electrospraying) e la valutazione delle loro prestazioni in relazioni ad applicazioni concernenti l'energia e la protezione dell'ambiente. Nello specifico in questo studio l'attenzione è stata focalizzata sulla produzione di membrane composite mediante electrospinning ed electrospraying in relazione al loro impiego come membrane a scambio protonico e come filtri catalitici per l'abbattimento di composti organici volatili. Di seguito è riportata una breve sintesi dei capitoli in cui la tesi si articola:

- *Capitolo 1*: fornisce una introduzione alle tecnologie elettroidrodinamiche descrivendo i processi di elettrofilatura ed elettrospray. Una breve descrizione degli sviluppi storici di queste tecniche è presentata assieme ad una descrizione dettagliata dei principali parametri che controllano il processo e un riassunto delle diverse applicazioni correlate, con particolare enfasi sul ruolo di nanofibre elettrofilate;

- *Capitolo 2*: descrive il problema dell'inquinamento indoor e della Sick Building Syndrome in relazione alla presenza di composti organici volatili (VOC). Sono evidenziate le principali tecniche di rimozione dei VOC e particolare attenzione è posta alla descrizione del processo di fotocatalisi e dei suoi meccanismi. Infine viene presentato una breve panoramica della letteratura scientifica concernente l'applicazione delle tecniche elettroidrodinamiche relativamente a tale processo;

- *Capitolo 3*: descrive lo stato dell'arte relativamente alla tecnologia delle celle a combustibile e delle membrane a scambio protonico. In particolare viene fornita una dettagliata analisi dell'elettrofilatura per lo sviluppo di membrane a struttura nanofibrosa come mezzi a scambio protonico per celle a combusitibile e dei differenti approcci seguiti per la loro realizzazione;

- *Capitolo 4*: fornisce un breve riassunto dei principali materiali impiegati per la parte sperimentale dello studio. Successivamente vengono spiegate le tecniche analitiche impiegate per la caratterizzazione delle membrane assieme ai loro principi di funzionamento, fornendo concetti teorici di base e descrizione della strumentazione impiegata.

- *Capitolo 5*: presenta la preparazione e caratterizzazione di fotocatalizzatori biossido di titanio/grafene con differenti metodologie di accoppiamento tra il catalizzatore e co-catalizzatore. Dal momento che il grafene è generalmente considerato come materiale promettente per applicazioni fotocatalitiche, due diversi compositi sono stati realizzati impiegando il tradizionale fotocatalizzatore TiO_2 con il grafene mediante accoppiamento per via fisica e per via idrotermale al fine di valutare l'entità del diverso tipo di interazioni create tra i componenti. Nel primo caso l'accoppiamento

è prodotto per deposizione fisica in cui un primo strato di grafene sulle membrane finali sui quali viene realizzata una successiva deposizione di TiO_2. Nel secondo caso il biossido di titanio e il grafene sono accoppiati con un trattamento idrotermale in cui l'ossido di grafene viene simultaneamente ridotto e depositato sulla superficie del fotocatalizzatore. I compositi ottenuti e i singoli materiali puri sono stati analizzati mediante diverse tecniche al fine di valutare le loro caratteristiche, soprattutto in relazione all'assorbimento nello spettro UV-visibile, di vitale importanza in relazione alle applicazioni fotocatalitiche. La presenza di grafene nei materiali compositi si è rivelata capace di migliorare le caratteristiche di assorbimento del biossido di titanio e l'intervallo di assorbimento della luce;

- *Capitolo 6*: in questa parte sperimentale i fotocatalizzatori compositi realizzati nel precedente capitolo sono depositati sulla superficie di membrane polimeriche mediante una procedura in due fasi (procedura strato per strato) al fine di sfruttare le proprietà di elevata superficie specifica fornita dalle nanofibre. La procedura impiegata è basata sulla produzione del substrato polimerico mediante elettrofilatura e la successiva deposizione dei fotocatalizzatori compositi mediante elettrospray al fine di coprire le nanofibre e ridurre l'agglomerazione delle particelle solide di fotocatalizzatore. Due diverse matrici polimeriche, PSU e PAN, sono state valutate come supporti delle membrane finali ma solo il secondo dei due polimeri si è rivelato capace di fornire una adeguata resistenza alla radiazione UV e per questo motivo è stato selezionato come materiale di riferimento per le successive fasi dello studio. Le membrane ottenute sono state caratterizzate mediante microscopia elettronica al fine di valutare la morfologia finale ed analisi TGA sono state condotte per la quantificazione del catalizzatore depositato sulle membrane. Infine le membrane ottenute sono state testate per l'abbattimento fotocatalitico del metanolo in fase gas, utilizzando un opportuno fotoreattore, e comparate per definire le relative prestazioni ed il ruolo del grafene sull'attività fotocatalitica. I risultati hanno dimostrato che i compositi contenenti grafene possiedono una superiore attività fotocatalitica rispetto al biossido di titanio e che il fotocatalizzatore ottenuto mediante l'accoppiamento fisico tra grafene e TiO_2 garantisce i risultati migliori grazie alla elevata mobilità elettronica del grafene che garantisce una minore ricombinazione dei portatori di carica prodotti nel fotocatalizzatore dalla radiazione UV;

- *Capitolo 7*: la stessa tipologia di membrane composite a base nanofibrosa sono state realizzate con una procedura a singola fase. Secondo questo metodo alternativo i fotocatalizzatori compositi vengono depositati mediante elettrofilatura a partire da una singola soluzione colloidale contenente sia le particelle solide di fotocatalizzatore che il polimero disciolto. Mediante un'opportuna scelta del rapporto catalizzatore/polimero è stato possibile ottenere delle fibre completamente ricoperte da una struttura porosa del fotocatalizzatore. Analisi morfologiche e termogravimetriche sono state condotte analogamente al caso precedente, sottolineando le differenze ottenute mediante i due diversi approcci. I risultati dell'analisi morfologica hanno rivelato una diversa distribuzione di fotocatalizzatore e co-catalizzatore, con

quest'ultimo maggiormente confinato nella parte interna delle fibre prodotte. Questo ha determinato prestazioni differenti delle membrane finali nei confronti della foto-ossidazione del metanolo, dipendenti dalla morfologia finale delle membrane composite nanostrutturate;

- *Capitolo 8*: presenta un diverso approccio diverso la produzione di fotocatalizzatori compositi. Qui la biossido di titanio è accoppiato con un secondo fotocatalizzatore (carbonato di argento) per produrre un eterogiunzione al fine di migliorare l'attività fotocatalitica e le membrane finali sono state realizzate utilizzando l'approccio a singola fase per avere una migliore dispersione catalizzatori sulle fibre. I test di elettrofilatura per la preparazione delle membrane hanno dimostrato che la produzione delle membrane finali è influenzata dalla dimensione delle particelle del fotocatalizzatore e dal metodo impiegato per il loro accoppiamento. Ancora una volta le membrane sono state testate usando metanolo come inquinante bersaglio e un confronto finale è stato realizzato sia nei confronti del fotocatalizzatore di riferimento (TiO_2) che con le membrane più performanti ottenute dall' accoppiamento catalizzatore/co-catalizzatore ottenute con lo stesso approccio a singola fase. Il carbonato di argento, grazie alle sue buone capacità di assorbimento della luce, migliora notevolmente le caratteristiche di assorbimento dei sistemi fotocatalitici prodotti mostrando assorbimento anche nello spettro della luce visibile. Ciò ha determinato un incremento nella attività fotocatalitica rispetto al TiO_2 e prestazioni simili a quelle ottenute con l'accoppiamento di TiO_2 con grafene per via idrotermica;

- *Capitolo 9*: riguarda la preparazione e caratterizzazione del polietereterchetone sulfonato (sPEEK), scelto come materiale di riferimento per la produzione di rinforzi conduttivi in membrane composite a scambio protonico per celle a combustibile. In questo modo il polimero può fornire stabilità meccanica senza sacrificare eccessivamente la conducibilità protonica delle membrane finali. Due diverse strade sono state intraprese per la sulfonazione del materiale, impiegando acido solforico o una miscela di acido metansulfonico e acido solforico. Al fine di ottenere un maggiore controllo sul grado di funzionalizzazione finale del materiale si è provveduto ad un'analisi cinetica della reazione, ottenendo buoni risultati. Il polimero sulfonato possiede una elevata temperatura di transizione vetrosa, una accettabile stabilità termica ed è solubile in solventi polari aprotici per gradi di sulfonazione medio-alti;

- *Capitolo 10*: a causa della mancanza di una pregressa conoscenza sull'elettrofilatura dello sPEEK e data la necessità di definire condizioni in grado di fornire un produzione stabile di nanofibre è stato fatto ricorso alla metodologia delle superfici di risposta per la modellazione e l'ottimizzazione del processo di elettrofilatura dello sPEEK, utilizzando un design Box-Behnken. L'analisi, basata su un modello polinomiale di secondo ordine, si è focalizzata sulla valutazione dell'effetto sia di variabili di processo (voltaggio, distanza ago-collettore, portata) e di materiale (grado di sulfonazione) sul diametro finale delle fibre. Il modello finale è stato analizzato mediante una serie di test statistici sui residui e validato mediante una procedura di compara-

zione di campioni a differenti gradi di sulfonazione, realizzati mediante condizioni ottimizzate, per la produzione di nanofibre sottili ed omogenee;

- *Capitolo 11*: viene presentato un primo approccio per la realizzazione di membrane composite a scambio protonico per incorporazione di un rinforzo fibroso in una matrice conduttiva di uno ionomero perfluorurato a corta catena lineare (Aquivion®), scelto per le sue spiccate doti di conduttore protonico. La procedura è basata sull'immersione del mat nanofibroso in una colata di soluzione contenente lo ionomero, ottenendo una membrana finale densa per evaporazione del solvente. Due mats di sPEEK dello stesso spessore ma di differenti gradi di sulfonazione sono stati inseriti nella matrice e le proprietà delle membrane finali sono state determinate mediante tecniche di analisi ex-situ ottenendo buone proprietà meccaniche in conseguenza del rinforzo poroso e conducibilità inferiori ma comparabili rispetto al riferimento del singolo ionomero castato;

- *Capitolo 12*: un secondo approccio è stato seguito per la realizzazione di membrane composite utilizzando una matrice di polimero non conduttivo accoppiata con il rinforzo conduttivo nanofibroso di sPEEK, realizzando membrane a diverso rapporto di composizione. In questo caso il polyviniliden fluoruro (PVDF) è stato scelto come matrice non conduttiva grazie alle sua buona stabilità elettrochimica e termica. La procedura seguito ha richiesto un processo di elettrofilatura congiunta mediante la simultanea produzione di nanofibre dei due polimeri come alternativa al precedente metodo di realizzazione delle membrane, impraticabile per problemi legati alla medesima solubilità dei due polimeri in questione. Le membrane finali sono state prodotte per densificazione tramite fusione della componente di PVDF per compressione a caldo. Alti gradi di solfonazione hanno impartito limitazioni nella produzione delle membrane finali poiché la elevata temperatura di transizione vetrosa non ha permesso una completa densificazione delle membrane. I campioni finali sono stati comparati con le controparti ottenute mediante casting, utilizzando i medesimi rapporti di composizione, ottenendo un significativo incremento delle proprietà meccaniche grazie ad una maggiore compatibilità indotta dal rinforzo poroso, un minore rigonfiamento ad alte umidità ma nel contempo una conducibilità protonica inferiore rispetto allo sPEEK puro ottenuto via casting;

ABSTRACT

The aim of the present work has regarded the development of nanostructured membranes produced by electrohydrodynamic techniques (electrospinning/electrospraying) and evaluation of their performances in relation to energy and environmental applications. Specifically, in this study the attention has been focused on the production of electrospun/electrosprayed composite membranes in relation to their application as proton exchange membranes (PEM) and photocatalytic filters for the abatement of volatile organic compounds. Hereafter is presented a brief synthesis of the thesis chapters:

- *Chapter 1*: provides an introduction to the electrohydrodynamic technologies describing the electrospinning and electrospraying processes. A brief outline of the historically development of these techniques is presented along with a detailed description of the main parameters controlling the process and a resume of the different related applications, with a particular emphasis on the role of electrospun nanofibers;

- *Chapter 2*: describes the problem of indoor pollution and Sick Building Syndrome (SBS) in relation to the presence of volatile organic compounds (VOCs). The main techniques for VOC removal are highlighted and particular care is provided to the description of the photocatalysis process and mechanisms. Lastly a scientific literature survey of the the applicability of electrohydrodynamic techniques to such process is resumed;

- *Chapter 3*: describes the state of art of the fuel cell technology and the proton exchanges membranes, providing a description of the application of electrospinning for the development of composite nanofibrous network membranes as proton exchange media in fuel cells and the different approaches followed for their realization;

- *Chapter 4*: here the main materials employed for the experimental part of the thesis are briefly presented. Subsequently the analytical techniques for the characterization of the membranes and their working principles are explained, providing basic theoretical concepts and description of the instrumentation employed;

- *Chapter 5*: presents the preparation and characterization of titania/graphene photocatalysts with different methodology of coupling between the catalyst and co-catalyst. Since graphene is generally considered as promising material for photocatalytic applications two different composites with the traditional benchmark of TiO_2 and graphene have been realized by physical and hydrothermal coupling, to evaluate the extent of the different type of interactions created between the components. In the first case the coupling is produced by physical deposition a first layer of graphene on the final membranes on which a subsequent deposition of titania is realized. In the second case the titania and graphene are coupled with an hydrothermal treatment in which graphene oxide is simultaneously reduced and deposited on the surface of the

photocatalyst. The obtained composites and pristine materials have been analyzed by different techniques to evaluate their characteristics, especially in relation to the absorption in the UV-visible spectrum as it is of vital importance in relation to photocatalytic applications. The presence of graphene in the composites has revealed to be capable to improve the absorption characteristics of titania and increase its light absorption range;

- *Chapter 6*: in this experimental part the composites photocatalysts produced in the previous chapter are deposited on the surface electrospun polymeric membranes by a two-step (layer-by-layer) procedure to take advantage of the high specific surface area of the nanofibers. The procedure employed is based on the production of the polymeric substrate by electrospinning and the subsequent deposition of the composite photocatalysts by electrospraying in order to cover the nanofibers and reduce the agglomeration of the photocatalysts solid particles. Two different polymeric matrix, PSU and PAN, have been screened as support of the final membranes but only the latter has proved to have resistance under UV irradiation and has been selected as reference material for the subsequent part of the study. The membranes obtained have been characterized by electron microscopy in order to obtain an evaluation of the final morphology while TGA measurements have provided the quantification of the amount of catalyst deposited on the membranes. Finally the membranes have been tested for the photocatalytic abatement of methanol in gas phase, using a custom made photoreactor, and compared to assess their relative performances and the role of graphene on the photocatalytic activity. The results have proven that the composites containing graphene have an higher photocatalytic activity than titania and that the composite photocatalyst comprising pristine graphene offers the best performances thanks to the high electron mobility of graphene which provides a lower recombination of the charge carrier produced by the UV irradiation on the photocatalyst;

- *Chapter 7*: the same type of composite nanofibrous membranes have been produced following a one-step approach. According to this alternative procedure the composite photocatalysts are deposited by electrospinning from a unique colloidal solution containing the photocatalyst solid particles and the polymer. By selecting a proper catalyst/ polymer ratio it has been possible to obtain fibers fully covered by a porous structure of the photocatalytic composites. Morphological and thermogravimetric analysis have been realized analogously to the previous case, highlighting the difference obtained in the two different approaches. The results of the morphological analysis have revealed a different distribution of the photocatalyst and co-catalyst, with the latter more segregated in the inner part of the fibers produced. This has determined different performances of the final membranes for methanol photooxidation, which are dependent upon the different morphologies obtained in the final composite nanostructured membranes;

- *Chapter 8*: presents a different approach for the production of photocatalytic composites. Here titania is coupled with a second photocatalyst (silver carbonate) to

produce an heterojunction to improve its photoactivity and the final membranes have been realized using the one-step approach to have a better catalysts dispersion over the fibers. Electrospinning tests have shown that the production of the final membranes is influenced by the dimension of the photocatalyst particles and by the method for their coupling. Once again the membranes have been tested using methanol as target pollutant and a final comparison has been realized both on the reference photocatalyst (TiO_2) and with the more performant membranes obtained by catalyst/co-catalyst coupling using the same one-step approach. Silver carbonate, thanks to its light harvesting properties, significantly improves the absorption characteristics of the photocatalytic systems produced with absorption even in the visible light spectrum. This determined a boost in the photocatalytic activity with respect to TiO_2 and similar performances as obtained by coupling TiO_2 with graphene by hydrothermal method;

- *Chapter 9*: deals with the preparation and characterization of sulfonated poly(ether ether ketone) (sPEEK), selected as reference material for the production of porous proton conductive reinforcement in composite membranes for fuel cells. In this manner the polymer should provide mechanical stability without sacrificing proton conduction of the final membranes. Two different routes have been followed to sulfonate the polymer employing sulfuric acid or a mixture of methanesulfonic acid and sulfuric acid. In order to obtain control on the final degree of functionalization of the material a kinetic analysis of the reaction has been conducted, obtaining good results. The sulfonated polymer exhibits high glass transition temperature, acceptable thermal stability and solubility in polar aprotic solvents for medium high sulfonation degrees;

- *Chapter 10*: due to lack of previous knowledge on the electrospinning of the sPEEK and the necessity to define proper conditions for a stable process production of the nanofibers, Response Surface Methodology (RSM) has been employed for the modelling and optimization of the sPEEK electrospinning process, using a Box-Behnken design (BBD). The investigation, based on a second order polynomial model, has been focused on the analysis of the effect of both process (voltage, tip-to-collector distance, flow rate) and material (sulfonation degree) variables on the final fibers diameter. The final model has been verificated by a series of statistical tests on the residuals and validated by a comparison procedure of samples at different sulfonation degrees, realized according to optimized conditions, for the production of homogeneous thin nanofibers. The optimal conditions defined by the model have subsequently applied for the realization of the electrospun mats of sPEEK;

- *Chapter 11*: a first approach for the production of composite proton exchange membranes is presented by incorporation of the fibrous reinforcement into a good proton conductive matrix of a short side chain perfluorosulfonic acid ionomer (Aquivion®). The procedure is based on the soaking of the electrospun mat into a casted solution of the ionomer, obtaining the final dense membranes by solvent evaporation. Two sPEEK mats of the same thickness but at different sulfonation degree have em-

bedded into the matrix and the membranes properties have been characterized by ex-situ techniques obtaining good mechanical properties thank to the porous reinforcement and lower but comparable proton conductivity than the reference of the pristine casted iononmer;

- *Chapter 12*: a second approach for the production of composite membranes is realized by using a non-proton conductive matrix coupled with the nanofibrous conductive reinforcement of sPEEK, realizing membranes at different composition. In this case PVDF has been chosen as non conductive matrix for its thanks to its good electrochemical and thermal stability. The procedure followed required a dual electrospinning process with the simultaneous production of the nanofibers of the two polymer as alternative to the approach of the previous composite membranes due to problems related to similar solubility behavior of the two polymers. The final dense membranes have been obtained by densification through melting of the PVDF component by hot pressing. Limitations are imparted for high sulfonation degrees where the high glass transition temperature prevent the complete densification of the membranes. The final membranes have been compared to casted counterparts at the same composition providing remarkable improvement of the mechanical properties due to an higher compatibilization imparted by the porous structure of reinforcement, lower swelling but also lower proton conductivity to the pure sPEEK obtained by casting.

INTRODUCTION

The important and characteristic features of the nanoarchitectures which can produced by electrohydrodynamic technologies like electrospinning and electrospraying have led as significant spread in their field of applications thanks to their easy implementation and wide range of material which can be processed, attracting the interest of the scientific research community. These techniques involves the application of high voltage to a needle through which a liquid solution is fed in order to generate a fine jet. According to nature of the solution employed the electric force is capable to produce the generation of small droplets by the coulombic explosion of the jet (electrospraying) or, in presence of suitable viscosity induced by a viscoelastic material, the stretching of the jet and the formation of thin fibers which can be deposited on a grounded collector. The structures obtained by these technologies have nanosized dimensions, low density, large surface areas, high pore volume, tight pore size and their final properties can be tailored according to the specific applications of interest. Despite this the commercialization of such technologies is still limited to specific applications but a vibrant activity is emerging around companies and enterprises which are developing proprietary products. In this context the research activity is an invaluable tool to help promoting an increasing awareness of the potential related to the employment of such technologies. Biomedical and air filtering are the traditional and most studied field of applications but in the last years recent advances have shown interesting premises for developments concerning power generation and environmental protection by green process technologies like photocatalysis. Specifically, in this study the attention has been focused on the production of electrospun/electrosprayed composite membranes in relation to their application as proton exchange membranes (PEM) and photocatalytic filters for the abatement of volatile organic compounds. The first are traditionally considered as one the decisive steps towards the commercialization of low temperature fuel cells for the generation of electricity for stationary and portable applications while the latter represents an intriguingly opportunity in relation of the problem of indoor pollution thanks to their high oxidative characteristics. Many approaches have been outlined to solve the limitation of PEM performances in hydrogen/air fuel cells and nanofiber network membranes have shown the possibility to impart mechanical strength and dimensional stability as well as improved proton conductivity according to the specific strategy for the production of the final membrane. On the other side electrospun nanofibrous membranes are suitable substrates for the deposition of photocatalysts in order to provide adequate porosity, high surface area and limitation of particles agglomeration in the context of photocatalytic oxidation processes. For these reasons the investigation carried in this work are related to the evaluation of different approaches in the production of the final membranes according to the selected applications, highlighting the advantages and the drawbacks of each in comparison to reference materials or methodologies.

1 EHD TECHNOLOGIES FOR NANOSTRUCTURED MATERIALS

The present chapter provides an introduction to the electrohydrodynamic technologies (EHD) for the production of nanostructured architectures, with a special emphasis on the generation of nanofibers. A literature review of the history, development, process parameters and main applications will be briefly discussed.
The two main techniques which belong to this particular type of technologies are electrospinning and electrospraying and they both rely on the application of high voltages for the generation of electrified jet for the production of nanofibers and nanoparticles, respectively. Both nanofibers and nanoparticles are a particular aspect of the field of nanotechnology, which is defined as the science that deals with materials, structure and devices that have at least a dimension equal or less than 100 nm [1]. Although by convention the dimension of 100 nm is the limiting value for talking about nanotechnology, even structures, materials or devices with dimensions of hundreds of nanometers (even up to 500 nm) are considered nano. The interests towards materials and architectures that can be produced and designed on such scale are related to the evolution of structural, thermodynamic, electronic, spectroscopic, electromagnetic, mechanical and chemical features of these finite systems with changing size. The outstanding properties of nanostructured materials have attracted tremendous attention in last years and are fueling an extensive interdisciplinary research activity involving physicists, chemists, material scientists and engineers all over the world.

1.1 NANOFIBERS PRODUCTION TECHNIQUES

Nanofibers production techniques, as well as those of nanostructures and nanodevices, are base on two different types of approach:

- *Top-down* approach: the idea is to start from an object of big dimensions and to reduce it to the desired dimensions;

- *Bottom-up* approach: in this case the nanostructure is built starting from the single bricks that compose it, which can be atoms of molecules.

The most employed methods for the preparation of nanofibers, which are based on these two approaches, are: drawing [2], template synthesis [3, 4], phase separation [5], self assembly [6], separation of multicomponent fibers, melt blown [7] and electrospinning [8].

1.1.1 Drawing

In this technique, very similar to dry-spinning, the starting point is a droplet of solution deposited on a surface (Figure 1.1 I), which will produce the final fibers. A micropipette with a diameter of some micrometers is dipped into the droplet close to the line of contact (Figure 1.1 II). Subsequently the micropipette is extracted from the liquid and removed from the droplet with a fixed velocity (Figure 1.1 III), dragging a nanofiber (Figure 1.1 IV).

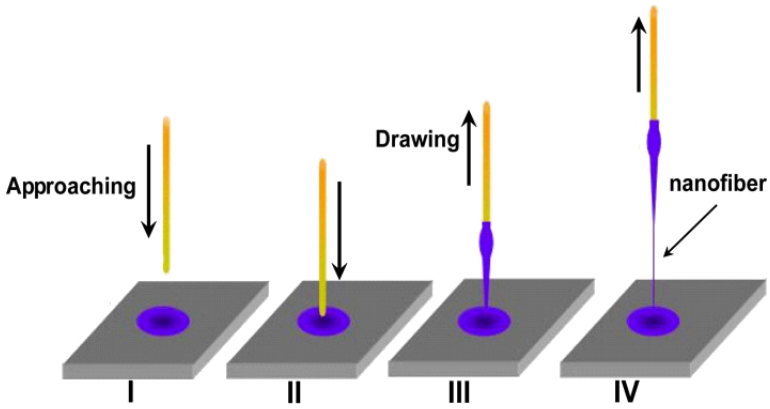

Figure 1.1: *Drawing of a nanofiber: I) droplet deposited on a surface, II) immersion of the micropipette on the droplet, III) extraction of the micropipette from the solution, IV) formation of the nanofiber*

The process is discontinuous and it is repeated several times starting form different droplets. It requires a material with a pronounced viscoelastic behavior to undergo strong deformation, while being cohesive enough to support the stresses developed during the pulling.

1.1.2 Template synthesis

This technique requires the employment of a template. The template consists of a ceramic or polymeric membrane with nanometric pores across its entire thickness. From one side of the membrane there is the polymer solution and above it there is water; on the other side there is a coagulating solution. The polymeric solution, by means of the pressure generated by the water and by the resistance of porous membrane is extruded and once in contact with the solidifying solution generates the nanofibers whose diameter is determined by the dimensions of the membrane pores.

1.1.3 Self-assembly, melt blown and multi-component fibers

With the self-assembly technique the nanofibers are produced by assembling smaller molecules, the bricks that constitute the fibers themselves. What makes possible the assembly of the molecules are the intermolecular forces. The shape of the fundamental units determines the shape of the macromolecular nanofiber obtained.
The melt blown technique employs air fluxes and high velocities: the polymer is blown

through the head of an extruder at high velocity and it is deposited on a collector as a fibrous net with nanometric and micrometric dimensions.
In the case of the separation of multicomponent fibers initially the single fiber is constituted of two different polymers. Subsequently a proper solvent is chosen in order to solubilize only one of the two polymers. By adding the solvent the soluble polymer dissolves leaving only the fibers of the non-soluble polymer.

1.1.4 Phase separation

The phase separation technique requires three different phases: the dissolution of a polymer into a suitable solvent, a subsequent reticulation process in which intermolecular bonds are established between the polymeric chains. In a third moment, the solvent phase is extracted. The separation is based on the physical incompatibility between two substances: a second solvent is added, which is compatible with the first but incompatible (from the physical point of view) with the polymer. In this manner the solvent in which the polymer was initially dissolved is extracted and the residue is a porous polymeric structure constituted by a net of nanofibers. This process allows the direct fabrication of a nanofiber matrix and the control on its mechanical properties but only a few polymers can be processed.

1.1.5 Electrospinning

The generation of nanofibers by electrospinning starts from a solution of a proper solvent in which the desired material is dissolved at a suitable concentration. This solution is usually poured in a syringe or a pipette from which it is let flown through a nozzle using a micro-pump and by means of an high voltage direct current power supply (5 to 50 kV) an electrostatic field is applied between the nozzle and a metal collector with opposite polarity. By increasing the intensity of the electric field a charge is induced on the surface of the solution at the tip of the capillary. The mutual repulsion of the charges elongates the hemispherical drop to form a conical shape (Taylor cone). Once that the electric filed has reached a threshold value, the electrostatic force overcomes the surface tension and a charged jet of solution is ejected from the tip of the Taylor cone, producing a jet that travel towards the metal collector. During this last phase the jet undergoes a whipping process in which it is stretched and the solvent of the solution evaporates leaving a fiber that is collected on a grounded collector. The main advantage of electrospinning process is the relative quick and simple way to fabricate aligned or randomly distributed nanofibers of a rich variety of different materials like synthetic and natural polymers [9], composites [10], ceramics [9, 11, 12], and metals [13–15].
The typical instrumental apparatus for electrospinning is shown in Figure 1.2 an it is constituted by:

- a glass or plastic syringe in which the polymeric solution is contained;
- a volumetric pump (syringe pump);

- an electrode in contact with the solution;
- an high voltage generator connected to the electrode;
- a grounded collector for the deposition of the fibers.

Usually a static collector is employed but other solutions can be selected, like a rotating drum or parallel electrode collectors.

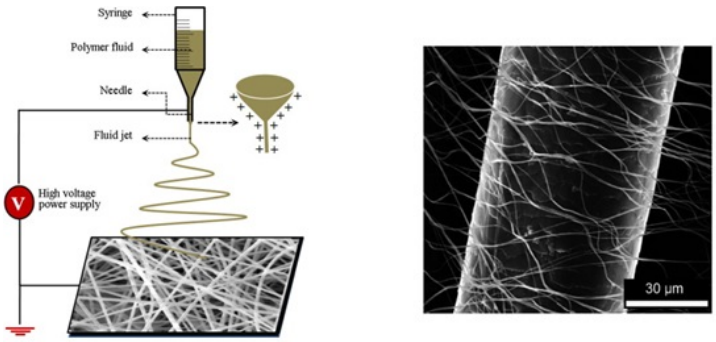

Figure 1.2: *(a) Electrospinning set-up and (b) comparison between nanofibers and a human hair*

If compared to other processing methods for the production of nanofibers, electrospinning is the only process which can be scaled up and allows control on the fibers dimension [1]. Moreover, despite being cost effective, the nanofibers can be produced continuously with method which represent the only alternative for mass production of nanofibers of different types of polymers.

1.2 HISTORY OF ELECTROSPRAYING AND ELECTROSPINNING

Although the idea of a process based on the electrospinning phenomenon for the production of nanofibers goes back to about 80 years ago, the first esperimental observations go back to more than 200 years ago. In 1745 Bose [16] described the generation of aerosols by means of high electric potentials applied to a liquid at the end of a capillary tube, producing an aerosol spray. In 1882 Rayleigh analyzed from a theoretical point of view the quantification of the electric charge required to overcome the surface tension of a liquid droplets [17]. Thanks to these studies, in the early 1900s the first apparatus for electrically dispersing fluids appeared in the works of Cooley [18] and Morton [19]. A more detailed study of the phenomenon of electrohydrodynamic jets was realized about 20 years later by Zeleny [20] with reference to the electrospray phenomenon of low molecular weight liquids. He observed the role of the surface instability in electrical discharges from charged droplets and a few years later [21] proved experimentally that the disintegration is caused by the hydrodynamical instability rather than to the formation of ionic current. Subsequently, between the 1934 and the 1944, Formhals published five patents describing the

realization of several experimental devices capable to produce polymer jets using electrostatic forces. In 1952 Vonnegut and Neubauer [22] were able to produce a simple apparatus of electric atomization capable to generate a continuous flow of highly electrified droplets of about 0.1 mm in diameter by applying potential 5-10 kV. Subsequently Droizin [23] investigate the dispersion of a series of liquids in the form of aerosols under the effect of high electric potentials. He found that the dielectric constant influenced the dispersibility of the liquid because of the electrostatic pressure which plays a predominant role int he process of dispersion, is in turn function of the dielectric constant and of the radius of curvature of the liquid in the capillary. Since the 60s the fundamental studies about the process of the jet generation during electrospinning were realized by Taylor [24]. He devoted himself to the analysis of the behavior of a droplet of polymer solution at the vertex of a needle when subjected to the action of an electric field and showed how the formation of a filament was realized starting from the deformation of the droplet to lead to the formation of a cone (Taylor cone). In 1966 Simons [25] was capable to patent an apparatus of non woven mats ultrathin and light with different schemes using electrospinning. With this apparatus a wide range of polymers could be processed such as cellulose esters and ether, vinyl resins, polystyrene, polyurethanes and polycarbonate. He also tested the effect of different process and solution parameters, supposing, for the first time, their interdependency.
In the following years the attention was concentrated on the study of the fibers morphology, thanks to the availability of more and more precise characterization techniques (WAXD, SEM, TEM) and to the study of the relation between the structural features and the process parameters [26]. In 1971 Baumgarten [27] realized an apparatus for the production of acrylic fibers with diameters comprised between 0.5 and 1.1 micron while in 1977 Martin *et al*. [28] developed an apparatus capable to providing the formation of a mat consisting of a plurality of fibers of organic materials. In 1981 Larrondo and Manley [29] were the first to produce electrospun fibers from a solutions of molten polyethylene and polypropylene. The produced fibers that were greater than 50 μm and their inability to spun sub-micron diameter fibers were ascribed to the large viscosity, many orders of magnitude higher than that of a polymer solution. Subsequently for about a decade the electrospinning process did not earn much success in the academic and industrial field until the beginning of the 90s, contextually to the growing interest towards nanotechnologies. Of particular interest and relevance is the work conducted by Reneker and his coworkes in the 90s, who demonstrated how this technique can be particularly interesting for the wide range of materials employed and for the potential end-use applications [30]. This growing interest is nowadays evident thanks to the fact that more than 200 between university and research institutes all over the world are dedicating to the study of the different aspects regarding the electrospinning process and even the number of patent related to applications based on electrospinning is growing in the last years [31]. At the same time different companies (e.g. eSpin Technologies, Nano Technics, KATO Tech) are actively involved in the task of applying the unique advantages showed by this technique, while company such as the Donaldson company and Fraudenberg already employ this process from twenty years for the realization of air filtering products [26, 31, 32].

1.3 THE MECHANISM OF NANOFIBERS GENERATION BY ELECTROSPINNING

The implementation of the electrospinning process is relatively simple but the mechanisms involved in the fiber formation involve high speed nonlinear electrohydrodynamics, complex rheology, and transport of charge, mass, and heat within the jet. The process can be broken down into several operational components [33, 34]: charging of the fluid, formation of the cone-jet, thinning of the jet in the presence of an electric field, instability of the jet and collection of the jet (or its solidified fibers) on an appropriate target. Subsequently each single stage of the process is briefly described.

1.3.1 Charging of the fluid

This first step can be in turn divided in two intermediate step: the generation of the drop and the formation of the Taylor cone jet. In the first part the polymeric solution is pumped through the needle of the syringe at low flow-rate. In absence of electric field on the tip of the needle there is the formation of solution droplets which fall due to the effect of gravity. Liquid surface tension (γ) and gravity (f_g) are the only forces acting on the drop surface. Under these circumstances the radius of the droplet (r_0) produced at the exit of the needle of internal radius R is:

$$r_0 = \sqrt{\frac{3R\gamma}{2\rho g}} \tag{1.1}$$

where ρ is the liquid density and g is the gravity acceleration. Droplets can also fall in presence of an electric field in case of low tensions. Once that the voltage has reached a sufficiently high value, the electric force and the gravity force can counterbalance the surface tension ($F_\gamma = F_E + F_G$) and the maximum diameter that is capable to maintain the droplet in equilibrium on the tip of the needle decrease with r (where $r < r_0$). The force of the electric field which is generated between the needle and collector, at a distance L between each other is:

$$F_E = \frac{4\pi\epsilon V^2}{\ln\left(\frac{4L}{R}\right)^2} \tag{1.2}$$

where ϵ is the permittivity of the medium (usually air) and V is the applied voltage. In this case the radius of the droplet is:

$$r = \sqrt[3]{\frac{3}{2\rho g}\left[R\gamma - \frac{2\epsilon V^2}{\ln\left(\frac{4L}{R}\right)}\right]} \tag{1.3}$$

By increasing the applied voltage, the value of the radius decreases until reaching the criti-

cal voltage (V_C) where the droplet experiences instability. Due to the electric field, a charge separation is established inside the solution droplet. Since the needle is, usually, charged positively on the surface of the droplet there is an accumulation of positive charges, while the negative ones migrate towards the inside, until an equilibrium point where the electric field inside the droplet is null. The charge separation generates a force which is opposite to the surface tension. The stability of the droplet positively charged on the tip of the needle is granted until the surface tension (which acts inward) prevails with respect to the repulsion generated by the charges accumulated on the surface (which acts outward); the equilibrium conditions in presence of the electric field is then:

$$F_E \leqslant r\rho\left(\frac{r^2}{\beta} - V\right) \tag{1.4}$$

where β is the shape factor of the droplet. However the maximum surface charge that a droplet can withstand is given by the Rayleigh conditions [17]:

$$Q_R = 8\pi\sqrt{\epsilon\gamma r^3} \tag{1.5}$$

for values of $|Q| > Q_R$ the droplets initially deforms and subsequently breaks into smaller droplets due to the repulsion that is created between the numerous positive charges accumulated on its surface.

1.3.2 Formation of the cone-jet

The droplet under the effect of the electric field is subjected to a deformation. The stretched droplet assumes the shape of a cone from which a thin liquid jet is emitted [35]. This is called the Taylor cone and it is formed in correspondence to the critical voltage (V_C) expressed as:

$$V_C^2 = \left(\frac{2L}{h}\right)^2\left[\ln\left(\frac{2h}{R}\right) - 1.5\right](0.117\pi R\gamma) \tag{1.6}$$

where h is the length of the needle and γ is the surface tension. It is this passage from a spherical to an ellipsoid which determines the generation of the stretching forces which can lead to the formation of droplets (electrospraying) or fibers (electrospinning). From the considerations drawn so far it is possible to comprehend that liquids with high surface tension requires higher critical voltage and the same follows for liquids at high viscosity and low conductivity. At this point it is important for the purpose of this discussion to understand the origin of the mobility of ions. A ionic species in a droplet of electrically charged solution is subjected to two forces: the electrostatic force (F_E) equal to the product between the ionic charge, the force of the electric field and the viscous drag force ($F_D = 6\pi\eta r\mu E$, where η is the viscosity of the solution and μ is the ion mobility). The two forces are opposite: while the electrostatic force moves the charges in the direction of the electric field, the viscous drag force try to hold the charges.

1.3.3 Jet thinning

The jet is produced at the moment in which the critical voltage is reached: its formation is instant. The repulsion force of the superficial charges accumulated in the jet, since the electric field has a specific direction, has its own direction. In particular it possesses an axial component which generates the thinning of the jet during its travel to the collector. Buer *et al*. [36] have demonstrated that the jet velocity increase progressively both by the jet stretching and by evaporation of the solvent. Therefore the jet, accelerating toward the collect, is thinned more and more. In this first phase the jet is stable and its stability is provided by the polymer chain entaglements.

1.3.4 Jet instability

The jet, which is straight during its initial path, becomes instable during its travel towards the collector and bends generating an undulating and oscillating trajectory. The jet bending allows the increase of the surface, decreasing the density of the charges. Several studies deals with the modeling of the jet under the effect of the electric field [37–40]: the whipping mode is generated by the concurrency of different types of instabilities, such as Rayleigh instability, instability symmetric to the axis and bend instability. In particular the type of instability obtainable depends on the electric field: intense electric fields favor the whipping mode. In this case the preponderant direction of the repulsive forces generated inside the jet is not axial. The jet movements, similar to hits of whip, are enclosed inside a conical shape space and arranged symmetrically with respect to the axis along which the straight jet lays. In this phase both the speed of surface area increment and the evaporation velocity of the solvent are quite high and the diameter of the jet is further reduced. The whipping instability is therefore mainly responsible for the reduction of the nanofibers dimension during the electrospinning. In this stage the forces which act on the jet are: gravity, the electrostatic force (introduces the jet and push it towards the collector), the viscoelastic forces (they oppose to the jet fragmentation in the electric field), the surface tension forces (they operate against the jet stretching), the frictional forces between the jet surface and the surrounding environment. The combination of all these forces influences the jet diameter. The quantitative description of the process is particularly difficult since the major part of these forces vary with high velocity due to the evaporation of the solvent and charges dissipation. As a consequence the mathematical models that are available regarding the description of the instability of the jet are not entirely satisfactory.

1.3.5 Jet solidification

During the travel of the jet towards the collector the solvent evaporates, leaving the formation of the polymeric nanofibers. Ideally no residual solvent should be present at the moment in which the jet hits the surface of the collector, to avoid partial welding of the fibers. The rate of solvent evaporation depends upon a series of factors, like the tip-

to-collector distance and the vapor tension of the solvent. This phase is very important in order to determine the value of the fibers diameter.

1.4 NANOFIBERS STRUCTURES

As previously seen by changing the process, solution and environmental parameters nanofibers with different morphology can be obtained. This variability is one the main advantages of the electrospinning technique thanks to the possibility to define a proper morphology in relation to the properties required by the fibers for a given application. Possible morphologies that can be obtained are: porous, flatten or ribbon like, branched, helical, hollow and core-shell (Figure 1.3).

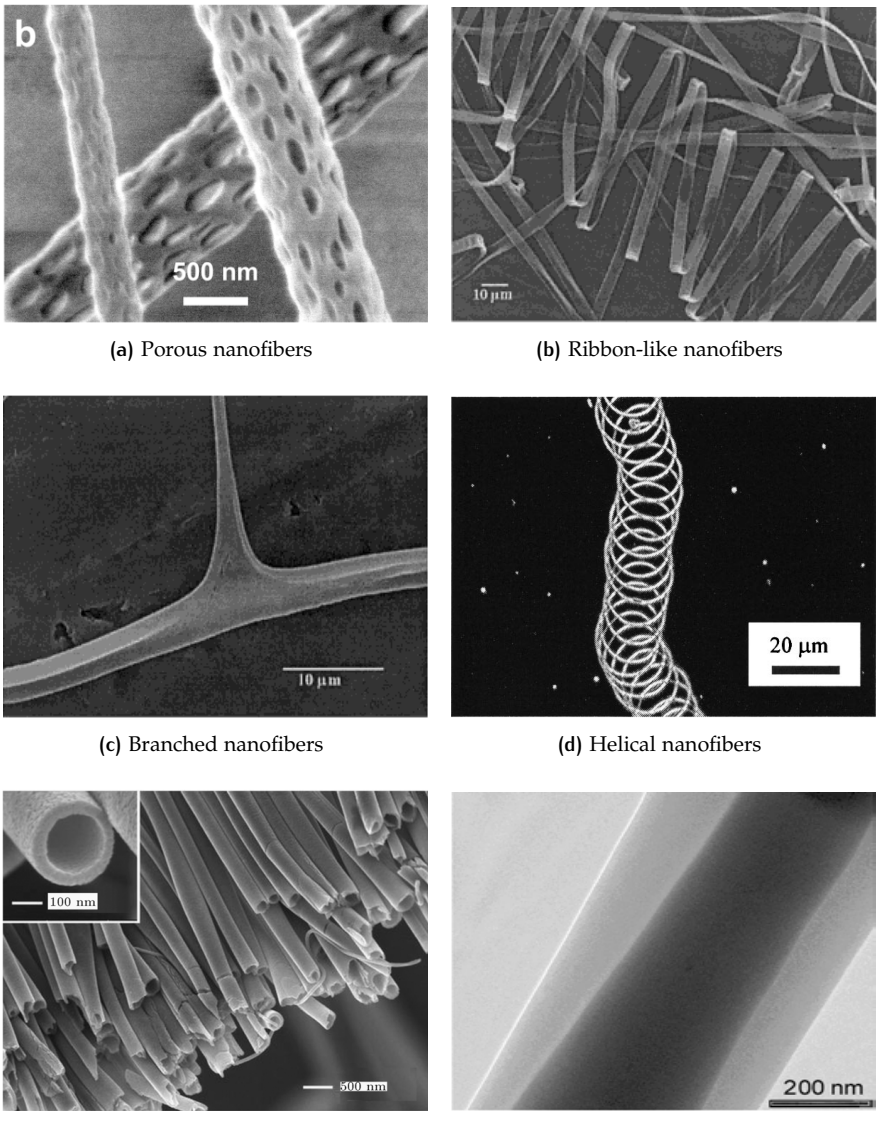

(a) Porous nanofibers

(b) Ribbon-like nanofibers

(c) Branched nanofibers

(d) Helical nanofibers

(e) Hollow nanofibers

(f) Core-shell nanofibers

Figure 1.3: *Different morphologies that can be obtained with electrospun nanofibers*

Koombhongse *et al*. [41] explained the ribbon like structure considering the presence of a thin, mechanically distinct polymer skin on the liquid jet. When solvent evaporation occurs, a tube structure takes place and because of the atmospheric pressure the latter collapse and the circular cross section becomes elliptical and then flat, forming a ribbon with a cross-sectional perimeter nearly the same as the perimeter of the jet.
In the same work the authors also proposed a possible mechanism for the formation of branched fibers. According to their conclusions branched fibers are obtained when secondary jets are developed from the primary jet, or when the jet breaks into more jets. This happens because during the stretching phase and evaporation of the solvent, the shape and charge quantity per unit of surface, which is present in the jet, are modified; it follows that the equilibrium between the electric forces and the surface tension is no more granted and the jet becomes instable. This instability leads to the formation of one or more jets of lower dimensions than the principal one.
Helical fibers are produced starting from a mixture of two different polymers, of which one is conductive. When the fiber is deposited on the collector the charges of the conductive polymer regions are transferred on fiber surface, producing an imbalance between the electrostatic repulsive forces and the viscoelastic forces. As a result the final structure is modified in order to attain a new condition of equilibrium between the competing forces, producing an helical structure [42].
Core-shell nanofibers can be obtained by using the coaxial electrospinning [14]. A coaxial jet is formed by a coaxial spinneret when two different liquids flow trough outer and inner capillaries simultaneously. Both the capillaries are connected to a high voltage power supply and nanofibers are consolidated during the solvent evaporation and stretching. The complex internal structure of nanofibers is formed via spontaneous phase separation during the electrospinning process. These kind of nanofibers can possess an eternal layer of active agents for imparting functional properties and are expected to be promising for a variety of applications, including drug delivery [43, 44]. Another technique which allow the production of fibers at different composition is the side-by-side electrospinning, where the capillaries are placed side by side and the two polymer solution just come into physical contact at the end of the spinneret tip [45]. The fabricated fibers benefit from both the intrinsic properties of the two polymers, simultaneously. For instance, one of the sides is able to absorb chemical, while the other side is capable of electric conduction.
Hollow nanofibers are produced with the same method of the core-shell nanofibers, but the difference relies in the dissolution of the core material with a selective solvent at the end of the process [46]. Porous nanofibers are useful for applications in which high surface area is required such as filtration [47], fuel cell [48], tissue engineering [5, 49], catalysis and drug delivery and release[14, 50]. Porous nanofibers can be obtained by selecting particular combination of solvents or solvent mixtures or polymer mixtures under controlled environmental mediums. Their formation start when the evaporation phase of the solvent the solution becomes thermodinamically instable and there is the formation of two distinct phases, one rich and the other poor in polymer content. The rich phase solidify very quickly and leads to the formation of the matrix whose inside the pores are formed as a consequence of the slow solidification of the other phase.

1.5 ELECTROSPINNING PARAMETERS

One of the most surprising aspect regarding the electrospinning process is the sharp contrast between the easiness of the realization of the process and the intrinsic complex nature of the physical phenomenon and its relative regulation. Despite what can be thought, electrospinning is a process influenced by a relative high number of factors, some controllable during the spinning and others during the preparation of the polymer solutions. These parameters can be classified in three different categories:

- Solution parameters: concentration, molecular weight, viscosity, surface tension, conductivity/surface charge density;
- Processing parameters: voltage, flow rate, collectors, distance between the collector and the tip of the syringe;
- Environmental parameters: humidity, temperature, pressure, type of atmosphere.

A further complications is due to the fact that some of these parameters influence each other and it is difficult, from an experimental point of view, to be able to isolate exactly the contribute of each single parameter on the properties of the final fibers obtained (Figure 1.4). However each of those parameters can affect the fibers morphologies and by a

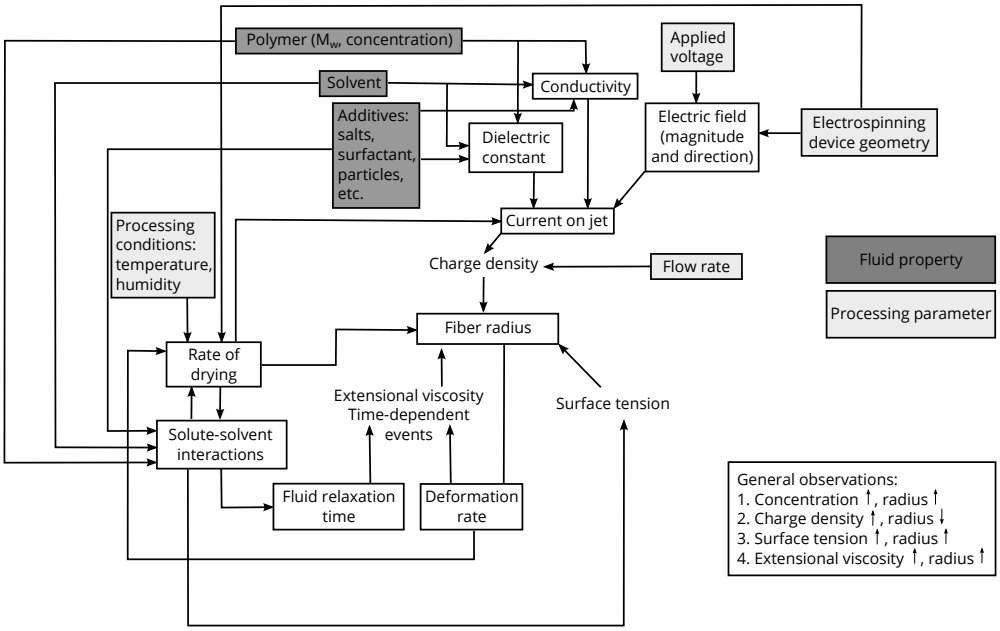

Figure 1.4: *Flow chart illustrating how material properties, processing parameters, and processing conditions affect the fiber diameter* [51]

proper control of those parameters it is possible to produce electrospun fibers with desired morphologies and diameters. From a general point of view it is possible to draw some general conclusions regarding the effect of the parameters involved in the electrospinning process and the ranges of the variables that allows to obtain a stable process. Some of

Table 1.1: *Effect of different parameters on the resultant morphology of electrospun fibers* [52]

Processing parameters	Effect on fiber morphology
Viscosity/concentration	· Low concentrations/viscosities yielded defects in the form of beads and junctions; increasing concentration/viscosity reduced the defects · Fiber diameters increased with increasing concentration/viscosity
Solution conductivity	· Increasing the conductivity aided in the production of uniform bead-free fibers · Higher conductivities yielded smaller fibers in general (exceptions were PAA and polyamide-6)
Surface tension	· No conclusive link established between surface tension and fiber morphology
Polymer molecular weight	· Increasing molecular weight reduced the number of beads and droplets
Dipole moment and dielectric constant	· Successful spinning occurred in solvents with a high dielectric constant
Flow rate	· Lower flow rates yielded fibers with smaller diameters · High flow rates produced fibers that were not dry upon reaching the collector
Field strength/voltage	· At too high voltage, beading was observed · Correlation between voltage and fiber diameter was ambiguous
Distance between the tip and the collector	· A minimum distance was required to obtain dried fibers · At distances either too close or too far, beading was observed
Needle tip design	· Using a coaxial, 2-capillary spinneret, hollow fibers were produced · Multiple needle tips were employed to increase throughput
Collector type and composition	· Smoother fibers resulted from metal collectors; more porous fiber structure was obtained using porous collectors · Aligned fibers were obtained using a conductive frame, rotating drum, or a wheel-like bobbin collector · Yarns and braided fibers were also obtained
Ambient parameters	· Increased temperature caused a decrease in solution viscosity, resulting in smaller fibers · Increasing humidity resulted in the appearance of circular pores on the fibers

these conclusions are summarized in Table 1.1.
For example an increase of the tip to collector distance has to be often integrated with an increment of the applied voltage in order to maintain a stable Taylor cone during the process. The increment of the solution flow rate and polymer concentration require the application of a stronger electric field and an higher distance between the tip and the collector determine an increment of the fiber diameters. However a more detailed description of those parameters and their influence in described subsequently.

1.5.1 Solution parameters

1.5.1.1 *Solvent*

Between the different types of solution parameters a significant number of them are influenced mainly by the choice of the solvent. This choice is essential for the realization and optimization of the electrospinning process. Indeed the morphology is significantly influenced by the physical (viscosity, surface tension) and electrical (conductivity) properties of the selected solvent (Table 9.2), that mostly determine those of the final solution. Essentially the solvent has two main functions regarding the electrospinning process:

- the dissolution of the polymeric molecules in order to produce an electrifying jet. In this perspective the solvent has to be properly chosen is relation to the type of polymer to dissolve and the intermolecular interactions between the components of the binary system of the solution have to be evaluated, since they can be attractive o repulsive in relation to the solvent selected;
- the conduction of the dissolved molecules towards the collector. In this phase the characteristics of the solvent in terms of volatility, surface tension and vapor pressure determine the final morphology of the fibers obtained, indeed:
    1. the vapor pressure influences the velocity and, consequently, the time required for the evaporation of the solvent;
    2. the solvent volatility determines the formation of nanostructures since it influences the phase separation and its velocity;
    3. the surface tension influences the dimension of the fiber diameter, the lower the surface tension is the lower is the fibers diameter produced. However this property depends both on the type of the solvent and the polymer concentration in the solution.

It is clear that once chosen a particular polymer with a given molecular weight it is the solvent that plays a fundamental role. However solvents that shows a good dissolution power towards a given polymer not necessarily lead to the formation of solution that allows a good electrospinning process [53]. The solvent acts in a complex manner since it is capable to influence the jet instability that is originated from the Taylor cone [41] and, thus, the final microstructure obtained. This instability is linked to factors such as the rheology of the solution, the charge density, the surface tension and the volatility that can be considered as different for each type of polymer-solvent system.

Table 1.2: *Properties of solvents commonly employed in electrospinning*

Solvent	Surface Tension [mN/m]	Dielectric Constant	Boiling point [°C]	Density [g/ml]
Chloroform	26.5	4.8	61.6	1.498
Dimethyl formamide	37.1	38.3	153	0.994
Hexafluoro isopropanol	16.1	16.7	58.2	1.596
Tetrahydrofuran	26.4	7.5	66	0.886
Trifluoro ethanol	21.1	27	78	1.393
Acetone	25.2	21	56.1	0.786
Water	72.8	80	100	1.000
Methanol	22.3	33	64.5	0.791
Acetic acid	26.9	6.2	118.1	1.049
Formic acid	37	58	100	1.21
Dichloro methane	27.2	9.1	40	1.326
Ehtanol	21.9	24	78.3	0.789
Trifluoroacetic acid	13.5	8.4	72.4	1.525

1.5.1.2 *Solution viscosity and molecular weight*

The viscosity of the solution employed, as well as its conductivity, determine the jet elongation from which the fiber is originated. Solution viscosity depends both on the molecular weight of the polymer employed and on the polymer solution concentration as well as from other factors such as type of temperature and pressure. In particular the molecular weight of the polymer is important because represents the length of the polymer chain, which in turn have an effect on the viscosity of the solution since the polymer chains length will determine the amount the interactions between them in the form of the Van de Waals forces and chain entanglements [1]. Their relationship is expressed by the Mark-Houwink equation:

$$[\eta] = KM^{\alpha} \tag{1.7}$$

where $[\eta]$ is the intrinsic viscosity of the solution, M is the molecular weight of the dissolved polymer, K and α empirical constant to be determined for each polymer-solvent system. In the electrospinning process the viscosity of the solution plays an important role in determining the range of concentrations from which continuous fibers can be obtained. For solutions with low viscosities, surface tension is the dominant factor and just beads or beaded fibers are obtained. For low molecular weight liquids there is a capillary breakup of the spinning jet by surface tension. For polymer solution the pattern of the capillary breakup is changed radically. Instead of breaking rapidly, the filaments between the droplets are stabilized and a stable beads-on-string structure is formed. The reason for this is that the coiled macromolecules of the dissolved polymer are transformed by the elongational flow of the jet into oriented, entangled networks that persist as the fiber solidifies. The contraction of the radius of the jet, which is driven by the surface tension,

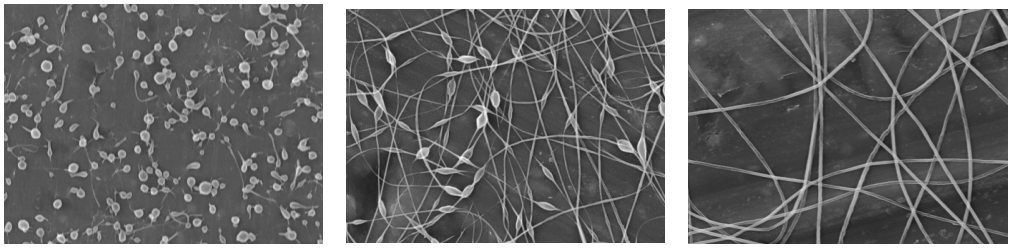

(a) 13 centipoise **(b)** 160 centipoise **(c)** 1835 centipoise

Figure 1.5: *Effect of solution viscosity on the morphology of electrospun polyethylene oxide (PEO) nanofibers. Image reproduced from* [54]

causes the remaining solution to form beads. As can be seen from Figure 1.5 when the viscosity of the solution is increased, the beads become bigger, the average distance between the beads is longer, the fiber diameter larger and the shape of the beads changes from spherical to spindle-like, while the diameter of the fibers become smaller [54]. Decreasing the surface tension makes the beads disappear gradually. From a theoretical point of view the phenomenon can be described according to the classification of the polymer solutions into four concentration dependent areas:

- the dilute regime;
- the un-entangled semi-dilute regime;
- the entangled semi-dilute regime;
- concentrated regime.

In the dilute regime, where $c < c^*$ (c^* is the critical chain overlap concentration), the polymer chains are individual, well separated, chains. When the concentration is increased, the chains start to overlap at the critical chain overlap concentration (c^*). Above this concentration is the semi-dilute regime ($c > c^*$), which is divided into un-entangled and entangled semi-dilute regime. The boundary between the unentangled semi-dilute regime and the entangled semi-dilute regime is the critical entanglement concentration, c_e, and is the concentration where polymer chain entanglement starts to occur. The reason why chain entaglement does not occur until c_e is reached compared to c^* is that a significant amount of overlap is necessary for polymer chains to entangle. The unentangled semi-dilute regime is defined as $c^* < c < c_e$ and here the polymer chains partly overlap but not enough for entanglement. A critical minimum concentration c_e is needed to allow molecular chain entaglements and for electrospinning to proceed. This critical minimum concentration is defined as the minimum concentration required for forming beaded nanofibers. Concentrations below c_e will produce droplets when electrified(electrospraying). At concentrations above c_e electrospun fiber diameter increases and frequency of bead-on-string formation decreases with increasing concentration [55]. However four different concentrations should be noted:

- for low concentration electrospray occurs instead of electrospinning, leading to the formation of polymeric micro or nano-particles;

- with a little higher concentration, a mixture of beads and fibers will be obtained;
- at a suitable concentration, smooth nanofibers can be obtained;
- for very high concentration helix-shaped micro-ribbons will be observed.

At a given value of viscosity the regime of the process changes from spraying to spinning thanks to the viscous forces of the solutions which oppose to the electric forces that tend to promote the formation of drops due to the repulsive forces exerted by charges of the same sign transported in the jet. The operative upper limit is represented by high concentration of polymer chain up to a value over which processing is prohibited by an inability to control and maintain the flow of a polymer solution to the tip of the needle and by the cohesive nature of the high viscosity as well as the drying of the solution after a short time from the process beginning [56]. At high concentrations also a smaller deposition area can be obtained since the high viscosity of the solution discourage the bending instability of the jet, which in turn determines a lower stretching and higher fiber diameters [57].

1.5.1.3 *Solution conductivity*

The deformation of the pendant drop at the syringe tip, the following formation of the electrospun jet, its stretching and the bending instability are phenomena caused by the Coulombic force established between the charged particles present in the solution and the force due to the external electric field. Both these forces are related to the superficial charge present in the jet, which can be modified by changing the solution conductivity. The common method to increase this property is the addition of ionic species to the solution, usually salts [58]. Their presence determines an increase in the amount of charge density carried by the jet and thus, stronger elongation forces are imposed to the jet due to the self-repulsion of the excess charges under the electric field, resulting in a substantially straighter shape and smaller diameters of the electrospun fibers [59, 60]. Zong *et al*. [61] observed that beyond the quantity of charge present in the solution even the dimension of the ions has a certain influence. Ions with a lower atomic radius have an higher mobility and produce a solution with an higher charge density under the effect of the same electric field.

Angammana *et al*. [62] have shown how certain solutions with high conductivity do not lead to the formation of the Taylor cone since in that condition, although the normal stresses are unaltered, it lead to the decrease of the tangential electric field (namely of the electrostatic force that acts along the surface of the liquid) which dominates the effect linked to the increase of the surface charge density. Moreover they have noticed a linear decrease of the fiber diameter with the increase of the conductivity thanks to the fact that this feature is linked to the stretching in the whipping region, which increases at the expense of the length of the linear tract of the jet, determining an higher time of flight of the last.

The solution conductivity depends also on the solvent conductivity. The addition of a solvent with an higher dielectric constant to a polymer solution in order to improve its electrospinnability might lead to an interaction between the solvents that can affect the

morphology of the resultant fibers. Solutions prepared using solvents of higher conductivity generally yield fibers without beads while from solutions characterized by zero conductivity no fibers are obtained [63]. However Wannatong *et al*. [64] have shown for the case of polystyrene solutions that the addition of a solvent with an higher dielectric constant (dimethylformamide) is capable to lead to the formation of beads even though it improves the electrospinnability. This behavior can be explained as a result of the little interaction between PS and the solvent molecules, thus other factors can influence the effect of the solvent conductivity.

1.5.1.4 *Solvent dielectric constant*

The dielectric constant of the solvents may influence the electrospinning because it affects the stability of the jet in terms of bending instability. The dielectric constant is a measure for the polarity of the solvent. Charges have a much greater effect to polar solvent than to a non-polar one. It is considered that solvents with a larger dielectric constant have a higher net charge density in solution and then results in thinner electrospun fibers [65]. Sun *et al*. [66] have highlighted that a careful choice can eliminate the onset of the bending instability and that the bending instability is promoted by high conductive solvents. Solvents with low dielectric constant and high purity are thus able to produce fibers with an high degree of spatial orientation

1.5.1.5 *Surface tension*

In order to produce fibers with the electrospinning process it is important that the solution charged by the effect of the applied electric field is capable to overcome its surface tension. However, once that the jet is formed, the surface tension can still have a negative effect. It is important to remember that the surface tension has the effect to decrease the surface area for mass unit, changing the shape of the jets into spheres and producing the formation of beads and beaded fibers. On the other side the repulsion due to the presence of charges into the polymer jet tends to increase the surface area, leading to the formation of thinner fibers [54]. The result of the competition between this two forces is influenced by the viscoelastic force of the polymer solution, which can resists to rapid changes in shape. In the case of a low viscous solution, the interactions between the solvent molecules and the polymer chains are limited, thus, there is a huge quantity of free solvent molecules that tents to agglomerate between each other by the action of the surface tension. This does not happen in the case of more viscous solution, where the interactions between the solvent and the polymer are more significant. When the solution is stretched under the effect of an electric field the solvent molecules are distributed on the polymeric chains (which in turn interact between themselves by the entaglements): in this manner there is a reduction of the solvent molecules tendency to interact between each other to form agglomerates produced by the surface tension. The formation of smooth fibers is favored by the employment of solution with low surface tension. To reduce the surface tension of the solution it is possible to choose solvent with low surface tension, or introducing surfactants in the solution.

1.5.2 Process parameters

1.5.2.1 *Voltage*

The electrospinning process starts at a threshold voltage capable to induce the polarization of the fluid or of the solution that comes out from the tip of the nozzle. When the electrostatic force is capable to overcome the surface tension there is the formation of the Taylor cone and the jet of solution. According to the flow rate and the polymer solution viscosity this critical voltage has to be varied in order to allows the stability of the jet itself. However Doshi and Reneker [67] have pointed out that a stable electrospinning jet can only be obtained in a smalle range of voltages for a polymer solution. If the voltage is too high the jet becomes instable and multiple jet can be ejected. Regarding the effects of the variation of the applied voltage above the threshold value there is a controversy in the scientific literature between those who affirm that there is not a substantial effect on the diameter of the resulting fiber [68] and those who claims that the increase of the applied tension leads to the increment of the ejected material and this leads to the formation of fibers with an high diameter [10, 69, 70] and, finally, those that claims that an increase of the applied tension determines the increase of the repulsion forces in the fluid and, thus, favors the thinning of the fiber and the acceleration of the solvent evaporation [71, 72].
Kessick *et al.* [73] performed the electrospinning of PEO solutions using both DC and AC potential, observing that in latter there was a significant reduction in the amount of fiber whipping and the resulting mats exhibited an high degree of fibers alignment, but with an higher amount of residual solvent. They suggested that with alternating potential the net charge on the fiber is reduced and the AC spun fiber should consist of short charge segments of alternating polarity, with the length of the charge segments depending on the fiber production rate as well as the frequency of the AC potential.

1.5.2.2 *Flow rate*

The flow rate of a polymer melt or solution influences the jet velocity and the solvent evaporation during the electrospinning process. For a given voltage, there is a corresponding flow rate if a stable Taylor cone is to be maintained. An increase in the feed rate results in a greater fiber diameter or beads size as well as a longer time for the jet drying due to a major volume of solution that comes out of the tip of the needle. The eventual residual solvent may cause the fibers to fuse together where they make contact forming webs.

1.5.2.3 *Type and geometry of the collector*

In most electrospinning setup, the collector plate is made out of conductive material such as aluminum foil which is electrically grounded so that there is a stable potential difference between the source and the collector. In the case when a nonconducting material is used as a collector, charges on the electrospinning jet will quickly accumulates on the collector which will result in fewer fibers deposited [42, 74]. Fibers that are collected on the nonconducting material usually have a lower packing density compared to those collected on a conducting surface. This is caused by the repulsive forces of the accumulated charges

on the collector as more fibers are deposited. For a conducting collector, charges on the fibers are dissipated thus allowing more fibers to be attracted to the collector. The fibers are able to pack closely together as a result [74]. Collectors can be stationary, such as metal plates or parallel electrodes, or rotating-type disks or mandrels [10]. Generally speaking with static targets it is possible to obtained randomly oriented webs of fibers whereas aligned fibers [75] are collected on spinning substrates rotating at very high velocities (from hundreds to thousands of rpm). A rotating collector provide an increase in the rate of evaporation of the solvents on the fibers, aiding the increase in the yield of dry fibers. Li *et al*. [75] analyzed the effect of the rotating speed of a metal rotating wheel collector on the average fiber diameters of a PAN solution in DMF. By simply starting the rotation of the collector to a few tenth of rpm the fiber average diameter halved their values and slightly decreased linearly by progressively increasing the speed up to 300 rpm. A more pronounced effect was found on the degree of fibers' alignment, with an exponential decrease of the fiber average angle by increasing the speed velocity of the wheel. Collector geometry can influence mat morphology, such as fiber alignment and pattern but no significant differences in fibers diameter have been observed until now.

1.5.2.4 *Distance between the collector and the tip of the syringe*

By changing the distance between the tip and the grounded collector both the time required for the jet to reach the collector and the electric field force are changed. Decreasing this distance allows the jet to experience a lower travel distance, while the higher intensity of the electric field produces an increase of the acceleration towards the collector. This conditions leads to the decrease of the amount of solvent evaporated and lowers the stretching and elongation of the fibers, which will have higher diameters. On the other hand an excessive distance between the tip and the collector decreases the intensity of the electric field leading to the reduction of the fiber stretching. For higher distances there is no deposition of fibers. As a consequence given a fixed electric field, it is necessary to identify the distance that allows to minimize the fiber stretching and the evaporation of the solvent in order to obtain fibers as thin as possible.

1.5.2.5 *Needle diameter*

The needle diameter has a certain effect on the diameter of the fibers produced by electrospinning. Small diameters reduce the possibility of clogging at the tip of the needle and lead to a less exposition of the solution to the external environment during the process. Decreasing orifice radius tends to decrease the average fiber diameters [76]. Wang *et al*. [77] electrospun solutions of PAN with different needle diameters and find out that the size of the Taylor cone and the electrified jet are apparently increased with an increase in the needle diameter. They observed that the fiber diameter increased from 256 to 502 nm, accompanied by a lower drawability and less birefringence, when the needle diameter was increased from 0.57 to 2.77 mm.

1.5.3 Environmental parameters

The effect of the electrospinning jet surrounding is one area which is still poorly investigated. Any interaction between the surrounding and the polymer solution may have an effect on the electrospun fiber morphology. High humidity for example was found to cause the formation of pores on the surface of the fibers. Since electrospinning is influenced by external electric field, any changes in the *electrospinning* environment will also affect the electrospinning process.

1.5.3.1 *Temperature*

The temperature has double effect in the electrospinning process since it leads to an increase in the solvent evaporation rate and reduces the viscosity and surface tension of the polymer solution [77], producing opposite effects [78].
With a lower viscosity the Coulombic forces are able to exert a greater stretching force on the solution determining fibers of smaller diameters. Demir *et al*. [70] also reported an increase in the deposition rate with increasing temperature, resulting in higher thickness of the nonwoven mat. Attention must be paid in cases where biological substances such as enzymes and proteins are added to the solution for the electrospinning, which are quite thermosensitive. Usually electrospinning is carried at room temperature but particular situation can requires higher temperatures, like in the case of melt electrospinning.

1.5.3.2 *Humidity*

The humidity of the electrospinning environment may have an influence in the polymer solution during electrospinning, but its extent depends on the chemical nature on the polymer [78, 79]. At high humidity, it is likely that water condenses on the surface of the fiber when electrospinning is carried out under normal atmosphere. As a result, this may have an influence on the fiber morphology especially polymer dissolved in volatile solvents [71, 80]. An example is the formation of pores on electrospun nanofibers at high humidities. This is due to water vapor that condenses on the surface of the jet due to cooling of the surface of the jet as a result of rapid evaporation of the volatile solvent.
The humidity of the environment also determines the rate of evaporation of the solvent in the solution. At a very low humidity, a volatile solvent may dries very rapidly and if the evaporation of the solvent is faster than the removal of the solvent from the tip of the needle the electrospinning process may only be carried out for a few minutes before the needle tip is clogged [27].

1.5.3.3 *Pressure*

Under enclosed condition, it is possible to investigate the effect of pressure on the electrospinning jet. Generally, reduction in the pressure surrounding the electrospinning jet does not improve the electrospinning process. When the pressure is below atmospheric pressure, the polymer solution in the syringe will have a greater tendency to flow out of the needle and there causes unstable jet initiation. As the pressure decreases, rapid bub-

bling of the solution will occur at the needle tip. At very low pressure, electrospinning is not possible due to direct discharge of the electrical charges.

1.6 THEORETICAL MODELS

As previously stated, Taylor introduced the concept of critical voltage and determined its evaluation; thus the critical voltage is the voltage value that, if all parameters are maintained constant, deforms the shape of the solution drop at the tip of the needle until it forms a cone (the Taylor cone) and remains in equilibrium under the action of the electric field and of the surface tension. The critical voltage is given by:

$$V_c^2 = \left(\frac{4L^2}{h^2}\right)\left[\ln\left(\frac{2h}{R}\right) - 1.5\right](0.117\pi R\gamma) \tag{1.8}$$

where V_c is the critical voltage, h is the length of the needle, R is the inner diameter of the needle, L is the distance between the tip of the needle and the collector and γ is the surface tension. It is important to note that the formula just shown does not take in consideration neither the conductivity nor the viscosity of the solution; however, it can be employed as a reference in the case of solutions with medium/low viscosities and little conductive. A similar relation was found by Hendricks *et al.* [81] for the potential required for the electrostatic spraying from a hemispherical drop pendant from a capillary tube:

$$V = 300\sqrt{20\pi\gamma r} \tag{1.9}$$

Rayleigh defined the relation between the radius of the jet and the parameters of the process:

$$r_j = \left(\frac{9d\gamma}{2\pi^2}\right)^{\frac{1}{3}}\left(\frac{f}{i}\right)^{\frac{2}{3}} \tag{1.10}$$

where r_j is the jet radius, i is the injection current, f is the solution flow-rate, γ is the solution surface tension, d is the solution permittivity. In 1971 Baumgarten [27] observed that the increase of the viscosity causes an increase of the fiber diameter, according to:

$$d \sim \eta^{0.5} \tag{1.11}$$

where d is the diameter of the nanofibers and η is the viscosity of the solution.
Other studies [1] report quantitative methods capable to evaluate the optimal conditions to realize the electrospinning process, trying to analyze the different aspects involved, such as shape and charge density of the jet that exits from the capillary. These methods are based on the mass, momentum and charge conservation equations and their basic starting equation are shown in next paragraphs.

1.6.1 Momentum conservation

For the conservation of momentum:

$$\rho\pi D^2 v^2(dt)|_z - \rho\pi D^2 v^2(dt)|_{z+dz} + p\pi D^2(dt)|_z - p\pi D^2(dt)|_{z+dz} = 0 \tag{1.12}$$

where p is the fluid pressure. From this equation we have:

$$\frac{\partial v}{\partial t} + v\frac{\partial v}{\partial z} = -\frac{1}{\rho D^2}\frac{\partial p D^2}{\partial z} \tag{1.13}$$

The equation below provides the balance obtained by Feng [82], which is more detailed since it takes in consideration more phenomena and factors which can influence the jet behavior:

$$\frac{d}{dz}(\pi D^2 \rho v) = \pi D^2 \rho g + \frac{d}{dz}[\pi D^2(-p + \tau_{zz})] + \frac{\gamma}{D}2\pi D D' + 2\pi D(t_t - t_n D') \tag{1.14}$$

where g is the gravity acceleration, γ is the surface tension, D' is the distance between the surface of the jet and the the axis of the jet, t_t and t_n are forces of traction, tangential and normal to the jet surface respectively, due to the electric field.

1.6.2 Mass conservation

Let's consider an infinitesimal small portion of jet of length dz; the mass contained in the jet is given by:

$$m = \rho\pi D^2(dz) \tag{1.15}$$

where ρ is density of the solution and D is the diameter of the jet. After an infinitesimal time interval dt we have:

$$\rho\pi D^2 v(dt)|_z - \rho\pi D^2 v(dt)|_{z+dz} = 0 \tag{1.16}$$

where v is the velocity of the liquid. From this equation follows that:

$$\frac{\partial D^2}{\partial t} + \frac{\partial D^2}{\partial z} = 0 \tag{1.17}$$

1.6.3 Charge conservation

Feng [82] has proposed the relation for the charge conservation:

$$I = \pi D^2 K E + 2\pi D v\sigma \tag{1.18}$$

with I is the electric current, K is the liquid conductivity, E the vertical component of the electric field, σ the surface charge density.
The forces involved have to satisfy the second law of Newton and Reneker (2000) suggested a model which, however, doesn't take into account of the jet instability:

$$m\frac{d^2P}{dt^2} = f_C + f_B + f_V + f_S + f_A + f_G \tag{1.19}$$

in which the different components are given by:

- Coulombic force (f_C)

$$f_C = \frac{e^2}{l^2} \tag{1.20}$$

- Electric force (f_E)

$$f_E = -\frac{eV}{L} \tag{1.21}$$

- Viscoelastic force (f_V)

$$f_V = \frac{d\sigma_V}{dt} = \frac{G}{l} - \frac{dl}{dt}\sigma_V \tag{1.22}$$

- Surface tension (f_S)

$$f_S = \frac{\alpha\pi D^2 k}{\sqrt{(x^2+y^2)}}\left[i|x|sign(x) + j|y|sign(y)\right] \tag{1.23}$$

- Frictional force with air (f_A)

$$f_A = 0.65\pi D\rho_{air}v^2\left(\frac{2\nu D}{\nu_{air}}\right)^{-0.81} \tag{1.24}$$

- Gravitational force (f_G)

$$f_G = \rho g\pi D^2 \tag{1.25}$$

where e is the electric charge, l is the length of the ideal straight jet, V the potential difference, L the distance between the drop and the collector, σ_V the viscoelastic tension, G the elastic modulus, η the viscosity, α the coefficient of the surface tension, k the jet curvature, ρ the density and ν the kinematic viscosity.

1.7 APPLICATIONS OF ELECTROSPUN NANOFIBERS

The interesting properties related to the possibility to obtain nanometric fibers from electrospinning, its simplicity and versatility along with the wide range of different materials which can be processed allow their employment for several potential applications, ranging from nanofiber-based filtration to the biomedical area, which represents the main research

Figure 1.6: *Potential applications of electrospun nanofibers*

field of applications of nanofibers up to now. A summary of these applications is shows in Figure 1.6.

The growing interest towards the applications of electrospun nanofibers is confirmed by the constantly increasing rate of the published scientific contribution (Figure 1.7). So far more than 2500 articles with a peak of more then 1.4×10^4 citations per year.

Broadly speaking it is possible to identify four main areas of interest: Bioengineering, Environmental Engineering and Biotechnologies, Energy and Electronics and, finally, Defense and Security [1]. Most of these applications have not already reached their industrial level, but just a laboratory research and development stage. However, their promising potential has attracted the attentions from academia and industry and the continuous effort in the development of the available technology for nanofibers production si expected to rapidly transfer electrospinning processes and products toward commercialization [83].

1.7.1 Bioengineering

Nanofibers research applications in the biomedical field have a multifaceted perspective spreading between tissue engineering, drug delivery and wound dressing [84–86]. Tissue engineering is an emerging multidisciplinary area in which nanofibers represent an important advancing front for the production of suitable scaffold of different materials that can

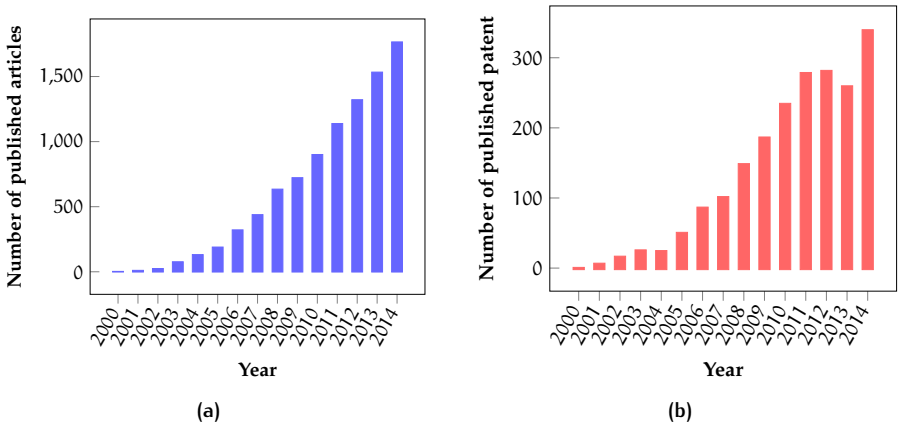

Figure 1.7: *(a) Statistics of published research articles about electrospun polymer nanofibers (keywords:"polymer", "nanofibers" and "electrospinning", from 2001 to 2014, Web of Science Database). Source: Thomson Reuters Web of Knowledge., (b) Statistics of published patents on polymer nanofibers made by electrospinning (keywords: "polymer", "nanofibers," and "electrospinning", from 2001 to 2014), as provided by WIPO-PATENTSCOPE*

mimic natural extracellular matrix. To this purpose electrospun nanofibrous membrane (ENMs) have been tested as natural, synthetic and composite scaffold [87] for different type of targeted tissue [88] including blood vessel, cartilage, bone, nerve and many others. The small diameter of the fibers and their high surface area are beneficial for cell attachment and bioactive factor loading, enhancing cell growth. Drug delivery membranes incorporate a drug component that can be patched on wound of surgery or encapsulated into pharmaceutical capsules to deliver the drug through the digestive system of the patient. Polymeric electrospun drug delivery systems are advantageous for such task because they can deliver drugs efficiently to a localized area, with the possibility to vary the release rate by simply varying the fiber diameter or the loading dosage. The possibility of choosing different materials, processes and processing conditions allows to reach the desired encapsulation efficiency, preserving bioactivity [89]. Several drugs has been incorporated successfully into electrospun media obtaining better performance over normal cast film and with the possibility to load insoluble drug for enhancing their dissolution [90]. ENMs have also exhibited potential in wound dressing thanks to the possibility to generate homogeneous scaffold, provide uniform adherence and wet wound surface without fluid accumulation. They can provide high gas permeation and protection from infection and dehydration, extending their applications on different types of wounds as compared to traditional wound dressing materials and opening new doors for the next generation of wound dressing materials [91].

1.7.2 Environmental engineering and Biotechnologies

ENMs high specific surface, porosity and permeability, tailorable thickness and fiber diameters are desirable features for filtration applications. These materials have been em-

ployed from several years for air filtration and recently, at a research level, even for microfiltration, ultrafiltration and nanofiltration in the field of water treatment. The advantages of electrospun nanofibers compared to conventional air-filter media are related to an higher filtration efficiency, lower pressure drops and energy savings. Indeed nanofibers with diameters lower than 0.5 μm have much higher capability to collect fine particles because of the slip flow that increases diffusion, interception and inertial impaction efficiencies, determining a lower drag force around the fibers and, thus, lower pressure drops. In addition this media are easy to clean, enabling to significantly extend the life of filters and reducing the maintenance costs. Their potentials have shown possible applications in air filtering media [92–94], especially for high-efficiency particulate and low penetration air filters, filters for transportation applications, adsorptive catalytic gas filter for respirators, filter media for pulse clean cartridges in dust collection and cigarette filter for smoke filtration. ENMs can be employed also for water treatment [95] and generally show high-flux rate and low trans-membrane pressure with performance comparable to those commercially available. The main interesting application in this area are related to desalination, VOC gas stripping [96], oil/water emulsion separation [97–101], microbial [102] and heavy metal removal [103–107]. However for solid-liquid filtration very high surface to volume ratios promotes membrane fouling. For this reason and for improving membrane performances ENMs can be surface modified [108, 109], in order to add functional groups or functionality, with process like in situ, graft and interfacial polymerization, plasma treatment, wet treatment, coating and blending with surface modifying agents. A main drawback for the employment of electrospun nanofibers for such applications is their mechanical strength which is not sufficient to withstand macroscopic impact during filtration application such as normal liquid or air flows passing through them. Hence, they need to be used as active coating layer on existing melt blown supportive fibrous media (composite membrane) or the fibers need to be bonded to enhance mechanical properties.

1.7.3 Energy and Electronics

Another area in which ENMs can have promising applications is that of energy related applications and devices [93, 110, 111], especially for polymer fuel cell and lithium ion batteries electrolyte membranes. Research efforts on polymeric proton exchange membranes for fuel cells have led the interest of researchers towards the employment of ENMs as porous reinforcing mats to minimize in-plane swelling and shrinking [112]. Nanofibers can also be able to increase proton conductivity with respect to bulk film, thanks to their highly oriented ionic domains [110], and provide good mechanical strength while the remarkable flexibility of their production process allows to adequately tailor their final morphology for composite membranes. Fuel cells membranes are semipermeable membranes that have the function to be proton conductive, electron insulating and dense in order to avoid fuel crossover. For this reason two types of approaches can be used when employing electrospinning for such application. The first is related to the electrospinning of non-conductive or less conductive polymer into a porous matrix, which acts as mechanical reinforcement when the pores are filled with a highly proton conductive component. Alternatively, a

highly proton conducting matrix is electrospun into a porous fiber mat and subsequently reinforced with a secondary polymer to provide mechanical stability. The proton conductive polymers are usually chosen between perfluorosulfonic acid [113–117] or sulfonated polymers [118, 119] that can be coupled with organic [120, 121] and inorganic particles [122, 123] as conductor enhancers or to improve strength and hydrophilicity. Electrospun mats are also attractive alternatives to polymer gel electrolytes for lithium-ion batteries, since they can be employed as matrix in which the electrolyte can be encapsulated improving ionic conduction across the membrane and mechanical strength, while providing good water uptake. In these field the most widely studied polymer has been poly(vinylidene fluoride) (PVDF) thanks to its good electrochemical and thermal stability. However PVDF based gel polymer electrolyte with its high crystallinity limits the ion migration, lowering the battery performance. ENMs with their porous membrane are capable to overcome this problem and PVDF and other alternative polymers [124, 125] and blend [126, 127] have been explored by electrospinning with encouraging results.

1.7.4 Defense and Security

In the field of defense and security nanofibers found application in the protective clothing from chemical and biological agents and different types of sensing devices [93],[128] (including acoustic, wave, resistive, gravimetric, photoelectric, optical and amperometric). current protective clothing is based on full barrier protection suits or permeable adsorptive protective overgarments with obvious limitations in terms of weight and moisture retention. The nanostructured of ENMs are considered ideal for such applications due to their light weight, high surface area, and breathable (porous) nature[129]. Besides they can provide site-specific *in vivo* prophylaxis and they can bt surface modified to enhance their capture and decontamination capability of warfare agents.
The characteristics of ENMs also match well the requirements for sensors thanks to their high surface area which has the potential to provide unusually high sensitivity, fast response time and lower detecting limits. In this case different approaches can be employed to provide a sensing capability to nanofibers, such as electrospinning of a polymeric sensing material, incorporation of sensing molecules into nanofibers or application of sensing material on nanofiber surface via coating/grating technique, employing organic and inorganic polymer.

1.8 ELECTROSPRAY

The essential features of electrospinning are also common to electrospraying. The main difference between the two processes is centered around the role of chain entaglements and the resulting elongational viscous forces that are present in polymer solutions. This results in the production of a fiber, opposed to the production of droplets due to the Coulombic explosion of a supercharged drop of solution at the end of a tip (Figure 1.8).
There are many modes of electrospray (Figure 1.9):

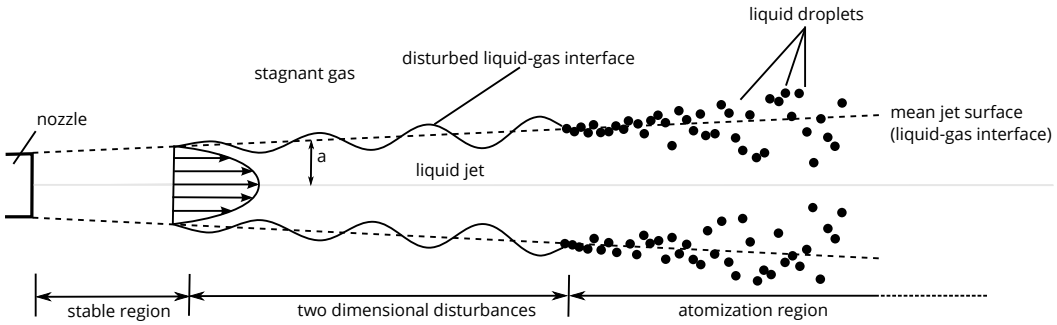

Figure 1.8: *Representation of the electrospray process*

- dripping and microdripping, when spherical droplets detach directly from the Taylor cone;
- spindle and multispindle mode, in which the jet is elongated into a thin filament before it breaks into droplets;
- oscillating or cone-jet mode, in which drops are emitted from a twisted or non-twisted jet attached to the nozzle:
- precession mode, in which a rapidly whipping jet is emitted from the nozzle, before its breaks into droplets.
- multijet mode, where multiple jets are emitted from the nozzle without formation of a visible cone

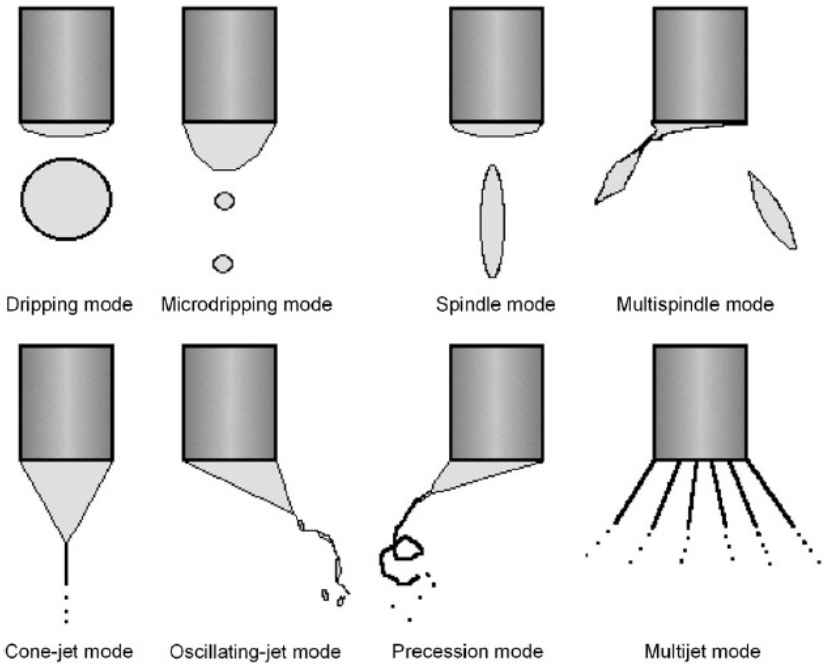

Figure 1.9: *Representation of the electrospray process*

Between them the most important mode is the cone-jet mode where the liquid meniscus assumes the form of regular, axisymmetric cone with a thin jet (< 100 μm in diameter) at its apex, stretching along the capillary axis. The end of the jet undergoes instabilities of one of two types: varicose and kink [130]. Polydisperse droplets and resulting particles can be obtained in the precession, multijet, or the cone-jet with kink instabilities modes of spraying. Production of particles of uniform size can be accomplished by generation of the cone-jet mode with varicose instabilities or the microdripping mode [131–133]. This modes of spraying depend on liquid properties such as conductivity, surface tension, and viscosity, and on the voltage and liquid flow rate. However, the conditions for generating a required mode of spraying, and the size of the droplets obtained in each mode cannot be predicted from the liquid parameters.
Although not commonly employed for nanoparticles deposition, electrospray possesses several are the advantages with respect to other conventional mechanical spraying systems [134]:

- Droplets have size smaller than those available from conventional mechanical atomisers, and can be smaller than 1 μm;
- The size distribution of the droplets is usually narrow, with low standard deviation; droplets can be of equal size only for dripping and microdripping modes, or for Rayleigh jet breakup due to varicose wave instability;
- Charged droplets are self-dispersing in the space, that results in absence of droplet agglomeration and coagulation;
- The motion of charged droplets can be easily controlled (including deflection or focusing) by electric fields;
- The deposition efficiency of charged spray on an object is much higher than for uncharged droplets.

The main drawback in the application of electrospray, which limits its widespread use in industry, is the low throughput. Some industrial applications, for example electrostatic painting or coating, fuel atomization, agriculture chemical spraying or electrostatic scrubbing require much larger amount of liquid than that produced by a single nozzle. To overcome this problem several solution have been proposed such as multi-nozzle or slit-nozzle systems and mechanical atomizers (pneumatic, or rotary) with induction charging. The main applications of the process are related to the deposition of ultra-thin films of organic, inorganic and biological materials, generation of nanoparticles and quantum dots, promotion of the dispersion and delivery of nanomaterials. Commercial applications of electrospray regards the field of mass spectrometry, painting and inkjet printing. Electrospray ionization mass spectrometry (ESI-MS) in a popular technique for the characterization of biomolecules, pharmaceutical, coordination complexes, supramolecular assemblies and organometallic catalysts [135, 136]. Electrohydrodynamic spraying it is also considered an alternative process to inkjet printing due to its possibility to provide high resolution patterning and lower size of the jetting needle, while it is extensively used in the biotechnology field to process cells and biological material [137].

2 INDOOR POLLUTION & PHOTOCATALYSIS

The present chapter provide a first introduction to the topic of indoor pollution, specifically to the presence of organic pollutant in confined environments. The main sources of pollution are presented as well as the effect on human health. Finally the principal techniques for VOCs abatement are reviewed with particular emphasis on the employment of photocatalysis.

2.1 INDOOR POLLUTION

Until the late 1960s the attention to air quality was primarily focused on the outdoors because, by that time, outdoor pollution was considered responsible for many adverse health effects. In the early 1970s scientists started to investigate the cause of complaints in indoor working environments. U.S. Environmental Protection Agency (EPA) studies of human exposure to air pollutants indicated that indoor air levels of many pollutants may be two to five times, and occasionally, more than 100 times higher than outdoors levels [138]. Over the past several decades, our exposure to indoor air pollutants is believed to have increased due to a variety of factors, including the construction of more airtight buildings, reduced ventilation rates to conserve energy, the use of synthetic building materials and furnishing, and the use of chemically formulated personal care products, pesticides, printing inks and household cleaners. The importance of indoor air quality has become an important community concern also due to the increased amount of personal time spent in indoor environment. Today, people in industrialized countries spend more than 90% of their lifetime indoors [139]. The increasing attention to indoor air quality has contributed to the awareness of poor health associated to indoor environment. Two main illnesses are related to poor indoor air quality: sick building syndrome (SBS) and building related illness (BRI). SBS can be defined as the discomfort or sickness associated with poor indoor environments with no clear identification of the source substances. Symptoms of SBS include irritation of sensory organs, eyes, nose, throat, ears, skin, fatigue, headache, respiratory disorders and nausea [140]. BRI is defined as a specific, recognized disease entity caused by some known agents that can be identified clinically [141]. Symptoms of BRI include hypersensitivity, pneumonities, humidifier fever, asthma and legionella.
In general, three methods are suggested to improve the indoor air quality, namely source control, increase ventilation, and air cleaning. Source control is often ungovernable and unavoidable in the metropolis. Increased ventilation might even transport more pollutants from the outdoor environment. Thus, air cleaning remains to be the most feasible option

to improve the indoor air quality.
The determination of the pollution in closed environments can be realized by qualitatively and quantitatively detecting the polluting agents whose presence is suspected. Generally it is necessary to proceed with a gas phase sampling which is subsequently analyzed. The research of biological agents is done by favoring the growth in specific culture medium of microorganisms taken from conditioning and ventilation systems.
In Italy a specific legislation for the control of air in closed environments is not presents but, after an agreement between the Ministry of Health, regions and districts, a series of guidelines for the protection and promotion of health in confined environments have been defined (Gazz. Uff. Suppl. Ordin. n. 276, 27/11/2001). These guidelines provide fundamentals informations for the evaluations and managing of the health risks connected to the pollution in indoor air and technical advices to define the prevention actions for the control of such risks. For example, it is useful to construct or renovate buildings by their hygienization, make them compatible with the environment, energy efficient and define a periodical maintenance of the air conditioning and ventilation systems. At the same time it is important incentivize healtier lifestyles, develop products which are significantly less hazardous to health or capable to reduce the damage to the environment. In this context it is of primary importance to prohibit and discourage smoking. In the domestic environment it is possible to use detergents and disinfectants equally effective but less irritant and toxic than those containing chlorine, ammonia and formaldehyde. Between painting products it is possible to chose water based colors, which give the same durability of the traditional products based on organic solvents. Moreover there are many other potentially hazardous products in this context like pesticides, stain removers, some types of glues, *etc.*, whose employment should always be done according to the safety procedures defined in the corresponding user's manual.

2.2 VOLATILE ORGANIC COMPOUNDS (VOCS)

Volatile organic compounds (VOCs) are chemical compounds characterized by molecules with different functional groups, different physical and chemical behavior, but characterized by a given volatility interval. VOCs are classified both as the hydrocarbons that contain carbon and hydrogen as unique elements and as compounds containing oxygen and chlorine or other elements such as aldehydes, ethers, alcohols, esters, chlorofluorocarbons (CFC) and hydrochlorofluorocarbons (HCFC). They are defined by the Italian legislation as volatile organic compounds that have a vapor pressure of 0.01 kPa or more at 293.15 K (20°C).
According to the World Health Organization (WHO) VOCs are compounds with a boiling point in the 50-260°C range with the exclusion of pesticides. The WHO has divided these organic compounds into three categories on the basis of their boiling temperature:

- very volatile organic compounds (VVOCs);
- volatile organic compounds (VOCs);

- semi-volatile organic compounds (SVOCs).

Such subdivision, in terms of boiling point range, is reported in Table 2.1.

Table 2.1: *Classification of volatile organic compounds according to the (WHO)*

Compounds	Boiling point range [°C]	Examples
Very volatile organic compounds	from <0 to 50-100	Propane, Buthane, Chloromethane
Volatile organic compounds	from 50-100 to 240-260	Acetone, Toluene, Methanol
Semi-volatile organic compounds	from 240-260 to 380-400	Pesticides

In Table 2.2 [142] are reported the main classes of organic pollutants that pertain to the indoor pollution, with the relatives emission sources while in Table 2.3 [143] are reported the sources of emission for single organic compounds. The health effects due to the exposure to organic volatile compounds depend on the duration to the exposure, frequencies of exposures, type and concentration of the pollutant. Frequent and prolonged exposures to VOCs like benzene, p-dichlorobenzene, chloroform, methyl chloride *etc*. can lead to the development of cancers. For such reason it is of fundamental importance the study of their abatement with innovative processes.

Table 2.2: *Volatile organic compounds: classes and main emission sources. 1: Established buildings, 2: new and renovated buildings, 3: school, 4: new car interiors, 5: carpets, 6: floor coverings, 7: wood-based panel and furniture, 8: solid woods, 9: paints, 10: cleaning products, 11: unflued gas heaters and electric ovens, 12: office equipment* [142]

VOC	Possible emission sources
Aliphatic and cyclic hydrocarbons	1,2,4,5,7,9-11
Aromatic hydrocarbons	1-7,9,11,12
Aldehydes	1-12
Terpenes	1-4,7-10
Alcohols	1-9,11
Esthers	1,2,4,7-9
Halocarbons	1,2,7,11
Ketones	1-4,6-12
Alkenes	2,7
Organic acids	2,3,7-9,11
Ethers	9
Others	1,2,4,7,11

2.2.1 Methanol

Methanol is the simplest alcohol, and is a light, volatile, colorless, flammable liquid with a distinctive odor.
In indoor environment different emission sources of methanol are present, like stain removers, aerosol and liquid paints. This compound (risk phrases: R11, R23/24/25 and R39) besides ingestion and skin contact it is toxic by inhalation. The methanol toxicity can be acute or chronic. The acute toxicity, which refers to the effects of a single dose or more

Table 2.3: *Indoor sources of volatile organic compounds* [143]

Compound	Source of emission
Acetaldehyde	Glues, deodorants, fuels, preventives, mold growth on leathers
Acrylic acid, esters, epichlorohydin,vinyl chloride	Monomers may escape from polymers
Acrolein	Component of oak-wood, by-product of the combustions of wood, kerosene and cotton
Alcohols	Aerosols, window cleaners, paints, paint thinners, cosmetics and adhesives
Aliphatic hydrocarbons	Paints, adhesives, gasoline, combustion products
Amines	Volatilized with the steam boiler systems (corrosion inhibitors of steam pipes and other equipment)
Aromatic hydrocarbons	Paints, adhesives, gasoline, combustion sources
Benzyl chloride	Vinyl tiles plasticized with butyl benzyl phthalate
Benzene	Smoking
Carbon tetrachloride	Industrial strength cleaners
Chlordane	heptachlor Termicide
Chloroform	Chlorinated water (showering, washing clothes, dishes)
Chloropyrifos (Dursban)	Household insecticides
Diazinon	Termicide
Ethers	Resins, paints, varnishes, lacquers, dyes, soaps, cosmetics
Esters	Plastics, resins, plasticizers, lacquers solvents, flavors, perfumes
Ethylene oxide	Sterilizers (hospitals)
Formaldehyde	Pressed wood products, foam
Ketones	Lacquers, varnishes, polish removers, adhesives
Lindane	Wood preservative formulations
Methylene chloride	Paint removers, solvent usage
p-dichlorobenzene	Moth crystals, room deodorants
Phthalic acid anhydride	Epoxy resins
PCBs	Transformers, PCB-containing fluorescent light ballasts, ceiling tiles
PAHs	Combustion products (smoking, woodburning, kerosene heaters)
Polychlorinated dibenzofurans	Incinerator stack emission
Polychlorinated dibenzo-p-dioxins	Contamination of pentachlorophenol used as wood preservative
Pentachlorophenol	Wood preservative agent
Styrene	Insulation, textiles, disinfectants, plastics, paints
Terpenes (limonene, α-pinene)	Scented deodorizers, polishes, fabrics, fabric softeners, cigarettes, food beverages
Tetrachloroethylene	Wearing or storing dry-cleaned clothes
Toluene diisocyanate	Polyurethane foam, aerosols
Trimellitic acid	Epoxy resins
Triethylene tetraamine	Epoxy resins
1,1,1-trichloroethane	Wearing or storing dry-cleaned clothes, aerosols sprays, fabric protectors
Volatile amines	Putrefactive degradation of casein-containing building materials

doses in a close time interval, determines sight problems (blurred vision) which can lead to blindness; also neurological problems, like mobility dysfunctions, can be a consequence. Chronic toxicity is related to exposure to small doses over time, which singularly do not

Table 2.4: *Toxicity levels for methanol defined by NIOSH (National Institute for Occupational Safety and Health)*

Exposure limits	Concentration [mg/m^3]
TLV-TWA	260
TLV-STEL	325
LD50 (mice,inhalation)	83200 (4h)

provide any adverse effect. It is the accumulation of the substance inside the organism which determines the toxic dose. The effect associated to the chronic toxicity of methanol are: headaches, dizziness, insomnia, nausea, digestive disorders, conjunctivitis, sight problems and blindness. The California Environmental Protection Agency (CalEPA) has calculated a chronic inhalation reference exposure level of 10 mg/m^3 based on developmental effects in mice [144]. Studies on the effects on human reproduction and development as a consequence of methanol inhalation are not present. However it has been calculated that in the case of mice the methanol leads to malformations of the skeletal apparatus, cardiocirculatory and central nervous systems. No information is available on the possible carcinogen effects both for humans and animals and at the moment methanol is not classified as carcinogen. Table 2.4 presents the limit values of the main toxicity parameters of methanol To that regard it is important to remember:

- TLV-TWA (*Threshold Limit Value-Weighted Average*): average exposure on the basis of a 8h/day, 40h/week work schedule;
- TLV-STEL (*Threshold Limit Value Short-Term Exposure Limit*): spot exposure for a duration of 15 minutes, that cannot be repeated more than 4 times per day with at least 60 minutes between exposure periods;
- LD50 (*Lethal Dose 50*): concentration of a substance which it is expected to cause the death (during the exposure or within a defined time consequently to the exposure) of 50% of the exposed animal for a given period of time.

Once present in the atmosphere the half life of methanol in vapor phase is equal to 17,8 days. From the reaction with hydroxyl radicals (present in atmosphere as a consequence of the photochemical reactions) it is possible to produce formaldehyde, a volatile organic compound which is suspected to be carcinogen. Thus the importance of methanol removal is not only related to reduce the effect produced by the compound but also to reduce the possible formation of formaldehyde.

2.3 VOCS REMOVAL TECHNIQUES

Herein is presented a set of techniques employed for the removal of volatile organic compounds. The last of these techniques is photocatalysis and, being of significant importance for the thesis work, it will be analyzed more in depth in specific paragraph

2.3.1 Incineration

This technique is based on the combustion of VOCs to obtain the oxidation of the pollutants to carbon dioxide and water, with efficiencies higher than 95%. The efficiency is dependent on several parameters, especially on the reactor residence time, temperature and turbulence. Two different type of incineration can be identified: thermal and catalytic. Thermal incineration has a vast field of applications and its operative conditions requires pollutant concentrations lower than 50% of the LEL (Lower Explosive Level) and, according to the compound to be removed, they requires temperatures between 870 and 1200°C and residence times between 0.87 and 2 s. The abatement efficiency varies between 95% and 99.99% where for the last oxidation percentage of abatement is necessary a residence time of at least 1 s. The catalytic incineration is realized in presence of a catalysts and in this case the operative conditions require pollutant concentrations lower than 25% of the LEL, temperatures comprised between 315 and 540-650°C, with spatial velocities (gas velocity/height of the catalytic bed) comprised between 10000 (alkaline metals) and 40000 (noble metals) h^{-1}. The operative temperature changes according to the compound to be treated while the spatial velocity is determined by the type of catalyst employed. The employed catalysts are noble metals oxides, like those of platinum and palladium as well as alkaline metals oxides, such those of vanadium, titanium or manganese.

2.3.2 Adsorption

In the adsorption processes the pollutant is removed from the gaseous stream in which is present by means of a solid material with adsorbent properties. Active carbons (GAC: granular activated carbon, PAC: powdered activated carbon) are generally employed, but also silica gel, molecular sieves, polymers and activated alumina can be employed. The abatement efficiency is high and with a properly designed carbon activated system it is possible to obtain efficiencies of 95-98%. The adsorption can be chemical of physical. The chemical adsorption involves the formation of chemical bonds between the adsorbate and the adsorbent and it is less employed, due to the difficult regeneration of the adsorbent material. In the physical adsorption the molecules of the pollutant interact with the adsorbent material by secondary electrostatic forces, remaining weakly trapped. The capacity of the adsorbent material to retain the compound to be removed is a function of several parameters, such as boiling temperature, concentration and molecular weight of the pollutant, humidity and eventual presence of particles in the gaseous stream which can obstruct the adsorption sites. Due to the necessity to regenerate the active carbon the abatement efficiency is not very high as for other techniques and to strip and recover the organic contaminant the active carbon employed should not adsorb more than 10-15% of pollutant in weight. The compound to be removed should not have an high boiling point (generally between 50 and 100°C) and the molecular weight should be at least higher than 50 g/mol in order to facilitate the subsequent recovery. An additional condition is the humidity of the gaseous stream to be treated which should not be higher than 50%, otherwise the water molecules can compete with pollutant adsorption and saturate the active carbon.

2.3.3 Condensation

If a gaseous stream rich in vapor is cooled, the molecular agitation lowers and the molecules increase their mutual interaction. The intermolecular electrostatic forces established between them at the dew point are responsible for the condensation phenomenon. A further decrease in the temperature determines a concurrent decrease in the pollutant concentration in gas phase. This technique generally produces efficiencies higher than 90%.
Three different typologies of condensation can be distinguished: conventional condensation, refrigeration and cryogenic condensation. The conventional condensation employs air or water in order to lower the temperature to 4°C. With refrigerants it is possible to reach -18°C. The condensers employed can be at direct contact or at surface. In the first case the gaseous stream and the refrigerant are directly in contact without the presence of any separating surface while the latter require an heat exchange which separates the two components. For what concerns refrigeration compressed coolants are employed and the operative temperatures arrive down to -100°C, while in the cryogenic condensation liquefied gases are employed, like nitrogen and carbon dioxide, obtaining temperatures down to -195°C.

2.3.4 Biofiltration

Biofiltration is a process employing an organic matrix (e.g. barks but also inert materials like clay or polyurethanes) containing microorganisms for which the pollutants present in a gaseous stream represent nutrients. Presence of sulfur or chlorine compounds leads to the formation of by-products like salts of various nature. The aim of the technique is the possibility to obtain the complete degradation of the pollutant with the formation of carbon dioxide and water as main products. Biofilters can be divided into conventional and engineered, with the latter possessing an higher surface area. The organic matrix through which the polluted stream passes is arranged in beds of variable height between 0.5 and 1.5 m in order to provide enough contact time with the pollutant (averagely 30 s) but at the same time to avoid an excessive packing due to the weight of the same bed. Above the filter water spraying jets are usually placed in order to humidify the mass, provide eventual nutrients necessary to the bacteria and to regulate the pH. The main limitations of the technique are the high contact times with respect to other techniques and the possible presence of hazardous compounds for the microorganisms in the biological matrix which limits its applicability. The labour is not significant but at the same time it is necessary to provide reshuffling of the bed by mechanical devices which is usually done once a year. Biofilters are thus useful because they can treat very different streams, operate at ambient temperature, are not expensive and do not require high amount of chemical additives.

2.3.5 Heterogeneous photocatalysis

Photocatalysis represents is an advanced oxidation process (AOP) which has recently gained the attention of the scientific community in relation to the problematics concerning air cleaning and water purification. This processes represent an innovative approach and a promising strategy for the promotion of green chemistry and the development of sustainable chemical technologies.
Generally speaking AOPs are based on the generation of high concentration of $^{\cdot}OH$ radical with strong oxidant power, capable to produce the complete oxidation of most organic compound into carbon dioxide, water and mineral acids or salts. In this context photocatalytic oxidation (PCO) is a process that promote the generation of these radicals by the employment of semiconductors activated by light irradiation [145]. The main advantages related to the employment of PCO with respect to other more common technologies for VOCs abatement are [146, 147]:

- the use of greener safer photocatalyst, as TiO_2 which is a component of pharmaceuticals and toothpastes;
- the use of mild oxidants, such as molecular oxygen;
- the possibility to work with mild reaction conditions running closer to room temperature and pressure;
- the requirement of very few auxiliary additives;
- no production of harmful chemicals.

Besides the pollutant is not merely transferred from one phase to another such as in condensation or adsorption but completely converted. In most of the cases the process in carried in presence of UV radiation since the employed catalysts are photoactive in this wavelength interval. However in the last year numerous studies have been published in relation to the development or modification of photocatalyst in order to promoted visible light photoactivity [148, 149].

2.4 PRINCIPLES OF HETEROGENEOUS PHOTOCATALYSIS

The use of solid photocatalysts in air cleaning and wastewater treatment is based on the dual attitude of photocatalysts to adsorb reactants and, at the same time, efficiently absorb photons. As in heterogeneous catalysis, the heterogeneous photocatalysis is characterized by a five steps process, with only one difference:

1. Transfer of reactants inside the fluid phase
2. Adsorption of reactants on the catalyst surface
3. Reaction in the adsorbed phase
    a) Photons adsorption by the solid

b) Generation of photoinduced electrons and holes

c) Electron transfer reactions

4. Desorption of the reaction products

5. Transfer of the reaction product in the fluid phase

The distinctive feature of the photocatalysis is in the third step which requires the adsorption of photons with an energy $\geqslant E_G$ (E_G = band energy gap) on the solid surface of the photocatalyst in order to obtain its activation . Such process can be explained by the band-gap model illustrated in Figure 2.1. An exciton is produced as a consequence of the

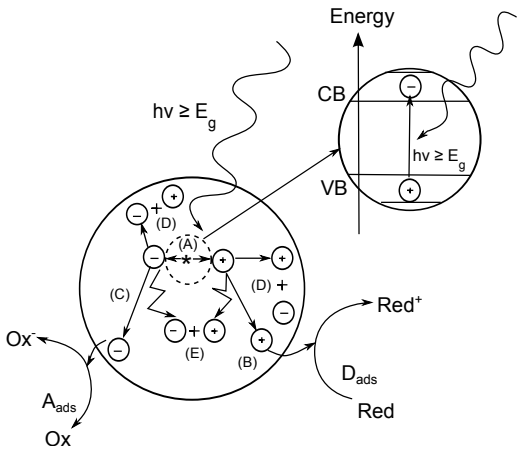

Figure 2.1: *Principles process involved in during the photo-excitation of a semiconductor particle: (A) electron-hole generation, (B) oxidation of donor, (C) reduction of acceptor, (D) and (E) electron-hole recombination at surface and in bulk. Adapted from* [150]

absorption of a photon with energy higher than the band gap energy of the semiconductor. This is followed by charge separation which leads to the formation of an electron-hole pair. Upon excitation, the fate of the separated electron and hole can follow several pathways. The photoinduced electron transfer to adsorbed organic or inorganic species or to the solvent results from migration of electrons and holes to the semiconductor surface. While at the surface the semiconductor can donate electrons to reduce an electron acceptor (usually oxygen in an aerated solution) (pathway C); in turn, a hole can migrate to the surface where an electron from a donor species can combine with the surface hole oxidizing the donor species (pathway D). The probability and rate of the charge transfer processes for electrons and holes depends upon the respective positions of the band edges for the conduction and valence bands and the redox potential levels of the adsorbate species. In competition with charge transfer to adsorbed species is electron and hole recombination. Recombination of the separated electron and hole can occur in the volume of the semiconductor particle (pathway E) or on the surface (pathway D) with the release of heat.
Efficient photocatalytic activity of semiconductor photocatalysts should benefit from:

1. the band-gap of semiconductors allows absorption of incident light across the region the solar spectrum to generate the electron-hole pairs;

2. electron-hole pairs separate effectively from each other and arrive at the semiconductor surface, minimizing the recombination of electron-hole pairs;

3. the photocatalysts supply adequate quality and quantity of active sites, offering more adsorption sites and photocatalytic reaction centers;

4. the bottom of the conduction band should locate at a more negative potential than the reduction potential, and the valence band must have a more positive potential than the oxidation potential [151].

In summary, the efficiency of a photocatalyst depends on the competition of different interface transfer processes involving electrons and holes and their deactivation by recombination.

2.4.1 Band structures

A semiconductor possesses a band structure, roughly characterized as a series of energetically closed energy levels associated with covalent bonding between atoms composing the crystallite (the valence band) and a second series of spatially diffuse, energetically similar levels lying at higher energy and associated with conduction in the macromolecular crystallite (the conduction band). The energy difference between the conduction band and the valence band is called the band gap. The behavior of semiconductor materials has been explained by the band theory of solids. When a large number of atoms are linked together to form a solid, their external orbitals begin to overlap, and then a large number of levels are formed with a close spacing so that it can be considered as a continuous band of energy levels. The gap of an energy band depends only on the interaction of neighbors, while the number of levels within the band depends on the total number of particles interacting (and therefore the number of atoms in a crystal). According to this theory the differences between metals, semiconductors and insulators depend on the band structure of each one, the filling of the bands and the extent of the energy gap between full and empty bands.
Another important aspect in the band theory is the Fermi level: at 0 K electrons occupy the individual molecular orbitals of the bands in accordance with building-up principle. The energy levels that the electrons occupy are quantized, and the levels are filled from the bottom with two electrons per level. The higher occupied energy level in a solid at absolute zero is known as Fermi level. For metals, Fermi energy (E_F) lies within the conduction band while, for semiconductors and insulators, falls into the band gap energy. In a semiconductor the Fermi level is located near the middle of the gap and E_g is small, and appreciable numbers of electrons are thermally excited from the valence band to the conduction band. Because of the many empty levels above the thermally filled levels in the conduction band, a small applied potential difference (or photonic energy) can easily raise the electrons in the conduction band into available energy states, giving result to the formation of charge carriers. Charge carriers in a semiconductor can be negative, positive or both. When an electron moves from the valence band (VB) into the conduction band (CB) it leaves behind a vacant site, the hole. This hole behaves as a charge carrier because

a free electron from a nearby site can transfer into the hole; as electron leaves a site a new hole is created; thus the neat effect can be viewed as the hole which migrates through the material. Therefore, the holes acts as a particle with a positive charge. Electrons that are promoted into the conduction band are the negative charge carriers and the positives holes move in the opposite direction of the electrons in the presence of an electric field. In crystalline solids, since the band structures depend on the electron wavevector **k**, there are two types of band-to-absorption corresponding to direct and indirect transition. In contrast, in

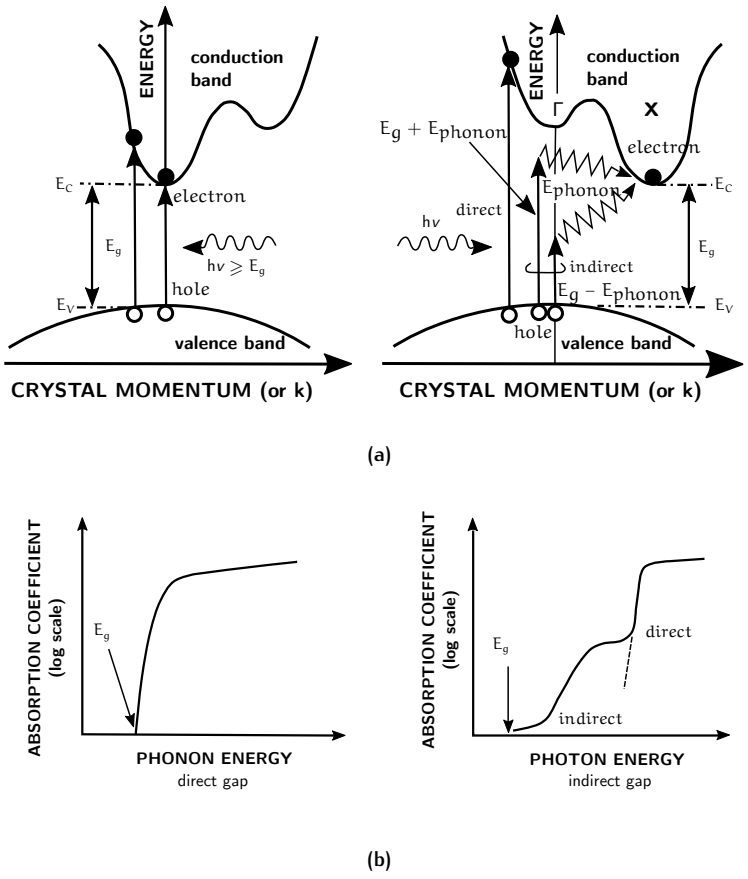

Figure 2.2: *Simplified illustration of the fundamental absorption processes in direct and indirect band-gap semiconductors (adapted from.* [152])

amorphous solids, where no long-range order exists only direct transitions are meaningful. The first case the two possible situations can be described as follow (Figure 2.2):

- when the lowest energy excitation of an electron from the valence band to the conduction and involves no change in momentum (*k*) the semiconductor has a direct band gap and the absorption probability is high for these transitions (i.e. GaS, ZnO and CdTe). In this case the transition in the energy-**k** diagram is represented by a vertical transition from an initial energy E and wavevector k in the VB to a final energy E' and wavevector k' in the CB, where k'=k. The absorption coefficient of the material is then derived from the quantum mechanical transition probability from E to E', the occupied density of states at E in the VB from which electrons are excited and the unoccupied density of the states E in the CB at E + hν; direct band gap materials

provide more efficient absorption and emission of light, but the penetration depth is lower at the band-gap energy since all light is absorbed close to the surface.

- An indirect band gap is presented in a material where the k at the valence band maximum is different from the k at the conduction band minimum. For photons to be absorbed, momentum conservation requires coupling to a lattice vibration (a phonon) to compensate for the change in the wavevector during the transition, and then the required input photon energy is lower. Since phonons must assist absorption or emission, the light penetration depth is larger in these materials and it is temperature dependent. In other words, the absorption coefficient is less at the band-gap energy or close to it, so thicker films are needed to absorb more photons. GaP, TiO_2 and CdS are examples of semiconductors with an indirect band gap.

Figure 2.3 present the band gaps of several common semiconductors and photocatalysts.

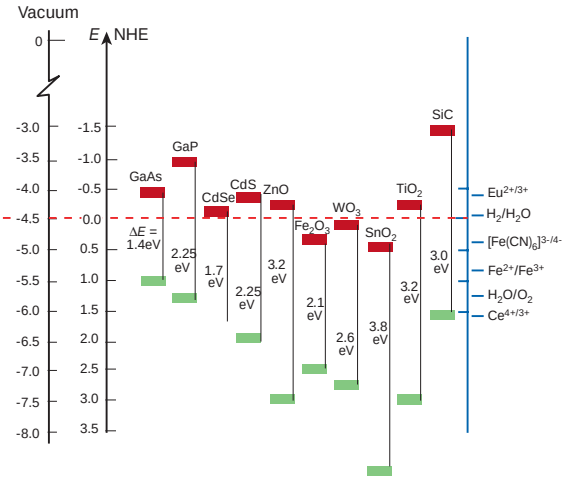

Figure 2.3: *Band gaps and band positions of several semiconductors*

2.4.2 Kinetics of photocatalytic processes

Since photocatalytic reactions always involve adsorption steps, adsorption isotherms play a fundamental role in the kinetic models. The different kinetic equations present in the scientific literature are based on the following mechanisms [153]:

- Mars-Van Krevelen (MVK) mechanisms, which involves the oxidation-reduction of the surface of the photocatalyst. The solid behaves as an intermediates reactant. Its surface oxygen anions are the oxidizing species, which are regenerated by gaseous oxygen;
- Stationary-State-Adsorption (SSA) model, which is based on the oxidation-reduction of the adsorbed phase;
- Eley-Rideal (EA) mechanism, which involves the reaction between adsorbed oxygen and the gaseous reactant; For all the pollutant concentration (or partial pressure), the reaction rate remains of the first order with respect to the reactant;

- Langmuir-Hinshelwood (L-H) mechanism, which includes the reaction occurring between both reactants and their equilibrium of adsorption.

Historically the L-H model has been the most widely employed for the kinetic description of the photocatalytic reactions. According to the model the reaction rate *r* that is proportional to the surface coverage of the reactants. For a bimolecular reaction:

$$A + B \rightarrow C + D \tag{2.1}$$

where the reaction rate *r* varies as:

$$r = k\theta_A\theta_B \tag{2.2}$$

where k is the reaction constant, θ_A and θ_A the fractional coverage of the species A and B adsorbed on the photocatalyst surface. On the basis of the Langmuir model for monolayer adsorption, the surface coverage of every reactant can be expressed as:

$$\theta_i = \frac{q}{q_S} = \frac{K_i X_i}{1 + K_i X_i} \tag{2.3}$$

where q_S is the total number of adsorption sites for unit weight or volume of the photocatalysts, K_i is the adsorption constant (in the dark) and X_i represents the concentration in liquid phase or the partial pressure P_i in gas phase. As a consequence the rate of reaction r becomes:

$$r = k\theta_A\theta_B = \frac{kK_A K_B X_A X_B}{(1 + K_A X_A)(1 + K_B X_B)} \tag{2.4}$$

where k is the real reaction constant. It is important to underline that, besides the catalyst's mass, the kinetic constant *k*, in thermocatalysis depends only from the temperature (according to the Arrhenius law). On the other hand, in photocatalysis the kinetic constant of the reaction depends only by the light intensity (or radiant flux). However even if the kinetic constant *k* of the reaction is independent from the temperature, the rate of the reaction depends on the temperature since the coverages θ_A and θ_B depend to it. In general one of the reagents, let's suppose B, is in excess or is maintained constant. Thus, θ_B = 1 or θ_B = constant. θ_B is equal to one, for example, for a pure reactant in liquid phase; θ_B is constant but < 1, for example, for oxygen in the oxidation reactions or in atmospheric air ($P_{O2} \approx 0.2$ atm) or in liquid phase by its dissolution according to the Henry law. Thus:

$$r = k\theta_A\theta_B = k'\theta_A = \frac{k'K_A C_A}{1 + K_A C_A} \tag{2.5}$$

where k' = k θ_B = pseudo-real kinetic constant.
Other most common kinetic expression employed are reported in Table 2.5.

Table 2.5: *Kinetic mechanism of PCO reaction. Mechanism: ULH: Unimolecular Langmuir–Hinshelwood; BLH: Biomolecular Langmuir–Hinshelwood; +W: with water competitive adsorption; +T: Temperature-dependent; +MC: with the inhibiting effect of multi-compounds. Symbol description: r: reaction rate; k: reaction rate constant; K: adsorption coefficient; C: concentration; E: apparent activation energy; ΔH: change in enthalpy; R: gas constant; T: temperature (K). Subscripts: A: decomposed pollutant; W: water vapor; i: multi-compounds.* [154]

Mechanism	Kinetic equation
Power law	$r_A = kC_A^n$
ULH	$r_A = k\left(\frac{K_A C_A}{1+K_A C_A}\right)$
ULH + MC	$r_A = k\left(\frac{K_A C_A}{1+K_A C_A+\sum_i K_i C_i}\right)$
ULH + W + T	$r_A = \frac{k\ exp(-E/RT)K_A(exp(-\Delta H_A/RT)C_A T^{-0.5})}{1+K_A\ exp(-\Delta H_A/RT)C_W T^{-0.5}}$
BLH	$r_A = \frac{K_{A1}C_A}{1+K_{A1}C_A+K_{W1}C_W}\frac{K_{A4}C_W}{1+K_{A2}C_A+K_{W2}C_W}$

2.4.3 Influence factors in photocatalytic oxidation processes

Different are the type of factors which can influence the rate of a photocatalytic process and should be taken into consideration to improve the degradation of volatile organic compounds.

For all types of photocatalytic reactions, that the rate of reaction r is proportional to the radiant flux ϕ. The dependency of the degradation rate with the photon flux is linked to the activation of the catalyst and it is usually expressed by means of a power law relation [155]:

$$r \propto \phi^n \tag{2.6}$$

For low light intensities the degradation rate is linear with the photon flux ($n = 1$), while for an increasing value of photon flux (higher than 25 mW/cm^2 [132]) the reaction rate becomes proportional to $\phi^{1/2}$ [132]. Traditional light sources use ultraviolet (UV) radiation which possesses an emission in the 200-400 nm wavelength region of the electromagnetic wave spectrum. For photocatalytic purposes artificial UV sources made of different metals including mercury, sodium, zinc/cadmium and rare gas (neon,argon) are employed. Mercury UV lamps have emission lines usually in the desired range of energy for driving the photochemical reactions and according to the classification provided by Bolton *et al.* [156] (Table 2.6) they can grouped into low pressure mercury lamp, medium pressure mercury lamp and high pressure mercury lamp.

Another important aspect in the pollutant concentration which influence the kinetics of the reaction according to the models shown in the previous paragraph. However it is worthwhile to note that the pollutant concentrations used in the models should be the concentrations on the reactions surface but not the inlet ones and for a real PCO reaction process they may be very different because of limited mass transfer [157].

Besides pollutant concentration also catalyst concentration represents an important factor

Table 2.6: *UV light sources as reported by Bolton et al.* [156]

Parameter	Low pressure mercury lamp	Medium pressure mercury lamp	High pressure mercury lamp
Life time (h)	>5000	>2000	>3000
Output range	80% in a narrow range around 254 nm	Broad but not much below 250 nm	Strong below 250 nm
Energy density	Low (~1 W/cm)	Moderate (~125 W/cm)	High (~250 W/cm)
Electrical energy to photon energy	High (~30%)	Moderate (~15% for 200-300 nm)	High (~30% for 200-300 nm)

to take into consideration. Salaices *et al*. [158] have shown that a minimum amount of catalyst is required to activate the photocatalytic process and that the rate of the reaction increase logarithmically by increasing the amount of the catalyst until reaching a stable value over which the rate is independent of the catalyst loading. For too low catalyst loading the amount of photons absorbed is very low to help promoting significant charge separation while above the optimal amount of catalyst there is the full absorption of photons by the photocatalytic bed. The initial proportionality between the reaction rate and the mass of catalyst is the same as in conventional thermo-catalysis, meaning that the activity or reaction rate is proportional to the total number of active sites at the surface catalyst. Temperature has usually not a significant relevance in the photocatalytic process since they carried at low temperature, however the adsorption is a spontaneous and exothermic phenomenon and low temperatures favor adsorption, including that of the final products which become inhibitors. On the opposite, high temperatures are detrimental for the adsorption of the reactants and the reaction rate declines [159]. Humidity has an important role in the photocatalytic reactions since the molecular water adsorbed on the photocatalyst reacts with the hole generated and generate some hydroxyl groups, such as $OH^{\cdot}$ which, in turn, oxidizes pollutants. In the absence of water vapor, the photocatalytic degradation of some chemical compounds is seriously retarded [160, 161]. However, excessive water vapor on the catalyst surface will inhibit the reaction rate because the presence of water vapor competes with pollutants for adsorption sites on the photocatalyst (competitive adsorption), thus reducing the pollutant removal rate [162].

2.4.4 TiO_2 photocatalysis

TiO_2 is broadly used as a standard photocatalyst because of its high photocatalytic activity, good thermal stability, low cost and low toxicity. TiO_2 is an n-type semiconductor and usually exhibits three main crystal structures involving rutile, anatase and brookite, in which anatase TiO_2 has attracted more attention because of its high photocatalytic activity [163].
The optical band gap of anatase is 3.2 eV which correspond to an absorption edge of 387 nm, meaning that its photoactivation require the employment of UV radiation. The follow-

ing reactions are those proposed to describe the mechanism of photocatalytic degradation on titanium dioxide [164]:

- *charge carriers generation*

$$TiO_2 + h\nu \rightarrow e^-_{cb} + h^+_{vb} \tag{2.7}$$

- *charge carriers entrapment*

$$Ti^{IV} - OH^- + h^+_{vb} \rightarrow Ti^{IV} - OH^{\cdot} \tag{2.8}$$

- *surface entrapment*

$$Ti^{IV} - OH^- + e^-_{cb} \rightarrow Ti^{IV} - OH^{\cdot} \tag{2.9}$$

- *deep entrapment*

$$Ti^{IV} + e^-_{cb} \rightarrow Ti^{IV} \tag{2.10}$$

- *electron-hole recombination*
  - *free electron with trapped hole*

$$Ti^{IV} - OH^{\cdot} + e^-_{CB} \rightarrow Ti^{IV} - OH^- \tag{2.11}$$

  - *free hole with trapped electron*

$$Ti^{III} + h^+_{vb} \rightarrow Ti^{IV} \tag{2.12}$$

  - *free electron with free hole*

$$e^-_{cb} + h^+_{cb} \rightarrow heat \tag{2.13}$$

- *hydroxyl radicals generation in aqueous media*
  - *reactions involving the hole*

$$Ti^{IV} - H_2O + h^+_{vb} \rightarrow Ti^{IV} - OH^{\cdot} + H^+ \tag{2.14}$$

  - *reactions involving the electron*

$$Ti^{III} + O_2 \leftrightarrows Ti^{III} - O_2^{-\cdot} \tag{2.15}$$

$$Ti^{IV} - O_2^{-\cdot} + 2H^+ + e^-_{cb} \leftrightarrows Ti^{IV} - H_2O_2 \tag{2.16}$$

$$Ti^{IV} + O_2^{-\cdot} + H^+ \leftrightarrows Ti^{IV} - HO_2^{\cdot} \tag{2.17}$$

$$Ti^{IV} - HO_2^{\cdot} \rightarrow Ti^{IV} - H_2O_2 + O_2 \tag{2.18}$$

$$Ti^{IV} - H_2O_2 + O_2^{-\cdot} \rightarrow Ti^{IV} - OH^{\cdot} + OH^- + O_2 \tag{2.19}$$

- *adsorption-desorption of reductant (any organic substrate S)*

$$Ti^{IV} + S \leftrightarrows Ti^{IV} - S \tag{2.20}$$

$$Ti^{IV} - OH^{\cdot} + S \leftrightarrows Ti^{IV} - OH^{\cdot} - S \tag{2.21}$$

- *adsorption-desorption of oxidant (for example a metal ion)*

$$Ti^{IV} + M^{n+} \rightarrow Ti^{IV} - M^{n+} \tag{2.22}$$

- *photo-oxidation of the reductant*
  - *direct attack of the hole*

$$Ti^{IV} - S + Ti^{IV}(h^{+}_{vb}) \rightarrow Ti^{IV} + Ti^{IV} - I \rightarrow CO_2 + H_2O \tag{2.23}$$

  - *attack of the hydroxyl radical*

$$Ti^{IV} - S + Ti^{IV} - OH^{\cdot} \rightarrow Ti^{IV} + Ti^{IV} - I \rightarrow CO_2 + H_2O \tag{2.24}$$

$$Ti^{IV} - S + OH^{\cdot} \rightarrow Ti^{IV} - I \rightarrow CO_2 + H_2O \tag{2.25}$$

$$Ti^{IV} - OH^{\cdot} - S \rightarrow Ti^{IV} - I \rightarrow CO_2 + H_2O \tag{2.26}$$

- *adsorption-desorption of the organic intermediate*

$$Ti^{IV} + I \leftrightarrow Ti^{IV} - I \tag{2.27}$$

- *photo-reduction of the metallic ion*

$$Ti^{IV} - M^{n+} + me^{-} \rightarrow Ti^{IV} - M^{(n-m)+} \tag{2.28}$$

The reaction 2.7 is the entrapment of the hole by the hydroxyl groups on the surface of titania and the reactions 2.8, 2.9 are the reversible entrapment of the electrons on the surface of the catalyst and the irreversible entrapment of the same in the depth of the conduction band. The reaction 2.10, 2.11 describe the electron-hole recombination reactions that happen on the surface of TiO_2 or in the reaction media thanks to the delocalization of electrons and holes. This is one of the harmful reactions for photocatalysis and it influences the surface charge transport phenomena and thus the efficiency of the photocatalytic process. The reaction 2.14 shows the generation of hydroxyl radicals by the adsorbed water on the surface of the catalyst which reacts with the holes. Reactions 2.15, 2.16, 2.17,2.18,2.19,2.20 and 2.21 represent the formation of superoxide species ($O_2^{-\cdot}$), hydroperoxide ($HO_2^{\cdot}$) and hydroxylic ($OH^{\cdot}$) thanks to the path of the electron. These reactions are negligible if the process is in a non aqueous media, while reaction 2.8 becomes more important. Once generated the active species, the reagents are adsorbed on the surface of the photocatalyst (reactions 2.20, 2.21, 2.22). This is followed by the oxidation of the reductant and the reduction of the oxidant thanks to, respectively, to the attack of the hydroxyl radicals and the electrons of the conduction band. The oxidant power of the holes of the valence band is always higher than the reduction power of the electrons in the conduction band, besides the steps of electron transfer on the surface are competitive with the electron-hole recombination reactions and thus the real efficiency of the process is always inferior to that of the theory. The organic compound is eventually degraded through the formation of intermediates (I) to form CO_2 and water. Reaction 2.27 shows the desorption of the products, releasing the active sites of the catalyst. Reaction 2.28 shows that if in the system

are present metal ions, they are reduced to their oxidized stable form by the electrons of the conduction band. The whole reaction can be summarized by the following reaction, where the oxidants are reduced and the reductants are oxidized thanks to the action of the UV radiation on the catalyst:

$$(Ox_1)_{ads} + (Red_2)_{ads} \rightarrow Red_1 + Ox_2 \tag{2.29}$$

2.4.4.1 *Photoxidation of methanol on TiO_2*

Here is reported the reaction mechanism of methanol photocatalytic degradation on titania. This compound has been taken into consideration as targeted pollutant for the evaluation of the performance for the membranes developed in the subsequent study. According to several publications [165, 166], in the photocatalysis of n-type semiconductors, organic molecules are oxidatively degraded by direct hole transfer reaction, or by products formed by these holes (e.g. $^{\cdot}OH$ radicals), indirect hole transfer reaction:

$$TiO_2 + h\nu \rightarrow e^-_{CB} + h^+_{VB} \tag{2.30}$$

$$CH_3OH(ads) + h^+_{VB} \rightarrow^{\cdot} CH_2OH(ads) + H^+ \tag{2.31}$$

$$^{\cdot}CH_2OH(ads) \rightarrow CH_2O + H^+ + e^- \tag{2.32}$$

$$^{\cdot}CH_2OH(g) + 2O(a) \rightarrow^{\cdot} CHO(g) \rightarrow HO^{\cdot}_2 \tag{2.33}$$

$$^{\cdot}CHO(g) + 2O(a) \rightarrow CO(g) + HO^{\cdot}_2 \tag{2.34}$$

$$CO(g) + HO^{\cdot}_2 \rightarrow CO_2 + HO^{\cdot} \tag{2.35}$$

$$H_2O + h^+_{VB} \rightarrow^{\cdot} HO + H^+ \tag{2.36}$$

$$CH_3OH +^{\cdot} HO \rightarrow^{\cdot} CH_2OH + H_2O \tag{2.37}$$

$$^{\cdot}CH_2OH +^{\cdot} HO \rightarrow CH_2O + H_2 \tag{2.38}$$

$$CH_2O(g) + 2O(a) \rightarrow CO_2(g) + H_2O \tag{2.39}$$

In the latter reactions, $^{\cdot}OH$ can react with organic substances by hydroxylation through $^{\cdot}OH$ addition onto the organic molecule, followed by further oxidation. A few studies have demonstrated that $O_2^{\cdot}$- could be also the major oxidant in photocatalytic reactions [167]. Nevertheless, irrespective of the radical species which initiate the PCO reactions, each oxidation step may proceed on the photocatalyst surface either by the direct interaction of the adsorbed organic species with valence band holes, ${h_{VB}}^+$, or by an indirect path involving hydroxyl radical attack. From the reaction scheme it is possible to underline that the methanol degradation is obtained through the production of formaldehyde as reaction intermediate, followed by the complete oxidation to water and carbon dioxide. However, recently also the formation of methyl formate has been identified in recent gas-phase studies of the photochemical reactions of methanol over anatase particles [168]. In this case it is worthwhile to note that the $^{\cdot}HCO$ + $^{\cdot}CH_3O$ radical coupling path and the H-transfer step followed by formaldehyde dimerization, is the most validated hypothesis for methyl formate generation [167, 169]. Other hypothesis are related to the generation of methyl

formate by esterification of formic acid obtained by the oxidation of formaldehyde with methanol. A further reaction mechanism is plausible and it requires the condensations of methoxy with the formaldehyde to produce hemiacetals, subsequently dehydrogenated to methyl formate.

2.4.5 Electrospinning for photocatalytic applications

Chemical reactions employing catalysis are a fundamental part in chemical processes due to the possibilities of increase reaction rates as well as mild processing conditions. Immobilized catalysts are extensively employed due to their stability, easiness of separation and their availability for continuous processes. Their efficiency depends both on the pore size and distribution and on the diffusion limitations of the substrate material. In these terms, nanofibers represent a good candidate as catalysts support because of their great surface area and their size, in nanoscale rage, that allows to neglect the diffusion terms. Moreover nanofibers can also be characterized by an high catalyst loading [170].
The electrospun nanofiber-based photocatalysts take advantage of the optional design of nanostructures (porous, hollow, core-sheath, hierarchical, etc.) in order to provide higher photocatalytic activity. In this context two different approaches can be outlined:

- the employment of an organic nanofiber on which the photocatalyst particles are deposited;
- the realization of an electrospun mat of a precursors which is subsequently treated to obtain inorganic nanofibers of the desired photocatalyst.

Subsequently the two different approaches are review by a brief survey of the scientific literature about their employment.

2.4.5.1 *Electrospun nanofibers of semiconductors for photocatalysis*

With this approach several types of semiconductor and and photocatalyst systems have electrospun to generated high surface nanofibers and generally a classification can be done according to the type of system prepared in terms of:

- single catalyst system: here a single semiconductor is employed and the electrospinning technique is employed in order to promote the formation of different type of structures to promote the increase of the surface area of the material. Zhang *et al.* [171] produced TiO_2 nanofibers and showed their higher photocatalytic performances with respect to TiO_2 thin films. Other examples are the increment of surface area achieved by producing porous TiO_2 nanofibers with an alkali-dissolution process employing composite TiO_2/SiO_2 to remove silica [172] and calcination of an of electrospun mixture of titania precusor and carbon nanosphere [173]. Generally this type porous nanofibers have proved to provide higher photocatalytic activity than their non porous counterparts. ZnO hierarchical structures with higher photocatalytic activity than traditional ZnO nanofibers and mesoporous structures have been produced by electrospinning and successfully tested towards organic compounds

abatement both in liquid [174] and gas phase [175], showing easy diffusion and mass transportation of pollutants. Other example of single semiconductor electrospun-based nanostructures includes TiO_2 nanotubes [176], SnO_2 nanofibers [177] and hollow tubes [178], NiO rime-like nanowires/nanofibers [179] hierarchical structures and WO_3 nanofibers [180];

- noble metal/semiconductor composite: the coupling a semiconductor with a metal is a common strategy to improve the photocatalytic activity of a bare semiconductor in terms of electron trapping, high Schottky barrier and surface plasmon resonance. The nanofibers obtained with this strategy are generally comprised of a dense fibrous structure of the semiconductor on which are deposited the noble metal particles. Such morphology is achieved by electrospinning of a precursor of the semiconductor and a noble metal salt employing a polymer as fiber promoting agents. Once that the nanofibrous web is formed the final structure is achieved by calcination [181]. However other processes like photoreduction [182], solvothermal methods [183], or sputtering [184] can be employed for the deposition of the noble metal particles. Examples includes Ag/TiO_2 [183, 185], Au/TiO_2 [184] and Ag/ZnO [186] with enhancements even 25 times higher than bare semiconductor nanofibers [186].

- coupled semiconductor system: electrospinning allows the coupling of mixed semiconductor to provide the formation of hierarchical structures with extremely high specific surface area and enhanced heterojunction density (Figure 2.4). The reduced scale and the intimate contact of these heterostructures are capable to improve the photocatalytic activity with respect to the bare semiconductors and the mixture of nanofibers semiconductors [187]. In this case the two semiconductors are coupled during the electrospinning process by side-by-side electrospinning or their precursors [188], coaxial electrospinning to produce core-shell structures [189], or decoration of one semiconductor on the surface of the other semiconductor nanofibers by hydrothermal reaction [190]. Examples are SnO_2/TiO_2 composite [188, 191] and core-shell nanofibers [189], ZnO/SO_2 composite nanofibers [192], V_2O_5/TiO_2 nanoheterostructures [193], SnO_2/Fe_2O_3 nanofibers [194].

- doped semiconductor photocatalyst: in this case the approach is the doping of a wide band gap semiconductor (e.g. TiO_2) in order to extend its absorption into the visible light spectrum. Usually this approach is achieved by doping the semiconductor with metal ions (Co, Fe, Ni, Cu, etc.) or non metallic elements (C, N, etc.). Between them N-doped TiO_2 nanofibers have attracted much attention because of the effect of band gap narrowing, oxygen vacancies creation, intra-band gap surface states generation. These fibers have been produced by using ethylenediamine as nitrogen source, using a heat treatment [195], or a surface nitridation of electrospun TiO_2 nanofibers with NH_3 [196]. These nanofibers have proved to possess a factor more than 12 times higher in temrs of photocatalytic activity than pure TiO_2 nanofibers under visible light irradiation.

Generally speaking the photocatalysts prepared by this method are able to display very high photocatalytic activity by taking advantage of the high surface area and aspect ra-

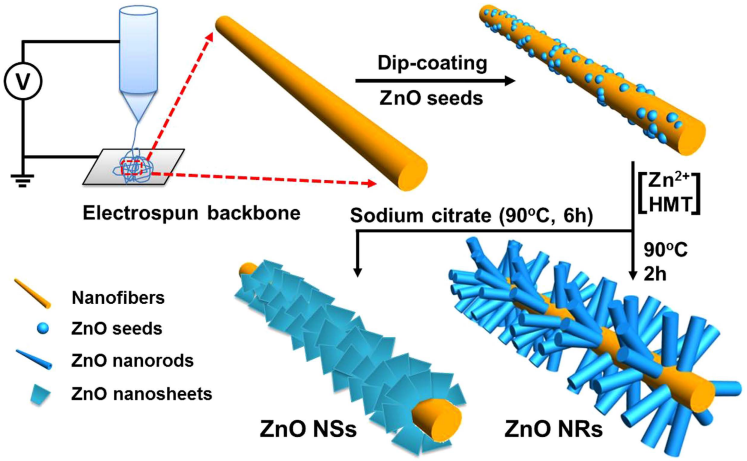

Figure 2.4: *Assembly of SnO_2/ZnO hierarchical nanostructures. Image taken from* [191]

tio and the different morphology achievable by modifying the electrospinning process. However their preparation requires several steps and make them more suitable for the employment in context of water treatment.

2.4.5.2 *Electrospun polymeric nanofibers as support for semiconductor photocatalysis*

For this second approach TiO_2 nanoparticles support on polymeric electrospun nanofibers have been the most widely system investigated due to the high photocatalytic activity of this semiconductor under UV irradation. Examples are the deposition of TiO_2 nanoparticles by electrospraying on PAN [197] and PSU [198] or the production of electrospun nanofibers or TiO_2/fluoropolymer composite nanofibers obtained by combining electrospinning and an hydrothermal complex-precipitation, showing higher photocatalytic activity than bar TiO_2 nanoparticles.
ZnO-based composite nanofibers have been produced by ZnO nanorods deposition on polyimide nanofibers [199] while core-shell structures have been obtained combining electrospinning with atomic layer deposition using nylon as polymeric support [200].
This second approach is less employed and the photocatalytic systems prepared according to this procedure may have lower photocatalytic activity than the previous type but on the other side they present advantages in terms of higher recyclability, easy recovery, higher manageability and less preparation effort. This aspects are particularly important when it is necessary to recover easily the photocatalyst using a low-cost support.

3 FUEL CELLS AND PROTON EXCHANGE MEMBRANES

The present chapter provide a first introduction to the topic of fuel cells technology. The discussion present a first description of the working principle of this devices with a subsequent analysis of proton exchange membranes (PEM) and the employment of the electrospinning techniques for the preparation of such membranes.

3.1 FUEL CELLS

Fuel cells are electrochemical systems capable to convert the chemical energy of a fuel (usually hydrogen) directly into electric energy, without the employment of a thermal cycle, obtaining conversion yields that are higher than those of conventional thermal machines. The birth of fuel cells is dated back in 1839 when William Grove reported the results of an experiment in which he was able to generate electric energy in a cell where two electrodes, made of two thin platinum foils, were immersed in sulfuric acid and fed with hydrogen and oxygen. The interest towards this technology stagnated until the second part of the 20th century when they were taken more in consideration for application that were more compatible with the emerging energy needs.
A fuel cell operates analogously to a battery, since it produces electric energy from an electrochemical process; however, differently from that, it consumes the substances coming from the outside thus it is able to operate without interruptions until the system is provided with the fuel (e.g. hydrogen) and oxidant (oxygen and air) [201].

As can be seen from Figure 3.1 the core of the cell is represented by the membrane electrode assembly (MEA). This composed of two electrodes made of porous material and separated by an electrolyte. The electrodes act as catalytic sites for the cell reactions that consume essentially hydrogen and oxygen, with the production of water and the passage of electric current in the external circuit. The electrolyte has the function to conduct the ions produced by one of the reactions and consumed by the other, closing the electric circuit inside the cell. The electrodes are made of porous material that support the catalyst, usually composed of platinum dispersed on carbon powder with an ionomeric binder, which increases the kinetic of the dissociation and oxidation reactions according to the

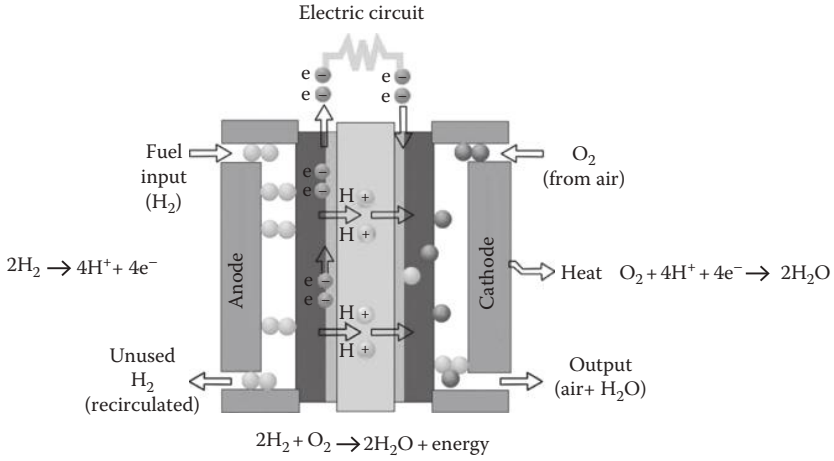

Figure 3.1: *Schematic representation of a fuel cell*

following scheme:

$$H_2 \rightarrow 2H^+ + 2e^- \qquad \text{anode} \tag{3.1}$$

$$\frac{1}{2}O_2 + 2H^+ + 2e^- \rightarrow H_2O \qquad \text{cathode} \tag{3.2}$$

$$O_2 + \frac{1}{2}H_2 \rightarrow H_2O \qquad \text{overall reaction} \tag{3.3}$$

Gas diffusion layers (GDL), typically carbon paper or carbon cloth are attached to the electrodes and permit hydrogen and air transport to the electrodes, minimizing the condensation of liquid water on the electrode surface. According to the reaction scheme during hydrogen/air fuel cell operation, hydrogen gas (the fuel) is supplied to the anode and oxygen (the oxidant) to the cathode. Hydrogen undergoes oxidation at the anode to form protons and electrons. The electrons provide electrical energy and the protons migrate through the PEM toward the cathode where they react with oxygen and electrons to form water. The electrochemical transformation is accompanied by the production of heat that is necessary to extract in order to maintain constant the operative temperature of the cell.
The electrochemical processes that happens in a fuel cell are not governed by Carnot's cycle thus their operation is simple and more efficient compared to internal combustion engines that realize the same combustion reaction (55% vs. 20% operating efficiencies [202]). However this yield is referred to reversible conditions that are far from those achievable in real operations. Moreover single cell usually produces voltages of about 0,7 V only and currents comprised between 300 and 800 mA/cm^2, thus in order to obtain the desired power and voltage usually more cells are arranged in series, between bipolar plates, to form a so-called "stack". Stacks are in turn assembled in modules, to obtain generators with the desired power [203].
A brief overview of the principal advantages and drawbacks of fuel cell is reported in Table 3.1.

Table 3.1: *Advantages and disadvantages of fuel cells* [201]

Advantages	Disadvantages
efficient energy conversion	complex to operate
modular construction	best as primary energy source
non-polluting	impurities in gas stream shorten life
low maintenance	pulse demands shorten cell life
silent	limited availability
safe	low durability
high energy density	low power density per volume

3.1.1 Types of fuel cells

There are different fuel cell technologies, with different characteristics and different degree of development. Normally the cells are classified upon the type of electrolyte employed or the operating temperature.
The electrolyte determines or influences significantly:

- the temperature range;
- the types of ions and the direction though which they diffuse along the cell;
- the nature of the construction;
- the composition of the reacting gases;
- the different options of disposal of the reaction products;
- the mechanical resistance and employment characteristics.
- the life of the cell

The main types of cells are:

- *Alkaline Fuel Cells*(AFC): that employ an electrolyte based on potassium hydroxide and operate at temperatures around 120°C. They have reached a good level of technological maturity for special uses (military and space applications). Their characteristics (they require extremely pure feeding gases) have limited their diffusion so that today there are not development programs in progress;
- *Polymer exchange membrane Fuel Cells* (PEMFC): that use a polymeric membranes with high protonic conductivity as electrolyte and work with temperatures between 70 and 100 °C; they are developed mainly for traction and small size generation/cogeneration;
- *Phosphoric Acid Fuel Cells* (PAFC): they operate at temperatures close to 200°C with an electrolyte made up of a concentrated solution of phosphoric acid; they represent the more mature technology for stationary uses, with a commercialization already in progress for cogeneration applications in the tertiary and residential sectors;

Table 3.2: *Characteristics of the different types of fuel cells* [203]

Fuel cell type	Operating temperature	Efficiency	Suitable applications			
			Domestic power	Small scale power	Large scale cogeneration	Transport
AFC	50-90	50-70	V	V	X	V
PEMFC	50-120	40-50	V	V	X	V
PAFC	175-220	40-45	X	V	X	X
MCFC	600-650	50-60	X	V	V	X
SOFC	800-1,000	50-60	V	V	V	X

- *Molten Carbonate Fuel Cells* (MCFC): they use as electrolyte a solution made up of alkaline carbonates that are molten at the operative temperature of the cell (about 650°C) and contained in a porous ceramic matrix; they are promising especially for the generation of electric energy and the cogeneration from some hundreds of kWs to some tenths of MWs;

- *Solid Oxide Fuel Cell* (SOFC): that work at high temperature (about 900-1000°C) to ensure a sufficient conductivity to the electrolyte, made up of a ceramic material (zirconium oxide doped with yttrium oxide); like the MCFC they are promising especially for the generation of electric energy and the cogeneration from some kWs to some tenths of MWs;

- *Direct Methanol Fuel Cells* (DMFC): they are subclass of PEMFC employing methanol as fuel instaed of hydrogen. They operate at temperatures from 70 to 120°C and like the PEMFC use a polymeric membrane as electrolyte. Their advantage is the employment of a liquid fuel but they have lower thermodynamic efficiency, they require high catalyst loading and produce carbon dioxide. For these reasons are still in the research study stage

The main characteristics and applicability of each type of fuel cell is briefly resumed in Table 3.2.

3.1.2 Characteristics of a fuel cell

Fuel cells have a significant interest for the generation of the electric energy, since they present such energetic and environmental characteristics to make their adoption potentially advantageous. Their main characteristics are:

- High electric efficiency with values that varies from 40-48 % (referred to the lower heating value of the fuel) for systems with cells operating at low temperatures, to over the 60% for those with cells operating at high temperatures employed in combined cycles

- Possibility to employ different types of fuels like methane, methanol, natural gas, syn-gas (produced from liquid fuels, gasification of coal, biomasses)

- Modularity that allows to increase the installed power as the electric energy demand increases, with remarkable savings from an economical point of view and with construction times that can be significantly reduced
- Efficiency dependent on the charge and the dimension of the system. The yield of the cells is not very sensitive to variations in the electric load, differently from what happens with conventional systems. Basically a fuel cell can operate between the 30 and the 100 % of the load, without big efficiency losses. Moreover the efficiency is dependent on the installed power within a wide power range, while in the traditional system the efficiency decreases with the decrease of the system size
- Very low environmental impact both from the gaseous emissions point of view and from that of the acoustic ones. This allows to allocate the plant even in residential areas, making the system particularly useful for the production of distributed electric energy
- Possibility of cogeneration. The heat cogenerated can be available at different temperature,in the form of vapor or hot water and employed for healthcare, air conditioning, etc.

3.2 PROTON EXCHANGE MEMBRANES (PEM)

Traditionally the perflurosulfonic acid (PFSA) ionomer Nafion®, developed by DuPont in 1960s, is considered the traditional benchmark for H_2/air fuel cells. As will be seen several drawbacks limits its employments for fuel cell technology and during the years several attempts have been made in order to find suitable alternatives by the research community. Three different approaches are normally followed in order to develop proton exchange membranes for fuel cells, namely:

- modified perfluorinated ionomer membranes;
- functionalization of aromatic hydrocarbon polymers/membranes;
- composite membranes based on solid inorganic proton conducting materials and the organic polymer matrix or prepare acid-base blends and their composite to improve their water retention properties

Subsequently this three type of approaches are review along with the description of the main requirements for good proton exchange membranes.

3.2.1 Properties requirements for PEMs

The desired properties for a membrane to be employed as a proton conductor in a fuel cell are shown in Figure 3.2 and can be summarized in the following requirements [203]:

- Chemical and electrochemical stability in fuel cell operating conditions;

- Elevated proton conductivity to support high currents with minimal resistive; losses and zero electronic conductivity;
- Good water uptakes at high temperatures of approximately 100°C;
- Thermal and hydrolytic stability;
- Chemical properties compatible with the bonding requirements of membrane-electrode assembly;
- Extremely low permeability to reactant species to maximize efficiency;
- Mechanical strength and stability in the operating conditions. (The membrane must be resistant to the reducing environment at the anode as well as the harsh oxidative environment at the cathode.);
- Resistance of fuel transport through it. (This is a concern in a DMFC, in which methanol crossover takes place, and gets oxidized at the cathode. This reduces the cell voltage by formation of mixed potential at the cathode.);
- High durability;
- Facilitation of rapid electrode kinetics;
- Flexibility to operate with a wide range of fuels;
- Production cost compatible with the commercial requirements of the fuel cell.

In addition to the preceding properties, hydration of the membrane (water management) and thickness also play important roles in affecting the overall performance of fuel cells. Especially water uptake from the membrane is important since the ionomer itself does not provide sufficient conductivity thus the membrane needs to be swelled to ensure proton conductivity. It is generally accepted that two types of proton-conducting mechanisms in proton exchange membranes (PEMs) occur: the vehicle mechanism and the Grøtthuss-type mechanism, also called structure diffusion. The vehicle mechanism, occurs by the formation of an ion adduct composed of a proton and a diffusible carrier molecule (e.g., H_2O). The Grøtthuss-type mechanism is the transport of protons from site to site without a carrier molecule, and its activation energy depends on the hydrogen bond breaking energy and the distance between sites. In most cases, these two proton-conducting mechanisms are not entirely separated from each other and can occur simultaneously to some degree. The dominant mode of proton conduction in Nafion® at low relative humidity (RH) is via the vehicle mechanism, while for PEMs in a high humidity environment, protons are rapidly exchanged between hydrated proton exchange sites via the Grøtthuss mechanism. Proton conduction at low RH requires that water diffuses through the membrane, which can occur effectively through continuous hydrophilic pathways by the vehicle mechanism, such as those found in Nafion®. The proton conductivity of hydrated polymer electrolyes dramatically increases with water content and reaches values of 10^{-2}-10^{-1} S/cm.
Mechanical strength of fuel cell membranes is important since a stronger membrane degrading at a fixed rate will presumably take longer to fail than a comparable membrane

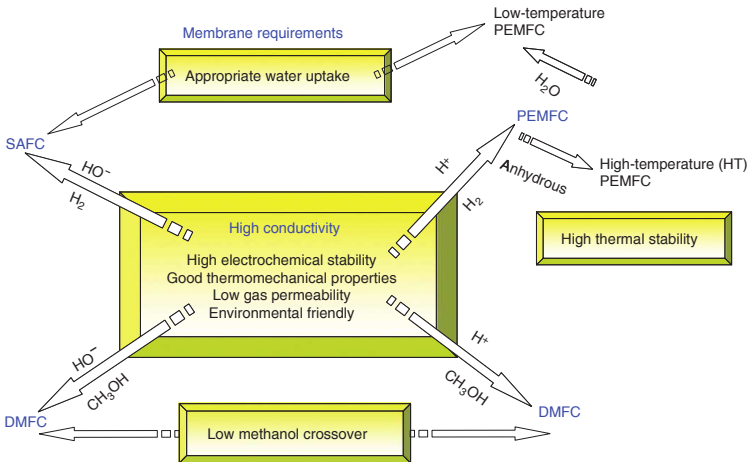

Figure 3.2: *Properties requirements for the different types of fuel cells membranes*

that had lower strength properties at the beginning of life. The mechanically stability is very important especially under conditions of humidity, where the membranes generally show adequate conductivity, thus appropriate choice of

3.2.2 Perfluorosulfonic acid ionomers for fuel cells

Conventional PEMFCs tipically employ perfluorosulfonated membranes in order to provide a good proton exchange. The most common of this kind of polymer is Nafion®. This material is comprised of an hydrophobic main chain of tetrafluoroethylene (TFE) with pendant side chains that incorporate perfluorovinyl ether groups terminated with sulfonate groups. The structure and composition of this polymer provide important properties that are desirable to its employment as PEM [204]. The perfluorinated backbone provide optimal thermal and chemical resistency (only alkali metals can degrade the Nafion® at normal temperatures and pressures), while the presence of highly electronegative fluorine atoms along the side chains of the polymer provide an high acidity ($pK_a \approx$ -6) which is thought to be one reason why the conductivity of perfluorosulfonic acids is higher at lower relative humidities as compared with hydrocarbon membranes that have similar conductivity in the fully hydrated state [205]. At 95% relative humidity, both types membranes have high proton conductivity, but as the water content (i.e., relative humidity) is decreased, the conductivity of the hydrocarbon membrane decreases at a faster rate than that of the PFSA.
Nafion® possesses high proton conductivity due to the formation of hydrogen bonding of the -SO_3H groups which is promoted both at high and low humidity and allows the formation of an interconnected hydrophilic membranes. Gierke and Hsu [206] (Figure 3.3) were the first to suggest the formation of ion clusters in Nafion®; according to their model the high proton conductivity is ascribed to the formation of a structure in which the sulfonic side chain of the polymer aggregate into inverse micelles connected by narrow channels. The cluster diameter, number of exchange sites per cluster and the number of water molecules per exchange site increase linearly with water content.
Gierke and Hsu also proposed the use of percolation theory to explain the correlation of

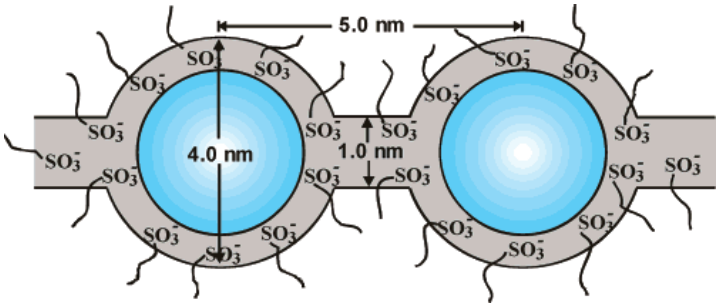

Figure 3.3: *Ionic cluster arrangement defined by the model of Gierke et al.* [206]

electrical conductivity with the water content of the membrane. According to this theory there is a critical amount of water available in the membrane below which ion transport is extremely difficult due to the absence of extended pathways. Recent studies propose an interpretation of the percolation properties of proton conductivity as a function of water content using a "random network model" [207], which is a modification of the "cluster network model". This model includes an intermediate region wherein the side chains ending with pendant sulfonic acid groups, that are ionically bonded to the perfluorinated backbone, tend to cluster within the overall structure of the material resulting in the formation of hydrated regions. Unlike the "cluster network model", the hydrated regions in this model are distributed randomly in the polymer matrix, which facilitates quicker transport of protons upon the rotation of these side chains. In this case although the hydrated regions drift apart, the traverse motion of protons through the membrane is possible.
With reference to Figure 3.4 commercial membranes of Nafion® possess a value of y/x which range between 5 and 11, giving an equivalent weight (EW, grams of material per moles of proton exchanging site) of 1100 to 1500 g of dry Nafion® for mole of sulfonic acid groups and an ion-exchange capacity (IEC) comprised between 0.67 and 1.1 meq/g. The membranes are generally designated with three numbers: the first two referring to the EW and the last to thickness of the membrane (e.g. Nafion® 117 possesses an EW of 1100 and a nominal thickness of about 7×10^{-3} inches).

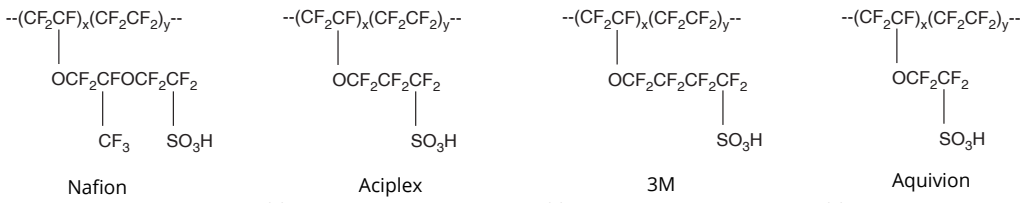

Figure 3.4: *Chemical structure of different perfluorosulfonic acid membranes*

Dow Chemical company, Asahi, 3M and Solvay have synthesized advanced perfluorosulfonic acid membranes that in comparison to Nafion® possess and higher ratio of SO_3H to CF_2 groups (Figure 3.4). This is reflected in a shorter side chain containing the sulfonic acid groups, with the advantage of either higher TFE content at a given acid concentration or higher acid content at the same copolymer ratio. In addition, this polymers have higher

transition temperatures, extending the operating temperatures to higher values.
The main disadvantage of the PFSA membranes is their high cost, due to the inherent expense of the fluorination step. Another disadvantage is their inability to operate above 100°C at atmospheric pressure due to the evaporation of water from the membrane. Higher operating temperatures can be achieved with higher pressures, but this has a negative effect on the system efficiency.

3.2.3 Hydrocarbon based polymer membranes

Many are the advantages of hydrocarbon polymers that have made them particularly attractive as substitute of fluorined based membranes for PEM [208]. Hydrocarbon polymers are cheaper then perfluorinated ionomers and many kinds of materials are commercially available. When containing polar groups this materials show an higher water uptake over a wide range of temperature and absorbed water is restricted to the polar groups of the polymer chains. Decomposition can be depressed to some extent by proper molecular design and the polymers are easily recycled by conventional methods. Of

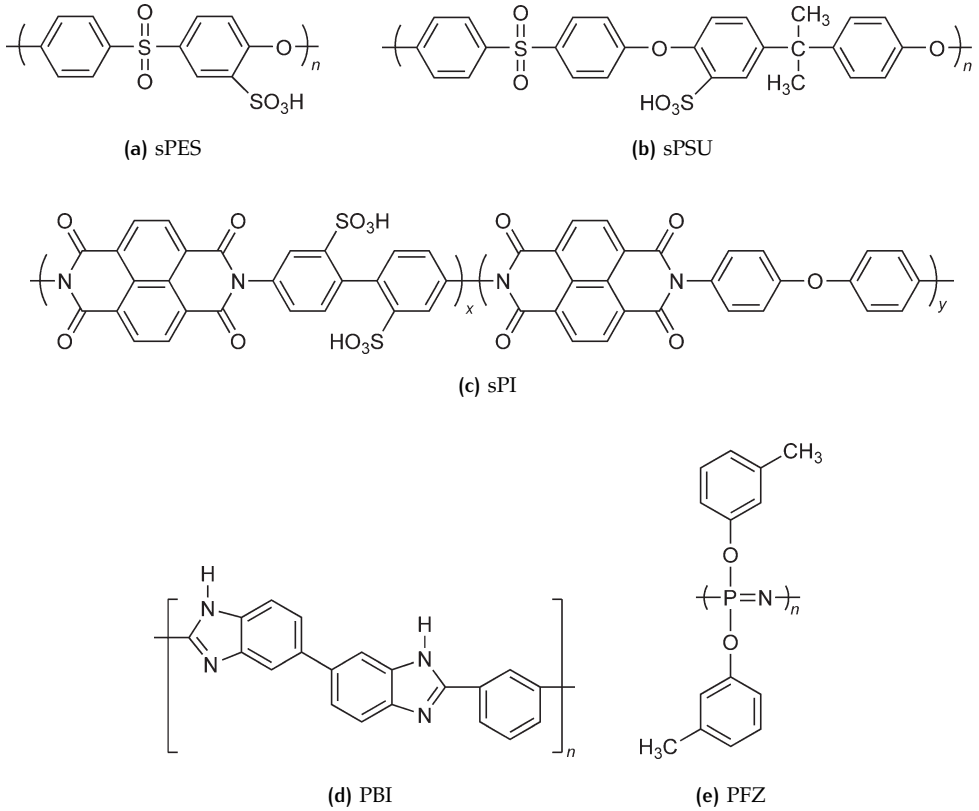

(a) sPES **(b)** sPSU

(c) sPI

(d) PBI **(e)** PFZ

Figure 3.5: *Examples of nonperfluorinated polymer for PEMs (sPES: sulfonated polyethersulfone, sPSU: sulfonated polysulfone, sPI: sulfonated poyimide, PBI: polybenzoimidazole, PFZ: polyphosphazenes)*

the nonfluorinated polymers, the most studied are sulfonated poly(phenyl quinoxalines),

poly(2,6-diphenyl-4-phenylene oxide), poly(aryl ether solfone), acid-doped polybenzimidazole (PBI), partially sulfonated polyether ether ketone (SPEEK), poly(benzyl sulfonic acid)siloxane (PBSS), poly(1,4-phenylene), poly(4phenoxybenzoyl-1,4-phenylene) (PPBP), and polyphenylene sulfide. These and other polymers (some examples are provided in Figure 3.5) can be used as backbone structures for proton-conducting electrolytes and may easily be sulfonated using sulfuric acid, chlorosulfonic acid, sulfur trioxide, or acetyl sulfate producing random copolymers. Most of these polymers can also be modified to give more entanglement of the side chains thereby increasing the physical robustness of the materials. Some of these materials do have improved thermal stability, but unfortunately most have generally lower ionic conductivities than Nafion® at comparable ion-exchange capacities, due to the weaker nature of their acid groups (pKa ~1 as compared to pKa ~-6 of PFSA)[209]. Many of them are also more susceptible than Nafion® to oxidative or acid-catalyzed degradation.
Another widely used approach is the realization of block copolymer with controlled structure [210]. This strategy is useful to tailor the hydrophobic and hydrpophilic characteristics of the polymer in order to promote formation of separated domain not achievable by post processing (sulfonation) of traditional polymers. As in the case of random copolymers the preparation of these sulfonated block copolymers can be performed by postsulfonation of non sulfonated block copolymers or from monomers bearing sulfonic acid groups [211]. These copolymer show higher proton conductivity than their random counterparts thanks to their microdomain size and orientation but can suffer from limited solubility [212].

3.2.4 Composite membranes

Composite membranes have been developed in the continuous effort to improve the limitations of the previously described membranes. Two approaches have been followed to overcome the limitations of PFSA membranes and increase their water management: reducing membrane thickness and realize composite membranes. In the first case thinner membranes can reduce internal ionic resistance but they are limited due to low mechanical strength, they can lead to limited fuel crossover with decrease with reduction in observed cell voltage and require a suitable reinforcing material. In the second approach composite membranes have been obtained by inclusion of small particles of hygroscopic oxides such as SiO_2 and TiO_2 [213] or heteropolyacids [214] to improve water retention, mechanical properties and selectivity of the PFSA. However the incorporation of such particles normally led to a reduced proton conductivity to the reference materials and mechanical brittleness at high loadings. Better results have been obtained by incorporation of proton-conducting materials [215].
In an attempt to avoid the difficulties associated with hydrated polymers in which protons are conducted as hydronium ions, many research groups have sought to immobilize an anhydrous acid such as H_2SO_4,H_3PO_4, or HCl by complexing it within a basic polymer. Polymers that have been investigated for use in such systems include polyethylene oxide (PEO), polyvinyl alcohol (PVA), polyacrylamide (PAM), polyvinylpyrrolidone (PVP), polyetheleneimine (PEI), various polyamino silicates, and polybenzoimidazole (PBI). In

these materials, the acid molecule is attached to the polymer via hydrogen bonding and can be thought of as a solution of acid in polymer. The acid provides the means of proton conduction and, as would be expected, the higher the acid content, the greater is the proton conductivity of the membrane. High acid contents unfortunately also reduce the mechanical stability of the membrane particularly above 100°C. Inevitably, the acids are not perfectly anhydrous and a certain amount of water is often added to improve conductivity and mechanical properties.

3.3 ELECTROSPINNING OF IONOMERS FOR FUEL CELL MEMBRANES

While the investigations about the *electrospinning* process of common polymers are abundant through the scientific literature, the studies related to the production of nanofibers of ionomers started only in the last years due to the increasing interest towards their applications for ion-exchange, gas separation and proton exchange membranes (PEMs) [216].
Of particular interest in the field of energy applications is the possibility of employ nanofibrous/porous structures, produced by *electrospinning*, for PEMs as reinforcements to minimize in-plane swelling and shrinking. [217]. Nanofibers of polymer electrolytes can also be able to increase proton conductivity with respect to bulk film, thanks to their highly oriented ionic domains [110], and provide good mechanical strength, while the remarkable flexibility of their production process allows to adequately tailor their final morphology for composite membranes.
Polymer membranes for fuel cells are semipermeable membranes that have the function to be proton conductive, electron insulating and dense in order to avoid fuel crossover. For this reason two types of approaches can be used when employing *electrospinning* for such application [218]:

1. the *electrospinning* of non-conductive or less conductive polymer into a porous matrix, which acts as mechanical reinforcement when the pores are filled with a highly proton conductive component;

2. alternatively, a highly proton conducting matrix is electrospun into a porous fiber mat and subsequently reinforced with a secondary polymer to provide mechanical stability.

This second approach is particularly suitable as an alternative for system with dispersed nanoparticles in a polymer matrix since electrospun nanofibrous mats of proton conducting polymers always provide a percolated structure thanks to the high number of contacts for each nanofiber in the mesh, ensuring a conductive pathway between the electrodes [219]. On the other side composite membranes with nanofibers show superior mechanical strength, than membranes based polymer blends, due to a better dispersion of the reinforcement polymer throughout the membrane.
For the development of composite PEMs based on electrospun polymers the first studies

were related to the investigation of perfluorosulfonic acids nanofibers production, especially Nafion®. Unfortunately this polymer shows poor electrospinnability even at high concentrations and with different solvents, due to the low viscosity of the resulted solutions which favors the production of electrosprayed beads [220]. Small angle neutron scattering (SANS), small-angle X-ray scattering (SAXS) [221] and electron spin resonance (ESR) [222] studies have demonstrated that Nafion® solutions show a colloidal dispersion structure, while by Dynamic light scattering (DLS) [220] it has been showed that generally these solutions present multi- or bimodal distributions. The smaller particles are essentially single polymer chains while the medium and large ones are attributable, respectively, to primary rod-like aggregates due to the hydrophobic interaction of the fluorocarbon backbone and secondary larger aggregates formed by the ionic interactions of the side chains. The existence of one or more of these aggregates is imputable to the impossibility of Nafion® nanofibers generation. As a consequence a partial solution of the problem has been found by *electrospinning* solutions of Nafion® with a small percentage of a high-molecular weight carrier polymer, capable to induce the production of Nafion® nanofibers (see Table 3.3). Despite this alternative it is important to use a low concentration of the carrier polymer since it dilutes the ion-exchange material and it can be prone to degradation in some membrane application. Extraction of the carrier polymer after *electrospinning* can be easily accomplished, but the fibers could be significantly weakened with high carrier concentrations [227]. Generally this is accomplished by using high molecular weight carriers which can be employed at low concentrations and at the same time are able to maintain a suitable viscosity of the solution to be electrospinned.

Table 3.3: *Overview of Nafion® electrospun nanofibers studies for fuel cell membrane applications*

Polymer	Solvent	Carrier	Reference
Nafion®	IPA/H_2O	PAA	[220]
Nafion®	IPA/H_2O	PVA or PEO	[223]
Nafion®	MeOH	PEO	[110]
Nafion®	EtOH	PVP	[224]
Nafion®	Alcohols/H_2O	PEO	[225]
Nafion®	H_2O	PEO, PVA or PVP	[226]

Ballengee and Pintauro [225] studied the *electrospinning* of Nafion with low concentrations of PEO as carrier polymer. They observed that the quality and morphology of the fibers are affected by several *electrospinning* parameters. High humidities and applied voltages favor the development of a beads-on-fiber morphology while high molecular weights of the carrier polymer lead to a ribbon like structures. They were able to obtain nanofiber dimension ranging from 300 to 900 nm according to variation in air humidity, solution solvent, electrospinning flow rate and carrier polymer molecular weight.

Subianto et al. [228] analyzed the effect of side-chain length of perfluorosulfonic acid ionomers on the properties of nanofibers obtained by *electrospinning* ionomers dispersions using PEO as polymer carrier. They concluded that the side chain length produced rad-

ically different properties on *electrospinning*. With shorter side chain the *electrospinning* process is facilitated resulting in lower average fiber diameters and the *electrospinning* process produces more uniform fibers by using polar aprotic solvent rather than water or alcohols.

3.3.1 Composite PEMs based on electrospun nanofibers

As described previously two main approaches have been followed for the implementation of the electrospinning techniques for the development of PEMs membranes. According to the first approach non- or low-conducting electrospun nonwoven acts as reinforcement for a ionomer, which fills void spaces within the fibers and ensure the proton conduction through the membrane. For fuel cell applications, a low-density electrospun mat is required since the volume of the pores and their interconnectivity should be maximized to ensure an efficient proton transfer. Furthermore, using this strategy a higher through plane conductivity is expected compared to blend or conventional reinforced membranes due to better interconnectivity of ionic domains along the thickness direction and a more homogenous distribution of the reinforcing fibers within the ionomer matrix [229]. In the second approach a highly proton conducting polymer is electrospun into a porous fiber mat that is impregnated with a secondary polymer providing mechanical stability. In this case, the mechanical properties can be improved due to the nonconducting, inert filler acting as a sheath around the ionomer nanofibers limiting their swelling. Thus, this approach requires a dense nanofiber mat that would ensure a contiguous proton-conducting path throughout the membrane [229]. Hereafter an overview of the results related to the employment of these two approach is presented and the different polymer systems employed are summarized in Table 3.4 and Table 3.5.

Laforgue et al. [223] realized nanostructures of Nafion-poly(vinyl alcohol) (PVA) and Nafion-poly(ethylene oxide) (PEO) obtaining nanospheres and/or nanofibers in relation to the ratio between the two polymers. They observed that the fiber morphology is more conductive than sphere ones and at the same time that the Nafion/PVA mats were more conductive than Nafion/PEO. However all the electrospun mats presented ionic conductivities slightly lower than extruded Nafion 115 and Nafion/PVA cast films.

Chen et al.[220] electrospun a polymer solution blend of Nafion and poly (acrylic acid) (PAA). They first attempt to electrospin pure Nafion in solutions at different concentration, but without success. Then they were able to produce nanofibers with diameter ranging from 90 to 600 nm with solution of Nafion/PAA blend with constant Nafion concentration but varying the amount of PAA added.

Choi et al. [227] electrospun two low equivalent weights perfluorosulfonic acid polymers by adding a 0.3% high molecular weight PEO. By a four steps procedure they were able to weld the fibers at the intersection points with each other, compress the mat in order to increase the volume of fibers, imbibing an inert polymer to create a continuous membrane which had been subsequently crosslinked by UV light and removing the PEO fraction in the membrane by an acid treatment. The composite membranes showed a better proton

conduction with respect to a commercial Nafion 212 at medium and high humidities. Improvements have been realized both in terms of low water swelling and high mechanical properties with respect to recast homogeneous PFSA films.

These attempts were related to the will of comparing normal casted membrane with electrospun ones to discover possible improvements for their applications in fuel cell devices. To this end Dong et al. [110] analyzed the proton conductivity of a single high-purity Nafion nanofiber. They observed that the proton conductivity of the single nanofiber is about an order of magnitude higher than a bulk film of Nafion, and increased sharply by decreasing the fiber diameter. The explanation of this behavior was found by X-ray scattering analysis which showed an high orientation of the ionic domains along the axis of the Nafion nanofiber due to the shear force applied during the electrospinning process. Since other materials has been identified as possible candidates for substituting Nafion as PEM and tested as compact membranes by casting, even electrospun mats of other sulfonated polymers have been studied alone and as blend with or without Nafion.

Ballengee and Pintauro [230] simultaneously electrospun a dual fiber mat comprised of poly(phenyl sulfone) (PPSU) and Nafion. Nafion was electrospun by dissolving Nafion and PEO powders (1 wt % of PEO in the total polymer content) into a 2:1 weight ratio n-propanol:water mixture with concentrations between 20 and 25% while PPSU was electrospun from a different syringe from a 25 wt % solution, starting from a solution of 80:20 weight ratio of NMP and acetone. After the electrospinning process they were able to process the mat in order to obtain two different structures: a membrane with Nafion reinforced by PPSU fibers by the action of pressure and thermal annealing of the electrospun mat and a membrane with Nafion fibers embedded in PPSU by the action of pressure and solvent vapor exposure of the electrospun mat. They showed that the two kinds of membranes possess similar proton conductivity and scaled linearly with the Nafion volume fraction. These composites membranes showed better mechanical properties and lower water swelling than common fuel cell membranes which translates into an improved PEM/MEA longevity as compared to a Nafion 212 membrane.

Li et al. [231] electrospun a high sulfonated (DS = 100%) poly(ether ether ketone ketone) (sPEEKK), obtained by direct aromatic nucleophilic substitution polymerization, with DMF at a concentration of 15% by weight. They obtained a non-woven mat with fibers of 90 nm of average diameter. However they observed that the highest proton conductivity was achieved when the mat was deposited under the form of particles rather than fibers.

Takamura and Kawakami [232] synthesized a composite membrane of sulfonated polyimide nanofibers and sulfonated polyimide. The high orientation of the polyimide inside the nanofibers led to a significant improvement in oxidative and hydroliytic stabilities, with a decrease in oxygen permeability. They also observed that the proton conductivity of the membrane in the parallel direction had an higher value than for the perpendicular direction and in turn that in this last case the proton conductivity is higher than for the membrane without nanofibers, reaching the conclusion that nanofibers can be promising materials for proton exchange membrane.

Danying et al. [233] have electrospun a sulfonated poly(phthalazinone ether ketone)

(sPPEK) with low sulfonation degree (64%). By dissolving the sulfonated polymer in a 50:50 v/v mixture of DMAc and NMP they reached a uniform distribution of nanometric fibers (of about 50 nm of diameter) and realized an homogeneous composite membrane with phosphotungstic acid. The mat obtained showed a better performance than a sPPEK casted membrane in terms of proton conductivity probably due to the formation of a long-range proton conductivity pathways on the surfaces of the nanofibers.
Takemori et al. [234] analyzed the proton conductivity of uniaxially-aligned sulfonated polyimide (sPI) under different conditions of temperatures and humidity. They chose a suitable sulfonation degree (1.65 meq/g) in terms of proton conductivity, thermal stability and nanofiber formability [232, 235, 236]. The results of their experimental work showed how nanofibers present an unique proton conductivity at low humidities, higher than sPI membranes. They have an higher water retention that can be induced by the formation of continuous proton conductive channel generated by a hydrophilic/hydrophobic phase separation during the electrospinning process. The best results are shown in the case of the fibers with low diameters that allow a quasi-one-dimensional narrow conduction pathway and molecular orientation.
Besides the two approaches mentioned at the beginning, recently some works have pointed out the possibility to modify PFSA-based membranes in order to obtain highly proton-conductive membranes and, in some cases, simultaneously improve other properties such as mechanical strength In this case the idea is to develop PEMs based both on a polyelectrolyte matrix and nanofibers, since polyelectrolyte fiber-incorporated membranes can be unsatisfactory for practical fuel cell applications because of the presence of insulating polymer matrixes.
Yao et al. [237] realized an hybrid membrane based on sulfonated polystyrene (S-PS) electrospun fibers embedded into Nafion. The electrospun mat of polystyrene was post-sulfonated by soaking in a solution of H_2SO_4 and the hybrid membrane was realized by casting with Nafion. In this manner they were able to have embedded fibers with an inert core, to reduce the swelling and improve mechanical strength, and sulfonic acid groups on the surface, in order to ensure an optimum utilization of percolation pathways for proton transport along the fiber-Nafion interfaces. The results confirm an higher proton conductivity, with respect to casted S-PS and Nafion, at every level of relative humidity and an higher gravimetric water uptake percentage.

3.3.2 Proton conduction in electrospun membranes

The different morphologies achievable with the employment of electrospinning are capable to change even the transport proprieties of proton conductive materials if compared to standard techniques such as solution casting. To this regard two different hypotheses have been formulated to explain how protons can be transported when the material present such morphology. Li et al. [231] by comparing the SAXS spectra of different sulfonated poly(ether ether ketone ketone) (sPEEKK) samples have found that electrospun/electrosprayed membranes present a more distinct ionomerc peak, shifted to lower angles, than casted membranes. This peculiar result can be ascribed to an enhanced phase separation

Table 3.4: *Proton conductivity of composite membranes for fuel cells based on non-conductive electrospun polymers in a conductive matrix*

Electrospun Polymer	Filler	Proton conductivity [mS cm^{-1}]	Reference
PSSA-g-PVDF	Nafion	64 (20°C, 95% RH)	[238]
PVA	Nafion	11 (70°C,95% RH)	[239]
PVA	Nafion	22 (70°C,100% RH)	[240]
PVA	Nafion	19 (70°C, 95% RH)	[241]
PVDF-co-HFP/PBI	Nafion	13 (70°C, 95% RH)	[125]
PVDF	Nafion	60 (20°C, 95% RH)	[242]
SiO_2/sPEEK	Nafion	80 (90°C, 100% RH)	[243]
sPI	sPI	370 (80°C, 98% RH)	[235]
BPPO	sPPO	80 (RT, 100% RH)	[244]
sPES	Nafion	62 (20°C, 100% RH)	[245]
PBI	PBI	170 (160°C, 0% RH)	[246]
s-PS	Nafion	180 (80°C, 100% RH)	[237]
PBI-PBz	PBI	170 (160°C, 0% RH)	[246]
PLGA	Nafion	48 (RT, 100% RH)	[247]
$(Zr(OPr)_4)$/PVP	C-PAMPS	340(100°C)	[248]

Table 3.5: *Proton conductivity of composite membranes for fuel cells based on a conductive electrospun polymers in a non-conductive matrix*

Electrospun Polymer	Filler	Proton conductivity [mS cm^{-1}]	Reference
sPS/PEO (70:30 w/w)	PDMS	100 (25°C, 98% RH)	[119]
sPAES	PAN	166 (80°C, 100% RH)	[249]
sPAES	PU	94 (30°C, 80% RH)	[250]
PFSA/PEO	PU	160 (80°C, 80% RH)	[227]
sPFEK	PES	33 (80°C, 100% RH)	[251]

between hydrophilic and hydrophobic domains with the formation of ionic clusters of sulfonated groups and larger proton transport channels. Besides the authors have interpret the shift of the ionomeric peak in the spectra as a result of the increase in the "center to center distance" between two clusters, according to the so called "interparticle model" for SAXS of ionomers. This theory provide an explanation for their results of proton conductivity in which the highest conductivity was reached with a spherical rather than fibrous morphology, suggesting that proton transport occurs on the interface between particles rather than within the polymer itself.

On the other side several studies [110, 232] have shown that the apparent proton conductivity within of a single proton conductive nanofiber is relatively higher if compared to the value obtainable by solution casting of the same material due to the alignment of the ionic aggregates that happen during electrospinning. The increment is also enhanced by reducing the fiber diameter [110], suggesting a closer interaction of the ionic domains probably due to the alignment that the polymeric chains experience during the electrospinning process as a consequence of the high shear forces responsible for the formation of thinner

fibers. This has been suggested as a consequence of the reduction in the activation energy of proton conductivity in the nanofibrous mat than in the corresponding cast membranes due to the assumption of quasi-onedimensional narrow conduction pathway inside the thin nanofibers that permits rectilinear fast proton transport.
Thus the dispute on the real mechanism of conduction of electrospun membranes of proton conduction has not reached a clear result and other studies [252, 253] suggest that the orientation of the polymer chains of electrospun materials depends on the competing effect between the extensional forces (promoting chain orientation along the drawing direction) and orientation/relaxation (promoting a return to the isotropic state) due to residual solvent. However ionomers would be able to retain this oriented morphology through ionic bonding between charged groups locking the oriented structure and preventing relaxation [229].

4 MATERIALS AND INSTRUMENTATION

Here are briefly reported the main materials employed for the preparation of the nanostructured membranes employed in the experimental part of the thesis, with a short general exposition on the synthesis, properties and applications of each one. In the second part of the chapter a description is provided with regards to principal analytical techniques employed for the characterization study of the membranes.

4.1 MATERIALS

4.1.1 Poly (ether ether ketone) (PEEK)

Polyether ether ketone (PEEK) (Figure 4.1) is a polyaromatic, semicrystalline thermoplastic polymer which belongs to the polyaryletherketone (PAEK) family and its used in engineering applications. Its chemical structure is characterized by the presence of the ether bridges and ketone groups which link together arylene groups. Currently, the only product manufactured worldwide is Victrex PEEK, launched by Imperial Chemical Industries, Ltd. (ICI) in 1978 and by Amoco Chemicals Corp. in the middle 1980s under the trade name Kadel. It is produced by both companies in the United States [254]. PAEKs are

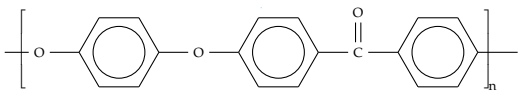

Figure 4.1: *Repetitive unit of PEEK*

a type of high performance thermoplastic polymers that are particularly useful in aggressive environments. This groups includes PEK, PEKK and PEKEKK, where the different names reflect the proportion and sequence of ether (E) and ketone (K) components in the monomer (Figure 4.2).
The first polymer of this group (PEK) was commercialized by Raytheon in the 1970s under the trade name Stilan. Equivalent materials were commercialized by Hoechst Celanese and Amoco, Whereas PEKEKK and PEKK were commercialized by BASF and DuPont, respectively.

4.1.1.1 *Synthesis*

Quite analogous to poly(ether sulfone)s, the synthetic methods reported for PEKs may be subdivided into three groups [255]:

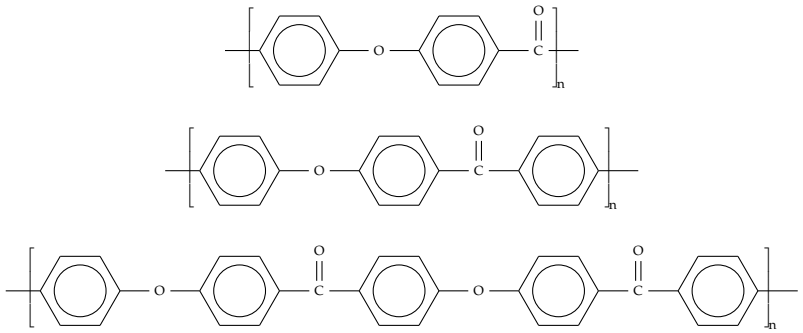

Figure 4.2: *Repeating unit of different polyether ketones: PEK, PEKK, PEKEKK*

1. Polycondensation involving an electrophilic substitution (i.e. acylation of a phenoxy group);
2. Polycondensation involving a nucleophilic substitution of chloro-, fluoro- or nitro-aromat activated by a keto group in para position
3. Modification of suitable precursor polymers

PEEK is obtained by step-growth polymerization by the dialkylation of bisphenolate salts and is produced in batches, with rather high production costs. Typical is the reaction of 4,4'-difluorobenzophenone with the disodium salt of hydroquinone, which is generated in situ by deprotonation with sodium carbonate. The reaction is conducted at high temperatures (around 300°C), under an inert atmosphere, in polar aprotic solvents - such as diphenyl sulphone (Figure 4.3).

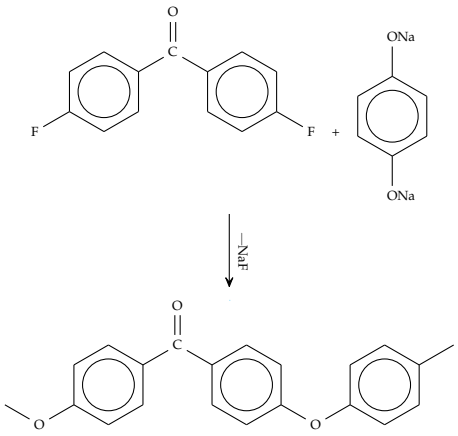

Figure 4.3: *Main reaction for the production of PEEK*

The polymer is isolated from the diphenyl sulfone and inorganic impurities, which can destabilize the polymer melt, by solvent extraction (leaching). A slight excess of 4,4-difluorobenzophenone is normally employed to prevent the formation of phenoxide chain ends which can destabilize the polymer. The water formed as a result of polycondensation could potentially hydrolyze the fluoro groups and prevent formation of high molecular mass polymer but is lost due to the high reaction temperature and the hydrophobicity of

solvent. The expensive difluoro monomer is required instead of the less expensive dichloro analogue because the weakly electronwithdrawing carbonyl group does not strongly activate the halogen to nucleophilic displacement and consequently a good leaving group is necessary for efficient reaction [256].

4.1.1.2 *Properties and applications*

PEEK is a semicrystalline due to the strong interchain forces between the polar groups in the backbone and the near equivalence of the ether and carbonyl units. Its crystallization behavior is very similar to that of poly (ethylene terephtalate) except that the main transitions occur about 75°C higher. This semycristalline morphology is largely responsible for its excellent resistant to solvent attack. PEEK is insoluble in all common solvents and its soluble at room temperature only in strongly acidic media (e.g. concentrated sulfuric acid, hydrofluoric acid and trifluoromethanesulfonic acid) that can protonate the carbonyl groups. At temperatures well above the glass transition temperature the polymer is soluble in few unusual media (e.g. diphenyl sulfone, some high boiling point esters, benzophenone and 1-chloronaphtalene). PEEK displays limited resistance to degradation by UV light, as is the case for all linear polyaromatics, but the problem is only serious in high insulation environment (i.e. prolonged exposure to intense sunlight) and is much reduced by incorporation of suitable pigment (e.g. carbon black, a famous UV adsorber) [256].
The PEEK resins is marketed as neat or filled pellets for injection molding, as powder for coatings, or as pre-preg fiber sheet and tapes. Applications include parts that are exposed to high temperature, radiation, or aggressive chemical environment.
The employed PEEK has been purchased by Aldrich (M_w = 20,800 Dalton, 1.32 g/cm^3)

4.1.2 Polyacrylonitrile (PAN)

Polyacrylonitrile is a synthetic resin prepared by the polymerization of acrylonitrile and member of the import acrylic resins family. Its repetitive unit is shown in Figure 4.4

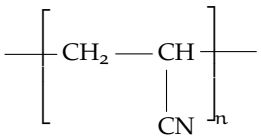

Figure 4.4: *Repetitive unit of PAN*

Although the polymerization of acrylonitrile had been known since the 1890s, commercial production of PAN fibre did not begin until the 1940s, after Ray C. Houtz of E.I. du Pont de Nemours & Company (now DuPont Company) discovered spinning solvents that could dissolve the polymer. DuPont introduced its trademarked Orlon acrylic fibre in 1948; Orlon was soon followed by the Monsanto Chemical Company's Acrilan, American Cyanamid's Creslan, Courtaulds' Courtelle, and others. The decade of the 1950s also saw the introduction of modacrylics such as Eastman Kodak Company's Verel and Monsanto's SEF.

4.1.2.1 *Synthesis*

All commercial methods of production of PAN are based on free radical polymerization of acrylonitrile (AN) obtained by reacting propylene (CH_2=$CHCH_3$) with ammonia (NH_3) and oxygen in the presence of catalysts (Sohio process).

$$nCH_3CH = CH_2 + nNH_3 + \frac{3n}{2}O_2 \rightarrow [CH_2 = CH - CN]_n + 3nH_2O \tag{4.1}$$

Acrylonitrile monomers (single-unit molecules) are suspended, almost always in combination with other monomers, as fine droplets in water and are induced to polymerize to PAN through the action of free-radical initiators (a peroxide or a mixture of $K_2S_2O_8$ and a reducing agent as $KHSO_3$). Anionic polymerization also can be used for synthesizing PAN. For textile applications, molecular weight in the range of 40,000 to 70,000 is used. For producing carbon fiber higher molecular weight is desired.
The PAN employed for the tests was purchased from Sigma-Aldrich (M_w = 150,000 Dalton)

4.1.2.2 *Properties and applications*

PAN it is a hard, rigid thermoplastic material that is resistant to most solvents and chemicals, slow to burn, and of low permeability to gases. Though it is thermoplastic, it does not melt under normal conditions and degrades before melting.
PAN is a versatile polymer used to produce large variety of products including ultra filtration membranes, hollow fibers for reverse osmosis, fibers for textiles, oxidized PAN fibers. PAN fibers are the chemical precursor of high-quality carbon fiber. PAN is first thermally oxidized in air at 230 degrees to form an oxidized PAN fiber and then carbonized above 1000°C in inert atmosphere to make carbon fibers found in a variety of both high-tech and common daily applications such as civil and military aircraft primary and secondary structures, missiles, solid propellant rocket motors, pressure vessels, fishing rods, tennis rackets, badminton rackets and high-tech bicycles. It is a component repeat unit in several important copolymers, such as styrene-acrylonitrile (SAN) and acrylonitrile butadiene styrene (ABS) plastic.

4.1.3 Graphene and graphene oxide

Graphene is a monoatomic layer of carbon atoms organized according to a honeycomb crystalline structure. Such structure has a planar configuration and as such the monoatomic layer is a bidimensional material. Graphene, whose carbon atoms are sp^2 hybridized, can be considered as the basic structure for the construction of all the other known graphitic materials such as fullerene (0D), carbon nanotubes (1D) and graphite (3D) [257] (Figure 4.5).

For several decades, even though recognized as integral part of the graphitic materials, graphene was studied as "academic" material since it was considered to be thermodinamically instable due to the tendency to curve and form structures like fullerenes and nan-

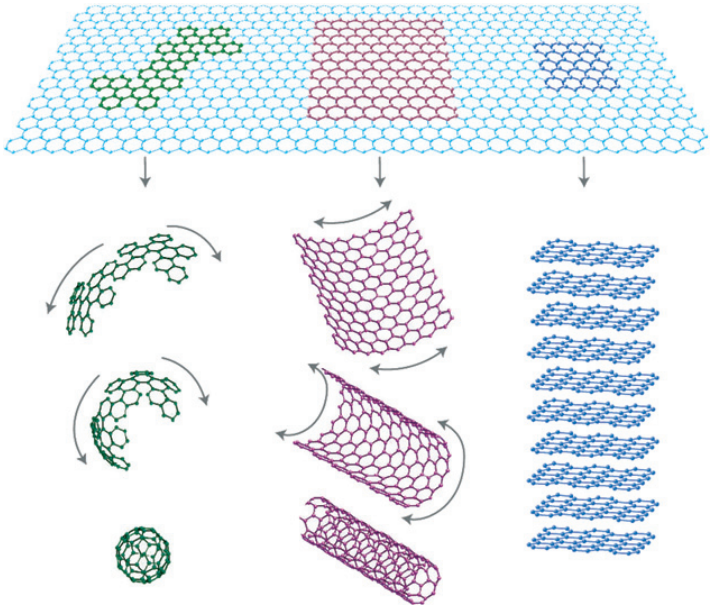

Figure 4.5: *Structure of the graphitic materials. From left to right: fullerene (0D), nanotube (1D), and graphene (2D) [257]*

otubes [258].
In 2004 Novoselov and Geim were able to isolate a layer of graphene by the "scotch tape method", namely a peeling process of graphite by micromechanical cleavage on a silicon wafer by an adhesive tape [259].

4.1.3.1 *Synthesis*

During the last ten years a number of methods for the production of graphene monolayers have been developed. it is important to note that nowadays there is no a single optimal method and the cost to obtain high quality and quantity graphene represents the most important limit of the entire research regarding this material. The current employed methods, both to a laboratory and industrial scale, can be divided into different categories depending on the chemical or physical process employed to obtain the single layer graphene. Graphene production techniques fall into one of the two categories: bottom-up or top down synthesis. In bottom-up approaches graphene is synthesized from atomic or molecular species, while in top down synthesis graphene is obtained by using graphitic microstructures microstructures (such as graphite or graphite oxide) as starting materials. Theoretically, the bottom-up techniques allows accurate control of size, shape, thickness and agglomeration [260]. However, these methods of synthesis have some disadvantages such as high price of processing and expensive starting materials, so they are not suitable for large scale production. On the other hand, in top-down processes the use of relatively cheap starting materials offers significant economic advantages. The latter methods make use of the particular crystal structure of graphite which is constituted by overlying layers of graphene held together by interplane Van der Waals forces with energies of about

$2eV/nm^2$ which accounts for its flaky nature in the direction parallel to the crystal plane. The most common production methods are:

- mechanical cleavage: the technique is based on the mechanical action of a scotch tape to remove the layers of an highly oriented pyrolitic graphite (HOPG). The tape with the graphite fingerprint is folded down on itself and unrolled several times. Each time the flakes deposited are divide in increasingly thin layers. At the end of the process the thin flakes on the tape can be easily transferred on an insulating substrate. The graphene so obtained shows the best properties, but the production method is unsuitable for industrial scale production [257, 261];

- chemical vapor deposition: this technique allows the growth of the material on metallic substrate, usually nichel (Ni) or copper (Cu) using a mixture of precursor hydrocarbons (i.e. methane or ethylene) in presence of H_2 at a temperature comprised between 700-1000°C. The growth mechanism require a first phase in which carbon diffuses in the metallic substrate, subsequently the system is cooled with segregation of the carbon on the surface and at the by using the chemical etching of the metallic substrate it is possible to remove the graphene layer.
  Another method provides for the thermal decomposition of SiC by heating at 1300°C of the chambers where the substrate is placed; these conditions determine the sublimation of the silicon atoms, while the carbon atoms remained on the surface are rearranged to form graphene planes.
  Despite lateral dimension in the order of 1 cm, with this method the graphene sheets requires the transfer on insulating substrate to be employed, while with SiC composite crystal with heterogeneous domains are obtained [257, 261, 262];

- chemical synthesis: this production method is based on the Hummers procedure for the production of graphene oxide [263], a product of oxidation of neutral graphite characterized to be a lamellar solid with unoxidized aromatic regions and aliphatic regions containing phenolic, carboxyl and epoxide groups. In this method HOPG is oxidized with concentrated sulfuric acid, nitric acid and potassium permanganate. As a consequence of these treatments highly polar groups (-OH,-COOH) are produced on the surface of the material, which becomes highly hydrophilic and easily exfoliable in water or polar solvents. Subsequently a reduction and dehydration phase is carried to obtain reduced chemically derived graphene. Another alternative is thermal annealing, which involves reaction of neighboring oxygen groups on the graphene oxide with molecules intercalated between the graphene oxide planes, liberating reaction products including carbon monoxide, water and carbon dioxide.
  The advantages of this method are the low cost and the scalability of the process but the materials has drawbacks in terms of higher defects and lower yield compared with other techniques along with the employment of highly toxic and corrosive solvents [257, 261, 264].

- Liquid exfoliation: with this method graphite dispersion are obtained by ultrasonic treatment of graphite in a suitable solvent. Acoustic cavitation provides unusual

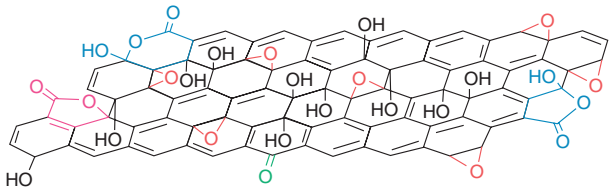

Figure 4.6: *Structural model of graphene oxide. Image taken from [265]*

chemical conditions because extremely high temperatures and pressures are reached for short times in the liquid [266]. After the sonication the suspension is characterized by the presence of an homogeneous phase and by a number of macroscopic aggregates that can be separated by centrifugation. Common employed solvents are NMP, DMF and water with surfactants. Organic solvents are preferred due to their higher interaction between the solvent the carbon surfaces and their surface tension which matches that of graphene. Sonication methods usually provide a mixture of several derivatives where single graphene represents a percentage of 1–15% and the rest consists of few-layer graphene nanosheets, where the number of layers range from 2 to 10. However prolonged sonication times could lead to radical reactions with a consequent reduction of the sheet size and a higher number of defects [267]. This method represents a compromise between quality, costs and process scalability; in particular, in many applications, even if in not risible quantity, the quality of the material should not be monolayer in order to obtain sensible improvement in the physico-chemical performances [268]

On the basis of these consideration it is clear that the different production methods of graphene provides different final characteristics to the material in terms of number of layers, purity, oxygen content, crystallinity and shape. The specific final characteristics of the material should be defined accordingly to final applications. In the present work few layer graphene produced by Avanzare Innovacion Tecnologica S.L. has been employed. This graphene is obtain by a combination of reduction techniques at high temperatures which produces $C_{50}O$ graphene.

4.1.3.2 *Properties and applications*

Graphene properties are essentially related to the peculiar 2D structures of the material and a complete physical and chemical characterization is ongoing due to its recent discovery. One of the most important characteristics of graphene is its nature of zero band gap semi-metal with a very high electric conductivity. The carbon atoms have six electrons in total: two in the first valence shell and 4 in the more external shell. The latter have the possibility to create chemical bond but in graphene each atom is bonded with other three atoms in the same x-y plane, leaving a free electron in the third dimension (z axis). The orbitals represented by these electrons, called π electrons, are placed above and below each graphene layer, they overlaps between each other and reinforce the carbon-carbon bonds. It has been demonstrated that in the Dirac point (energy spectrum in proximity of the maximum of valence band and the minimum of the conduction band) of graphene the

electrons and the holes have null mass. This happens because the energy-displacement relationship is linear at low energies in proximities of the vertexes of the Brillouin zone; the electrons and the vacancies are known as "Dirac fermions" and the corresponding six vertexes of the Brillouin zone as "Dirac points".
Several tests have proved the high mobility of the electronic cloud of graphene, with results ranging from 15,000 to 200,000 $cm^2/(V{\cdot}s)$ (limit due to acoustic scattering of the photons). These charge carriers are able to travel sub-micrometer distances without scattering; a phenomenon known as ballistic transport. The major limiting factor are the quality of graphene and the employed substrate; in the more frequent case of a silica substrate, the electronic mobility is potentially limited to 40,000 $cm^2/(V{\cdot}s)$. Graphene represents the material with the lowest resistivity ($1.0 \cdot 10^{-8}$ Ωm) ever known so far, lower than that of silver ($1.59 \cdot 10^{-8}$ Ωm). With graphene it is possible to obtain current densities even higher than 10^8 A/cm^2, namely six order of magnitude higher than those that can flow in silver [261, 269–271].
Another important characteristic of graphene is its mechanical strength. Since now it is considered the material with the higher strength known in nature, thanks to its ultimate tensile strength of 130 GPa combined with a very low density (0.77 $mg{\cdot}cm^3$), a value much higher than the strength of iron A36 (0.4 GPa) and that of Kevlar (0.38 GPa). Its elastic modulus is about 1 TPa, higher than those of diamond (0.82 GPa) and iron (0.2 TPa). These values can be highly variable due to the difficulties to determine the precise geometry of the graphene sample, the tension in the points of contact with the supporting membrane and the intrinsic defects of the material, which is never null [272–274].
Graphene's ability to absorb a rather large 2.3% of white light is also a unique and interesting property, especially considering that it is only 1 atom thick. This is due to its aforementioned electronic properties; the electrons acting like massless charge carriers with very high mobility. Due to these impressive characteristics, it has been observed that once optical intensity reaches a certain threshold (known as the "saturation fluence") saturable absorption takes place (very high intensity light causes a reduction in absorption). This phenomenon is important since allows to evaluate graphene in numerous electronic and optoelectronic devices (LCDs, OLEDs) and applications due to its low influence to the wavelength of the incident radiation.
Graphene is also a perfect thermal conductor. Its thermal conductivity (5,000 $W/(m{\cdot}K)$) is higher than all the observed values of the carbonaceous structures like nanotubes, graphites and diamonds. A monolayer of graphene deposited on a SiO_2, instead, shows a conductivity of 600 $W/(m{\cdot}K)$, higher than those of metals like copper (380 $W/(m{\cdot}K)$) and silver (430 $W/(m{\cdot}K)$). It is assumed that the abatement of about a factor of 10 of the conductivity of the graphene layer on a substrate with respect to that in a free state is due to the scattering of phonons and impurities at the SiO_2 interface [275, 276]. The ballistic thermal conductance of graphene is isotropic, similarly to the other properties of the material. The study of the thermal conductivity of this material has important implications for the generation of new electronic devices, which are continuously diminishing their dimensions with a concurrent increase in the density of the electronic circuits. In this sense an higher thermal conductivity could allow an efficient heat dissipation of the internal

circuits [277].
Similarly to graphite, the graphene can absorb or desorb various types of atoms or weakly bonded molecules which act as donors (e.g. CO, NH_3 and CH_3CH_2OH) or acceptors (NO_2, H_2O, I_2), leading to a charge variation of a gas flowing on its surface. This characteristic is employed in field of sensor, especially for environmental monitoring.

4.1.4 Titanium dioxide (TiO_2)

Titanium dioxide is a white solid inorganic compound which occurs naturally in several kinds of rock and mineral sands and it is the ninth most common element in the earth's crust. Titanium dioxide exists in three naturally occurring polymorphic forms: rutile (tetragonal, a = b = 4.584 Å, c = 2.953 Å) which is the most thermodinamically stable form, anatase (tetragonal, a = b = 3.782 Å, c = 9.502 Å) (Figure 4.7) which shows higher kinetic stability and brookite (orthorombic, a = 5.436, b = 9.166 Å, c = 2.953 Å).

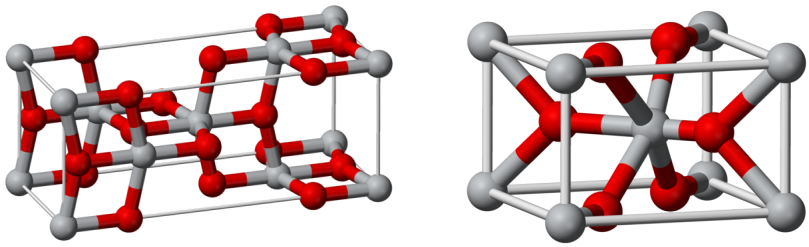

(a) (b)

Figure 4.7: *Unit cells of the two main crystalline phase of TiO_2: (a) Anatase (b) Rutile; (Ti atoms are grey, O atoms are red)*

4.1.4.1 *Synthesis*

Two different processes can be employed for the production of pure titania: the sulfate and the chloride processes. These two processes use the two principal ores of titania, ilmenite and rutile, respectively. Ilmenite contains 45-60% of TiO_2 while rutile contains up to 99% of TiO_2. Each of these processes produces the oxide in the rutile crystal form but the sulfate process can also produce the anatase form.
In the chloride process the rutile form of TiO_2 is heated in presence of chlorine and carbon coke at 900°C with the formation of titanium tetrachloride ($TiCl_4$), which is a vapour and can be easily separated from any impurity. $TiCl_4$ is then heated with O_2 at 1200°C leading to the formation of pure TiO_2 and Cl_2, which is recycled:

$$TiCl_4(g) + O_2(g) \rightarrow TiO_2(s) + 2Cl_2(g) \tag{4.2}$$

The titanium dioxide is formed as a fine solid in the gas stream and is filtered out of the

waste gases using cyclones or filters.
The sulfate process involve three main stages: the dissolution of the ore, the formation of hydrated titanium dioxide and the formation of anhydrous titanium dioxide. The starting point of the process is the grounding and dissolution of ilmenite ($FeTiO_3$) in sulfuric acid to form a mixture of sulfates:

$$FeTiO_3(s) + 2H_2SO_4(aq) \rightarrow TiOSO_4(aq) + FeSO_4(aq) + 2H_2O(l) \tag{4.3}$$

Before the extraction of titanium oxide the irons ions have to be removed, therefore the solution is reacled with recycled iron sources to convert all the iron (III) ions present to iron(II) ions:

$$2Fe^{3+}(aq) + Fe(s) \rightarrow 3Fe^{2+}(aq) \tag{4.4}$$

Subsequently the titanyl sulfate is subjected to hydrolysis in solution to give hydrated titanium dioxide:

$$TiOSO_4(aq) + H_2O(l) \rightarrow TiO_2(s) + H_2SO_4(aq) \tag{4.5}$$

In the final stage of the process the solid is heated in a calciner:

$$TiO_2 \cdot nH_2O(s) \rightarrow TiO_2(s) + nH_2O(g) \tag{4.6}$$

The high temperature in the calciner evaporates the water and decomposes any remaining sulfuric acid in the solid. After cooling, the product is milled to form crystals of the size needed.
Degussa P25 TiO_2 which is the material employed for the photocatalytic experiments in this thesis is produced through the high temperature (higher than 1200°C) hydrolysis of $TiCl_4$ in the presence of hydrogen and oxygen; subsequently the TiO_2 is treated with steam to remove HCl. The final product has a purity of 99.5% (anatase:rutile ratio 70:30) with cubic particles with round edges. The final powder has a surface area of 50 ± 15 m^2/g and an average particle diameter of 21 nm.

4.1.4.2 *Properties and applications*

The most important application areas of TiO_2 are paints and varnishes as well as paper and plastics, which account for about 80% of the world's titanium dioxide consumption. Other pigment applications such as printing inks, fibers, rubber, cosmetic products and foodstuffs account for another 8%. The rest is used in other applications, for instance the production of technical pure titanium, glass and glass ceramics, electrical ceramics, catalysts, electric conductors and chemical intermediates.
Another important field of application of titanium dioxide for the present work is its employment as photocatalyst for the photodegeneration of organic pollutant, which has

gained a growing interests in the scientific literature. The two main crystalline phase of TiO_2, anatase and rutile, have structural and functional differences. Anatase has a band gap of 3.2 eV, which correspond to a wavelength of 385 nm, while rutile has a smaller band gap (3.0 eV) with excitation wavelength that extend into the visible range at 410 nm. Anatase possesses an higher adsorptive affinity for organic compounds than rutile [278] and exhibits lower rates of electron-hole recombination due to its 10-fold greater rate of hole trapping [279]. The higher activity compared to rutile has led anatase to be conventionally considered the active component in mixed-phase catalyst, with rutile serving as an electron sink. Mixed-phase titania catalyst show greater photo-effectiveness due to three factors [280]:

- the smaller band gap of rutile extend the useful range of photoactivity into the visible range;
- the stabilization of charge separation by electron transfer from rutile to anatase slows recombination;
- the smaller size of the rutile crystallites facilitates this transfer, making catalytic hot spots at the rutile/anatase interface.

The titania employed in the photocatalytic tests for this work is the P25 Aeroxide® from Evonik-Degussa. The catalyst is in powder form with nanoparticles with an average dimension of 21 nm. According to the producer the titania is a mixture of anatase and rutile in a percentage amount of 80 and 20%, respectively, and it possesses a superficial area of $50 \pm 15\ m^2/g$.

4.1.5 Other materials employed

As regard to the production of the membranes for the subsequent testing the other material employed are:

- polysulfone (PSU) (Figure 4.8): purchased from Sigma-Aldrich (M_w = 35,000 Dalton)

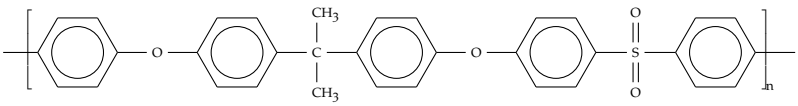

Figure 4.8: *Repeating unit of PSU*

- polyvyniliden fluoride (PVDF) (Figure 4.9): Kynar® 500 purchased from Arkema (melt viscosity = 34-40 kp)

- Aquivion® 830 (Figure 4.10): it is a short-side chain perfluorosulfonated ionomer by Solvay with an equivalent weight of 830 meq/g

All the materials have been employed without further treatments.

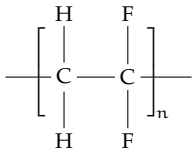

Figure 4.9: *Repeating unit of PVDF*

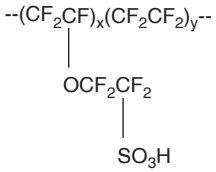

Figure 4.10: *Repetivive unit of Aquivion®*

4.2 ANALYTICAL TECHNIQUES & INSTRUMENTATION

4.2.1 Differential Scanning Calorimetry (DSC)

Differential Scanning Calorimetry (DSC) is a thermo-analytic technique that measures the heat fluxes associated with the thermal transitions of a sample with respect to a reference (inert), when both of them are subjected to a heating program in inert atmosphere. According to the classification of the thermodynamic phase transitions of a material given by Ehrenfest [281] it is possible to distinguish between:

- *first order transitions*: when there is a discontinuity in the first derivative of the Gibbs free energy with respect to a given thermodynamic variable (e.g. temperature, pressure). Since these derivatives correspond to quantities such as volume, entropy and enthalpy, processes such as melting, evaporation, crystallization, condensation and sublimation they are first order transitions
- *second order transitions*: when there is a continuity in the first derivative, but discontinuity in the second derivative of the Gibbs free energy. Examples are phenomena such as the magnetic transition of the Curie point, the superfluid transition of liquid helium, the glass transition and the second transitions in the case of amorphous and semicrystalline polymers.

In the case of polymers this technique is particularly useful in order to identify informations such as:

- melting temperature
- heat of fusion
- percentage of crystallinity
- crystallization
- presence of recycled/regrinded

- presence of plasticizers
- presence, composition and compatibility of polymer blends

The technique is based on the measurement of the energy necessary to compensate the temperature difference between a sample and a reference, usually constituted by an inert, while they are both subjected to the same temperature regimes inside an environment which is heated or cooled at a controlled velocity. There are two different types of DSC systems commonly used:

- *power compensation DSC*: where the analysis cell consists of two separated furnaces that are independently controlled according to a defined heating program. If an exothermic or endothermic phenomenon produces a temperature variation with respect to the reference the device provides or removes energy from the furnace of the sample in order to compensate this variation. The energy required to do so is a measure of the enthalpy relative to the sample with respect to the reference;
- *heat flux DSC*: in these case the sample and the reference are connected by a metal disk at low resistance and the system is enclosed in a single furnace. In this manner the temperature of the cell is varied according to a defined program, while the instrument measure the temperature difference between the sample and the reference, as a function of the temperature itself. This difference is proportional to the heat flux.

4.2.1.1 *Heat flux DSC*

These devices usually consist of a reference cell and a sample holder separated by a bridge which act as a heat sink, surrounded by a pad made up of a body at constant temperature (Figure 4.11). The pad is the housing that contains the cooling system, the sensors and the supports. The latters are raised platforms on which the containers of the sample and the reference are positioned (Figure 4.12). The heat dispersion simplifies a fast transport of the heat and allows a reasonable time for reaching the steady state. The differential behavior of the sample and the reference is registered and is subsequently used to determine the thermal proprieties of the sample. A temperature sensor is positioned at the base of each platform. Associated to the cell there is a furnace and a sensor. The furnace is designed to provide heating at a linear velocity. However not only the heating velocity has to be linear, but even the cooling one. This can be realized by cooling the housing until low temperatures. The heat flux operation of the DSC is based on the thermal equivalent of the Ohm law. The Ohm law states that the current correspond to the ratio between the voltage and the resistance, so, in the case of the thermal analogue:

$$\dot{Q} = \frac{\Delta T}{R} \tag{4.7}$$

where $\dot{Q}$ is the rate of the thermal flux, ΔT is the temperature difference between the sensors of the sample and the reference and R is the thermal resistance of the heat dissipator disk.

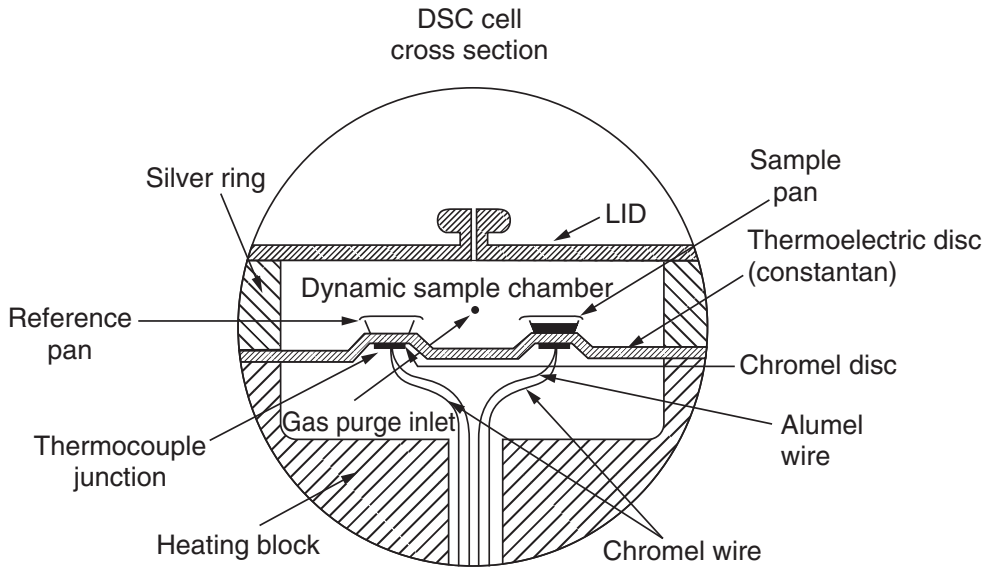

Figure 4.11: *DSC heat flux cell*

4.2.2 Thermogravimetrical Analysis (TGA)

Thermo Gravimetric Analysis (TGA) is a technique in which the variation in the mass of a sample is measured as a function of the temperature and/or the time while the sample itself is subjected to a heating program at a constant rate in a controlled atmosphere. This technique is commonly applied in the field of research and analysis of polymers since it provides useful informations about the thermal stability, the oxidative stability, the amount of humidity and volatile compounds absorbed, the amounts of organic and inorganic components (e.g. fillers) present inside the material. The data are registered on a thermogram that shows the decomposition of the sample by the decrease of its mass with the increase of the temperature. The essence of the device consists in a thermobalance, enclosed inside a cylindrical furnace, that measures the mass variations with respect to a reference as a function of the temperature on the basis of the heating program adopted. A mass variation of the sample produces a deflection in the beam that goes to interpose an octurator between the lamp and one of the two photodiodes. The resulting current variation of the photodiode is amplified and sent to a force coil which generates additional electromagnetic force to recover equilibrium. The amount of additional electromagnetic force is proportional to the mass change. During the heating process the temperature may go as high as 1500 °Cinside the furnace.

4.2.3 Fourier Transform Infra-red Spectroscopy (FTIR)

Such technique involves the absorption of electromagnetic radiation in the infrared region of the spectrum which results in changes in the vibrational energy of molecules. Since, usually all molecules will be having vibrations in the form of stretching, bending, etc., the absorbed energy will be utilized in changing the energy levels associated with them. It is

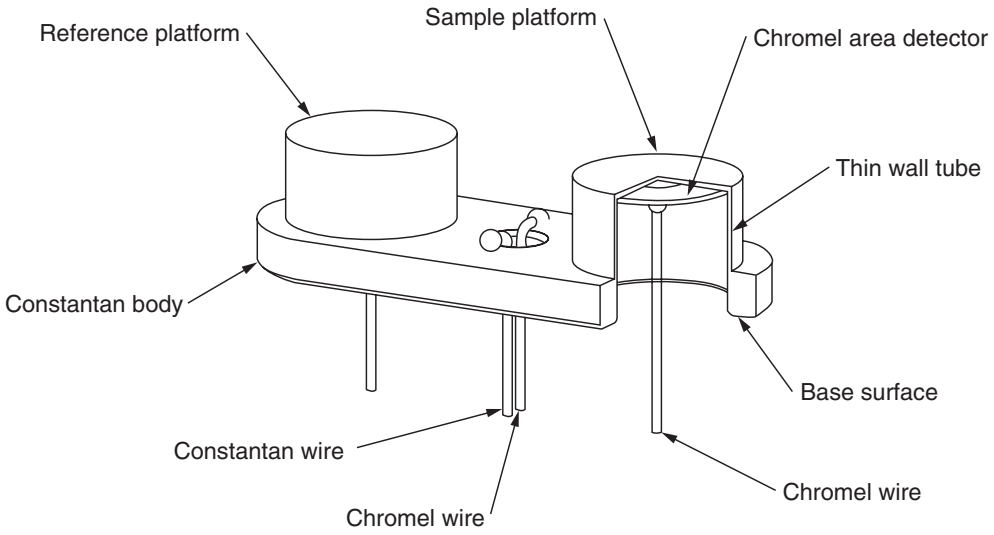

Figure 4.12: *DSC sensor assembly*

a valuable and formidable tool in identifying organic compounds which have polar chemical bonds (such as OH, NH, CH, etc.) with good charge separation (strong dipoles). The instrument utilizes a single beam of un-dispersed light. The technique is conducted with a Michelson interferometer and it is accomplished by sending infra-red radiations at variable frequencies, usually between 4000 and 400 cm^{-1} to the substance to be analyzed and identify those that are absorbed. The light beam exiting from the IR source is divided in two parts by means of a semi-transparent mirror (splitter): the two beams obtained and shifted in phase between each other, since the first is reflected by a fixed mirror and the second on a mobile one. The beams coming from the mirrors are recombined and passing through the sample and the absorbances at all wavelengths are received at the detector simultaneously to generate the interferogram. A computerized mathematical manipulation (known as Fourier Transform) is performed on this data, to obtain absorption data for each and every wavelength. Before scanning the sample a reference or a blank scanning is required.

4.2.4 X-ray diffraction (XRD)

The diffraction of X rays is a good tool to study the nature of the crystalline substances. In crystals the ions or molecules are arranged in well-defined positions along planes in three dimensions. The impinging X-rays are reflected by each crystal plane. Since the spacing between the atoms and hence the planes can't be same or identical for any two chemical substances, this technique provides vital information regarding the arrangement of atoms and the spacing in between them and also to find out the chemical compositions of crystalline substances. The sample under study can be of either a thin layer of crystal or in a powder form. Since, the power of a diffracted beam is dependent on the quantity of the corresponding crystalline substance, it is also possible to carry out quantitative determinations. The X-rays are produced when a electrically charged particle with a suf-

ficient kinetic energy is quickly decelerated. The X radiation is generated by a X-ray tube containing a electrons source and two metal electrodes at high potential difference. The electrons hit the anode with high energy and, during the collision, they produce X-rays that are emitted in all the directions. Some electron loss their energy during the collision producing X ray with a minimum wavelength λ. The relation between λ and the applied potential difference is:

$$\lambda_{min} = \frac{hc}{eV} \tag{4.8}$$

where c is the speed of light,V is the potential difference, h is the Plank constant and e is the electron charge. The X rays can interact with ordered structures through reflection and scattering phenomena by the crystalline planes. An X-ray which reflects from the surface of a substance has traveled less distance than an X-ray which reflects from a plane of atoms inside the crystal. The penetrating X-ray travels down to the internal layer, reflects, and travels back over the same distance before being back at the surface. The distance traveled depends on the separation of the layers and the angle at which the X-ray entered the material. For this wave to be in phase with the wave which reflected from the surface it needs to have traveled a whole number of wavelengths while inside the material. Bragg expressed this in an equation now known as Bragg's Law [282]:

$$n\lambda = 2dsin\theta \tag{4.9}$$

where n is the reflection order, θ is the Bragg angle, d is the interplane distance. When n is an integer (1, 2, 3 etc.) the reflected waves from different layers are perfectly in phase with each other and the overall radiation with Θ angle is intensified. Concerning semicrystalline materials, it is possible determine the average size of crystallites by using the Scherrer equation [283]:

$$D = \frac{K\lambda}{\beta cos\theta} \tag{4.10}$$

where D is the average size of the cristalline domains, K is a dimensionless shape factor, λ is X-ray wavelength, β is the line broadening at half of the maximum (FWHM) and Θ is the Bragg angle.

4.2.5 Nuclear Magnetic Resonance (NMR)

Nuclear Magnetic Resonance (NMR) spectroscopy is an analytical chemistry technique for determining the content and purity of a sample as well as its molecular structure. The principle behind NMR is the energetic absorption that are observed when nuclei that possess magnetic spin and immersed in a magnetic field are excited by electromagnetic radiation in the radio frequencies.
All the nuclei possess a charge and in some of them this charge spin around the nuclear

axis. This charge movement produces a magnetic dipole oriented parallel to the nuclear axis and characterized by a magnetic moment m. Besides at every nucleus is associated a spin quantum number (I) which is characteristic of each nuclei. I can assume values like I=0 for nuclei without spin or fractional or integer values (1/2 and its multiples). The spin quantum number determines the number of orientations that a nucleus can assume in a static magnetic field (B_0), according to the following formula:

$$2I + 1 \tag{4.11}$$

By considering nuclei with I equal to 172 there are two different possible orientations (namely two spin states) which correspond at two different energetic levels: to -1/2 which correspond to the state at lower energy or +1/2 which represents the state at higher energy. In absence of a magnetic field all the energetic state are degenerate, or at the same energy. When a magnetic field B_0 the difference in energy between two states depend from the intensity of the static magnetic field applied:

$$\Delta E = \frac{h\gamma}{2\pi} B_0 \tag{4.12}$$

where h is the Planck constant, g is the gyrometric ratio, a constant characteristics of each nucleus, linked to the magnetic moment m and the spin number. Due to the presence of two energetic level, if energy is provided in form of electromagnetic radiation by application of a radiofrequency field (n_1), the atoms are excited: this mean that they are excited from a lower energy to an higher energy level. In order to have this transition the applied frequency should obey to the following laws:

$$\Delta E = hn \tag{4.13}$$

$$n = \frac{\gamma}{2\pi} B_0 \tag{4.14}$$

By respecting the previous physic laws the system in resonance conditions. At this point the nuclei can not remain in the high energy state for long time but they return to the starting, lower energy level. During this energetic jump the nuclei have absorbed energy and subsequently when they return to the lower energy state they release energy which translated in an NMR spectrum. The precise resonant frequency of the energy transition is dependent on the effective magnetic field at the nucleus. This field is affected by electron shielding which is in turn dependent on the chemical environment. As a result, information about the nucleus chemical environment can be derived from its resonant frequency. In general, the more electronegative the nucleus is, the higher the resonant frequency. The nuclei that possess magnetic properties and largely employed for the identification of compounds are both more (^1H, ^{31}P) and less abundant (^{13}P,^{15}N) isotopes. Two are the methods that can be employed to obtain the resonance frequency. In the continuous-wave spectroscopy an electromagnet generate the magnetic field necessary to induce the

splitting between the energetic levels of the active atoms under examination. At the same time a proper source emits electromagnetic waves at fixed frequency. The magnetic field of magnet is then increased step by step: a detector records the absorbance of the sample at each intensity of the field, namely the amount of the incident radiation lost during the passage through the sample. The resonance frequency of an active nuclei is directly proportional to the applied field: by increasing the magnetic field, the resonance frequencies are higher. When the resonance frequencies are equal to that of the incident radiation (which is constant), then all the active nuclei will absorb energy quanta and the measured absorbance will be higher. The second method, employed in the modern spectrometer, consists in maintaining a fixed field, increasing the frequency of the incident radio wave. As previously stated the resonant frequency of the energy transition is dependent on the effective magnetic field at the nucleus. This applied field induces, in the electronic neighborhood of the nucleus, a local opposite magnetic field which depends on the nature of the chemical environment in which the active nuclei are present. This electronic neighborhood generates a local modulation of the applied field, called shielding. The effective residual field is:

$$B_{local} = B_0(1 - \sigma) \tag{4.15}$$

where σ is the electronic shield. Upon the observation of the relative position of the absorbance peaks it is then possible to draw conclusion on the electric shield associated to the different nuclei that have generated it. The chemical shift observed can be related to the shielding effect of the different nuclei using a standard, usually that of tetramethylsilane.
The analyses are generally carried on dissolved samples, although even solid-state NMR can be employed, and the vast majority of nuclei in a solution would belong to the solvent; thus, since most of the regular solvents are hydrocarbons they would contain NMR-reactive protons. The problem is solved with the employment of deuterated solvents. The most used deuterated solvent is deuterochloroform ($CDCl_3$), although deuterium oxide (D_2O) and deuterated DMSO (DMSO-d_6) are used for hydrophilic analytes. NMR spectra are often calibrated against the known solvent residual proton peak instead of added tetramethylsilane.

4.2.6 Proton conductivity

The measurement of the proton conductivity is one of the important methods to investigate the performance of membranes for PEMFC technology. To allow a reproducible measurement of the proton conductivity under real conditions it is necessary to operate the measuring cell under defined humidification and temperatures. A typical conductivity cell to carry such test is shown in Figure 4.13. The conductive cell applies the conventional four-electrode method to measure the in-plane conductivity. The advantage of the 4-electrode in-plane conductivity measurement is the ability to measure impedance (resistance) due only to charge transport and exclude interfacial and charge transfer resistances.

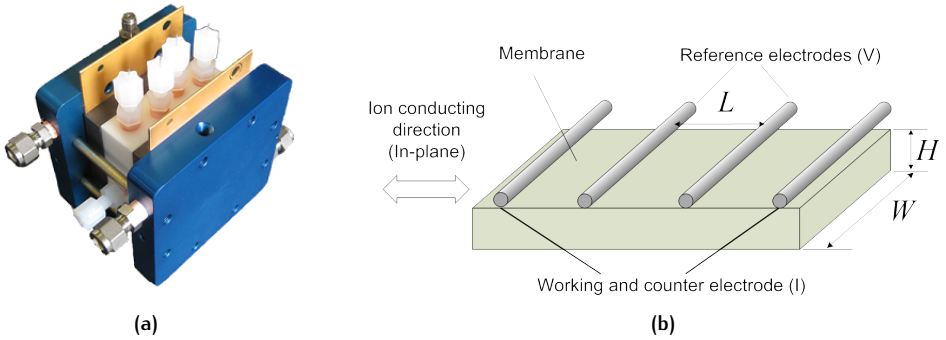

Figure 4.13: *(a) Four electrode proton conductivity cell, (b) Four electrode assembly*

By considering only resistance due to ion transport, accurate assessment of in-plane membrane conductivity can be made. The sample to measure should be cut into a rectangle and sandwitched between two platinum electrodes. The outside working and counter electrode apply DC voltage and a potential gradient occurs across the sample. At the same time, the reference electrodes measure the potential difference of the sample, sensing the flow of protons across the surface of the sample. The cell is operated in a wet gas-dry gas mixing mode for control of the humidity of the gas stream delivered to the conductivity cell and membrane. To precisely control the humidity in the testing chamber the cell is connected to a saturator and pressurized water system. The cell also has thermocouples to detect and control the temperature inside. PID (proportional-integral-derivative) controllers attached to the thermocouples are used to keep the temperature constant in each component, the conductivity cell, the humidifier, and the inlet. The temperature of the inlet connecting the humidifier to the cell has to be higher than others set point temperatures. Otherwise, there occurs vapor condensation inside the inlet, resulting in an incorrect RH value. The in-plane proton conductivity in gas phase can be measured as:

$$\sigma = \frac{L}{R \cdot A} \tag{4.16}$$

where σ is the conductivity (S/cm), R is the resistance (Ω), L is the membrane thickness or interval between electric potential sampling electrodes (cm), and A is the electrode area (cm^2).
Commonly, proton conductivity is measured along the plane of a membrane, since the measurement of the conductivity in the in-plane direction is much easier to carry out with higher stability, reproducibility and accuracy. However, in practice, the membrane requires proton conduction perpendicular to the membrane, this through-plane conductivity is also measured, especially for the evaluation of the performances in fuel cells.

4.2.7 Atomic Force Microscopy (AFM)

Atomic Force Microscope is an high performance scanning probe microscope (SPM) employed nowadays for the study of the surface of different type of compounds on the

atomic scale: thin films, thick ceramic or amorphous materials, glasses, synthetic or biological membranes, metals, powders, semiconductors, *etc*. The instrument can operate in air, under ultrahigh vacuum and in liquid (biological samples) and can analyze both conductive and insulating materials. The most powerful microscopes can reach resolutions of 0.01-1 nm along the x and y axes, and of 0.01 nm along the z axis. With the AFM it is possible to obtain the microtopography of a sample on a scale ranging from 100 to 150 μm. The working principles is based on a small tip of a very rigid and conductive material fixed at the edge of a cantilever pushed against the sample to be analyzed during the measurement. At a close look the tip appears rounded and the end radius represents a very important parameter in relation to the resolution of the instrument. The realization of probes with a continuous decrease in the curvature radius is the main limitation that afflicts the development of the atomic force microscopy. The entity of the probing rod deflection measured from the tunnel current generated between the rod and a secondary tip placed above the rod, is a measure of the force acting between the surface of the sample and the tip.

In the AFM the tip (with dimension of a few μm) runs along the surface of a sample that moves along the three Cartesian axes by an movement generated by a piezoelectric mechanism. A feedback system allows to establish a conditions of constant force, to obtain informations relative to the interaction force between the surface of the sample and the tip, or height, to acquire informations on the variation in the sample thickness. The oscillations of the cantilever are detected by an optical system that records even very low movements of the tip. A laser beam generated by a diode is focused on the the reflecting backside of the cantilever. In this manner, in the constant force mode, during the scanning movement of the sample surface the variation in the height produces the deflection of the laser beam. A photodetector analyzes the difference in the light intensities between the components of the binary photodiode which record the deflected beam and converts this signal in an voltage representing the output of the analysis. In the constant height mode, the measured tension is proportional to the force necessary to maintain a constant distance between the samples surface and the tip of the probe.

The piezoelectric system in the major part of the SPMs employ piezoceramics cylinders as generators of the surface scansion. With low displacements of the sample these microscopes are capable to measure quantitatively the microtopography of the surfaces, with a lateral resolution of 5 nm and a vertical resolution of 0.01 nm. The results of the observation consists in the production of a tridimensional matrix (x,y,z) of the surface of the sample analyzed. The first two coordinates provide the monodimensional informations of the object, the third provide the measure of the heights (distances between the surface of the sample and the tip). The effective microtopography can be reconstructed by elaborating the informations relative to:

1. the relative movement between the sample and the prove;
2. the results of the sample-tip distance point by point.

The force typically involved between the tip and the sample vary between 10^{-11} and 10^{-6} N. BY considering that between two atoms covalently bonded at a distance of ~0.1 nm acts

a force of 10^{-9}N, it is clear that the measurement are not destructive and are representative of the real nature of the sample. The main working modes are:

- contact mode;
- non-contact mode;
- dynamic mode.

The measurement realized for the present work have been conducted with the contact mode in which the tip is contact with the sample surface as a result of the action of the piezoelectric system acting on the cantilever. The deflection of the cantilever is measured and compared to the expected value. If the measured deflection is different from the expected one the feedback system apply a tension on the piezoelectric system so that, by moving the tip closer or farther to the surface, it is possible to re-establish the expected value for the deflection. The applied tension is a measure of the profile of the sample surface. The final image is obtained by expressing this tension as a function of the relative position of the sample.
The atomic force microscope presents several advantages over the electronic microscope: differently from the latter, which provides a 2D projection of a sample, the AFM produces a real 3D profile of the surface; besides the samples analyzed by such microscope do not require particular pre-analysis treatments (metalization and graphitization) which could modify or destroy irreparably the sample. An electronic microscope in order to work properly requires an high vacuum chamber while atomic force microscopes can work at room conditions or even in liquid environments making it suitable for the study of biologic molecules and living organisms. On the other side the disadvantage with respect to an SEM is related to the dimensions of the images that can be produced: the latter can produce an area of 1 x 1 mm and a background depth of 1 mm while an AFM can reproduce only a depth in the order of 1 μm and a maximum area of 100 x 100 μm. Another inconvenient is related to the high resolution and quality of the images which are limited by the curvature radius of the probe and a wrong choice of the probe can leads to the formation of artifacts. Besides the AFM is not capable to analyze the images as fast as an SEM: to obtain the scan of an area several minutes are generally required compared to a real time image provide by an SEM (after the creation of the vacuum in the analysis chamber). The long times required for the formation of the image can often lead to the thermal drift of the image and for such reason the atomic force microscope is not adapt for the accurate evaluation of the distances between the artifacts of such images. Lastly it is important to note that a many AFM images are characterized by the hysteresis of the piezoelectric materials and by the disturbs in the transmission produced by alteration and disorders in the signals between the different axis channels (x,y,z). The image must then be post-processed and filtered with a specific software.

4.2.8 Scanning Electron Microscopy (SEM)

The Scannning Electron Microscopy (SEM) (Figure 4.14), invented by the Germans Ernst Ruska and Max Knoll in 1931 and optimized by the brothers Janssen in 1935, is a mi-

croscope which, differently from the optical microscopes, does not employ the light as a source of radiations but rather an electron beam. Since the photons that constitute the light have an higher wavelength than the electrons and since the resolution of a microscope is inversely proportional to the wavelength of the radiation employed, by using electrons it is possible to obtain a resolution which is several orders of magnitude higher. SEM is, thus, an electro-optic instrument which allows, as a consequence of the emission of an electron beam, to analyze the different signals produced by the interactions of the electrons of the beam with the sample to be analyzed. The elaboration of these signals allows to obtain a vast amount of informations (morphological, compositional and structural) relative to the different parts of which it is constituted the sample to be analyzed The extreme versatility of this instrument is granted by the variety in the topology of the samples which can be analyzed, in terms of both their nature (only materials which contains fluids can't be analyzed) and their shape and dimension (of any shape, up to about a $1dm^3$). Even the preparation of the samples is quite simple since, if the samples is not conductive they need to be sputtered with a conducting material such as graphite or gold (metalization). The experimental apparatus is schematically composed by the following elements:

- an electronic column, where the electron beam is created
- a vacuum chamber in which the electron beam interacts with the sample
- several types of detectors that acquire the signals from the beam-sample interaction and transfer them to the computer
- a screen, on which the sample image is reconstructed on the base of the signals received

The electron source placed on top of the column is composed by a filament, usually tungsten or lanthanum hexaboride (LaB_6), which, heated to a given temperature, generate the electronic beam by thermo-ionic effect. The electrons are thus accelerated at variable energy (between hundreds and some tenths of thousands eV) thanks to an anode place behind the filament. The beam emitted from the source is divergent, but it is converged and focused by a series of electromagnetic lenses and fissures placed inside the column. At the bottom of the latter there are a series of scanning coils that deflect the beam, providing it an alternating movement along parallel and equidistant lines so that it covers a predefined area, once reached the surface of the sample. The beam focused by the final lens, exits from the column and hits the sample inside the vacuum chamber. As the electrons of the beam penetrate inside the sample, they lose energy which is ri-emitted from the sample in several forms. From the moment in which the electron beam hits the surface of the sample, the electrons of the beam start to interact with the nuclei and the electronic clouds of the atoms of the sample according to two different mechanisms: elastic and inelastic diffusion. The result of these processes is the production of a vast variety of signals: secondary electrons, back-scattered electrons, absorbed electrons, transmitted electrons, Auger electrons, electron-hole couple, electromagnetic radiation (in the UV-IR spectrum) and X-radiation. The region of the sample from which the interaction signals with the beam are generated and from which they exit to be detected is called interaction volume. The shape and the

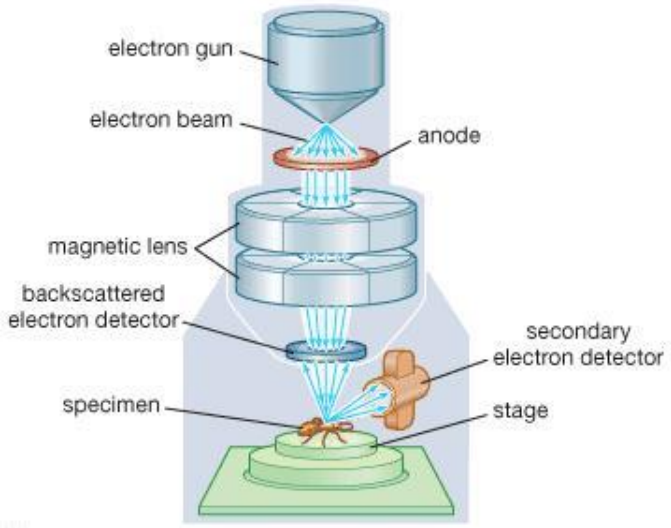

Figure 4.14: *Symplified scheme of SEM*

dimensions of this volume depend both on the characteristics of the incident beam and the composition of the sample and, often, result to be more extended of the beam diameter, determining the limit of resolution. Differently from the optical microscope, which produces the real image of the sample, SEM provides a virtual image from the signals emitted from the sample. The scan allows the beam to hit the surface of the sample line by line until the complete covering of the area to examined and the signals generated have different intensities as a function of morphological, chemical and structural anisotropies. These signals are collected by suitable detectors and from analog they are subsequently converted into digital in order to be elaborated appropriately. To visualize the signals in an image by a cathode-ray tube (CRT) screen, the deflection of the beam is realized in synchronous with the CRT panel, which is modulated with the intensity of the signal. In this manner the system create an association between each point to a pixel according to the signal received and creates the image.

4.2.9 Transmission Electron Microscopy (TEM)

Transmission electron microscopy (Figure 4.15) is used to study the local structures, morphology, and dispersion of multi-component polymers, cross sections and crystallization of metallic alloys and semiconductors, microstructure of composite materials, etc. In this technique, a beam of high-energy electrons (typically 100-400 keV) is collimated by magnetic lenses and allowed to pass through a specimen under high vacuum. The thickness of the sample must be enough thin to allow the transmission of some incident electrons: when they pass through the material, some of them are absorbed and some are irregularly scattered when they find discontinuity of uniform atomic arrangements. The transmitted beam and a number of diffracted beams can form a resultant diffraction pattern, which is imaged on a fluorescent screen kept below the specimen. The diffraction pattern gives the information regarding lattice spacing and symmetry of the structure under consideration.

Alternatively, either the transmitted beam or one of the diffracted beams can be made to form a magnified image of the sample on the viewing screen as bright-and darkfield imaging modes respectively, which give information about the size and shape of the microstructural constituents of the material. High-resolution image, that contains information about the atomic structure of the material, can be obtained by recombining the transmitted beam and diffracted beams together. The instrumentation comprises of a tungsten filament

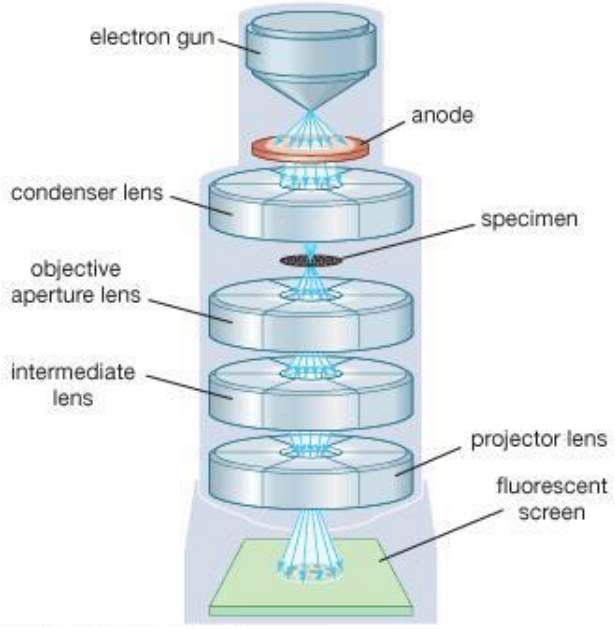

Figure 4.15: *Simplyfied scheme of TEM*

or LaB_6 or a field emission gun as source of electron beam, objective lens, imaging lens, CCD camera, monitor, etc. A simple scheme is shown in Figure 4.15

4.2.10 Raman spectroscopy

Spectroscopy is the principal experimental method for the determination of the vibration frequencies of a molecule. The technique is based on the interaction between light and molecules, which can lead to different effects like absorption and scattering by the target molecules. In the first case and infra-red spectrum is obtained, in the latter a Raman diffusion spectrum.
In the Raman spectroscopy the radiation emitted by a laser beam interacts with the roto-vibrational motions of the molecules with the consequent re-emission of light at different wavelengths of the incident light. The final spectrum obtained provides a sort of fingerprint of the molecule to be analyzed, allowing its identification. When a monochromatic radiation interacts with a substance two different effects can be produced:

1. The major part of the radiation pass across the sample
2. A little part of the radiation elastically in all the directions without loss of energy, thus at the same frequency of the incident radiation (elastic scattering or Rayleigh

scattering); such scattering is considered to be generated by elastic collision between quants and molecules

3. a very small part is anelastically diffused by losing (Raman Stokes scattering) or gaining (Raman anti-Stokes scattering) energy in the interaction with the molecule, vibrating at frequencies which differ by vibrational energy quants

The intensity of the scattered radiation (lower than the intensity of the incident radiation) depends both on the contribution provided both by the elastic and the anelastic scattering which, in turns, depend on the chemical structure of the molecules responsible of the scattering. A typical spectrum of scattered light is generally provided as intensity versus light frequency ($\Delta\nu$, defined as the difference between the scattered radiation emitted from the sample and that emitted by the source, a parameter which is independent on the laser wavelength). Raman spectrum is generally intended as the part of the spectrum containing the Stokes lines. These, as already mentioned, are considered as frequencies which differ for vibrational energetic quanta (anelastic scattering or Raman effect). The phenomenon described is illustrated in Figure 4.16. Such differences correspond to the separation of

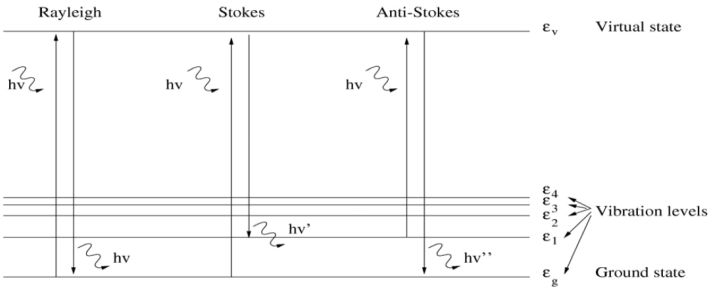

Figure 4.16: *Differences of vibrational quanta between the different components of the Raman spectrum*

two vibrational levels and are the characteristics emission frequencies of the molecules hit by the incident light: the set of these differences generate the Raman spectrum of the compound. It is originated from the absorption and re-emission due to vibrational excitements and relaxations. This scattered radiation can be spectrally resolved and recorded. In the Raman spectroscopy the energetic levels of the molecule are explored by analyzing the frequencies present in the scattered radiation by the molecule. In a typical Raman experiment, a beam of monochromatic light is impacted on the surface of the sample in order to detect the scattered radiation at an angle orthogonal with respect ot the direction of the incident radiation. When the incident photons hit the molecules, they can lose or gain energy. If the molecule absorb part of the energy from the photon in order to be promoted to an excited state, the photon will reemerge with an energy (frequency) lower than the incident one, generating the so-called Stokes lines in the Raman spectrum. If, however, the molecule is already in an excited state (the thermal energy at room temperature is capable to excite some rotational states) it can provide energy to the incident photon that will re-emerge with an higher energy, generating the anti-Stokes lines. The component of the diffused radiation in the same original direction without changes in frequency is called Rayleigh

radiation. The Raman lines are this the result of the anelastic dispersion of the incident radiation from the sample: the lines shifted to lower frequencies are produced by molecules that give energy to photons by promotion from the fundamental to the first excited state (Stokes lines), those at higher frequencies by molecules at an excited vibrational state that absorb energy from photons (anti-Stokes lines). The Stokes lines are more intense of the anti-Stokes lines and are those employed for analytical purposes. The line with the same frequency of the source, resulting from the Rayleigh scattering of the incident radiation, is the more intense component of the Raman spectrum and has to be removed. A system for Raman spectroscopy is synthetically composed by a laser source, a sampling system to send the laser beam on the sample and detect the Raman signal, a system to separate the Raman signal from the component of scattered light in an almost elastic manner (the so-called Rayleigh scattering), an interferometer and a detection system. The choice of the excitation source affects most of the other instrumental characteristics. In the major part of the real samples the low Raman signals are obscured by the background fluorescence. Generally the fluorescence decreases if the wave frequency change from the visible to the near infra-red region (NIR), namely if the energy of the source decreases. Therefore the common source of excitation are laser or laser diodes (which emit in the far infra-red and in the NIR, reducing the background fluorescence). Although the fluorescence decreases with the increase of the wavelength, also the Raman signal intensity decreases in the same sense. Since the intensity of the Raman signal is proportional to the fourth power of the frequency of the scattered light, the longest wavelength employable is 1064 nm. The ideal situation requires the selection of the lower laser wavelength that prevent the fluorescence phenomenon without introducing other problems, such as the overheating of the sample or photodegradation.

4.2.11 UV-visible spectrophotometry

When radiation interacts with matter, a number of processes can occur, including reflection, scattering, absorbance, fluorescence/phosphorescence (absorption and reemission), and photochemical reaction (absorbance and bond breaking). Scattering is considerable for colloids and solids when the wavelength is in the order of magnitude of the particle size. Diffuse reflectance spectroscopy is a technique which measure the reflected light by a sample and estract the absorption properties from this reflected light. In this case the absorption of the sample is derived from the Schuster-Kubleka-Munk theory as a function of the reflectance measured from the sample (Kubelka-Munk remission function):

$$F(R_\infty) = \frac{(1 - R_\infty)^2}{2R_\infty} = \frac{k}{S} \tag{4.17}$$

where R_∞ is the reflectance of the sample relative to a standard, k is the absorption coefficient and s is the scattering coefficient. Two types of reflections can be encountered: specular and diffuse. In the first case the incident light is reflected symmetrically with respect to the normal line while in the second the light is scattered in different directions typically due to the effect of small particle dimensions in solid samples (Figure 4.17). For the pur-

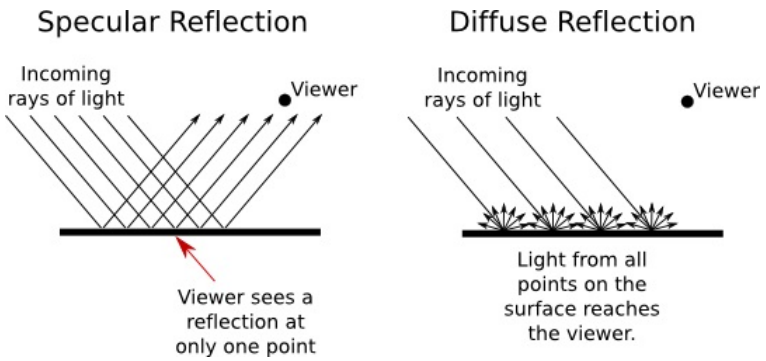

Figure 4.17: *Difference between specular and diffuse reflectance*

pose of this study such technique has been employed for the determination of absorption edge and band gap of semiconductors employed as photocatalysts. The absorption edge or band edge is defined as the transition between the strong short-wavelength and the weak long-wavelength absorption in the spectrum of a solid, generally a semiconductor. The spectral position of this edge is determined by the energy separation between the valence and conduction bands of the material in question. In the case of transparent solids, the absorption edge can be measured using transmittance techniques while diffuse reflectance measurements provide a more appropriate means of measurement for powdered materials. General light sources employed for the analysis are deuterium lamp for the operating range 180-350 nm supplemented by a tungsten filament lamp in the near UV, through the visible, into the near-IR, i.e. over the range 320-1000 nm. For band gap measurement of semiconductors an intergrating sphere is commonly employed in UV/vis measurements. An integrating sphere is essentially a hollow sphere internally coated with a white material of diffuse reflectance close to 1. The sphere has apertures through which a beam of radiant energy can penetrate and ports for mounting samples and standards and placing the appropriate detectors. Commercially available spheres range from 50 to 250 mm in diameter and are internally coated with highly diffusing polytetrafluoroethylene (PTFE) or barium sulfate ($BaSO_4$). The integrating sphere allows diffuse and specular reflectance and diffuse transmittance measurements to be performed. This allows absolute absorption to be calculated taking into consideration the losses due to scattering.

4.2.12 Gas chromatography & mass spectroscopy (GC-MS)

The GC-MS is an analytical technique which combines the separation capability of the gas chromatography with the potentiality of the mass spectroscopy for the qualitative and quantitative determination of a wide spectrum of compounds, mainly organic, with low polarity, low molecular weight and a boiling temperature lower than 300°C. The main advantages that are achievable by using mass spectrometry are the higher detector sensibility if compared with their GC counterparts, and the possibility to identify the compounds analyzed.

4.2.12.1 *Gas chromatography*

Gas chromatography is a technique which allows to obtain an analytical separation of the components. By this technique it is possible to analyze gaseous, liquid or solid samples. The main limitation of the technique is the necessity to have a sample which can be volatilized in a range between room temperature and 300°C in order to be compatible with the furnaces commercially available and the columns usually employed. As all kind of chromatographies it is based on the distribution of the different substances between a stationary and a mobile phase, according to the affinity of the different substances with the mobile phase, an inert gas. Each substance is distributed between the two phases in relation to its particular chemico-physical properties. Each substance is distributed between the two phases in relation to its particular chemico-physical properties. By indicating with C_m and C_s the concentration in the mobile and stationary phase, it is possible to evaluate the ration between the two concentration (K). This is called the distribution coefficient and it indicates how the substances are distributed between the stationary and the mobile phases. From the value of K depends the retention time, which is the time necessary to the substance to pass along all the stationary phase.
From the time that a compound spends inside the column depends the value of C_s respect to the value of C_m: thus an high concentration in the stationary phase than in the mobile phase, indicates an higher affinity for the first. In other words, the eluent (mobile phase) is encountering a certain difficulty in transporting some substances with it, while others which are relatively more affine with it and lesser towards the stationary one are going to be easily transported towards the end of the column and will be more easily separated. What happens is that between the stationary phase and the mobile phase some interactions are created and these are the reasons for which some substances are retained more than others inside the columns e show an higer retention time. The most important elements fo a gas chromatograph are:

- an injection chamber
- a column
- a detector

The main task of the injection chamber is to assure the instantaneous evaporation of the sample. The injection chamber is made up of a series of variable resistances by which is possible to fix the temperature which is judged to be more suitable for the vaporization of the mixture. The gas chromatograph employed for the tests has to different injection systems. The gases to be analyzed can be introduced inside an injector manually by a syringe or, alternatively, by a a 6 way valve (Figure 4.18) with a a loop of fixed and known volume which is properly emptied thanks to a rotary vane pump. In each case it is possible to use an adjustable split in order to define that only a specific quantity of the volume injected is actually sent into the column (situation that is particularly useful to avoid saturation of the signal at the detector). Differently from the injector the multiway valve has a delay time before the entrance in the column, but it allows the entrance of a quantity of the sample which is more precise and reproducible. The loop employed for the tests has a volume of

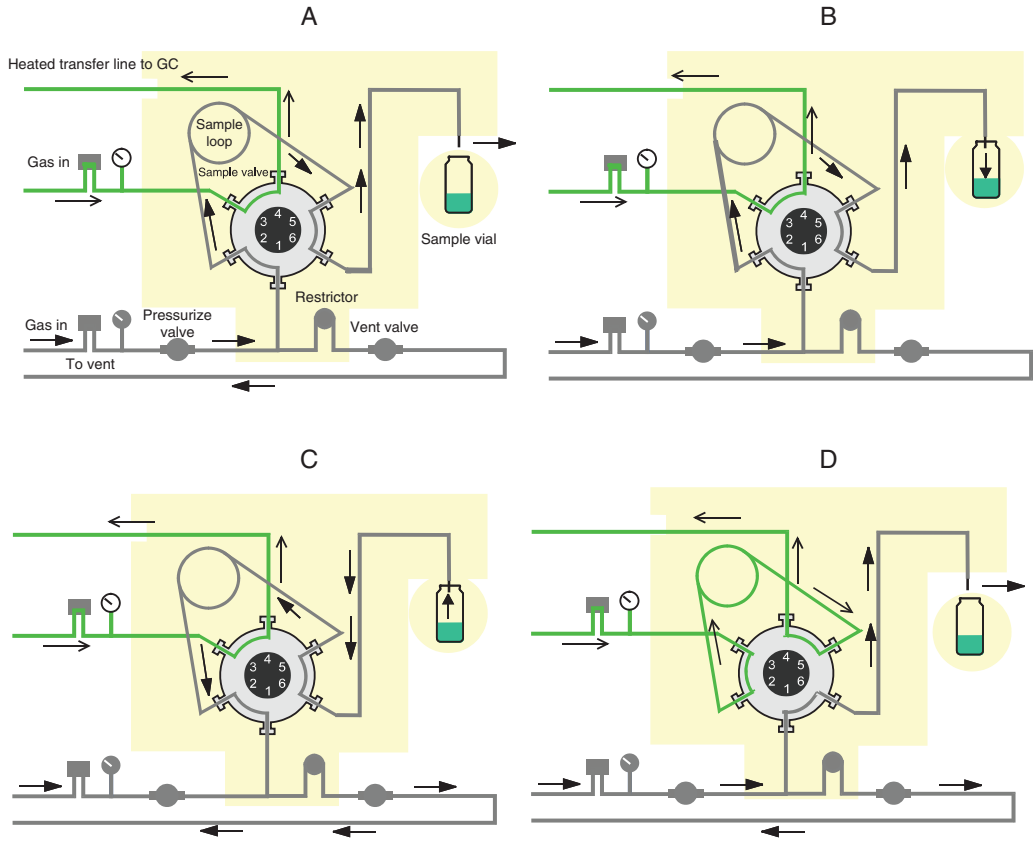

Figure 4.18: *A schematic illustrating the delivery of a gas sample from a vial to a gas chromatograph by a 6-way valve. In this case, the vial contains a liquid or solid sample, and the gas phase over the sample is to be delivered to a gas chromatograph or a GC-MS. (A) standby position where the sample is heated; (B) the sample is pressurized with carrier gas; (C) the vent valve is opened and the pressurized gas in the vial flows into the gas sample loop; (D) the core of the valve is rotated and the gas sample from the vial is swept out to the gas sample loop and into the GC column.*

500 µl. The stationary phase is generally made up of a non volatile liquid supported on a powder which fills a column (packed column) or distributed as a thin film, of a few micron of thickness, on the inside wall of the column (capillary column). The mobile phase is a gas (carrier). Generally chemically inert, low viscous and very pure gases (99.9%) are chosen, such as hydrogen of helium and sometimes nitrogen and argon.
As already said the sample inside the column is separated in its components according to the affinity of these with the stationary phase (usually by polarity). However to have a better separation, it is possible to act on the temperature which can be maintained constant or varied according to a desired gradient by a specific temperature program. When th sample exits from the end of the column it is collected by a detector. According to the different physical principle employed to detect the substances, the dectors are classified into thermal conductivity (TCD), flame ionization (FID), nitrogen-phosoporous (NPD), flame photometric (FPD), and electron capture (ECD) detectors. The FID is a universal detectors

but it is destructive. In a FID the carrier gas exiting from the column is mixed with hydrogen and oxygen and then burnt. In the flame, when a substance is eluted, there is the formation of ions which are collected on the surface of the detector producing an electric current which, once amplified, represents the signal of the detector. The diagram which represents the signal generated by the detector as a function of time (fixed at time zero the instant in which the sample is injected in the column) is the chromatogram of the sample. The latter is made up of a series of peaks of variable amplitude, distributed along the axis of time. From the retention time of each peak it is possible to deduce the identity of the eluted compound, while from the area or height of the peaks it is possible to determine the concentration of the different compounds in the sample analyzed.

4.2.12.2 *Mass spectrometry*

Mass spectrometry is an analytical technique employed for the identification and quantification of the components of the sample to be analyzed and to determine the molecular structure (organic, inorganic or biological). The working principle is the possibility to separate a mixture of ions in reason of their mass to charge ratio, by means of stable of oscillating magnetic fields. The mixture is obtained by ionization of the sample molecules by using an energy beam. The molecules ionized by this process are instable and fragments into lighter ions according to defined schemes which are typical of their chemical structure. The diagram which reports the the abundance of each ion as a function of the mass to charge ration is the so-called mass spectrum and it is typical of each compounds since it is directly correlated to the chemical structure of the compound and to the ionization conditions to which it has been produced. In this way, by means of appropriate libraries, is possible to identify the chemical species in the sample. A mass spectrometer is made up of three main components:

- a source for the ionization
- an analyzer for the separation of the ions (quadrupole)
- a detector

Regarding the injection phase, the amount of sample which is necessary to carry the analysis is just a fe micrograms. In such conditions the major part of the analytes is in gas phase; solid samples which does not sublimate are vaporized by inject them close to the ionization filament. If the mass spectrometer is coupled with a gas chromatograph the exit of the GC system is employed as entrance for the mass spectrometer. The sample, thus enters in the instrument at the end of the elution directly in has phase o by means of a vaporization device downstream of the column. From the ionization system depends the number, the nature and the abundance of the molecular fragments that appears in the mass spectrum. For this reason the techniques adopted are different and some of them give rise to particular variants in the mass spectrometry. However the main principle is the formation of ions by means of an electron beam bombardment at high energy (approximately 70 eV) of the gas coming from the GC. It is the impact of the electrons produced by the filament and the gas molecules which produces the ions. The energy provided by the

electrons beam and the instability in the molecular ions generally produce even a breaking of the molecule in smaller fragments which can be positively or negatively charges. Although both types of charged ions are produced it is commonly chosen a specific polarity (usually positive). The ions are then accelerated and focused by means of a series of lens towards the quadrupole. This type of analyzer is made up of four cylindrical metal bars in which the ions are separated in terms of their mass to charge ration (m/z), combining radio-frequency generated continuous and alternating electric fields. In this manner only the ions of a given mass can reach the detector. The detector is generally made of series of dynodes, essentially electronic multipliers which are capable to amplify the very low current generated by the ions which have passed the the analyzer. The signals produced in this manner are then transmitted to a calculator capable, thanks to the assistance of a software, of representing the abundance of an ion as a function of its mass by means of an histogram. The abundances are represented in relation to the most abundant peak observed in the spectrum since this normalization allows to have spectra which are only function of the analyte and of the analysis conditions. The use of the calculator allows also to combine the fast management of the instrument parameters with the bibliographic research in electronic libraries, in order to automatize the identification of the compounds in terms of their spectrum and of the operative conditions. With the combination of both gas chromatography and mass spectroscopy the identification of the compounds in the sample to be analyzed is realized by the comparison between the relative retention times of the analytes to be identified with those of the gaseous mixtures of reference and by the comparison of the mass spectra produced by the fragmentation of the molecules with known spectra contained in specific libraries published by NIST (*National Institute of Technology*). The analyses are usually carried in full scan mode in which the mass spectra are recorded at regular time intervals. Each peak of the chromatogram corresponds to a specific compounds with a given retention time, which can be identified by a (mass) spectrum characteristic of the compound to be analyzed. By the analysis of the mass spectra obtained it is possible to acquire informations on the structure of the analyte. As an alternative the mass spectra can be recored in SIR (*Selected Ion Recording*) mode, in which only some selected mass fragments, characteristic of the analyte to be determined, are employed. The main advantage of this type of recording is the increasing sensibility of detection, which can be increased up to 500 times with respect to the full scan mode. In this manner it is thus possible to detect very low concentration of a given species. The quantitative analysis is realized by integrating the peak obtained by the total ionic current of every compounds identified. The value of the area integrated has to be compared with the area value of the peak related to the internal standard or with a calibration line obtained from the analysis of gaseous mixtures with a known concentration. The calibration can be done on a single point, at a concentration very close to that of the analytes to be quantified or by constructing a proper calibration line obtained with standard mixtures at different concentrations. In the present work a GC-Ms with a MEGA 1 (30 m $\times$ 0.5 mm $\times$ 5 μm) capillary column at intermediate polarity has been employed. The analysis have been carried in SIR mode in order to amplify the signal, once identified the masses related to the compounds involved in the degradation process. In order to obtain a quantitative

analysis a calibration line has been employed in order to correlate the GC-MS areas with a known amount of the species involved.

Part I.

Nanostructured membranes for VOCs photodegradation

INTRODUCTION

The development of new solutions in pollution sensing and prevention by using adequate nanostructures with unique properties has gained more interest according to a pressing need for new advanced solutions both for indoor and outdoor pollution. Nanoengineered membranes obtained by electro-hydrodynamic technologies are promising filtering media that can enable high levels of filtration and environmental clean up performances in a broad range of applications since they have proven to be a good candidate for promoting a significant increase in filter efficiency and more contaminate holding capacity [284]. Photocatalytic oxidation has proven to be a promising technology for air purification and nanostructured membranes based on electrospun nanofibers offer a proper support in the production of active filtering media which combined the physical activity with the chemical degradation of harmful pollutants [197]. In this context TiO_2 is a well known n-type semiconductor generally considered as the traditional benchmark photocatalysts due to its high photocatalytic activity, no toxicity, chemical stability and low price [163]. Between the different strategies to improve its performances the combination of TiO_2 and graphene is promising candidate for the generation of high efficient composites that simultaneously possess excellent adsorption, transparency and conductivity, which could facilitate the effective photodegradation of pollutants during the photocatalysis. Indeed among carbon nanomaterial graphene is attracting widespread attention because its sp^2-hydridized two-dimensional honeycomb carbon structure provides outstanding thermal conductivity, charge carrier mobility and large surface area [285–287]. Several research articles have been published in relation to the employment of these composites mainly dealing with the photocatalytic abatement of organic dyes in water [287–296] and only a few have reported the employment of such systems for the photo-oxidation of organic compounds in gas phase [297–299]. The present work shows the production, characterization and performances evaluation of nanostructured membranes based on electrospun scaffolds and graphene/titania based photocatalysts for gas phase photoxidation. Two different approaches for the deposition of the photocatalytic systems have been followed:

- in the "layer-by-layer approach" the membranes are produced by a sequence of electrospinning/electrospraying techniques. In the first step the support of the photocatalyst is obtained by the generation nanofibers by electrospinning of a suitable polymeric matrix, followed by the deposition of the catalyst and/or photocatalyst on the surface of the nanofibrous membrane;

- in the "one-step approach" the membranes are produced starting from a single colloidal solution in which the dissolution and the dispersion of the photocatalytic are obtained at the same time and the membrane in produced by a single electrospinning process.

For both the approaches three different photocatalytic systems based on TiO_2, TiO_2 and graphene and a nanocomposite of TiO_2 and reduced graphene oxide have analyzed. Their performances have been compared with respect to the gas phase photoxidation of methanol, a common indoor-air pollutant that has a high photoefficiency, which makes photocatalytic oxidation an attractive method for its removal [300–303].
In the second part of the work photocatalytic nanocomposites by coupling of silver carbonate (Ag_2CO_3), TiO_2 have been produced in search of a possible improvement of the photocatalytic abatement of methanol due to a synergistic effect of the presence of a semiconductors coupling, with a possible improvement of the absorption in the visible spectrum. In this context common strategies for the enhancement of the photocatalytic performances or for the absorption extent of TiO_2 under UV light includes deposition of noble metal particles [304], doping [305–308] or coupling with other semiconductors [149]. In particular the latter case allows the formation of heterojunctions for the efficient separation of the photogenerated charge carriers [309–311]. However the formation of effective semiconductors couples is generally based on the employment of hazardous or non-environmental friendly compounds. The necessity to find suitable alternative which can combine high photosensitivity, being environmental friendly and capable to extend the photocatalytic activity towards the visible spectrum in order to be employed for indoor applications is still a major challenge. Between the different alternatives which have been pointed out in the last years silver based photocatalyst (e.g. AgCl [312], AgBr [313], AgI [314], Ag_2O [315], Ag_3PO_4[316, 317], Ag_3VO_4 [318], Ag_2CO_3 [319] *etc.*) have recently received great attention. Between then Ag_2CO_3 has been successfully employed for the degradation of organic pollutant in liquid phase both alone [319] or coupled with other compounds [320–325]. The high appeal for its easy synthesis has determined it choice for the evaluation of the its performance in conjunction with the employment of TiO_2. To obtain a better contact with the two semiconductor to enhance the photocatalytic activity the one-step approach has been followed for the deposition of the mixture of photocatalysts. The membranes obtained have been tested and their performances compared with the best results obtained in the first part of the study for the same type of approach followed.

5 SYNTHESIS OF GRAPHENE-TITANIA BASED NANOCOMPOSITES FOR PHOTOCATALYSIS

5.1 RAW MATERIALS

Polyacrylonitrile (PAN, M_w = 150,000 Dalton) and PSU (M_w = 35,000 Dalton) were employed as polymeric support for the production of the electrospun membranes and were purchased from Sigma-Aldrich. Two dispersing agents, Dynasylan 4144 (Evonik-Degussa) and sodium dodecyl sulfate (SDS, Sigma-Aldrich) were added in the suspensions employed for the electrospraying process in order to improve the suspension stability. TiO_2 nanoparticles (Aeroxide P25, Evonik Industries) was used as photocatalyst, while graphene oxide (Sigma-Aldrich) and few layer graphene (Avanzare Innovacion Technologica S.L., La Rioja, Spain) were employed as co-catalysts.

5.2 CHARACTERIZATION

5.2.1 Raman spectroscopy

Raman spectroscopy of the graphene and graphene based composites have been performed with a Micro Raman DRX (Thermo Fisher). All the samples were analyzed using a laser excitation wavelength of 532 nm (2.33 eV) and 0.5 mW laser to preserve sample from damaging or laser induced heating, using a 100 x objective.

5.2.2 AFM

Atomic force microscopy analysis of graphene samples were carried out using a Veeco Digital Instruments mod. CP-II in contact mode using a Microlever ML06A tip and were prepared by electrospraying of a graphene suspension (1 mg/ml in N,N-dimethylformamide) onto silicon wafer.

5.2.3 TEM

High resolution (0.2 nm) transmission electron microscopy (FEI Tecnai G12, 100KV with TVIPS Tietz F114 photocamera) was employed for the morphological analysis of graphene.

5.2.4 FT-IR

FTIR spectra of the pristine and composite photocatalysts and co-catalysts were collected with an infrared spectrometer (ThermoFisher Nicolet 670) in transmission mode, using KBr tablets, in the 4,000-400 cm^{-1} wavenumber range (64 scans, 4 cm^{-1} resolution). Before the analysis a background spectrum was run and samples spectra were normalized against it.

5.2.5 XRD

Wide Angle X-ray diffraction (WAXD) patterns were recorded in the $1.5° \leqslant 2\theta \leqslant 40°$ angular range with a Philips X'Pert PRO diffractometer, working in reflection geometry and equipped with a graphite monochromator on the diffracted beam (CuKα radiation). The scanning step size was 0.02° with a measured d-spacings uncertainty of about 0.05 nm (2σ).

5.2.6 TGA

Thermogravimetric analyses were carried with a SDT Q600 (TA Instruments) TGA under air or nitrogen flow at a flow rate of 100 ml/min and at a constant heating rate of 5°C/min from room temperature up to 900°C.

5.2.7 UV-visible spectrophotometry

Diffuse reflectance UV-visible spectra were acquired with an UV-visible-NIR spectrophotometer (Cary 5000, Agilent Technologies) with an integrating sphere attachment, in the range of 200-800 nm. $BaSO_4$ was used as the reflectance standard material.

5.3 RESULTS AND DISCUSSION

5.3.1 Photocatalysts preparation

The catalyst employed for the experimental tests were:

- pristine TiO_2;
- grafene and TiO_2 (G+TiO_2);

- partially reduced graphene oxide coupled with TiO_2 (rGO-TiO_2) by hydrothermal method.

TiO_2 and graphene were purchased and not subsequently modified. The G+TiO_2 composite has been realized by physical coupling of the two materials produced on the surface of the membrane by simple alternate deposition of a layer of titania nanoparticles on top of a layer of graphene sheets by electrospraying and the conditions for its realization are described in §6.2.2.2.
The synthesis of the rGO-TiO_2 nanocomposite has been developed according to the procedure developed by Zhang *et al*.[287] but modified according to Kalid *et al*. [288]. Briefly, 80 ml of distilled water were added in a glass container along with 40 ml of ethanol. 20 mg of Graphene oxide were added to the mixture which has been subsequently sonicated (tip sonication at a 40% of amplitude with intermediate cooling breaks of about 10 minutes every 30 minutes) for 2 hours and 45 minutes in order to exfoliate the graphene oxide sheets. During the process the dispersion has progressively became darker until reaching a light gray color and losing its transparency. The sonication process has been conducted for a time necessary to avoid the presence of visible particles of graphene oxide. After the sonication about 200 mg of TiO_2 were added to the mixture and the color of the final colloidal suspension has changed to light brown (Figure 5.1). At this point the suspension has been stirred for three hours in a closed container. In the final step microwave heating (MicroSYNTH, Milestone Inc.) has been used as alternative to autoclave treatment. In this case the program included a first step of heating to 120°C in 10 minutes, followed by an isothermal treatment at 120°C in closed containers under stirring using a power of 300 W.

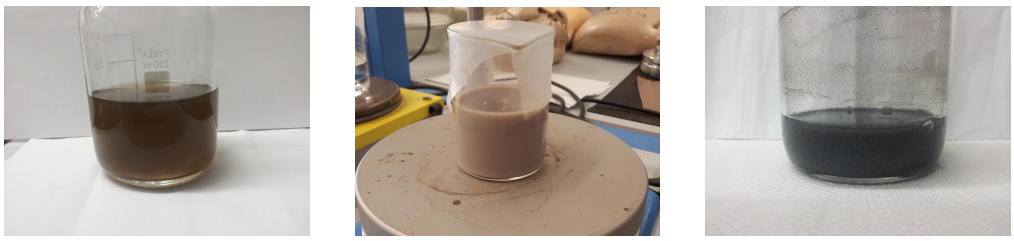

(a) (b) (c)

Figure 5.1: *Phases for the preparation of the photocatalyst: (a) Dispersion of graphene oxide in water, (b) addition of titania to the dispersion, (c) suspension of rGO-TiO_2 after hydrothermal treatment in microwave*

After the hydrothermal treatment the obtained suspension changed color from brown to dark gray (Figure 5.1) and the powder has been recovered, filtered, washed and rinsed several times with distilled water and ethanol. Finally, the recovered solid has been dried in oven at 45°C for one day and recovered as grey powder.

5.3.2 Raman spectroscopy

Raman spectroscopy is a useful analytical technique for the characterization of carbon based materials thanks to its high sensitivity to highly symmetric covalent bonds with

little or no natural dipole moment, as in the case of carbon-carbon bonds [326]. This sensitivity to geometric structure is useful for the study of the different carbon allotropes (i.e. diamond, carbon nanotubes, fullerenes, carbon nanoribbons, *etc.*) which differ only in the relative position of their carbon atoms and in the nature of their bonding. In the last years due to the growing interest emerged towards graphene it has become a useful and simple characterization of this new material thanks to the possibility to evaluate the number of layers and to provide a qualitative evaluation of the structural order. The Raman spectra of graphene and graphite are quite similar and they are characterized by the following peaks:

- G band at $\approx$ 1582 cm^{-1}, which represents the planar configuration sp^2 bonded carbon that constitutes at graphene sheets
- D band at $\approx$ 1350 cm^{-1}, which represents a ring breathing mode from sp^2 carbon rings, although to be active the ring must be adjacent to a graphene edge or a defect [327–329]
- 2D band at $\approx$ 2700 cm^{-1}, which is due to the phono lattice vibrational process, but unlike the D-band, it does not need to be activated by proximity to a defect

Many articles have also demonstrated that it is possible to find two bands which indicate disorder and defects on the carbonaceous samples: the first peak is located around 2950 cm^{-1} (D+G band) whereas the second one is located around 3250 cm^{-1} (2D′ band) [328–330].
There are many criteria which could be applied to Raman spectra in order to distinguish between one or few layer (graphene) or many sheets (graphite).
The most important are:

- position of the two main peaks (2D and G);
- I_{2D}/I_G, i.e. the ratio between the intensity of 2D and G peak;
- I_D/I_G, i.e. the ratio between the intensity of D and G peak;
- the FWHM (full width half maximum) of 2D band;
- the shape of the 2D band.

All these criteria have an important drawback: they are able to distinguish well the number fo layers if it is low (best results are obtained for less than 10 layers) while discriminating between nanographite and micrographite is a very complicated task.

The main characteristics of the Raman spectrum of graphene can be seen in Figure 5.2 and can be briefly summarized in a low pronounced 2D band (with respect to G band) centered around 2690 cm^{-1}, an intense D band and the presence of the D+G band around 2900 cm^{-1}. Considering the position of the 2D band, it can be stated that the graphene used is a few-layer graphene, while the presence of several chemical and/or physical defects can be inferred from the high D band absorbance. The confirmation of these conclusion can be

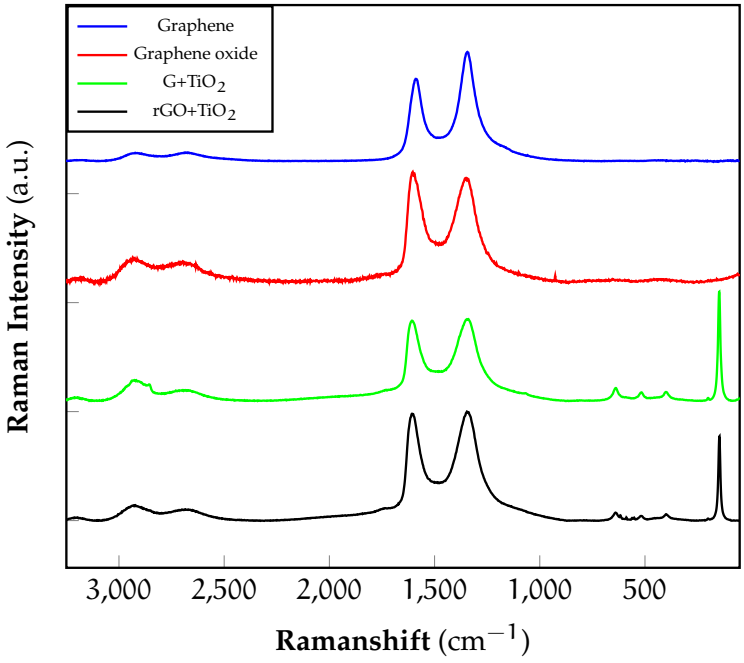

Figure 5.2: *Raman spectra of pristine graphene, graphene oxide and graphene based composites*

found by comparison with the spectrum of a typical monolayer graphene in which the 2D band is higher than the G band with the absence of the D peak, but these characteristics are actually achievable with specific process like "Scotch tape method" or CVD [327]. The Raman spectra of GO and rGO-TiO_2 nanocomposite after hydrothermal methods show strong D (at 1345 cm^{-1}) and G (at ~1590 cm^{-1}) peaks, suggesting very small crystal sizes [328]. In addition, I_D/I_G ratio was used to measure structural disorder which was slightly decreased from 1.05 to 1.02 probably because of the decrease in the sp^2 domain size of carbon atoms and the reduction of sp^3 to sp^2 carbon during the hydrothermal process [331]. Moreover in the rGO-TiO_2 and G+TiO_2 spectrum the anatase phase exhibits peaks at 146, 397, 518, and 639 cm^{-1} [332].

5.3.3 TEM

The conclusion drawn from the previous analysis regarding the employed graphene are confirmed from the TEM micrographs reported in Figure 5.3.
It is possible to note that by the edge counting of the graphene sheets the thickness of the material is very low. The sheets are quite folded and without the planar distension typical of the samples produced via "Scotch tape method" or CVD, meaning an high degree of difects.

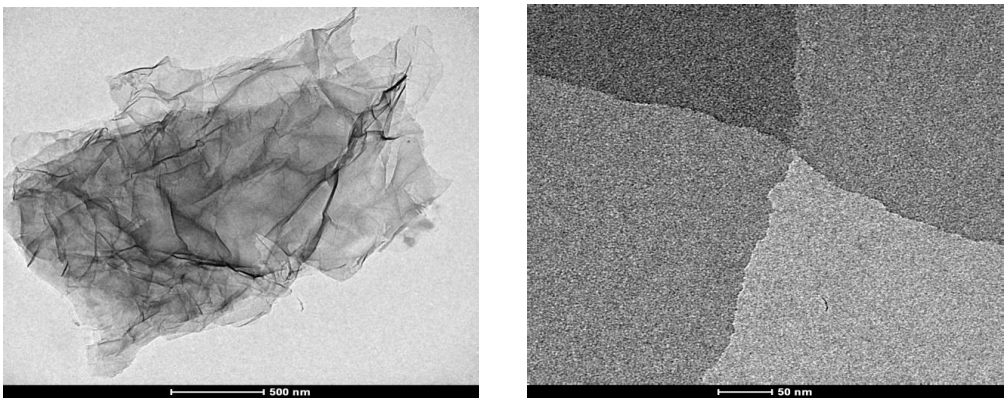

(a) (b)

Figure 5.3: *TEM images of graphene samples: (a) folded sheet, (b) detail of the edges*

5.3.4 AFM

Figure 5.4 shows the image of some graphene particles analyzed by atomic force microscopy (AFM). The analysis the particle profiles analyzed shows that, despite the fact that the height of monolayer graphene should be around 0.35 nm, the measured values vary in the range between 2 and 8 nm, and this can be associated to different causes [333–337], namely:

- instrumental offset which usually start from values around 0.8 nm;
- presence of structural defects and chemical groups which dilates the interplanar distances between the layers of graphene;
- practical impossibility to isolate graphene particle by particle with the employed deposition method and thus, the formation of agglomerates with more superimposed particles.

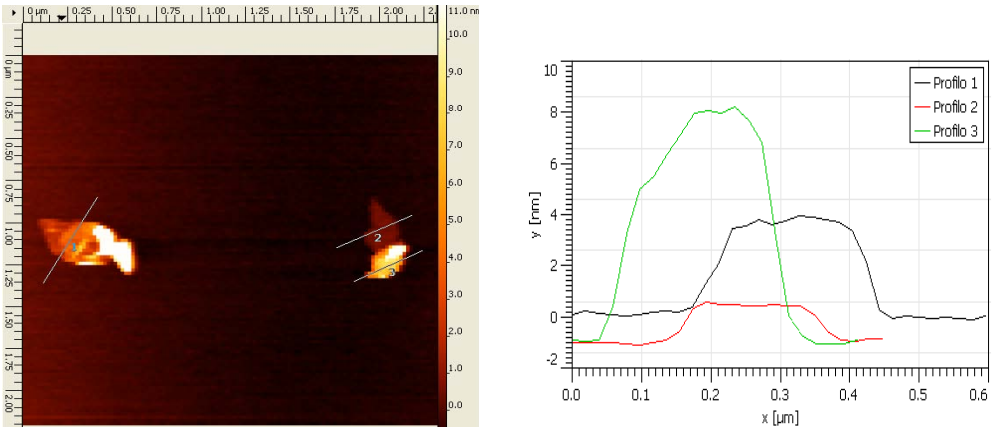

(a) (b)

Figure 5.4: *(a) 2D image of the graphene; (b) height profiles of the particles*

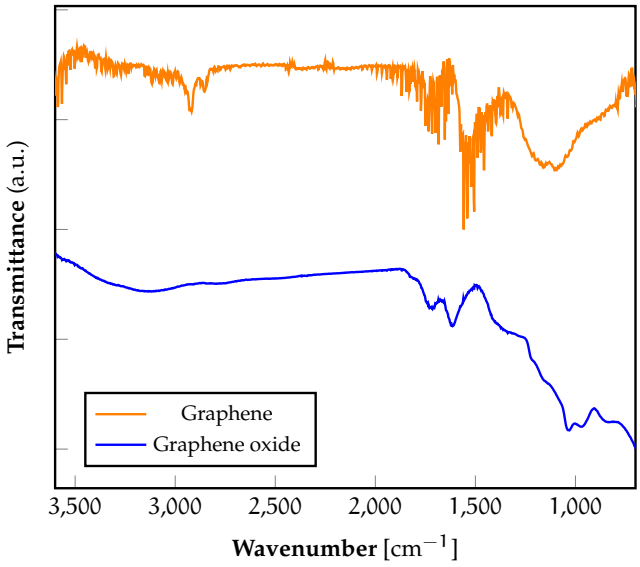

Figure 5.5: *FTIR spectrum of graphene and graphene oxide*

Hypothesizing an indicative value of 0.6-1 nm of thickness for a single layer it is realistic to conclude that the material employed is a few layer graphene. It is worthwhile to note also that the particles have an average dimension of about 200-400 nm.

5.3.5 FT-IR

FT-IR spectroscopy has been employed as characterization techniques for the analysis of the composites realized by hydrothermal treatment to investigate possible evidence of reduction and coupling with TiO_2. In Figure 5.5 the FTIR spectrum of graphene oxide presents a first peak at 1,050 cm^{-1} which arises from the epoxide groups (C-O-C). The broad absorption band between 3100 and 3500 cm^{-1} is associated to the -OH stretching vibration while the two peaks at 1720 and 1615 cm^{-1} can be identified as C=O stretching of the COOH groups and, respectively, the O-H bending vibration, epoxide groups and skeletal ring vibration [338]. The FT-IR spectrum of graphene is characterized by an intense background noise due to the presence of humidity. The most intense peaks can be found at 1,600 cm^{-1} and are related to absorption associated to the lattice vibration of the graphitic domains as well as the presence of OH groups (vibrational stretching at ~3400 cm^{-1}), C=O (1,720 cm^{-1}), C-OH (vibrational stretching at ~1,220 cm^{-1}) and C-O (vibrational stretching at 1060 cm^{-1}). Thus from the FT-IR it is possible to assess the presence of several defects of chemical nature for the graphene employed [339] as previously noted from the Raman analysis.

The spectrum of pristine TiO_2 in Figure 5.6 shows two typical peaks at 505 cm^{-1} and 650 cm^{-1} determined the O-Ti-O bonding in anatase morphology along with a tiny peak at 1,630 cm^{-1} and a broad absorption band with a maximum at 3,420 cm^{-1} that can be ascribed to the characteristic of bending and vibration of surface-adsorbed water and hydroxyl groups [340, 341]. The rGO-TiO_2, G+TiO_2 and GO+TiO_2 nanocomposite presents

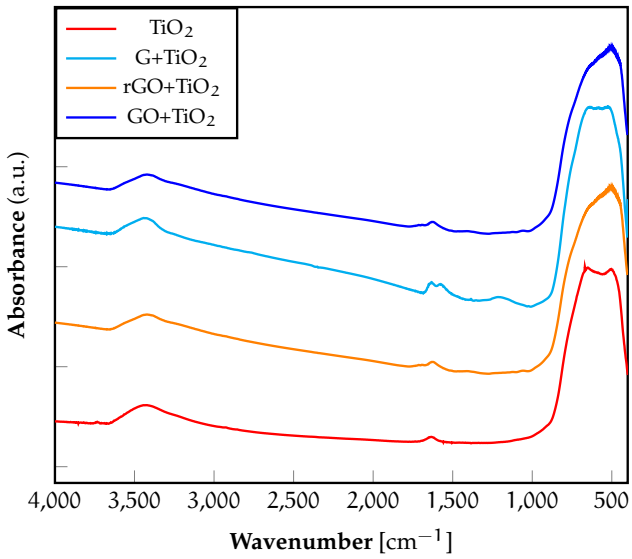

Figure 5.6: *FTIR spectrum of TiO_2 and its composites with different types of graphene*

similar features. First of all the broad absorption at low frequency (below 1,000 cm^{-1}) has been attributed to the vibration of the O-Ti-O bonds similarly to that in the spectrum of titania. The absorption peak appearing at *ca.* 1,630 cm^{-1} can be ascribed to the skeletal vibration of the graphene sheets as well as water absorbed on the surface of titania. A main distinctive features of the GO+TiO_2 and rGO-TiO_2 composites is the absorption bands observed in the range of 400–1,000 cm^{-1} which, in pure TiO_2, correspond to Ti-O-Ti bonding. In this case these bands have a main peak which is shifted toward lower region by incorporating the two types of graphene . This result has been suggested as indicative the presence of both Ti-O-Ti and Ti-O-C bonds in the composites, indicating the chemical interaction between surface hydroxyl groups of TiO_2 and functional groups of graphene oxide [287, 342].

5.3.6 XRD

XRD diffractograms were collected for the pristine materials as well for the composite photocatalysts to identify the successful coupling of the different components, especially to provide evidence of the successful reduction of graphene oxide to rGO by hydrothermal method according to the results obtained in literature [299, 332]. The results are shown in Figure 5.7.

For the titania sample the peaks at 2θ values of 25.3°, 37.8°, 48.0°, 53.9°, 55.1°, 62.7°, 68.8°, 70.3° and 75.0° can be indexed to the (101), (004), (200), (105), (211), (204), (116), (220) and (215) crystal planes of anatase (JCPDS card n° 71-166). In addition also the characteristic diffraction peaks of rutile (JCPDS card n° 05-4165) at 27.4, 36.1, 41.2° are observed, which correspond to the (110), (101) and (111) faces of rutile in TiO_2. The mass percentages of

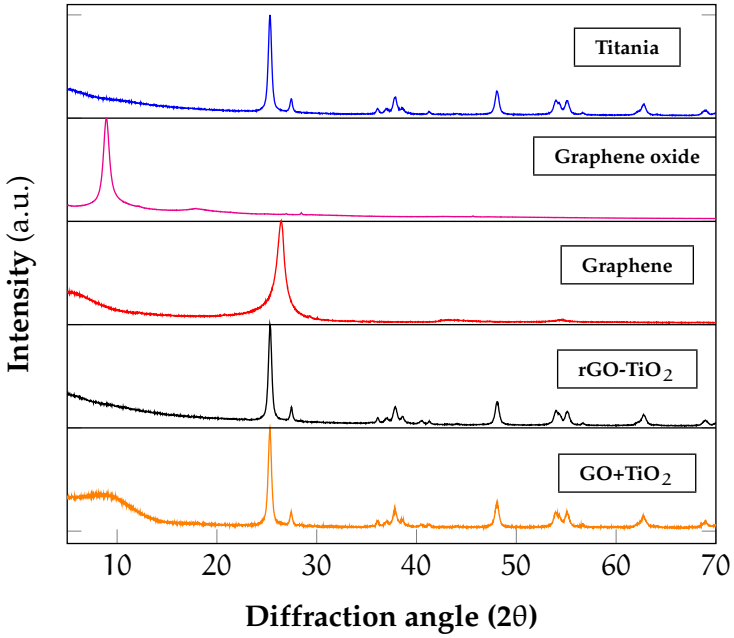

Figure 5.7: *XRD diffractograms of the pristine materials and composites for the graphene based photocatalysts*

rutile and anatase were determined using the following equations [343]:

$$\text{Anatase } (\%) = \left[\frac{0.79 \cdot I_A}{I_R + 0.79 \cdot I_A} \right] \times 100 \tag{5.1}$$

$$\text{Rutile } (\%) = \left[\frac{I_R}{I_R + 0.79 \cdot I_A} \right] \times 100 \tag{5.2}$$

where I_A and I_R are the peak intensities of the (101) and (110) reflection planes for anatase and rutile, respectively. On the basis of the calculations performed the amount of anatase is equal to 80.8% while the amount of rutile is 19.2%, in accordance with the values reported by the manufacturer.
The analyzed graphene oxide present a single peak at 9.28° corresponding to the (002) reflection plane which represents the typical diffraction peak of the basal plane due to the layers which constitute the material. No reflection at 2θ = 26.3-26.4° (peak that indicate the abundance of unoxidized graphite residues) allows to consider that the starting material can effectively be considered as graphene oxide. As highlighted by Khishnammorthy *et al.* [344] the angle of diffraction of this peak can be found at different diffraction angles according to the different degree of oxidation of the starting material. In their study they have shown that the higher is the degree of oxidation (namely a lower C/O ratio) the lower is the characteristic diffraction angle of the material, due to an increase in the interplanar distance related to presence of an higher amount of oxygen containing functional groups on the surface of the material along with the possible presence of intercalated water

molecules. According the diffraction angle of the peak the calculated interlayer distance can be obtained from the Scherrer equation [345]:

$$D_{002} = \frac{K\lambda}{B \cdot \cos\theta} \tag{5.3}$$

where D_{002} is the thickness of the crystallite, K is a constant dependent on the crystallite shape (0.89), λ is the X-ray wavelength, B is the full width at half maximum (FWHM), and θ is the scattering angle. From this equation the interplanar distance is approximately 0.89 nm. Larger interlayer spacing of GO maybe favorable to be fully exfoliated during the reduction process to produce layer controlled graphene.
Pristine graphene present a single peak diffractogram as well, which is a little more broad than that of graphene oxide and with a maximum centered at a diffraction angle of 26.5°, which is similar to that of graphite. In this case this confirms the presence of more than one layer, the absence of significant chemical defects in the materials and by the previous analysis allows to confirm the few layer nature of its structure
The diffractogram obtained from the coupling of graphene oxide and titania reflects the characteristics of the two materials: the characteristic peaks of titania are clearly visible and at approximately 9° it is possible to identify a broad peak that can be associated to the presence of graphene oxide, confirming the successful coupling of the two materials, whose broadening indicates poor ordering of the sheets along the stacking direction possibly implying that the sample is comprised mainly from single or only a few layers.
The titania-graphene nanocomposite obtained by physical mixing present a diffractogram which is indistinguishable from that of pristine titania, without peaks belonging to the separate graphene. The reason of this result can be ascribed to the fact that the main characteristic peak of graphene might be shielded by the main peak of anatase TiO_2 at 25.4° [288].
From this conclusion it is also possible to confirm that from the diffractogram of the rGO-TiO_2 nanocomposite the reduction of GO to few-layer graphene has been successfully accomplished thanks to the hydrothermal method because of the absence of the peak at 25.9° and simoultenous presence of a small peak at ~ 40.5° which can be ascribed to the (100) plane of graphene [346].

5.3.7 TGA

The thermogravimetric analysis have been carried in order to evaluate both the amount of catalyst present in the membranes, determine the deposition homogeneity on a single membrane and qualitatively judge the partial reduction of the nanocomposite obtained by hydrothermal treatment. Figure 5.8b presents the TGA of the nanocomposite compared to the thermal behavior of graphene and graphene oxide (Figure 5.8a) under inert atmosphere (nitrogen). In order to evaluate properly the real residue of the rGO component in the rGO-TiO_2 sample the analysis has been carried by evaluating the pure thermal degradation up to 800°C and subsequently switching to oxidant atmosphere to burn the organic residue in order to determine the real amount of titania. Graphene oxide presents a multi-step thermal degradation and starts to lose mass upon heating even below 100°C, which is

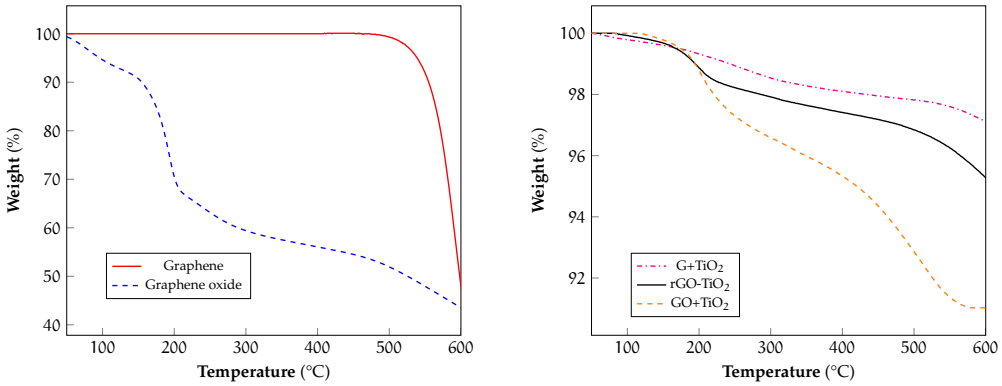

Figure 5.8: *TGA thermograms of the pristine graphenes and graphene-based photocatalysts: (a) comparison between the thermal stability of graphene and graphene oxide, (b) comparison between the thermal stability of rGO-TiO_2 (1:10) and GO+TiO_2 (1:10) composites*

associated to the elimination of loosely bound or adsorbed water and gas molecules. The first major mass loss starts at 125°C and sharply decrease to 380°C, subsequently followed by slow further decrease up to 600°C. The major mass reduction at $\approx$ 200°C is caused by the pyrolysis of the oxygen-containing functional groups, generating CO, CO_2, and steam [347]. On the other side graphene shows an significantly higher thermal stability and its pyrolytic decomposition starts around 500°C, as a consequence of the previously mentioned chemical defects. The thermal decomposition of the rGO-TiO_2 1:10 composite shown in Figure 5.8 is compared to a GO+TiO_2 powder mixture obtained by physical mixing of TiO_2 and GO, with the same mass proportions between catalyst and co-catalyst as rGO+TiO_2. In the latter case the coupling has been realized by dispersing graphene oxide in water by sonication with further addition of titania. The colloidal suspension thereby obtained has been filtered to recover the solid part which has been heated to complete dryness before analysis. The results of the TGA shows that the rGO-TiO_2 present an higher thermal stability with respect to the GO+TiO_2 which can considered as in indirect proof of the partial reduction of graphene oxide in the nanocomposite. Both the samples presents a final residue between 91 and 92% which is close to the theoretical values of 90% according to their composition. The higher thermal stability can be explained in terms of removal of oxygen-containing functional groups obtained during the hydrothermal treatment.

5.3.8 UV-visible spectrophotometry

Diffuse reflectance spectra have been collected with an integrating sphere on solid samples prepared by mixing $BaSO_4$ with a 5% by weight of the catalyst to be analyzed. The two powders have been mixed and pressed to produce a tablet which has been analyzed. The nature of the fundamental optical absorption in a semiconductor is of primary importance in determining the overall efficiency of the system. A direct band gap semiconductor

shows a square-root behavior just above the gap and thus has an optical absorption which rises much more rapidly than that of an indirect-gap semiconductor which exhibits a square root behavior [348]. The optical band-gap of a crystalline semiconductor can be determined according to the following equation using the optical absorption data near the band edge:

$$\alpha h\nu = A(h\nu - E_g)^n \tag{5.4}$$

where α is the absorption constant, ν is the light frequency [s^{-1}] , E_g is the band gap [eV], h is the Planck constant [J·s], while A is a constant. In Equation 5.4, n determines the characteristics of the transition in a semiconductor, i.e., direct allowed (n=1/2), indirect allowed transition (n=2) or and forbidden direct and indirect transitions (n=3/2 and 3) [349]. Since α is proportional to the Kubelka-Munk function $F(R)$, defined as:

$$F(R) = \frac{(1-R)^2}{2R} \tag{5.5}$$

where R is the reflectance, the final expression becomes:

$$F(R) \cdot h\nu \approx A(h\nu - E_g)^n \tag{5.6}$$

and the reflectance can be determined from the absorbance (A) data as:

$$R = \left(\frac{1}{A}\right)^{10} \tag{5.7}$$

The values of n and E_g can be determined using the following steps [350]:

1. plot of ln($F(R) \cdot h\nu$) versus ln($h\nu$ - E_g) using approximate value of E_g and then determine the value of n based on the slope of the straightest line near the band edge
2. construction of the Tauc plot [351] by plotting $(F(R) \cdot h\nu)^{1/n}$ versus $h\nu$ (photon energy) and then refine the band gap E_g by extrapolating the straightest line to the $h\nu$ axis intercept.

In this case for all the sample have been modeled with n = 2 and the values of calculated band gap and absorbance limits are shown in Table 5.1. According to its absorbance spectrum graphene oxide presents an absorption peak at 230 nm, attributed to the π-π transition of the aromatic C-C ring and a very weak absorption at 303 nm due to the n-π transition of the C=O bond [352–354]. The presence of the absorption edge at 303 nm confirms the semiconductor nature of the material, which can be only activated under UVB-UVC radiation. It is worthwhile to note that the electronic structure of graphene oxide are strictly dependent on its specific composition. GO exhibits a p-type conductivity due to the high electronegativity of oxygen compared to carbon. The valence band of graphene oxide origins from the oxygen covalently bonded on its surface from the O_{2p}

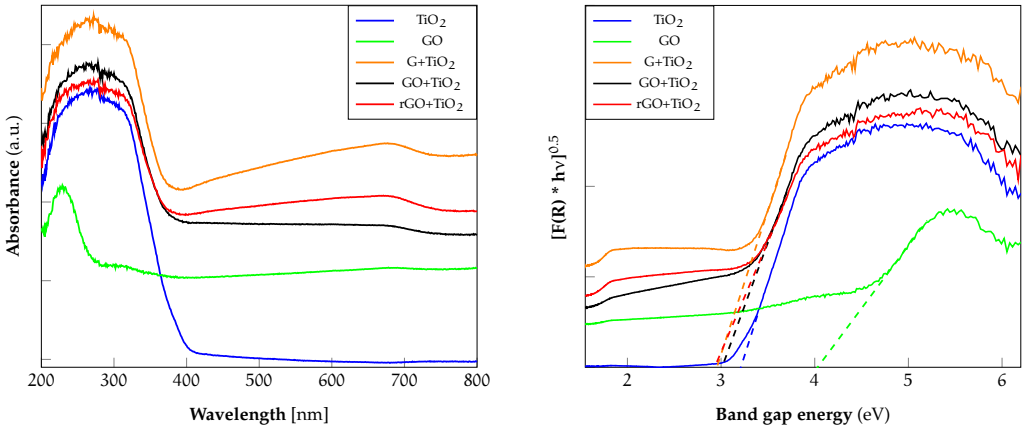

Figure 5.9: *UV-visible spectrum of photocatalyst and co-catalysts: (a) DRS spectra of pure components and composites for the determination of the absorbance edge and (b) plot of $(F(R)\cdot h)^{0.5}$ versus the energy for the determination of the band gap of the semiconductors*

Table 5.1: *Band gap energies and absorption edge calculated from DRS spectra for the photocatalysts and co-catalysts employed*

Catalyst	Band gap (n=1/2) [eV]	Absorption edge [nm]
TiO_2	3.21	388
GO	4.03	303
GO+TiO_2	3.01	412
G+TiO_2	2.95	420
rGO-TiO_2	2.93	423

orbital rather then the π orbital of graphene, leading to an increase in the band gap as the oxygen coverage increases. At the same time the conduction of graphene oxide is mainly attributed to the anti-bonding π^* orbital. The higher the degree, the more positive the valence band and the higher oxidative power, but the larger the bandgap is unfavorable since it requires shorter wavelength for photoexcitation [355].

Titanium dioxide has a very sharp absorption edge at 388 nm which correspond to a band-gap value of 3.21 eV, characteristic of the anatase crystalline phase of the compound [356] and due to the electron transition from the valence band to the conduction band ($O_{2p} \rightarrow Ti_{3d}$).

All the graphene based composites generally shows an increase in the absorption in the UV region with respect to TiO_2. The GO+TiO_2 composite obtained by colloidal blending shows a red shift of the absorption edge respect to titania and narrows the band gap of the material. As noted by Nguyen-Phan *et al.* [289] this could be ascribed to the modification that graphene oxide imparts on the optical properties of TiO_2 due to their interaction as suggested by the results of the FTIR analysis. Besides the sample present a non null

absorption below the main band gap, which is characteristic of the graphene oxide. The G+TiO_2 shows very good results; the presence of graphene induces a strong increment in the absorption all along the 200-800 nm range. The phenomenon is of difficult explanation since graphene should not present photocatalytic activity, but a reasonable explanation can be find in terms of interaction between the graphene employed with TiO_2 analogously to the case of carbon nanotube (CNT)-TiO_2 composite materials [357, 358] Finally rGO-TiO_2 nanocomposite shows a narrower band gap than the previous cases and this could be ascribed to the chemical bonding between TiO_2 and the surface of the carbon substrate on which the TiO_2 have been deposited during the hydrothermal treatment. The enhancement like in the case with bare graphene is also pronounced in the visible range with an increment of the absorption which is promising for the employment of the photocatalysts even un visible light irradiation.

5.4 CONCLUSIONS

A screening activity has been carried on photocatalytic composites based on titania and graphene as preliminary step for the preparation of nanostructured membranes for VOCs photooxdation. The composites have been produced by physical mixing and by an hydrothermal method for the partial reduction of graphene oxide and coupling with titania nanoparticles. Both the pristine materials and the composites have been analyzed by different techniques (Raman and infra-red spectroscopy, XRD and UV-visible diffuse reflectance spectroscopy) and particular attention has been paid to the analysis of graphene (Raman, AFM, TEM). The graphene employed has been identified has been composed of a few layer but with the presence of some chemical and physical defects in their structure. The rGO-TiO_2 composite has been successfully produced starting from graphene oxide and titania and the partial reduction of the starting graphene oxide has been confirmed by the XRD and TGA, in comparison to the GO+TiO_2 and G+TiO_2 with same co-catalyst/catalyst ratio. The UV-vis DRS spectra have shown a synergistic effect due to the coupling between the titania with the graphenes at different degrees of reduction. Generally there is an increase in the absorption in UV region, where the titania is photo-active, accompanied with a red shift which decreases the band gap of the photocatalyst along with a less strong absorption in the 400-800 nm range. These results are promising for the employment of the photocatalysts developed in combination with the nanofibrous support which can improve the dispersion of the catalyst.

6 LAYER-BY-LAYER APPROACH: MEMBRANE PREPARATION, CHARACTERIZATION AND PERFORMANCE EVALUATION

In this part of the work the main focus has been centered on the definition of the proper conditions to carry the electrospinning/electrospraying process for the production of the porous membranes and the deposition of the catalysts. In the layer-by-layer approach the first step has been the electrospinning of the polymer followed by a separated electrospraying deposition of the catalyst dispersed in a suitable solution (Figure 6.1).

Figure 6.1: *Steps for the membranes fabrication by the layer-by-layer approach*

In this manner the membranes obtained are porous and the catalyst cover only partially the membranes, specifically the upper part exposed towards the needle during the electrospraying process.

6.1 CHARACTERIZATION

6.1.1 SEM

Scanning electron micrographs were collected with a JEOL 6490 SEM on gold sputtered samples.

6.1.2 TEM

High magnification transmission electron microscopy (FEI Tecnai G12, 100KV with TVIPS Tietz F114 photocamera) was employed for morphological analysis. The membrane samples preparation for TEM imaging had been carried out as follows: the membrane samples were embedded in a proper epoxy resin and slices of 100 nm thickness were cut from the cured resin using a Leica ultracut UCT microtome.

6.1.3 TGA

Thermogravimetric analyses were carried with a SDT Q600 (TA Instruments) TGA under air flow at a flow rate of 100 ml/min and at a constant heating rate of 20°C/min from room temperature up to 900°C.

6.2 RESULTS AND DISCUSSION

6.2.1 PSU electrospinning

The first polymeric matrix that have been screened as support has been polysulfone (PSU) due to its remarkable mechanical strength and thermal resistance which makes it suitable to be employed even for applications in which the catalyst is activated thermally. The polymeric support processed in shape of nanofibers has the task to provide higher dispersion of the catalyst to increase the surface area available for the reaction. In order to reach such goal a first screening phase has been accomplished in order to find proper parameters for the electrospinning process, with particular interests towards solution flow-rate, humidity and applied voltage (Table 6.1). These parameters have changed to obtain six combinations without altering the others (tip-to-collector distance and needle diameter). The polymer has been electrospun from a solution at 20% by weight in DMF, taking into considerations the conclusion of a previous work which dealt with the same polymer and the same molecular weight [359].

Table 6.1: *Employed process parameters for the optimization of PSU nanofibers by electrospinning (needle diameter = 0.4 mm, tip-to-collector distance = 25 cm)*

Parameter	Value	Units
Relative humidity	30 45	%
Flow rate	1 2	ml/h
Voltage	14 18	kV

The temperature during the electrospinning tests has been maintained fixed at 20°C. The optimal conditions have been defined upon evaluation of the fibers diameter calculated from SEM micrographs for a minimum of 50 measurements for each image, evaluating both the fibers mean diameter and the relative standard deviation.
The results of the calculations are showed in Table 6.2 for the fibers obtained. The samples of all the tests realized at 30% of relative humidity have been discarded due to a bad final morphology. Indeed from the parameters that have been varied during the tests, humidity seems to be the one that produces the more significant effect on the final morphology of the fibers. As can be seen from Figure 6.2 when the relative humidity is at the lower value

Table 6.2: *Mean diameters and standard deviations for the electrospinning tests of PSU solution in DMF*

Run	Humidity [%]	Flow rate [ml/h]	Voltage [kV]	Mean diameter [nm]	Std.dev. [nm]
1	30	1	14	-	-
2	30	1	18	-	-
3	30	2	14	-	-
4	45	1	14	475	179
5	45	1	18	448	187
6	45	2	14	657	301

there is the formation of a beads-on-fiber morphology, which a consequent reduction in the surface available for the catalyst deposition.

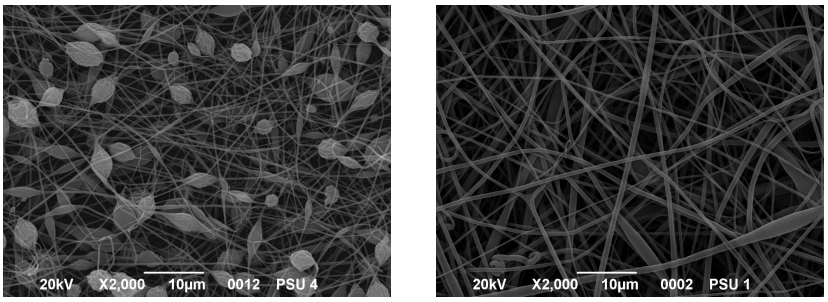

(a) (b)

Figure 6.2: *Electrospun samples of PSU nanofibers at different conditions of relative humidity: (a) 30%, (b) 45%*

The second important parameter is the flow-rate. As can be seen from the results of the calculation in Table 6.2 there is an increase of almost 200 nm (from approximately 470 to 650 nm) upon doubling the flow-rate from 1 to 2 ml/h. A possible explanation can be find in the fact that at higher flow-rates, for fixed values of the tip-to-collector distance and applied voltage, the time required for the solvent evaporation increases, determining a lower jet stretching and increasing the numbers of defects, mean diameter and standard deviation.

The third parameters investigated, the applied voltage seems to have a less pronounced effect on the final fibers dimension. Upon increasing the voltage from 14 to 18 kV there is a slight decrease in the final fibers mean diameter from 475 to 450 nm and less slight decrease in the standard deviation (Table 6.2). In general an low increase in the standard deviation is considered acceptable if the decrease in the mean diameter is much significant, being the fibers during the path between the tip to collector subjected to a much higher stretching force. In Figure 6.4 are shown the two tests carried at different voltages at a relative humidity of 45% and flow rate of 1 ml/h.

The final conditions selected for the electrospinning of PSU nanofibers after having take into consideration the results of this preliminary screening optimization are defined in

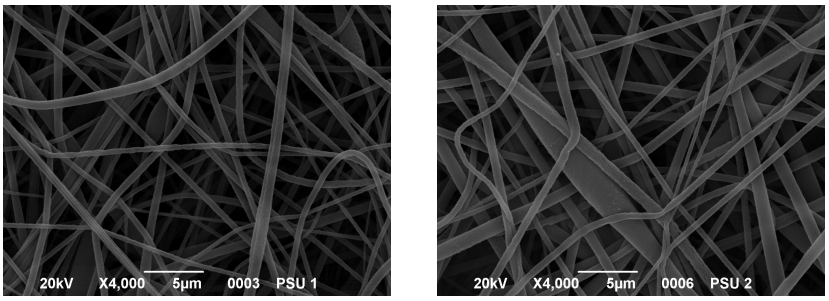

(a) (b)

Figure 6.3: *PSU electrospinning at different flow-rates: (a) 1 ml/h, (b) 2 ml/h*

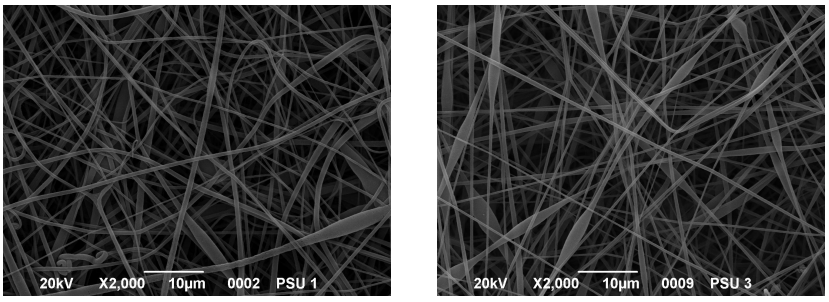

(a) (b)

Figure 6.4: *PSU electrospinning at different voltages: (a) 14 kV, (b) 18 kV*

Table 6.3.

Table 6.3: *Final process parameters for the optimization of PSU nanofibers by electrospinning*

Flow rate [ml/h]	Relative humidity [%]	Voltage [kV]	Distance [cm]	Needle diameter [mm]
1	45	18	25	0.4

For a single membrane the deposition time employed has been set at 45 minutes.

6.2.2 Catalyst electrospraying

The electrospraying technique has been employed in order to deposit the catalyst necessary for the photocatalytic reactions on the surface of the polymeric membranes. The technique is quite straightforward and the parameters involved have been screened in depth in previous works [360]. In the following paragraphs the conditions for the electrospraying of each system are described.

6.2.2.1 *TiO_2 deposition*

The first operation to be accomplished at this stage is the dispersion of titania in a suitable solvent. The solid nanoparticles inside a liquid can be present in two different

situations: completely separated from each other or aggregated in clusters; in the latter case the catalyst is not in the best conditions to accomplish its task, one deposited on the polymeric support. To avoid these drawbacks it has been necessary a sonication phase to disperse the titania particles followed by the addition of a dispersing agent in order to stabilize the suspension for a sufficient time to allow their deposition on the membranes. Between the most employed dispersing agent there are organosilanes: these are very useful as complexing agents, since they are capable to establish durable linkages between organic and inorganic substances. Generally a silane molecule has terminal groups with different functionalities, specific for the group. With reference to Figure 6.5 the group X

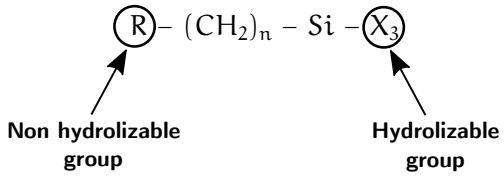

Figure 6.5: *Structure of a silane molecules*

represents the hydrolizable extreme, which, upon hydrolysis, determines the formation of the silanol group. This group is quite reactive and can reacts, by condensation reaction with molecules having hydroxyl groups, such as titania. These can react by condensation with a silanol giving rise to a siloxane group. The R group, viceversa, is not hydrolizable and establish a bond with similar surfaces, like polymer molecules. The catalyst molecules are then covered by silane. Figure 6.6 shows the reaction mechanism. On the basis of the optimization studies of previous works a suspension a 5% w/w of titania in ethanol has been realized. Subsequently the mixture has been sonicated at 40 min (200 W, amplitude 40%) during which the container of the mixture has been cooled with iced water to avoid ethanol evaporation. At the end of this operation the dispersing agent Dynasylan 4144 has been added at a 1% w/w with respect to the solvent. After the suspension preparation the electrospraying process has been carried according to the optimal parameters found by Folli [360], employing the principles of minimizing the lost of material and avoiding the dripping from the support. In Table 6.4 are reported the operative conditions for the deposition of the TiO_2 particles.

Table 6.4: *Electrospraying parameters for the deposition of TiO_2 nanoparticles from an ethanol suspension*

Flow rate [ml/h]	Voltage [kV]	Distance [cm]	Needle diameter [mm]	Deposition time [min]
8	15	12	0.4	14

The operation is carried by placing the syringe aligned to the axis of the collector where the metallic support with the electrospun polymeric membrane is placed. SEM micrographs (Figure 6.7) of the electrosprayed TiO_2 suspension shows that the nanoparticles tends to slightly agglomerate during the deposition, forming spherical porous micro- and nanos-

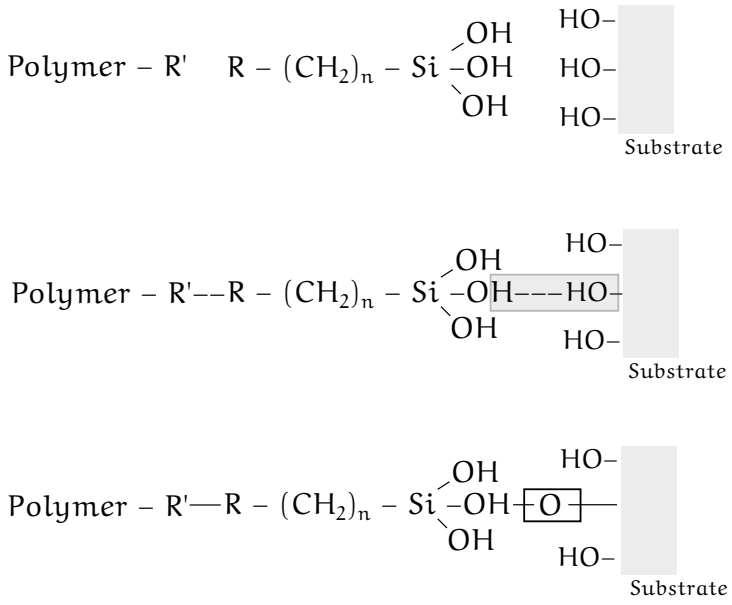

Figure 6.6: *Action mechanism of a silane molecule*

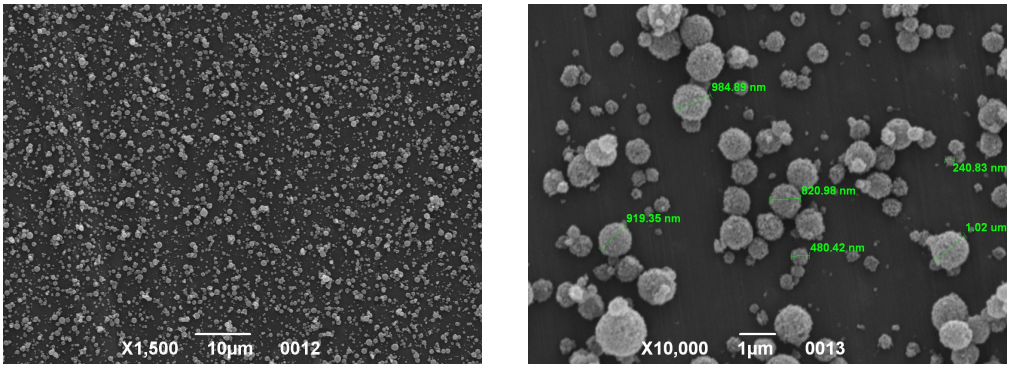

(a) (b)

Figure 6.7: *SEM micrographs of electrosprayed particles of TiO_2 at different magnifications*

tructures with an heterogeneous distribution of diameters ranging from 200 nm up to 2 µm.

6.2.2.2 *Deposition of graphene and TiO_2*

As in the previous case the main concern is the good dispersion of graphene before proceeding to its deposition. A suspension of graphene has been prepared at 0.025% w/w in ethanol which has been sonicated with a power of 200 W (amplitude of 40%) for 29 minutes; lastly a 1% w/w of dispersing agent has been added, in this case, sodium dodecyl sulfated (SDS) with respect to the solvent weight in order to maintain stable the suspension. After this operation a second sonication for 15 minutes has been realized. This sequence of operation allows to obtain a good dispersion of the graphene for a time which is sufficient for its deposition on the membranes. The choice of the dispersing

agent and the sonication times have defined on the basis of a reference work on carbon nanotubes [1] and the empirical observations during several trials in laboratory. Further tests have allowed to define the parameters to be employed for the electrospraying in order to obtain a 1/10 in weight of graphene with respect to that of TiO_2 averagely deposited (approximately 30 mg in order to obtain sufficient photocatalytic activity). In this case the deposition is accomplished by centering the syringe needle on the metallic annulus on which the polymer nanofibers are deposited using a coaxial displacement with air jet on the outer side of the coaxial device which helps to center the jet of particles and to improve their fine dispersion. In this manner there is a central needle with a 0.7 mm of internal diameter (i.d.) from which the ethanol/graphene suspension is ejected and an external needle of 1.2 mm of i.d. which enfolds the previous one: from the annulus created by the two needles the air is ejected.

Table 6.5: *Electrospraying parameters for the deposition of G+TiO_2 nanoparticles from an ethanol suspension*

Flow rate [ml/h]	Voltage [kV]	Distance [cm]	Needle diameter [mm]	Deposition time [min]
4.5	15	12	0.7	6

Once deposited the graphene on the surface of the membranes follows the deposition of TiO_2 with the same operative conditions described in §6.2.2.1. In this manner it is possible to obtain a polymeric support on which both graphene and titania are overlapped. It has been chosen to use this sequence of deposition since the catalytic activity is provided only by titania which, in this configuration, is completely accessible to the organic pollutant. The graphene, which has not directly photocatalytic activity, is anyway in close contact with TiO_2 acting as enhancer of its performance.

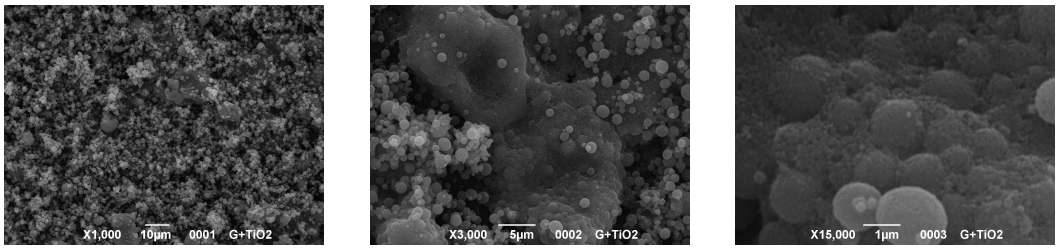

Figure 6.8: *Electrosprayed graphene+TiO_2 photocatalyst at different magnification: (a) 1,000X, (b) 3,000X and (c) 15,000X*

6.2.2.3 *Deposition of reduced graphene oxide and TiO_2*

In this case the catalyst is prepared according to the procedure described in §5.3.1. TEM micrographs of the composite (Figure 6.9) confirm that graphene is a solid support for TiO_2 nanoparticles. In this manner during the formation of the nanocomposite the TiO_2

1 Pasetto

nanoparticles adheres to the functional groups on graphene oxide plane and graphene oxide is reduced to form rGO-TiO_2 composite during the subsequent hydrothermal process [288].
After the hydrothermal treatment it is necessary to stabilize the catalyst particles to avoid their settling thus SDS is added at 1% w/w with respect to the solvent and the suspension so obtained is sonicated for 20 minutes. At the end of the sonication process the suspension is ready to be employed for the electrospraying deposition on the membranes.

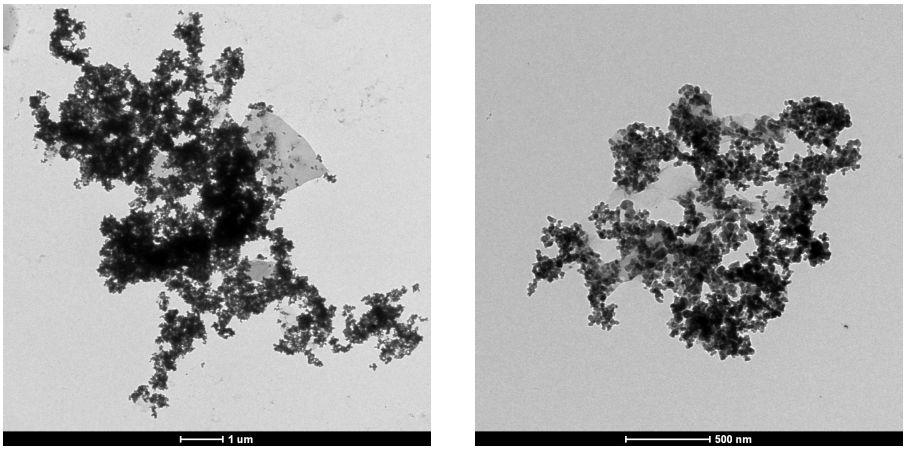

Figure 6.9: *TEM micrographs of two particles of the rGO-TiO_2 photocatalyst in which it is possible to see the deposition of titania nanoparticles on the surface of the reduced graphene oxide sheets: (a) reference bar 1µm, (b) reference bar 500 nm*

The deposition of the catalyst particles is accomplished with parameters reported in Table 6.6 while the needle of the syringe is centered on the annulus of the membrane. Even

Table 6.6: *Electrospraying parameters for the deposition of rGO-TiO_2 nanoparticles from an water/ethanol suspension*

Flow rate [ml/h]	Voltage [kV]	Distance [cm]	Needle diameter [mm]	Deposition time [min]
6	15	12	0.7	40

in this case the deposition in accomplished with a coaxial device where the suspension is ejected from a needle with a 0.7 mm i.d. inside the external needle of 1.2 mm i.d..

6.2.3 Photocatalytic membranes production

The realization of the membranes in PSU is accomplished with the parameters described in Table 6.3 while in Table 6.7 are present the optimized operative conditions defined from a previous thesis work with reference to the production of PAN nanofibers [360].
In this case the electrospinning of the polymer is carried for 60 minutes. The starting solution has a PAN concentration of 5% w/w in DMF. Using the methods described in the

Table 6.7: *Electrospraying parameters for the electrospinning of PAN nanofibers*

Flow rate [ml/h]	Relative humidity [%]	Voltage [kV]	Distance [cm]	Needle diameter [mm]
2	50	15	25	0.4

previous paragraphs four different membranes have been prepared for the experimental tests:

- PSU membranes with TiO_2
- PAN membranes with TiO_2
- PAN membranes with graphene and TiO_2
- PAN membranes with reduced graphene oxide and TiO_2

The different types of membranes are compared in Figure 6.10.

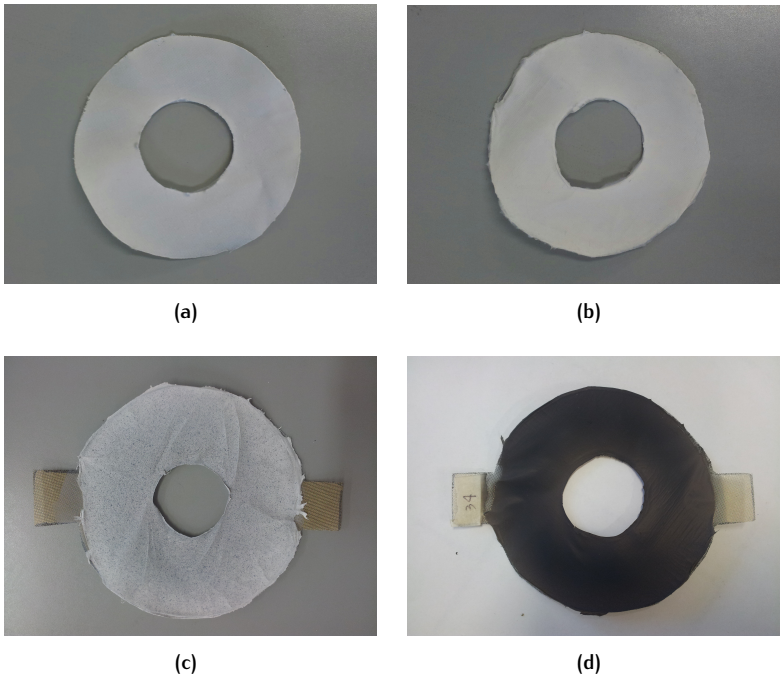

Figure 6.10: *The membranes produced for the photocatalytic tests: (a) PSU with TiO_2, (b) PAN with TiO_2, PAN with graphene and TiO_2, (c) PAN with graphene and TiO_2 (d) PAN with reduced graphene oxide and TiO_2*

In the first two type of membranes the only difference is the polymeric support while the procedure adopted is the same: electrospinning of the polymeric support followed by the deposition of the catalyst (TiO_2). The third typology is realized by the deposition of the nanofibers followed by the deposition of graphene and TiO_2 in this sequence. The last typology is obtained with the spraying of the rGO-TiO_2 composite on the surface of the PAN nanofibers.

6.2.4 Membrane characterization

The different membranes typologies have been analyzed morphologically by SEM and TEM and by thermogravimetry of a complete membrane before and after the photocatalytic test inside the reactor for comparison. The result of the morphological analysis are useful to assess the deposition of the photocatalyst and its eventual agglomeration as well as the extent of the contact between the catalyst and the co-catalyst according to the different procedures followed for their coupling while by evaluation of the residual weight with TGA it is possible to obtain the amount of catalyst deposited on the polymeric support for the comparison of the performances of the different types of membranes.

6.2.4.1 *PSU membranes with TiO_2 (PSU/TiO_2)*

The first type of membranes which have been analyzed are the PSU/TiO_2. As can be seen from the Figure 6.11 the minimum amount of catalyst which is necessary to employ to provide enough photocatalytic activity leads to the covering of the superficial nanofibers as well as partial clogging of the space between the fibers. In this manner it is possible to provide an higher contact time between the pollutant and the catalyst to improve the chances to start the photocatalytic reaction.

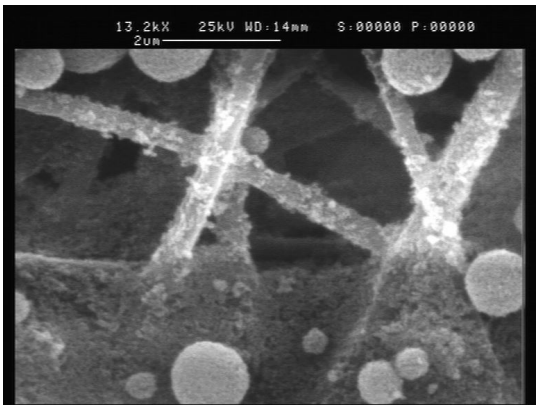

Figure 6.11: *SEM micrograph of PSU/TiO_2 membranes*

Figure 6.12a presents the thermogram of two different membranes, to evaluate the homogeneity of the photocatalyst distribution by the electrospraying process. Moreover the same analysis has been carried even after use to assess the stability of the nanoparticles adhesion on the surface of the polymer nanofibers.
From the analysis carried by TGA (Table 6.8) a significant difference is noted between the residues of the TGA analysis before and after the photocatalytic tests. The calculated increase in the residue after the tests do not concern the adhesion of the nanoparticles on the membranes surface, that if altered could only decrease the final residue. The higher residue is then ascribed to a partial degradation of the polymer during the exposition to the UV light justified by the lower onset temperature for the degradation of the membranes and a yellowing of their surface after the tests. This degradation process leads to the formation and release of gaseous products and decrease the final content of polymer

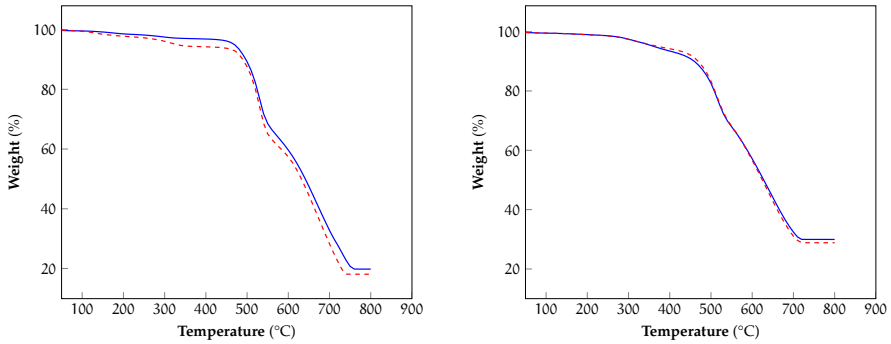

Figure 6.12: *TGA of PSU+TiO_2 membranes for the determination of the amount of catalyst deposited by electrospraying: (a) analysis of two membranes before the reaction, (b) analysis of two membranes after the reaction*

in membranes, increasing the percentage of the inorganic content. A detailed description of the phenomena involved and the mechanism for the degradation is presented in §6.3.2.

Table 6.8: *Amount of catalyst deposited on PSU/TiO_2 membranes for the photocatalytic tests from TGA analysis*

Sample	Catalyst for single membrane [mg]	Catalyst for a set of membranes [mg]	Specific amount of catalyst (10^3) [g/cm^2]
PSU/TiO_2	27.5 ± 3	137.25 ± 16	0.42 ± 0.05

The average amount of catalyst as reported in Table 6.8 is approximately 27.5 mg which correspond to an average total content of 137.5 mg for a set of five membranes (330 cm^2 of total surface) and a specific quantity of 0.42 mg/cm^2 of membrane surface.

6.2.4.2 *PAN membranes with TiO_2 (PAN/TiO_2)*

These membranes have been produced by depositing only the titania nanoparticles on the surface of PAN fibers with the parameters previously described (§6.2.2.1). The deposition of the photocatalyst is straightforward and the final morphology (Figure 6.13) is essentially the same as seen in the previous case for the PSU membranes.
Figure 6.14 presents the thermograms for the comparison of the membranes while Table 6.9 reports the exact catalyst quantity (TiO_2) deposited.
In this case the membranes start their degradation at 300°C as consequence of the lower thermal stability of the polymeric support. The percentage amount as well as the final absolute quantity of catalyst is higher than the previous case due to differences in the electrospinning solutions and process conditions for the two different polymers (PAN and PSU) which have led to a different amount of polymer deposited on the membranes support, but with final comparable quantities of catalyst.

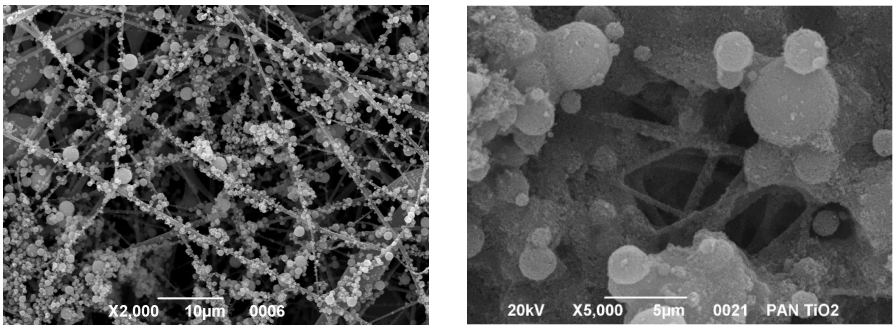

Figure 6.13: *SEM micrograph of PAN/TiO_2 membranes: (a) surface of the membrane, (b) particular showing the deposition of the photocatalyst on the nanofibers*

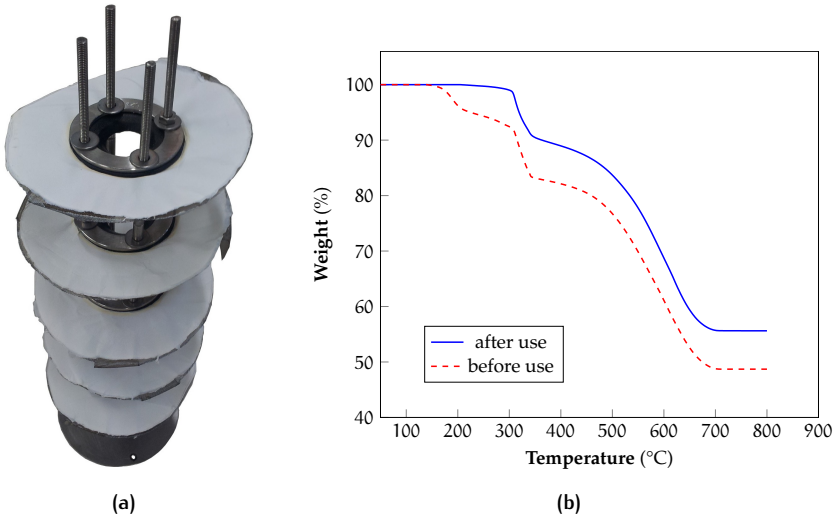

Figure 6.14: *TGA thermograms of PAN/TiO_2 membranes before and after use (the mass loss for the membrane before testing is attributed to solvent evaporation, which starts after 150°C, in accordance to its boiling temperature)*

Table 6.9: *Amount of catalyst deposited on PAN/TiO_2 membranes for the photocatalytic tests from TGA analysis*

Sample	Catalyst for single membrane [mg]	Catalyst for a set of membranes [mg]	Specific amount of catalyst (10^3) [g/cm^2]
PAN/TiO_2	39.75 ± 1	198 ± 5	0.60 ± 0.01

6.2.4.3 *PAN membranes with grafene and TiO_2 (PAN/G+TiO_2)*

These membranes are prepared according to the procedure reported in §6.2.2.2 with a first layer of PAN nanofibers as support, a second layer of graphene sheets and a third layer of titania.
SEM micrographs (Figure 6.15) do not show morphological difference in terms of deposition, with respect the typical behavior of TiO_2 nanoparticles, since the composite had

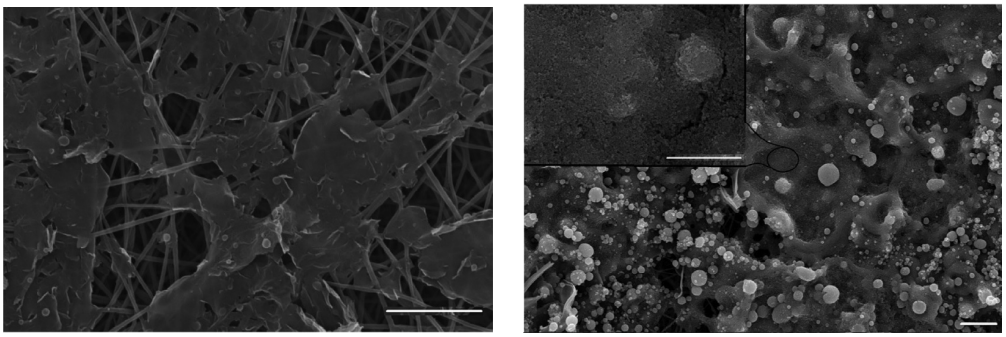

(a) (b)

Figure 6.15: *SEM micrographs of: (a) graphene layer electrosprayed over electrospun nanofibers (dimensional bar scale 5μm); (b) TiO_2 nanoparticles spread over graphene layer (dimensional bar scale 10μm) and in the left corner higher magnification (bar scale 5μm)*

the same tendency to create cluster over the nanofibers. The morphological difference

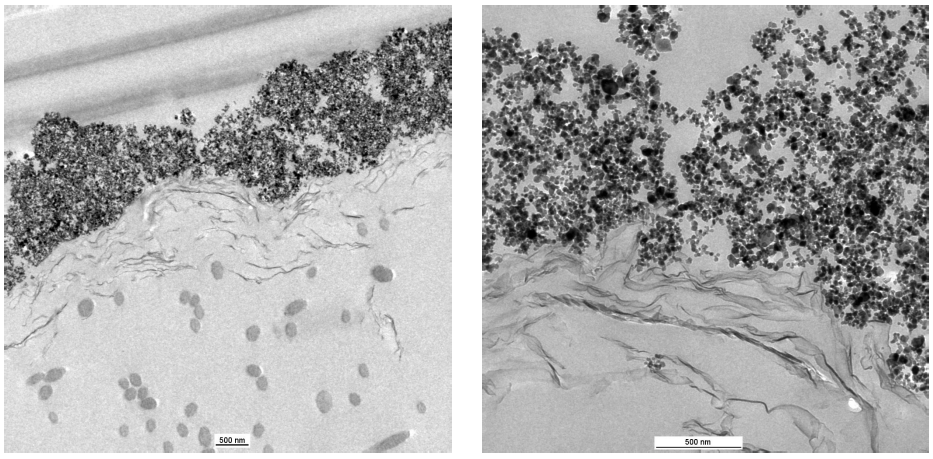

(a) (b)

Figure 6.16: *TEM micrography of: (a) membrane with graphene and TiO_2 (dimensional bar equal to 500 nm); (b) particular of the titania layer deposited on graphene sheets (dimensional bar equal to 500 nm). Both the images are taken along the cross-section of the membrane*

among the membranes can be better appreciated by performing TEM analysis. Figure 6.16 shows the TEM micrographs of the membrane along its cross-section. According to the procedure followed the surface of the polymeric nanofibers (spherical shape within the grey matrix) is covered by the folded sheets of graphene upon which are deposited the titania nanoparticles. In these case from the TGA thermograms (Figure 6.17) the average amount of titania on the membranes employed is 24.7 mg which is less then the previous cases. The membranes tested thus present a total amount of titania equal to 123.5 mg and a specific amount per unit of surface of $3.7 \cdot 10^{-4}$ g/cm^2 (Table 6.10).

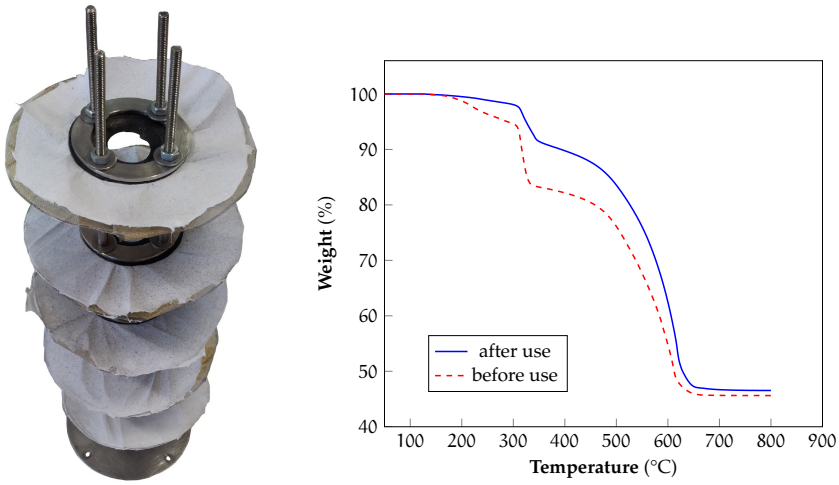

Figure 6.17: *TGA thermograms of PAN/G+TiO_2 membranes before and after use (the mass loss for the membrane before testing is attributed to solvent evaporation, which starts after 150°C, in accordance to its boiling temperature)*

Table 6.10: *Amount of catalyst deposited on PAN/G+TiO_2 membranes for the photocatalytic tests from TGA analysis*

Sample	Catalyst for single membrane [mg]	Catalyst for a set of membranes [mg]	Specific amount of catalyst (10^3) [g/cm^2]
PAN/G+TiO_2	24.7 ± 0.7	123.5 ± 3.3	0.37 ± 0.01

6.2.4.4 *PAN membranes with reduced graphene oxide and TiO_2 (PAN/rGO-TiO_2)*

The last type of membranes realized have been produced by a single electrospraying step (§6.2.2.3) of the photocatalyst obtained by hydrothermal treatment.

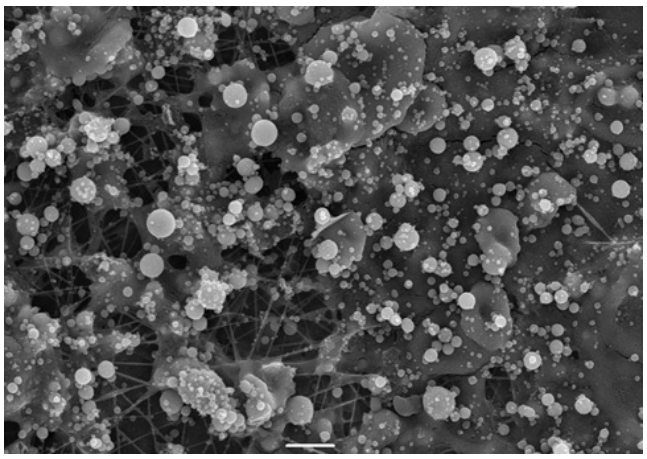

Figure 6.18: *SEM micrograph of rGO-TiO_2 membrane (dimensional bar scale 10 μm)*

SEM micrographs (Figure 6.18) do not show morphological difference in terms of depo-

sition, with respect the typical behavior of TiO_2 nanoparticles, since the TiO_2/graphene composite had the same tendency to create cluster over the nanofibers. The morphological difference among the membranes can be better appreciated by performing TEM analysis. Figure 6.19 shows the TEM micrographs of the membrane along its cross-section. At low magnifications it is not possible to distinguish all the components which are, however, clearly visible at higher resolution. In this case the graphene sheets are more dispersed in the composite and the titania nanoparticles are also partially deposited along the interfiber spaces.

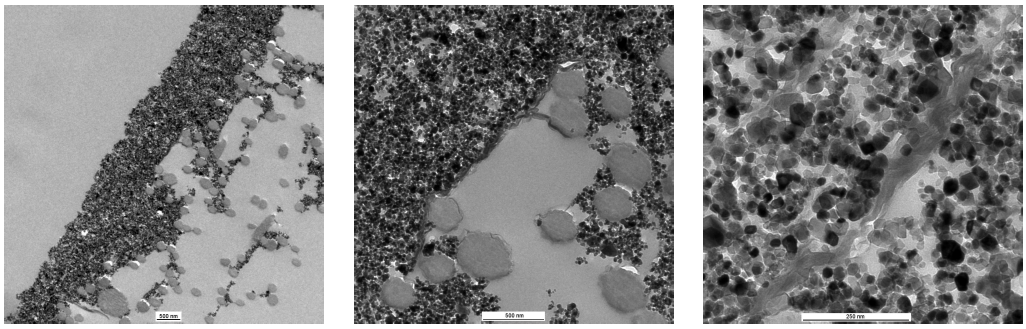

(a) (b) (c)

Figure 6.19: *TEM micrographs of a PAN membranes with reduced graphene oxide and titania: (a) cross-section of the membrane with the visibile distinction between the catalyst layer and the fibers below (dimensional bar equal to 500 nm), (b) same cross-section at higher magnification (dimensional bar equal to 500 nm); (c) particular of graphene sheets embedded in the catalyst layer and in close contact with titania*

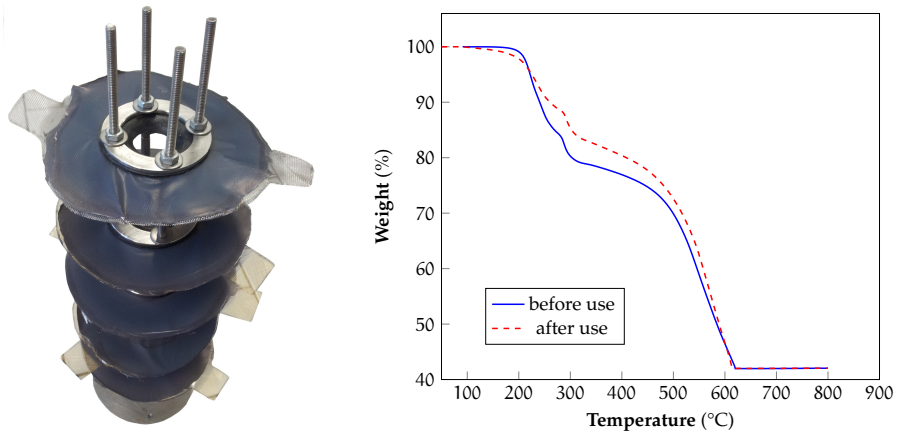

(a) (b)

Figure 6.20: *TGA thermograms of PAN/rGO-TiO_2 membranes before and after use*

The TGA analysis (Figure 6.20) present the same final residue both before and after use, confirming the good adhesion of the catalyst on the membrane and the higher reproducibility of the electrospraying process by employing a coaxial device for a deposition aided by compressed air. The thermal degradation of the membranes, starts at lower temperatures

Table 6.11: *Amount of catalyst deposited on PSU/TiO_2 membranes for the photocatalytic tests from TGA analysis*

Sample	Catalyst for single membrane [mg]	Catalyst for a set of membranes [mg]	Specific amount of catalyst (10^3) [g/cm^2]
PAN/rGO-TiO_2	36.2 ± 0.7	181 ± 3.5	0.55 ± 0.01

than the previous cause and the first degradation step is more pronounced due to the partial reduction of the graphene oxide and thus its lower thermal stability compared to pure graphene. The amount of the catalyst deposited is shown in Table 6.11.

6.3 PHOTOCATALYTIC TESTS FOR METHANOL ABATEMENT

Herein are summarized the results of the photocatalytic tests conducted in batch mode, with the membranes previously characterized, towards the abatement of methanol. The results of each set is presented and analyzed over at least three days and finally a comparison between the different membranes has been done to evaluate potential improvements due to the addition of graphene with different degree of contact with the reference catalyst. The only exception is represented for the case of PSU membranes were only the test at the third day of reaction is presented due to problem of polymer degradation under UV irradiation.

6.3.1 Introduction to the photocatalytic activity tests

6.3.1.1 *Irradiance measurements*

The performance of an UV lamp may vary depending on several factors and irradiance measurements are important to assess the amount of light which arrives on the surface of the photocatalyst to activate the chemical reaction for the degradation of the organic pollutant and to determine the quantum efficiency of the process. The lamp employed for the photocatalytic tests for the degradation of methanol is a UV-Stylo E16 (Light Progress). The light intensity measurements of the lamp employed for the experiment have been carried with an HD9021 photoradiometer (Deltaohm) equipped with an LP 9021 UVC photometric probe for measuring the radiation in the ultraviolet region C. The probe has been specifically chosen in order to evaluate the emission at a desired wavelength. All the measurements have been collected after having warmed up the lamp for 5 minutes to reach a steady-state emission condition and with the lamp enclosed into its quartz protection tube. It is a low pressure mercury vapor lamp (Figure 6.21) which has a power of 16 W and the radiation produced has a maximum peak of emission around 254 nm, inside the range of the UV-C spectrum. For this lamp irradiance measurements with two different configurations have been carried out: in the first configuration the probe has been positioned perpendicular to the body of the lamp in order to evaluate the amount of light

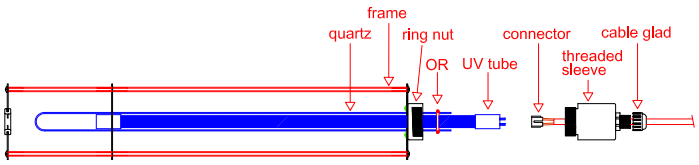

Figure 6.21: *Schematic of the lamp employed for the photocatalytic tests*

which hits the surface of the membranes as compared to a second configuration in which the probe is positioned in front of the body lamp, a traditional arrangement for photocatalysis. In each case eleven measurements have been done along the length of the lamp from the top to its bottom, each at a distance of 3 cm from the previous one in order to evaluate the irradiance along all the lamp length (30 cm). For each disposition the sensor has been placed along a rail at a constant distance of 2.5 cm from the lamp axis, which is approximately the distance of the lamp from the reactor walls. The output of the measurements have been multiplied for a correction factor, k_r (with $k_r = 1.54$), to take into account the fact that the sensor calibration is made on a large band spectral width (from 220 to 280 nm) rather than on the desired wavelength of maximum emission. The instrumental uncertainty is calculated to be 7.2%. By considering that the membranes set placed into the reactor is at a length between 6 and 24 cm of the body lamp, the mean irradiance flux using the first configuration is calculated as 1.35 W/m^2.

In the second configuration, by calculating the integral mean of the light flux between

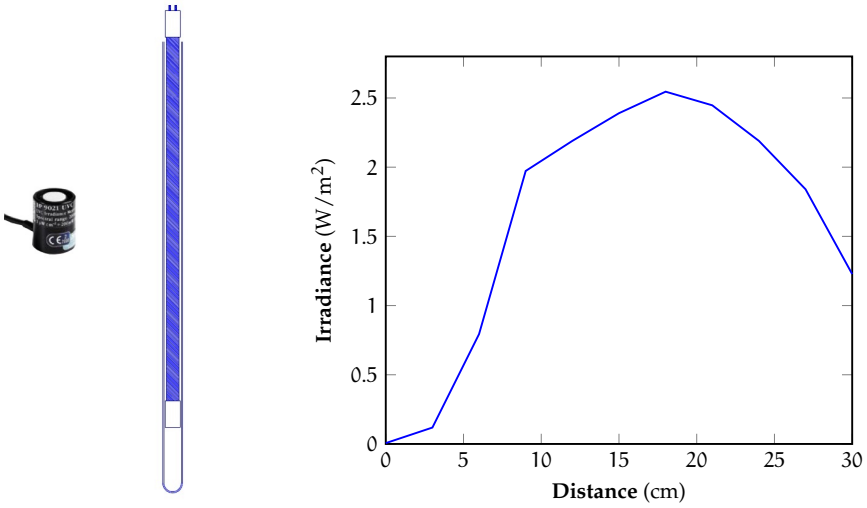

Figure 6.22: *Irradiance flux measurement for the second disposition of the sensor perpendicular to the axis of the lamp: (a) sensor position with respect of the lamp axis, (b) measured irradiance along the lamp axis*

the same extremes of the body lamp, the irradiance is 13.84 W/m^2. Obviously in both cases the amount of radiative flux is higher far from the lamp electrodes but for the first configuration the flux is much more homogeneous along the lamp. The curve shown in

Figure 6.22 presents a null irradiance value at the top of the lamp and progressively increase up to a maximum around the center of the lamp and then slightly decrease but does not return to a null value because of the particular disposition of the sensor that at the bottom of lamp receive part of the radiation emitted in the upper part. In the second configuration (Figure 6.23) the flux is asymmetric and the values are higher in the upper part of the lamp probably due to the high operative time of the lamp and partial damaging of the quartz cover.
From these results it is possible to observe a marked difference between the amount of light which arrives on the probe surface between the two configuration. In first configuration, which is adopted for the photocatalytic experiments in this work, the total irradiance is about ten times lower than the front configuration.

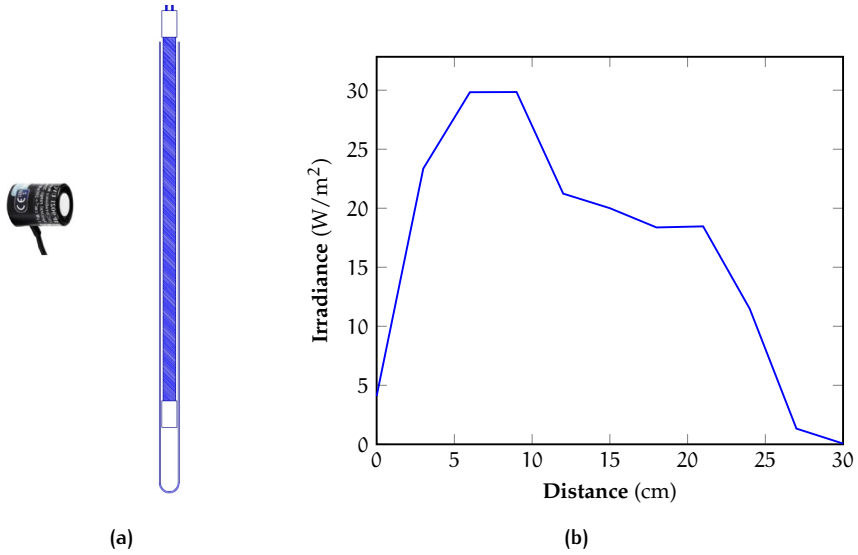

Figure 6.23: *Irradiance flux measurement for the second disposition of the sensor in front of the lamp: (a) sensor position with respect of the lamp axis, (b) measured irradiance along the lamp axis*

According to IUPAC [361], the photon irradiance (in $m^{-2} \cdot s^{-1}$) is defined as the numbers of photons per time interval (photon flux), incident from all upward directions on a small element of surface containing the point under consideration divided by the area of the element. In this case by considering the emission of photons at the single wavelength of 254 nm and using the Planck-Einstein relationship the energy of a single photon can be calculated to be $7.39 \cdot 10^{-19}$ J; thus, from the irradiance measurements it is possible to calculate the theoretical number of photons that hit the unit of sensor surface per unit of time (photon flux).

The configuration adopted in this work thus suffers of a low photon flux but at the same time this disposition allows higher contact times with the pollutant that is forced to pass through the membranes (especially by working in continuous but as well in batch mode by appropriate devices for forced convection), easy recovery of the photocatalyst and substitution of the photocatalytic membrane filters.

Table 6.12: *Results of the irradiance measurements for the two different configuration employed*

Configuration	Mean irradiance [W/m^2]	Photon flux [10^{-6} moles/(m^{2}s^1)]
Perpendicular	1.35	3.03
Frontal	13.84	31.1

6.3.1.2 *GC-MS*

The withdrawals have been analyzed by a gas chromatography-mass spectroscopy apparatus. The settings employed for the analyses comprised an initial isotherm at 32 °C for 6 minutes followed by a ramp at 30°C/min up to 220°C. The final temperature was then maintained for 2 additional minutes. The splitting ratio was 1:55 in order to obtain an optimal separation and resolution of the mass spectral peaks for quantitative purposes. The injection system is comprised of 500 µl loop. The analyses have been conducted in SIR (*Selected Ion Recording*) mode with 4 channel, choosing the quant ions 29 and 31 for methanol and 44 for carbon dioxide. The quant ion 29 is present both in the breaking of the methanol molecule and that of formaldehyde and methyl formate. In order to distinguish those compounds it has been necessary to add the quant ion 60 which, in this case, univocally distinguish the methyl formate.
For a quantitative analysis it has been necessary to determine a calibration line for the determination of the initial concentration of methanol in the reactor and the evaluation of the number of moles reacted. The methyl formate has not been quantified due to the low amount formed during the reaction which has prevented the possibility to obtain a correct calibration line. For the purposes of the study its evolution during the reaction has been analyzed only qualitatively.

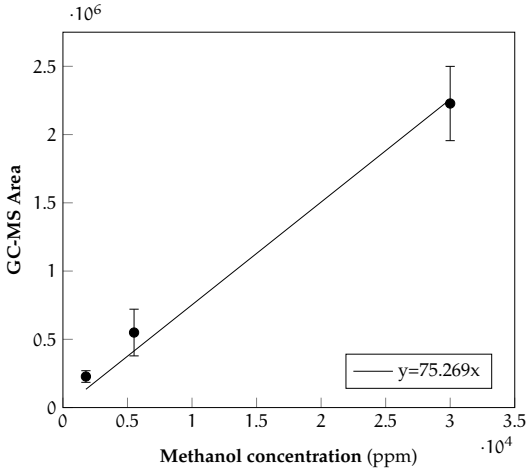

Figure 6.24: *GC-MS calibration line for methanol*

Figure 6.24 shows the calibration line obtained from the GC-MS instrument for methanol. The line has been obtained by measuring the area of the peak relative to six different gaseous mixture of methanol in equilibrium with the pure liquid, kept at three different

temperatures (-4, -27 and -40°C respectively). By knowing the temperature of these mixtures it has been possible to determine the concentration of methanol at the equilibrium and to associate this value to the peak area determined by GC-MS. The molar fractions of methanol in gas phase at the equilibrium are calculated by the Raoult-Dalton equation:

$$y_i P = \gamma_i x_i P_i^{sat}(T) \tag{6.1}$$

in which y_i is the molar fraction of the i-th compound (in this case methanol) in vapor phase, P is the system pressure (in this case considered as the atmospheric pressure), γ_i is the activity coefficient of the i-th compound, x_i is the molar fraction of the i-th compound in liquid phase and P_i^{sat} is the vapor tension at the given temperature. For the calculation of the latter the parameter in the simulation software ProII have been employed. Since the liquid phase is pure methanol, x_i and y_i are equal to 1 and the previous equation can be reduced to:

$$y_{MeOH} = \frac{P_{MeOH}^{sat}(T)}{P} \tag{6.2}$$

After the obtainment of the calibration line from the fitting of the experimental data it is possible to determine the unknown concentration of methanol by simply measuring the relative peak area from the chromatogram.

6.3.1.3 *Photocatalytic reactor*

The scheme of the reactor layout (Figure 6.25) is made up of a technical grade air line controlled by digital mass flow controller (Bronkhorst) which controls the air entering into a gas bubbler containing the liquid pollutant which is maintained at 0°C thanks to an iced water bath contained into in insulating container. The temperature has been set

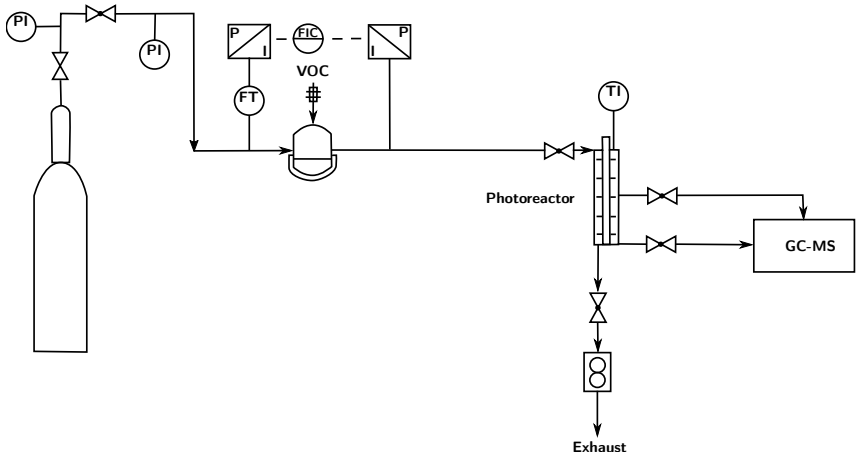

Figure 6.25: *Layout of the experimental set-up for the photocatalytic tests (PI = pressure indicator, FT = flow transducer, FIC = flow indicator-controller, TI = temperature indicator)*

constant at that value in order to avoid excessive vaporization of the pollutant and control

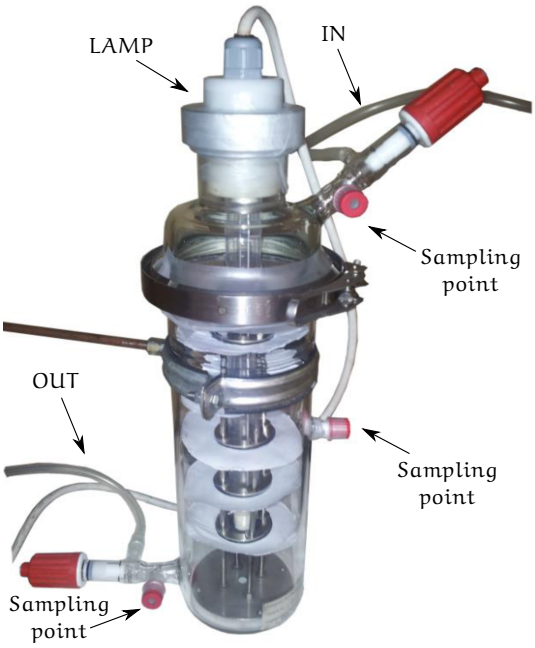

Figure 6.26: *Reactor employed for the photocatalytic tests*

its concentration by controlling the air volumetric flow. After being enriched by the vapors of the volatile organic compound the mixture is sent into the reactor where the membranes and the light source is placed. With this configuration the level of the pollutant prevent the bubbling of the liquid and the air simply transport the vapors formed in the gas phase. The molar fraction of methanol present in air is always lower than the equilibrium value thanks to the molecular diffusion of the same pollutant at the liquid-gas interface, which represents an internal resistance for this transport. In this manner the quantity of methanol in air depends on the vapor tension of the pure liquid, the diffusion coefficient of the pollutant in air and on the distance between the liquid level in the glass container and the point where the gas flow passes in the container.

The reactor employed is shown in Figure 6.26 and it is a cylindrical container in Pyrex with an inner diameter of 10 cm and an height of 37 cm. Its maximum volume is of 2780 cm^3. By observing the figure it is possible to observe that the reactor is made of two parts completely separable one from the other and hold together thanks to a clamp. At the bottom a scaffold holding the membranes is inserted; the membranes are fixed by using steel disks, properly coupled and separated by a rubber gasket, of 2.7 cm of diameter with four lateral holes of 2 mm of diameter. The employment of the scaffold and of the disks allows to choose the number of membranes to use and the distance between each other can be varied as desired. From the top of the reactor the lamp is fixed by a ring nut, in this manner the lamp is inserted coaxially with respect to the reactor position, minimizing the distance between the catalyst deposited on the membranes and the light source. The gaseous flux is introduced from the top of the reactor and exits from the bottom passing through all the membranes which have been inserted: in this manner the gas stagnation phenomena are limited and the formation of preferential paths is prevented. Gas leaks are avoided by using a proper gasket between the two halves of the reactor. Both the

entrance and the exit of the reactor are provided with a sampling port in order to carry the withdrawals. Two taps, at the entrance and at the exit, are present in order to close hermetically the reactor and to switch from a continuous configuration for the conditioning phase to the final batch configuration.

6.3.1.4 *Elaboration of the experimental data*

As previously anticipated, the tests have been conducted in batch mode and before the beginning of the reaction a conditioning phase has been necessary in order to allow the adsorption of methanol on membranes surface. In particular, a flux of contaminated air has been fluxed inside the reactor from top to bottom by opened discharge valves, using a flow-rate of 150 cm^3/min for an average time of 150 min. At this point, for the setup considered, the methanol concentration inside the reactor is statistically homogeneous [360], thus the valves are closed and the lamp is turned on to begin the reaction. However, before this last step, a sample of the gaseous mixture is collected from the center of the reactor in order to define the initial concentration for the calculation of the pollutant conversion over time. Below are reported the procedure employed for the calculation of results that will be showed in the following sections for all the type of membranes that have been employed.

- Calculation of the methanol molar fraction: this quantity evaluates the initial molar fraction of methanol at the end of the conditioning phase once the reactor has been switched into batch mode, before lighting the UV lamp. The concentration at the time t = 0 s is calculated by a calibration line obtained from §6.3.1.2:

$$y_{MeOH} = k \cdot A_{MeOH,0} \tag{6.3}$$

  where y_{MeOH} is the initial gas molar fraction of methanol inside the reactor, $A_{MeOH,0}$ is the area below the peak of methanol which corresponds to the first withdrawal (t = 0 s) obtained from the GC/MS and k is the correlation coefficient between the molar fraction and the peak area. The same procedure has been employed for the calculation of the molar fractions at every time interval correspondent to a withdrawal.

- Determination of the methanol conversion: once calculated the molar fractions at each withdrawal time with the method previously described it is possible to proceed with the determination of the methanol conversion to evaluate the extent of its degradation. The conversion is:

$$X_{MeOH} = \frac{y_{MeOH,0} - y_{MeOH,i}}{y_{MeOH,0}} \tag{6.4}$$

  where $y_{MeOH,i}$ is the molar fraction of methanol at the time instant i.

- Normalization of the results per gram of catalyst: in order to compare the results obtained with the different types of membranes realized it is necessary to normalize the data as a function of the catalysts amount of each membranes set.
  The first operation consists in the determination of the initial methanol moles inside

the reactor at each instant of time; the molar fraction of pollutant is then multiplied by the total number of moles present inside the reactor. Due to the low concentrations involved the total amount of moles have been considered constant during all the reaction time. For the calculation of the moles the ideal gas law can be employed:

$$n_{TOT} = \frac{PV}{RT} \tag{6.5}$$

where V is the reactor volume (2780 cm^2), R is the ideal gas constant (8.314 J/mol·K) and T is the temperature in Kelvins. To this purpose the temperature inside the reactor has been monitored during the reaction once that the lamp has reached a steady-state condition, giving a mean value of 323.15 K (50°C).
Once obtained the initial number of moles at each instant of time it is possible to calculate the amount of moles reacted:

$$n_{reag,i} = n_{MeOH,0} - n_{MeOH,i} \tag{6.6}$$

where $n_{MeOH,0}$ are the initial moles of methanol and $n_{MeOH,i}$ are the moles at the generic i-th time instant. At this point the reacted moles per gram of catalyst can be easily determined ($\hat{n}_{reag,i}$):

$$\hat{n}_{reag,i} = \frac{n_{reag,i}}{g_{cat}} \tag{6.7}$$

where g_{cat} are the grams of catalyst present on a membranes set.

The test are carried for five hours at the end of which the reactor is evacuated from the gaseous mixture by opening the sampling doors at bottom and the top. The subsequent day the conditioning step is performed again until reaching a steady-state condition before closing the reactor and starting the reaction. These operation have been replied for each set of membranes.

6.3.2 PSU/TiO_2 membranes

The first set of membranes tested have been those employing TiO_2 electrosprayed nanoparticles deposited on PSu nanofibers. The results of the tests are summarized in Figure 6.27 which shows the degradation of methanol during the third day of tests. It is interesting to note that at the starting of the reaction, immediately after the lighting of the lamp, the concentration of methanol has increased above the initial calculated values; this behavior has been hypothesized to be related to methanol-desorption, which is predominant to the degradation process in the first stage of the photocatalytic reaction. The membranes show a slow degradation rate which determine a decrease of the methanol to the starting value after 2 hours and a final conversion of 24% after 300 minutes of reaction. A possible explanation of the poor perfomances of this type of membranes can be ascribed to the significant yellowing of the membranes surface seen at the end of the tests, symptomatic

of a degradation phenomenon. Indeed, despite its remarkable mechanical strength and

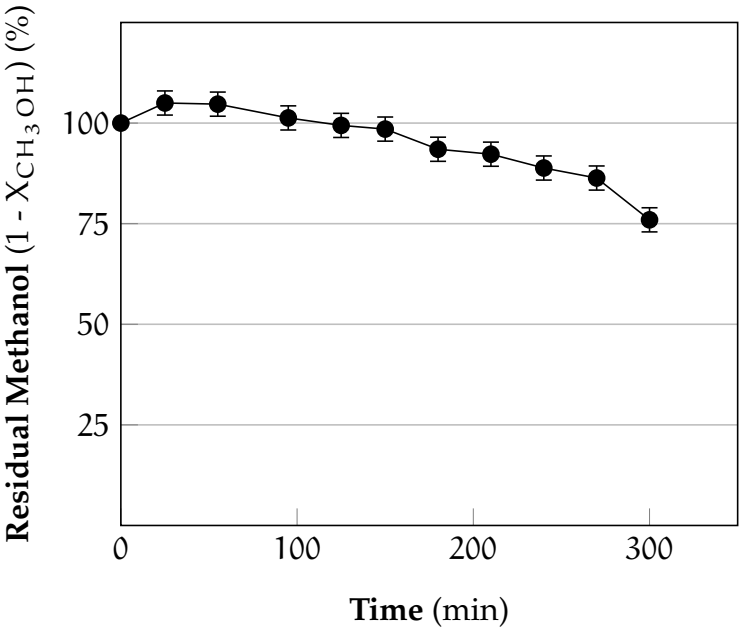

Figure 6.27: *Time evolution of the percentage of residual methanol for the tests for the PSU/TiO_2 layer-by-layer membranes during the third day of tests*

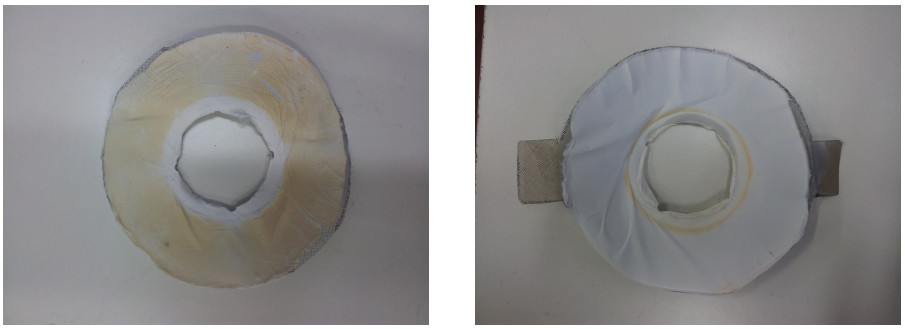

Figure 6.28: *Membranes of (a) PSU and (b) PAN with TiO_2 after the degradation test of methanol under UV-C radiation*

thermal stability PSU suffers of low resistance to the UV radiation, As outlined by Van Krevelen *et al.* [362]. Rivaton *et al.* (1999) [363] have hypothesized the possible mechanism of PSU degradation, which can be summarized into four principal events (Figure 6.29):

- the absorption of radiation in the ultraviolet spectrum leads to photolysis and photo-reduction of the dyphenyl-solfonic part of the aromatic polymeric chain with subsequent formation of benzensulfonic acids; this is due to the breaking of the C-S bonds. Other products of degradation are the cross-linked polyphenyls which explain the red shift in the absorption of the material under light;

- the breakage of the C-O bond by means of a photo-dissociative process which leads to the formation of fluorescent molecules at low molecular weight like phenolic groups. This is followed by the extraction of the hydrogens chain and photo-Claisen re-arrangement of aromatic ethers

- SO_2 has been identified between the photo-degradation process and this is important because of the increasing degradation of aromatic polymers in presence of sulfur dioxide;

- methane has not been detect between the degradation products showing how the part of the polymer deriving from the bisphenol A it has not negative influence in the photolytic process.

Finally it has been observed that the exposition of the membrane surface at low wavelength (254 nm as in this work) leads to the complete absorption of the radiation by the chromophore aromatic groups. From these results it is possible to conclude that the low conversion of methanol is due to all the reactions that involve the degradation of PSU, which are photo-oxidative in nature and compete with the reactions of photo-degradation of the pollutant.

As can be noticed in Figure 6.28 the difference between the two polymeric matrix (PSU

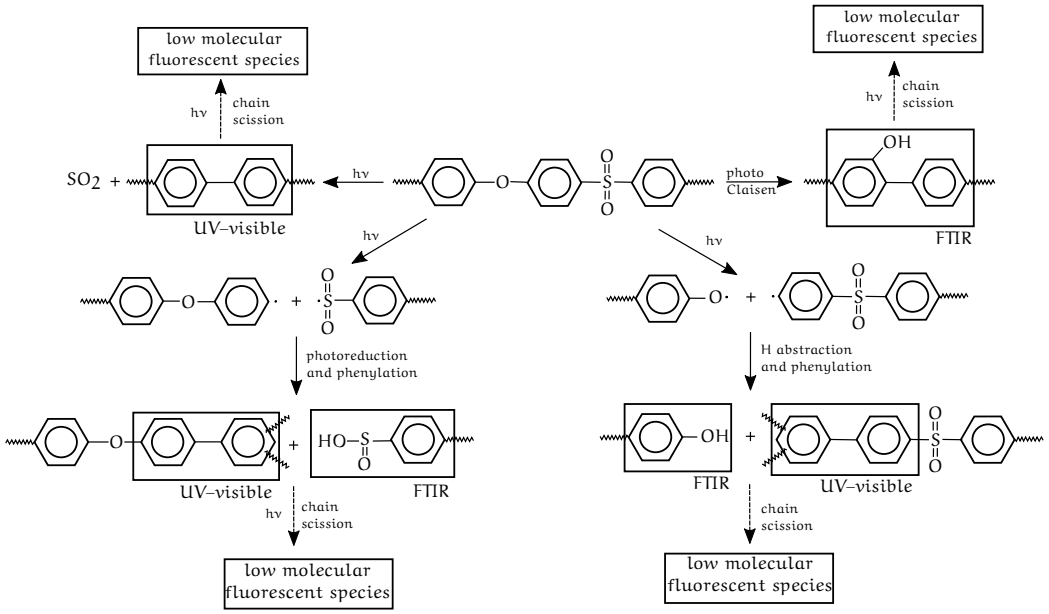

Figure 6.29: *Photolysis of PSU (adapted from Rivaton et al.) [363]*

and PAN) after the photocatalytic tests is significant. For this reason PSU has been discarded as possible matrix and all the other tests with the selected catalytic systems have been realized by using PAN as polymeric support.

6.3.3 PAN/TiO_2 membranes

Herein are reported the results relative to the photocatalytic tests for methanol abatement with the PAN/TiO_2 membranes, realized according to the conditions in §6.2.4.2. The results of three different days of reaction in terms of methanol abatement are reported in Figure 6.30.

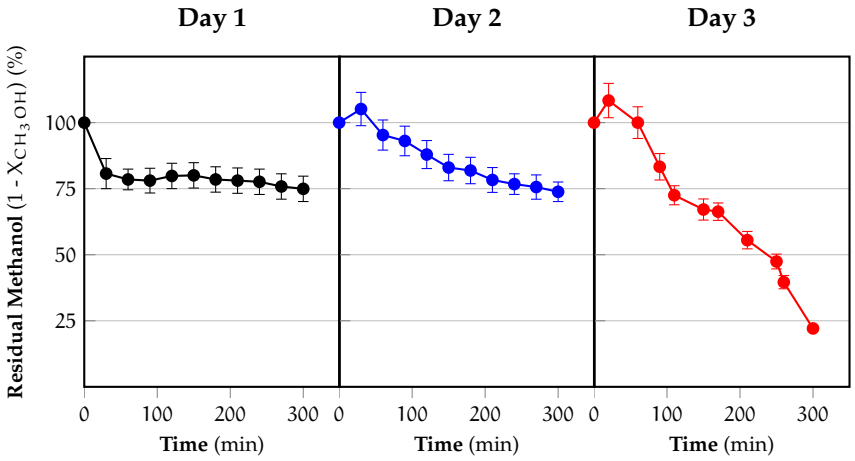

Figure 6.30: *Evolution over time of the percentage of residual methanol in the reactor for the PAN/TiO_2 layer-by-layer membranes in three different days of reaction*

For the first day of reaction the initial concentration inside the reactor has been 3500 ppm and the final conversion reached a stable value of approximately 26% after 300 minutes. In the second day of reaction the starting methanol concentration has been approximately 4700 ppm. In this case there is an initial increase in the methanol quantity just after the beginning of the reaction probably due to heating produced after the lighting of the lamp. The reaction in this case is less fast but the final conversion value is about 28%, very similar to the first day of reaction. The third day provides the best results in terms of methanol abatement with an initial quantity of pollutant equal to 5450 ppm. Even in this case there is an initial increase in the starting concentration of the pollutant after the lighting of the lamp but the degradation rate in much higher and already from the subsequent sampling the concentration is decreased to the initial value. Differently from the previous case here the concentration of methyl formate is null for about 110 minutes, and slightly increase in the following instant reaching a maximum value in the last three samplings. The fact can be explained by considering that at the beginning of the reaction the higher initial rate of the reaction leads to the complete conversion of methanol to carbon dioxide, which is also justified by the fact that during the three days of reaction the starting concentration is higher and thus the higher rate is also related to an higher amount of moles reacted.

6.3.4 PAN/G+TiO_2 membranes

The second series of photocatalytic tests have been carried for the evaluation of the performances of the PAN/G+TiO_2 membranes produced with titania deposited on a layer of

graphene sheets (§6.2.4.3). Differently from the previous tests here the analysis has been carried for a total of four days both for a more in depth control of the photocatalytic activity and to have a more wide evaluation of the conversion trend over the days. Figure 6.31 shows the plot of the percentage conversion of methanol over all the days. During the first

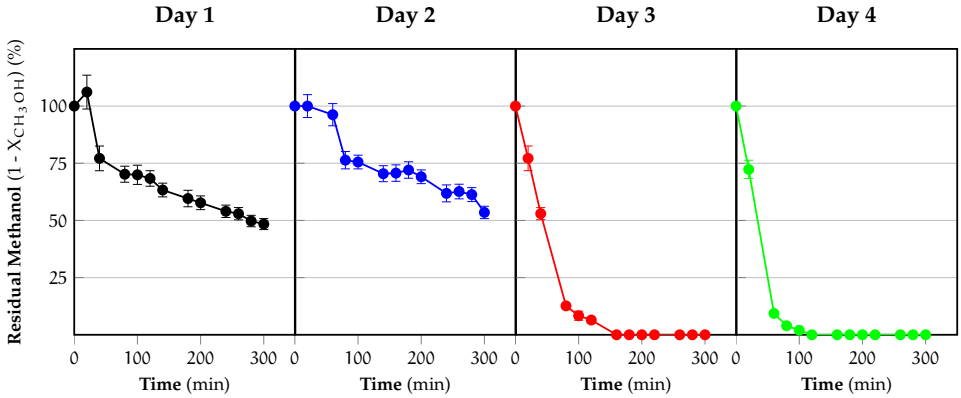

Figure 6.31: *Evolution over time of the percentage of residual methanol in the reactor for the PAN/G+TiO_2 layer-by-layer membranes in three different days of reaction*

day of tests the initial concentration is *ca.* 4700 ppm and the trend of the conversion shows an initial desorption effect due to the heating effect of the UV lamp as noted previously for the PAN/TiO_2. However in the case since the following sampling the concentration decrease well below the initial concentration and subsequently the conversion shows a liner trend over time with a final methanol conversion of 54%. If compared with the first day of reaction of the PAN/TiO_2 membranes, for which the initial concentration was approximately the same, the final conversion is almost doubled showing an net increase in the reaction rate that can be ascribed to the improvement provided by the presence of the co-catalyst. Here the GC-MS have shown the presence of methyl formate since the first samplings as well as a decrease of the carbon dioxide concentration in the reaction in comparison with the previous type of membranes, suggesting a possible modification in the reaction mechanism for the photoxidation of methanol. The second day of reaction shown in Figure 6.31, in which the starting concentration is approximately 4200 ppm, do not display the previously seen increment in the initial concentration, however presents a lower increase in the methanol conversion during the first samplings. The abatement increase subsequently and the final conversion reaches a final values of 50%. A significant improvement has been found during the third and fourth day of reaction, where there is a parallel decrease in the initial concentration (3000 and 3100 ppm) once achieved the equilibrium between the adsorption and desorption processes. In the first case the complete disappearance of methanol is achieved after 160 minutes and the initial concentration is halved after only 40 minutes. A further improvement during the last day of reaction have shown that the complete conversion can be achieved after 120 minutes, confirming the improvement in the reaction rate of the previous results. The increasing trend in the carbon dioxide concentration in the reactor is similar to that seen for the first two days while methyl formate is detected after 120 minutes of reaction and increase subsequently and reaches a constant value up to 300 minutes.

6.3.5 PAN/rGO-TiO_2 membranes

For the last type of membranes in which the rGO-TiO_2 has been employed as photocatalyst and deposited on the PAN nanofibers (see §6.2.4.4), the procedure followed has been similar to previous case with an investigation carried over 4 days of tests. The results are shown in Figure 6.32.

Over the first of reaction the final conversion reached by the membrane has been 46%

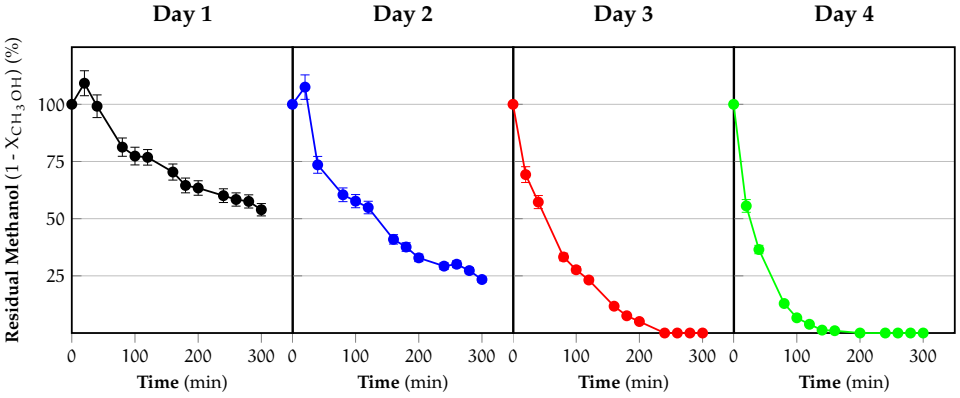

Figure 6.32: *Evolution over time of the percentage of residual methanol in the reactor for the PAN/rGO-TiO_2 layer-by-layer membranes in three different days of reaction*

with an initial concentration of 3550 ppm. In this case there is still a first increase in the methanol concentration at the first sampling which decrease, at the second sampling, to the initial value. The conversion behaves linearly over time and the final value can be considered satisfactory for the first day. From the second day of reaction a progressive increase in the reaction rate can be clearly seen over the days in a manner which is independent from the concentration, which slightly increases from 3500 up to 4200 ppm. The conversion reaches a final value of 77% during the second day, while in the remaining days the methanol in fully converted after 240 and 200 minutes, respectively. Differently from the previous two types the PAN/rGO+TiO_2 membranes present an immediate increase in the methyl formate, whose concentration stabilize after 180 minutes. Carbon dioxide trend is similar to the previous case and reaches a final value which half of the initial concentration of methanol. These evidences underline that altohugh the pollutant has been completely removed, there is not a complete conversion to the products of complete oxidation (H_2O and water) due to the presence of some reaction intermediate.

6.3.6 Comparison between the different photocatalytic membranes

In the present paragraph the results of the performances of the different types of photocatalytic membranes employed (PAN/TiO_2, PAN/G+TiO_2, PAN/rGO-TiO_2) are compared. In order to proceed for this comparison both the conversions obtained during the different days of reaction as well as the moles of reacted per gram of catalyst, calculated as reported in §6.3.1.4, are compared. This last passage is necessary to normalized the results on a common basis not influenced on the initial concentration of pollutant. The

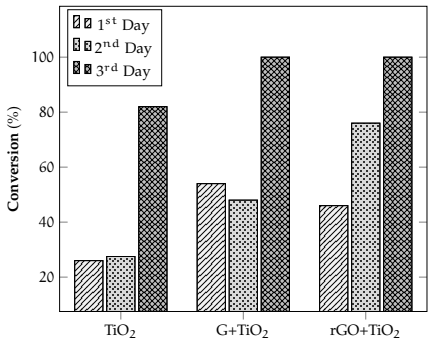

Figure 6.33: *Bar chart for the comparison between the conversion obtained during the days of reaction*

histogram in Figure 6.33 shows the trend of the final conversion of methanol during the days of employment of the membranes, for different typologies at the same reaction time. During the first two days for all the types of membranes it is not possible to obtain the complete degradation of methanol and usually the best performances are obtained in the last day of reaction. This result highlight the necessity for the membranes to be exposed to some hours of UV irradiation before achieving an higher and stable photocatalytic activity.

Figure 6.34 shows the comparison of the results for the different membranes at the third

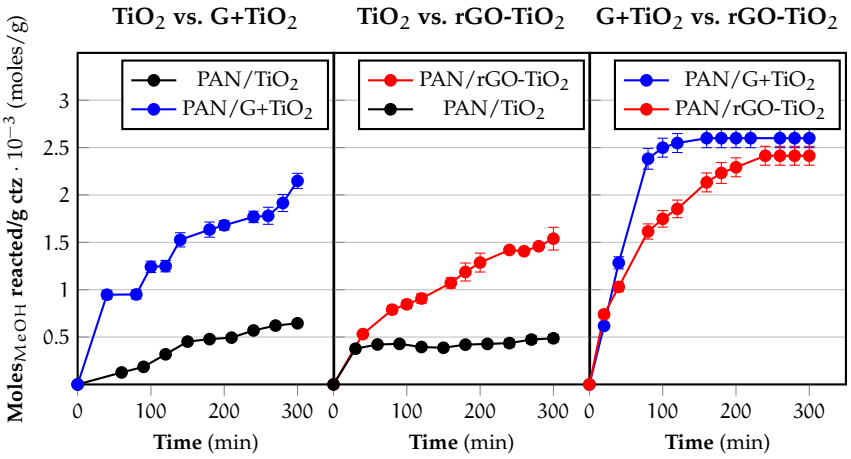

Figure 6.34: *Comparison of the performances of the different types of membranes in terms of moles reacted per gram of catalyst for similar initial concentration of pollutant in the reactor*

day of reaction, where all the membranes have shown an higher photocatalytic activity, in terms of moles reacted per gram of catalyst as a function of time. As can be seen, both the graphene based membranes show superior photocatalytic activity with respect to the reference titania. In particular the only difference between the nanostructured membranes is the reaction rate in the intermediate region of time, by means that the methanol degradation has been completed on the PAN/G+TiO_2 membranes in a shortest time than the nanocomposite PAN/rGO-TiO_2 membranes. This result could be ascribed to the fact that while the reduced graphene oxide si dispersed in a more finely fashion, in the G+TiO_2

system graphene sheets have a wider area, thus they can act more efficiently as barrier to increase the path of the pollutant across the membrane, increasing the contact times and providing more adsorption site. Besides, as seen from the UV-vis measurement the absorption of this composite is higher than the other photocatalytic systems meaning a probable increased amount of photogenerated holes and electrons on the surface of the photocatalyst which is in contact with graphene.

6.3.7 Effect of graphene on the photocatalytic activity of TiO_2

A common strategy for improving traditional photocatalysts is the possibility to couple them with other semiconductors or co-catalyst in order to reduce the phenomenon of charge carrier recombination. An attractive coupling partner for titania is represented by carbon materials such as graphite, fullerenes, carbon nanotubes and graphene [364]. The delocalized conjugated π electron system as well as its favorable energy level positions with respect to the TiO_2 conduction band in these carbon allotropes has been proved to cause a rapid photo-induced charge separation in electron-transfer processes. However, factors such as interfacial area, defects, optical, and electronic properties differentiate their performance. The electron storage of conducting carbon is assigned to a large array of carbon double bonds and defects in it while the conducting nature of carbon improves charge transport in composites.
The exact nature of the phenomenon can be investigated by analyzing the mechanisms involved during the photocatalytic process. Upon illumination of TiO_2 by the UV radiation, photons from the light source are capable to promote the excitation of an electron from the valence band to the conduction band of the semiconductor, leaving holes in the valence band. When in contact with a carbonaceous material the excited electrons are transferred from the surface of the semiconductor the carbonaceous substrate, acting as a sink for the the photogenerated electrons [365]. The proposed mechanism for this charge separation effect is similar for all types of conducting carbon materials [287]. These electrons can then react with surface adsorbed oxygen leading to the formation of a series of active oxygen radicals such as $O_2^{\cdot}$. In turn the photogenerated holes are made available for the formation of $^{\cdot}OH$ radicals, promoting the photocatalytic activity towards the oxydation of methanol.

6.4 CONCLUSIONS

Electrospun polymeric membranes have been produced for the photocatalytic abatement of methanol using a layer-by-layer approach. Three different catalytic systems have been tested in order to determine the effect of different coupling of graphene with titania with either physical contact (G+TiO_2 composite) of chemical interaction (rGO-TiO_2 composite). Two different polymeric supports, PSU and PAN have been employed for the dispersion of the photocatalyst but preliminary test have shown that PSU is unsuitable for the applications to to extensive degradation under UV irradiation. This leads to a fast yellowing of the

reaction, lost of mechanical stability and low methanol conversion due to the competitive effect of the concurrent degradation reactions. The tests conducted with PAN as support have been carried in comparison with the reference of TiO_2 and the membranes morphologies have been determined both SEM and TEM. The amount of catalyst deposited on each type of membrane has been quantified by TGA in reference to the amount of TiO_2. The results of the tests have shown that generally the photocatalytic activity improves over the days and that the graphene based photocatalysts are capable to produce the conversion of methanol after 150 minutes of reaction. The enhancement in the kinetic of the reaction has been determined by a comparison of the moles reacted per gram of catalyst on the basis of similar starting concentration of the pollutant. The best performances are provided by the G+TiO_2 system probably due to the high mobility of free electrons on the surface of graphene and reduced recombination of the electron-hole couple generated in the photocatalyst. The rGO+TiO_2 shows better result than bare titania but the performances are not good as in the case of G+TiO_2. This could be due to the fact that after the hydrothermal treatment the graphene obtained has much higher defects which in turns can determine lower electron mobility and thus lower efficient charge separation.

7 ONE STEP APPROACH: MEMBRANE PREPARATION, CHARACTERIZATION AND PERFORMANCE EVALUATION

On the basis of the results obtained in the first phase of the study the attention has been focused on the possibility to have a better exploitation of the nanofibrous morphology using a different approach (hereafter called "one step approach"), employing colloidal solutions of solid particles and polymer as alternative strategy for the deposition of the photocatalysts previously employed. Thus, with the aim of using the polymeric support of the fibers as simple binder, the catalyst has been added to the solution for the electrospinning tests in order to deposit the fibers and obtain their coverage by the catalyst at the same time and starting from a single solution (Figure 7.1). With this approach the solution requires a first dispersion of the employed photocatalyst in the solvent for the electrospinning process, followed by the addition of the polymer employed as binder for the membranes. This solution is more advantageous when using solid particles that are dif-

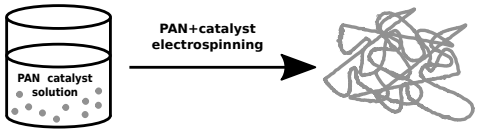

Figure 7.1: *One-step approach for the production of photocatalytic membranes*

ficult to disperse in specific solvents even in presence of a dispersing agent. In such cases when using the electrospraying techniques as in the layer-by-layer approach, the deposition time should be minimized to avoid particle settling in the syringe which could lead to non uniform distribution of the solid particles on the final substrate or use dispersions with very low concentrations. With the single solution (one-step) approach the solution is stabilized upon the addition and dissolution of the polymer in the solvent. Indeed by taking into consideration the Stokes law, we have:

$$v_s = \frac{g(\rho_p - \rho)D_p^2}{18\mu} \tag{7.1}$$

where v_s is the settling velocity, ρ_p and ρ are the densities of the particles and of the fluid, D_p is the particles diameter and μ is the fluid viscosity. The equation states that if the density difference between the solvent and the solid phase is significant it is possible to decrease the settling velocity of the particles by increasing the viscosity of the system up to a certain value. In this manner by suspending the solid particles during the poly-

mer dissolution by mechanical stirring it is possible to prevent their settling thanks to the increasing viscosity of the final mixture. These conclusions have been confirmed by the observations that after few days the solid phase in completely segregated from the rest of the polymeric solution. In this manner it is possible to mimic the formation of a complete inorganic nanofibrous structure, avoiding the employment of sol-gels and the problems related to post electrospinning process with the possibility of broaden the category of electrospinnable materials [366].
The approach has been applied to the same photocatalytic systems employed in the previous part of the study with the addition of a composite of graphene oxide and titania (mass ratio equal to 1:10) in order to evaluate also the difference in role played by different types of graphenes.

7.1 CHARACTERIZATION

7.1.1 SEM

Scanning electron micrographs were collected with a JEOL 6490 SEM on gold sputtered samples.

7.1.2 TEM

High magnification transmission electron microscopy (FEI Tecnai G12, 100KV with TVIPS Tietz F114 photocamera) was employed for morphological analysis. Sample preparation for TEM imaging had been carried out as follows: the membrane samples were embedded in a proper epoxy resin and slices of 100 nm thickness were cut from the cured resin using a Leica ultracut UCT microtome.

7.1.3 TGA

Thermogravimetric analyses were carried with a SDT Q600 (TA Instruments) TGA under air flow at a flow rate of 100 ml/min and at a constant heating rate of 20°C/min from room temperature up to 900°C.

7.2 RESULTS AND DISCUSSION

7.2.1 Membrane preparation by electrospinning

The electrospun membranes have been produced by a the one-step approach according to which the solution to be electrospun is characterized by the simultaneous presence of polymer and catalyst. The procedure is the same for each type of membrane and

requires a first dispersion of the catalyst in DMF for an hour followed by the addition of PAN. The solution is kept under stirring overnight before electrospinning to ensure complete polymer solubilization. The conditions employed for the electrospinning of the membranes have been the following:

- PAN/TiO_2: the catalyst-to-polymer ratio has been fixed to 70:30 while the amounts of the components of a solution for the preparation of a five membranes set have been 4g of DMF, 0.47 of TiO_2, 0.2 g of PAN (5% w/w with respect to the solvent). The electrospinning conditions employed for the production of the membranes are

  Table 7.1: *Electrospinning process parameters for the production of the PAN/TiO_2 composite membranes with the one-step approach*

Parameter	Value	Units
Flow-rate	0.5	ml/h
Voltage	15	kV
Tip-to-collector	15	cm
Needle (i.d)	0.700	mm
Relative humidity	< 30	%
Deposition time	60	min

  reported in Table 7.1.

- PAN/G+TiO_2: even in this case the catalyst-to-polymer ratio has been fixed to 70:30, employing a fixed mass ratio of graphene-to-titania equal to 1:10. The employed quantites for a membrane set have been 10 g of DMF, 1.17g of nanocomposite, 0.5 g of PAN (5% w/w with respect to the solvent). The electrospinning conditions

  Table 7.2: *Electrospinning process parameters for the production of the PAN/G+TiO_2 composite membranes with the one-step approach*

Parameter	Value	Units
Flow-rate	0.9	ml/h
Voltage	15	kV
Tip-to-collector	17	cm
Needle (i.d)	0.700	mm
Relative humidity	<30	%
Deposition time	50	min

  employed for the production of the membranes are reported in Table 7.2.

- PAN/GO+TiO_2: in this case two different ratio of catalyst-to-polymer have been employed (70:30 and 50:50) with a fixed graphene oxide-to-titania mass ratio of 1:10. In the first case (70:30 catalyst/polymer) the amount of quantities for membrane set have been 7.55 g of DMF, 0.93 g of nanocomposite, 0.4 g of PAN (5% w/w with respect to the solvent). In the second case (50:50 catalyst/polymer ratio) the quantities employed have been 4.7 g of DMF, 0.25 g of nanocomposite, 0.25 g of PAN (5% w/w

Table 7.3: *Electrospinning process parameters for the production of the PAN/GO+TiO_2 composite membranes with the one-step approach*

Parameter	Value	Units
Flow-rate	1	ml/h
Voltage	15	kV
Tip-to-collector	15	cm
Needle (i.d)	0.700	mm
Relative humidity	< 30	%
Deposition time	50	min

with respect to the solvent).
The electrospinning conditions employed for the production of the membranes are reported in Table 7.3.

- PAN/rGO-TiO_2: in this case the catalyst-to-polymer ratio has been fixed at 70:30 with a fixed mass ratio of graphene-to-titania equal to 1:10. The employed quantites for a membrane set are 3.97 g of DMF, 0.47 g of nanocomposite, 0.2 g of PAN (5% w/w with respect to the solvent). The electrospinning conditions employed for the production of the membranes are reported in Table 7.4.

Table 7.4: *Electrospinning process parameters for the production of the PAN/rGO-TiO_2 composite membranes with the one-step approach*

Parameter	Value	Units
Flow-rate	0.9	ml/h
Voltage	18	kV
Tip-to-collector	15	cm
Needle (i.d)	0.700	mm
Relative humidity	< 30	%
Deposition time	45	min

As can be noted from the previous table the conditions for the electrospinning of the membranes have been defined for each specific type of membranes. This has been necessary because the results of a preliminary evaluation carried employing the same conditions for each type of membranes have shown significant differences in the final amount of catalyst deposited. As a consequence the condition have been change accordingly in order to limit significant discrepancies among the different membranes.

7.2.2 Membrane characterization

Due to the variety of in polymer-to-catalyst ratio and catalyst/co-catalyst systems all the membranes have been characterized by SEM; for some of them it has been considered

necessary to make a further investigation by TEM. A second analysis has been TGA for the evaluation of the catalyst content on each membrane type.

7.2.2.1 *PAN/GO+TiO_2*

The first type of membranes which have been characterized are the PAN-GO+TiO_2 for which the final morphologies of the fibers has been evaluated by varying the ratio between the polymer and the catalyst. Two different weight ratios have been considered (50:50 and

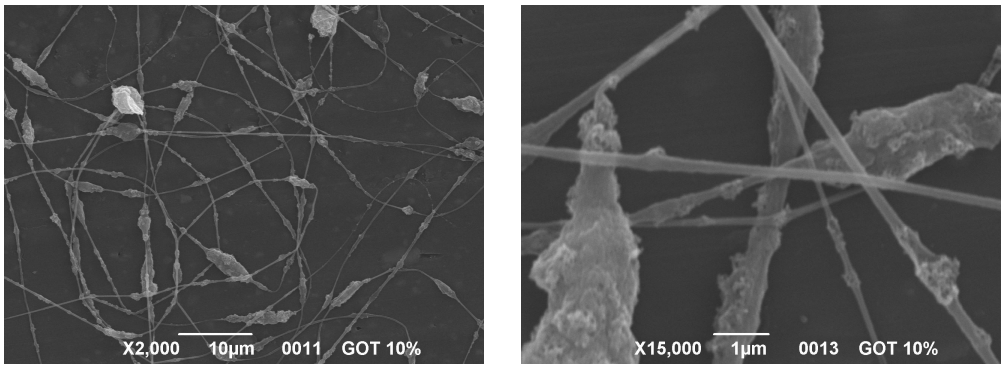

Figure 7.2: *SEM micrographs at different magnification of the PAN/GO+TiO_2 membrane (GO/TiO_2 = 1:10 w/w) with a catalyst-polymer ratio of 50:50 w/w*

70:30 by weight) because low relative amount of catalyst are detrimental due to confinement of the catalyst inside the fibers. In the present case the lower catalyst-to-polymer ratio leads to a heterogeneous morphology (Figure 7.2) in which the catalyst do not cover completely the polymeric binder and it is possible to distinguish inorganic agglomerates of titania along the smooth surface of the polymer fibers without visible evidence of the graphene oxide presence. By employing a 70:30 ratio the morphology shows a good im-

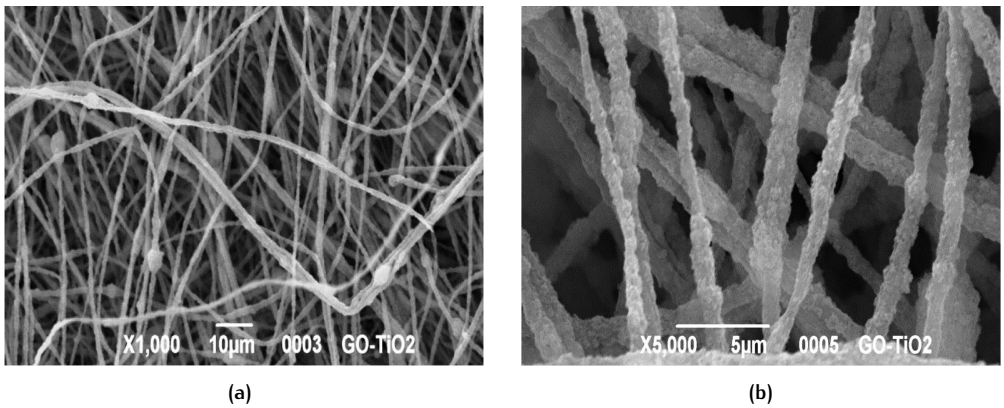

Figure 7.3: *SEM micrographs at different magnification of the PAN/GO+TiO_2 membrane (GO/TiO_2 = 1:10 w/w) with a catalyst-polymer ratio of 70:30 w/w*

provement (Figure 7.3). The higher relative content of catalyst allows a complete coverage

of the fibers which can exploit their function of catalyst binder, providing a continuous structure with high deposition area for the photocatalyst, thus restraining its possible agglomeration and possibly limiting the effect of mass transfer limitations. The final fibers are rough due to the high porosity of the titania nanoparticles and even in this case the graphene oxide is not visible, possibly due to its low particles dimension an high dispersion in the catalyst which prevents its individuation by SEM. On the basis of these preliminary conclusions the catalyst-to-polymer ratio of 70:30 has been chosen and fixed for the production of all the subsequent different type of membranes. A further morphological

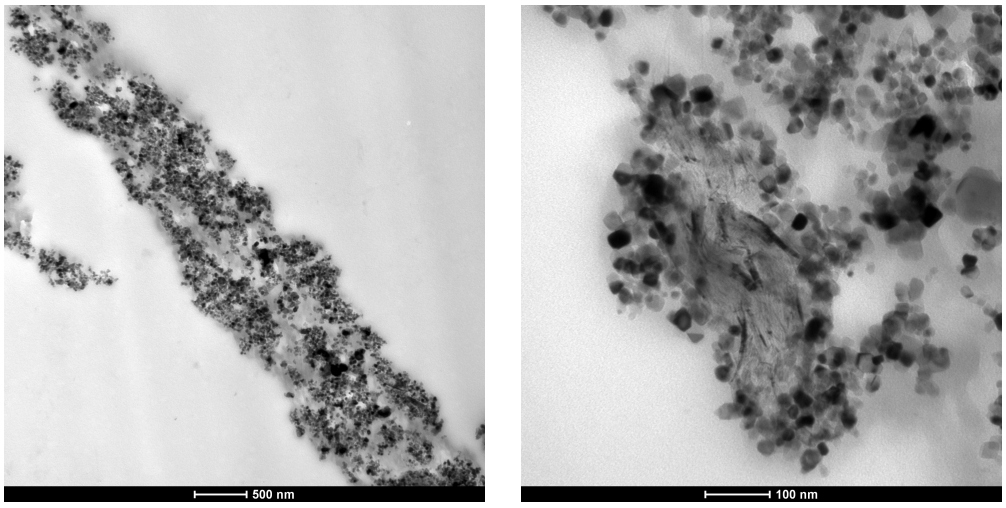

Figure 7.4: *TEM micrographs of the PAN/GO+TiO_2 photocatalyst on polymer nanofiber: (a) cross-section of the fibers,(b) particular of part of the cross-section with the presence of graphene oxide and titania nanoparticles*

characterization in order to define the presence and the dispersion of graphene oxide has been carried by TEM analysis on the cross-section of a piece of the membrane. As shown in figure Figure 7.4 the catalyst is deposited along the external surface of the fibers as well as in inner part of the same. Due to its low relative amount graphene oxide is dispersed in the system in the form of folded sheets, prevalently deposited close to the externally surface of the fibers and covered by titania. In this manner graphene oxide do not provide a continuos structure but rather provide separate "islands" in contact with titania and this particular configuration can effectively explain the difficulty in its identification by SEM. Graphene oxide should be as close as possible to the surface of the fibers in order to be exposed to the organic pollutant to enhance its adsorption and to act as photocatalyst.

Figure 7.5b shows the thermogravimetric curve of the PAN/GO+TiO_2 membrane. The analysis has been carried by dividing the membrane in two equal part which have been analyzed separately. In this manner it has been possible to evaluate, for each sample, the amount of catalyst deposited and for a single membrane the homogeneity of the catalyst deposited along the fibers. From the similar trend of the two curves and from the percentage residues almost identical it is possible to deduce a good homogeneity of the catalyst

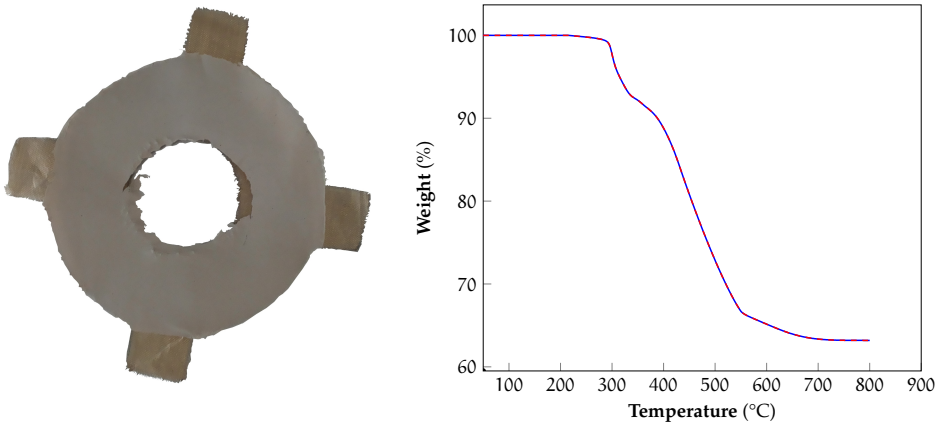

Figure 7.5: *(a) Electrospun PAN/GO+TiO_2 membrane, (b) Thermogravimetric analysis of the PAN/GO+TiO_2 membrane showing the final residue corresponding to the titania mass percent content*

distribution on the membrane. Indeed the porous structure of the titania nanoparticles allows the degradation of the polymer and the release of the gaseous product along with the degradation of the graphene oxide content. The theoretical residue that can be ascribed only to the inorganic content of the membrane should be 63% by weight which is exactly the final residue calculated from the thermogram assuming the complete degradation and volatilization of the polymer and the co-catalyst.

Table 7.5: *Amount of catalyst deposited on PAN/GO+TiO_2 membranes for the photocatalytic tests from TGA analysis*

Sample	Catalyst co-catalyst ratio	Catalyst for single membrane [mg]	Catalyst for a set of membranes [mg]	Specific amount of catalyst (10^3) [g/cm^2]
PAN/GO+TiO_2	1:10	62.3 ± 3.5	312 ± 18	0.94 ± 0.05

Thus the amount of photocatalyst calculated is referred to only the TiO_2 content present on a single membrane, the total amount of photocatalyst on a set of five membranes and the specific quantity of catalyst per unit of surface are reported in Table 7.5.

7.2.2.2 *PAN/TiO_2*

On the basis of the conclusion of the previous paragraph a second type of membrane have been produced using only TiO_2 in the PAN solution and employing a catalyst-to-polymer ratio of 70:30 by weight. SEM images provide evidence of the successful deposition of the catalyst on the fibers, confirming that the ratio employed is effectively for the production of the fibers with the desired morphology.
Similarly to the previous case it is reported the thermogram of the final membrane in Figure 7.7 and in Table 7.6 the quantities relative to the amount of catalyst present for single membrane and for a set of membranes.

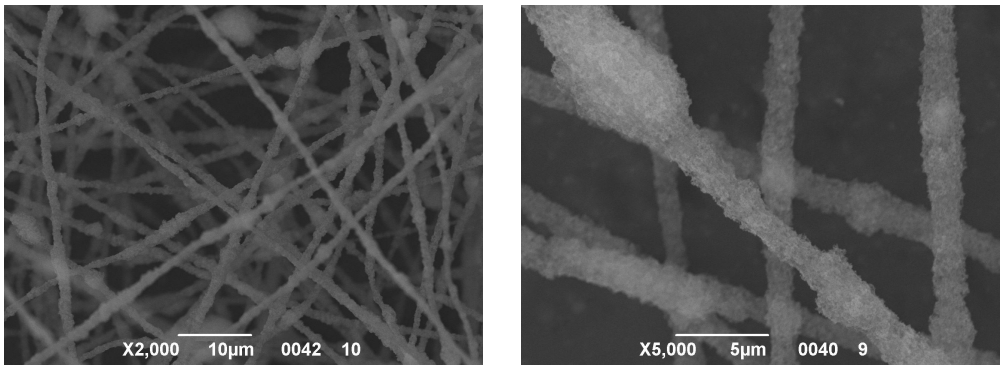

(a) (b)

Figure 7.6: *SEM micrographs of the PAN/TiO_2 membrane with a catalyst-polymer ratio of 70:30 w/w*

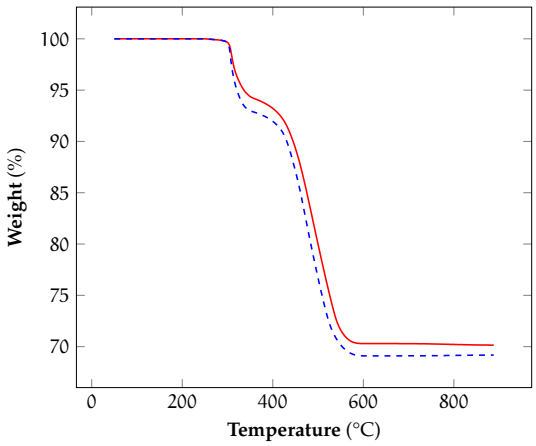

Figure 7.7: *TGA of PAN/TiO_2 membranes*

Table 7.6: *Amount of catalyst deposited on PAN/TiO_2 membranes for the photocatalytic tests from TGA analysis*

Sample	Catalyst for single membrane [mg]	Catalyst for a set of membranes [mg]	Specific amount of catalyst (10^3) [g/cm^2]
PAN/TiO_2	48.9 ± 0.6	191.3 ± 3	0.58 ± 0.01

7.2.2.3 *PAN/G+TiO_2*

SEM micrographs of the PAN/G+TiO_2 electrospun membranes are shown in Figure 7.8. The fibers are completely covered by the photocatalyst and the final morphology is similar to previous membranes. Similarly as the case of the membranes with graphene oxide, graphene has not been identified along the the surface of the fibers,even if its presence is justified by the dark gray color of the electrospun membranes.

The proof of the presence of graphene and its disposition in or along the fiber has been investigated by TEM. As previously done also in this case the analysis has been conducted

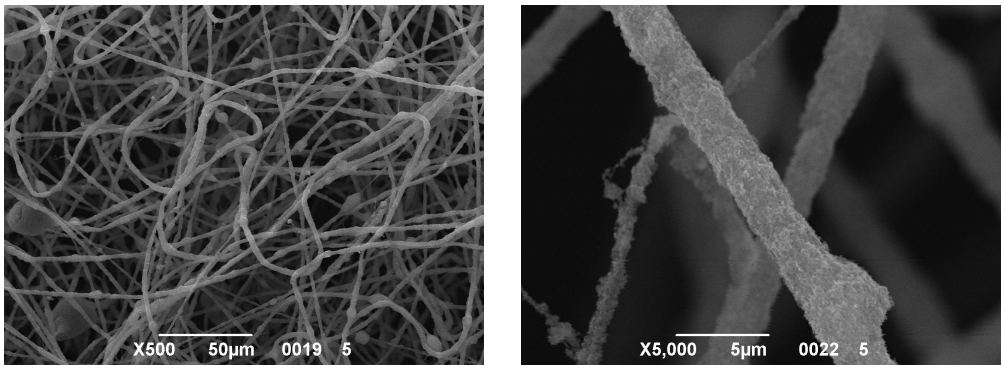

(a) (b)

Figure 7.8: *SEM micrographs of the PAN/G+TiO_2 1:10 membrane with a catalyst-polymer ratio of 70:30 w/w*

by evaluate the disposition of the composite along the cross-section of the membrane.

Figure 7.9a shows an image of the analyzed sample in which the graphene is present as

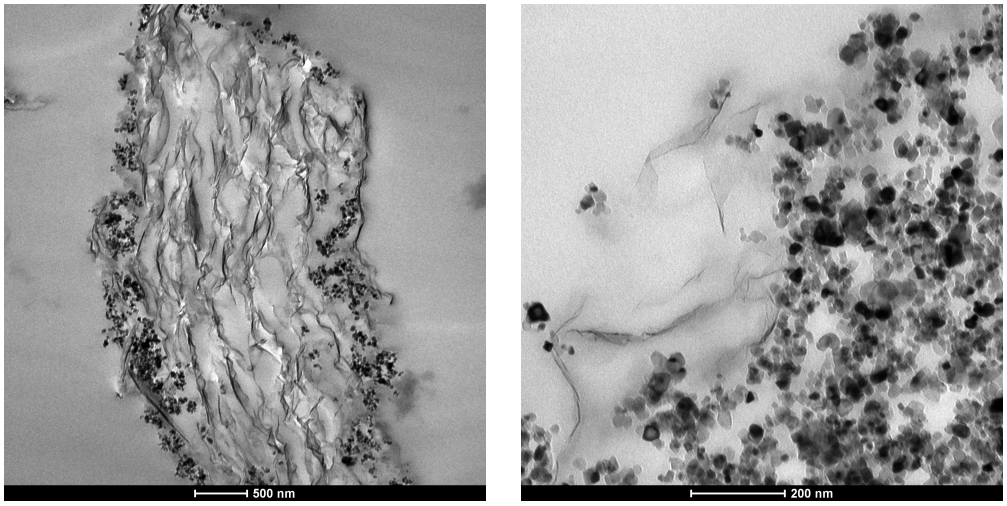

(a) (b)

Figure 7.9: *TEM micrograph of the PAN-G+TiO_2 1:10: (a) cross-section of single fibers that shows the confinement of graphene, (b) a zone of a membrane zone where graphene is placed on the external part of the fiber*

semi-transparent folded sheets inside the section of the fibers with the titania nanoparticles confined on the external surface of the membrane. This situation is quite predominant in all the sample, although with some exceptions (Figure 7.9b) and it is representative of the partial confinement of graphene inside the fibers. This situation might be detrimental towards the improvement of the performance of the catalyst leading to an inefficient exploitation of the role of the co-catalyst.

Finally the membranes have been analyzed by TGA and Figure 7.10 shows the weight change as a function of the temperature while the amount of catalyst deposited in both cases are reported in Table 7.7.

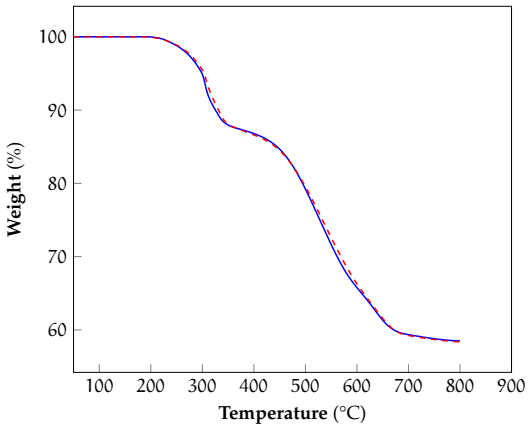

Figure 7.10: *TGA of the PAN/G+TiO_2 (1:10) membranes*

Table 7.7: *Amount of catalyst deposited on PAN/G+TiO_2 membranes for the photocatalytic tests from TGA analysis*

Sample	Catalyst co-catalyst ratio	Catalyst for single membrane [mg]	Catalyst for a set of membranes [mg]	Specific amount of catalyst (10^3) [g/cm^2]
PAN/G+TiO_2	1:10	55 ± 3	244 ± 13	0.83 ± 0.04

7.2.2.4 *PAN/rGO-TiO_2*

The last type of membranes are shown in Figure 7.11 and differ from the previously due to the hydrothermal method followed to obtain the coupling between reduced graphene oxide and TiO_2.

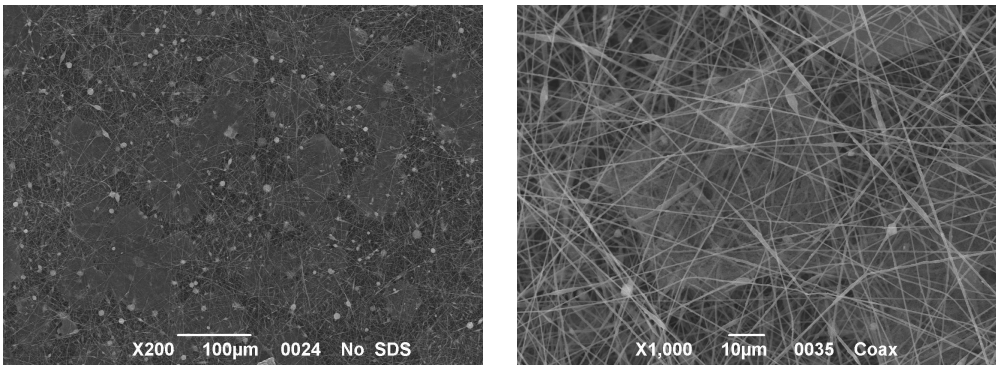

(a) (b)

Figure 7.11: *SEM micrographs of the PAN/rGO-TiO_2 1:10 membrane with a catalyst-polymer ratio of 70:30 w/w*

In this case the SEM images show a different situation from the previous membrane type. At low magnification it is possible to identify solid aggregates distributed between the nanofiber mat. Here the fibers are more smooth and have lower diameters than the previous cases. This can be explained in terms of reduced dispersion of the photocatalytic

composite in the polymer solution which leads to a partial separation from the fibers generated during the spinning process. This hypothesis is further confirmed by TEM micrographs of the fibers section (Figure 7.12) where it is possible to notice that the catalyst is present in lower amount in the fiber, with a visible portion of polymer material. Here the graphene is much more in contact with the TiO_2 nanoparticles and the particular final morphology of the deposition seems to be more promising to obtain a boost in the photocatalytic activity due to a more efficient exploitation of the co-catalyst that is much more exposed to the free surface of the membrane. On the other side the major drawback is the lower exploitation of the nanofibers surface that do not act as binder but as simple support in a manner which resemble the layer-by-layer approach for the same type of photocatalytic composite. The thermogravimetric curve and the amount of photocatalyst

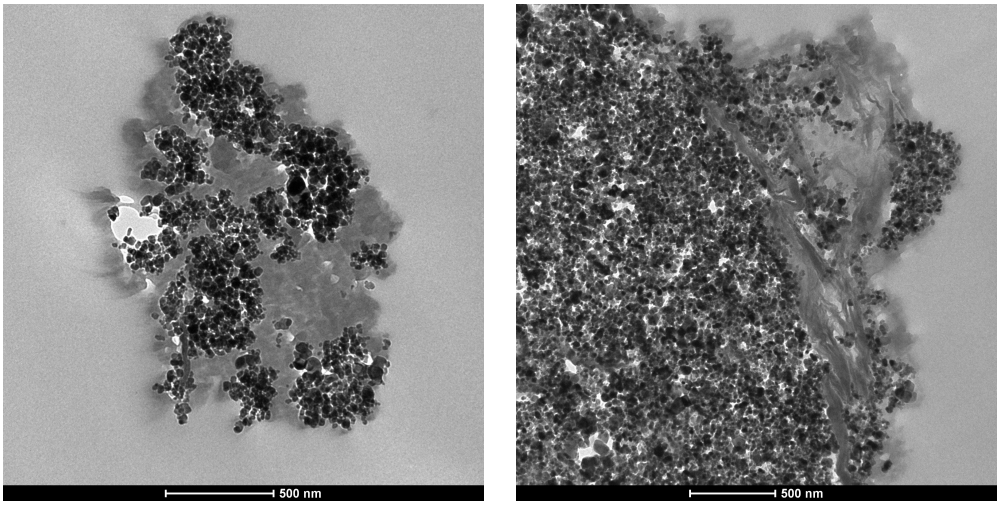

Figure 7.12: *TEM micrographs of the PAN/rGO-TiO_2 photocatalyst on polymer nanofiber: (a) cross-section of the fibers,(b) particular of part of the cross-section with the presence of graphene and titania nanoparticles*

Table 7.8: *Amount of catalyst deposited on PAN/rGO-TiO_2 membranes for the photocatalytic tests from TGA analysis*

Sample	Catalyst co-catalyst ratio	Catalyst for single membrane [mg]	Catalyst for a set of membranes [mg]	Specific amount of catalyst (10^3) [g/cm^2]
PAN/rGO-TiO_2	1:10	59 ± 1	170 ± 5	0.52 ± 0.02

deposited on the membranes are shown in Figure 7.13 and Table 7.8, respectively.
Generally the results show an higher amount of catalyst on the fiber with respect to the case of the membranes with a layer-by-layer approach. This is an intrinsic limitation due to the fact that the required ratio between the catalyst and the polymer is quite high to have a complete coverage of the membrane support; besides to have a sufficient deposition

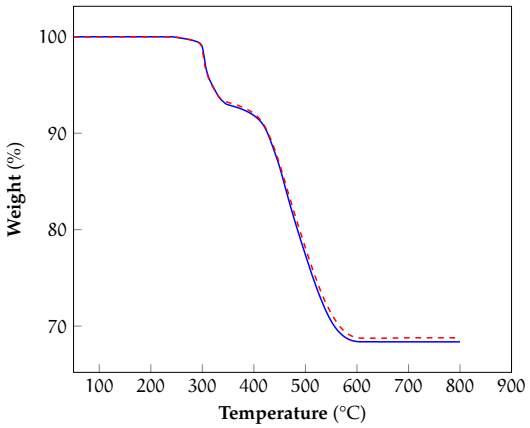

Figure 7.13: *TGA of PAN/rGO-TiO_2 membranes*

of membrane on the support in order to avoid the formation of preferential paths for the passage of the gas during the subsequent photocatalytic tests.

7.3 PHOTOCATALYTIC TESTS FOR METHANOL ABATEMENT

The following paragraphs present the results of the photocatalytic tests towards the degradation of methanol using the membranes obtained with the one-step approach. The membranes have been produced according to the conditions reported in §7 and with the catalyst content calculated from the thermogram of §7.2.2. The conditions for the tests are the same for the photocatalytic experiment carried with the membranes obtain with layer-by-layer approach, carrying three different tests for each membranes in three different days. This conditions allows a comparison of the performances between the two different approaches which is the main objective of the study.

7.3.1 PAN-TiO_2

The first tests have been carried with the PAN/TiO_2 membranes and the results of the photocatalytic abatement of methanol is reported in Figure 7.14. The starting concentration of methanol have been approximately 6000, 5800 and 6400 ppm, respectively. On the basis of the result it is possible to observe that the similar initial concentrations of pollutant in the reactor allows to consider a progressive increment of the kinetic of the reaction over the day, similarly for what has been seen with the test carried with the layer-by-layer type of membranes. Despite the first day the concentration of methanol rapidly decrease during the first hour of the reaction and then follows linear behavior with time until the end of the tests. The third day, where the starting concentration is higher, present the best performances and the final conversion of methanol reach the value of 92%. Even for this type of membranes the main by-product of the reaction is methyl formate, which is formed concurrently with the degradation of methanol. Its increase is generally linear

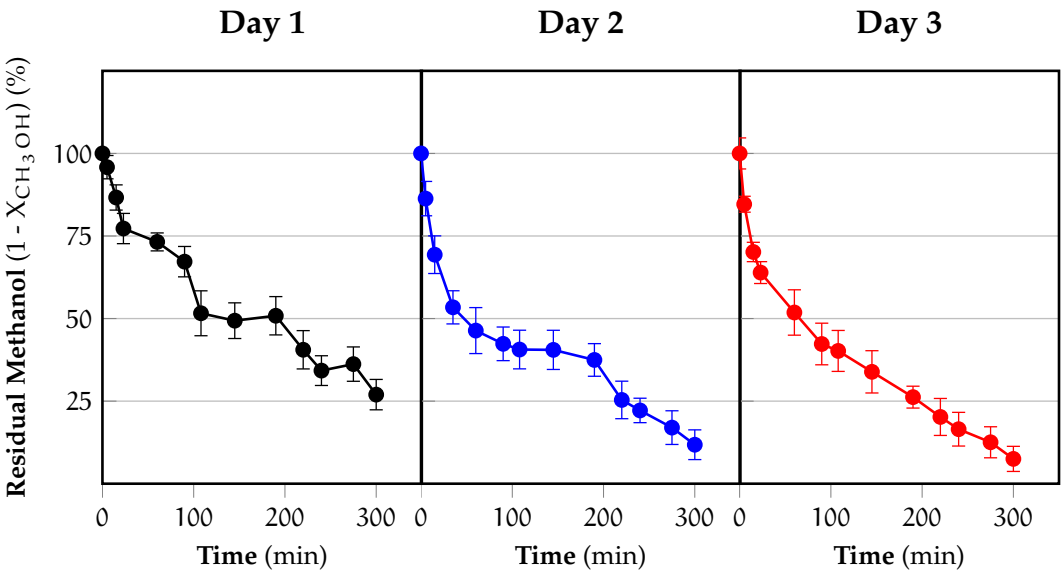

Figure 7.14: *Evolution over time of the percentage of residual methanol in the reactor for the PAN-TiO_2 one-step membranes in three different days of reaction*

over time and reaches a maximum up to 200 minutes, after which it decrease in the same fashion. Since for these membranes methanol is not completely converted in any of the testing days, methyl formate does not disappear at 300 minutes of reaction, while carbon dioxide shows a linear trend over the entire duration of the tests.

7.3.2 PAN-G+TiO_2

The results of the methanol photoxidation for the PAN/G+TiO_2 1:10 membranes are showed in Figure 7.15. In these case the starting concentration after the equilibration between the absorption/desorption process in the dark have shown a lower starting concentration of methanol over all the three days of reaction (3200, 3500 and 3300 ppm, respectively). The methanol abatement shows a linear dependency over time as well as the increase of methyl formate does. The kinetics is slightly improved over the days (from 76% to 85%) but in no case the methanol is completely converted.

7.3.3 PAN-GO+TiO_2

Here are reported the results relatively to the membranes set PAN/GO+TiO_2 which has not been previously tested with the layer-by-layer approach. The methanol abatement over the days of reactions is reported in Figure 7.16. The starting concentration are approximately 3550, 3900 and 3450 ppm for the first, second and third day of reaction, respectively. The results are much better than the previous type of membranes for which the starting concentrations were quite the same. Here the methanol conversion is reached since the first day of reactions and the trend shows an exponential decay. There is an increase in the

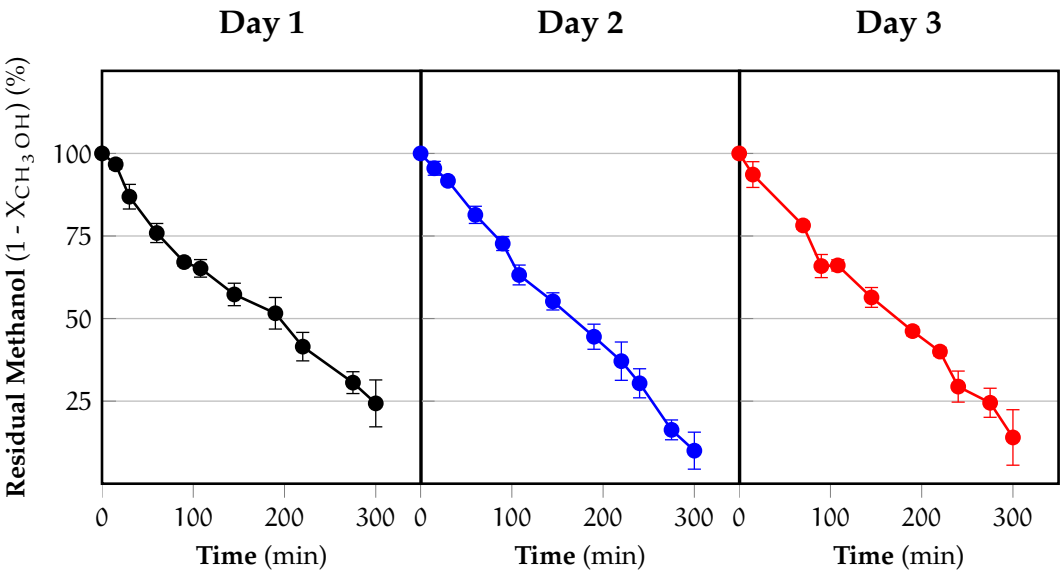

Figure 7.15: *Evolution over time of the percentage of residual methanol in the reactor for the PAN-G+TiO_2 (graphene/titania ratio = 1:10 w/w) one-step membranes in three different days of reaction*

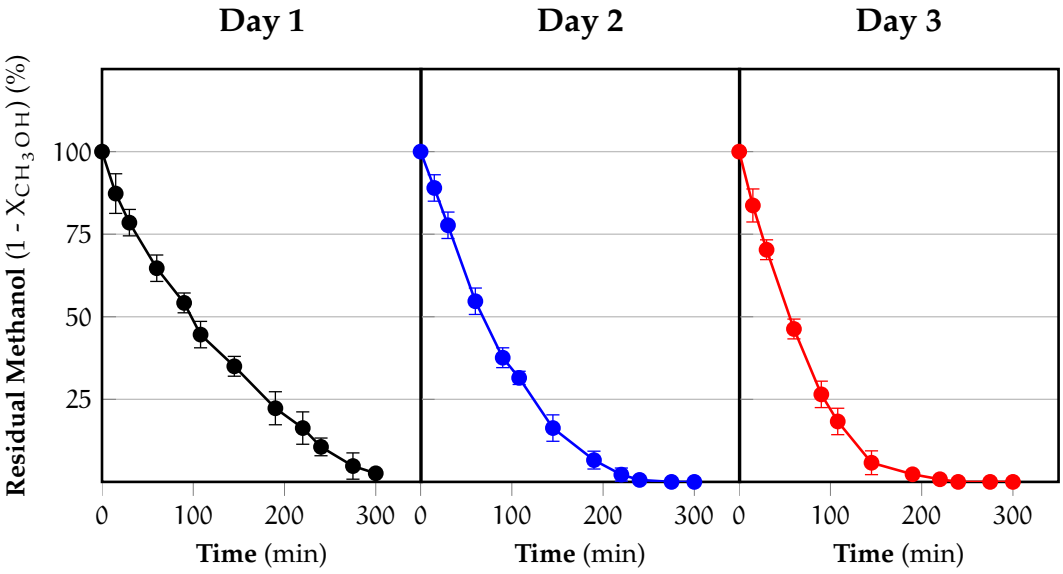

Figure 7.16: *Evolution over time of the percentage of residual methanol in the reactor for the PAN-GO+TiO_2 one-step membranes in three different days of reaction*

photocatalytic activity in second and third day of reaction where the complete conversion of methanol is reached in after, approximately, 220 minutes.

7.3.4 PAN/rGO-TiO_2

The last membranes set which has been tested has been PAN/rGO-TiO_2 and results are reported in Figure 7.17. During the first day of reaction the starting concentration after the

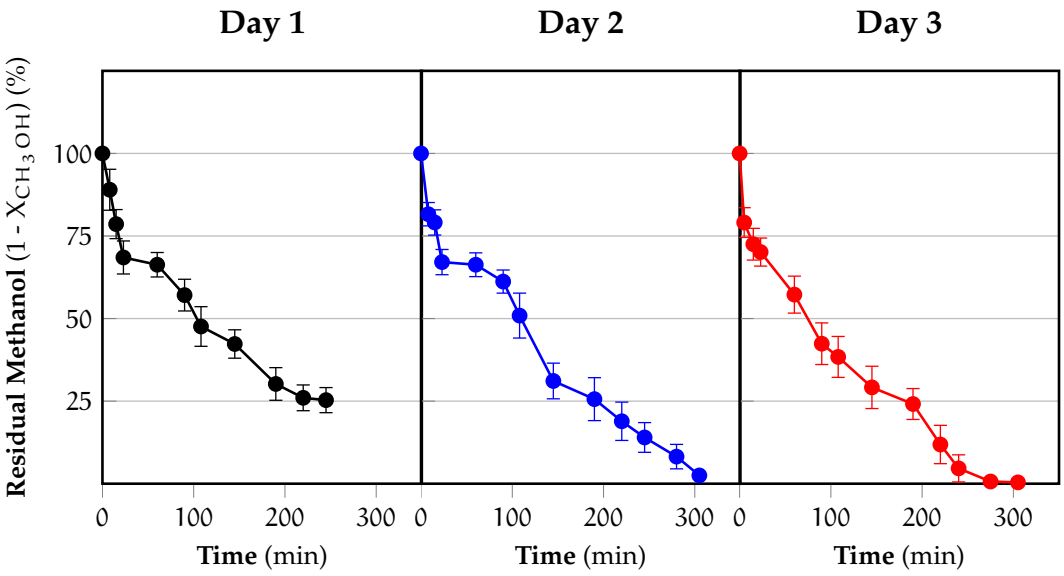

Figure 7.17: *Evolution over time of the percentage of residual methanol in the reactor for the PAN/rGO-TiO_2 one-step membranes in three different days of reaction*

equilibration of the system during the conditioning phase has been 7700 ppm and final conversion is 75% after 240 minutes. For the second day of reaction the starting concentration has been 6700 ppm and the membranes have shown similar performances to first day. Here the reaction has been followed up to 300 minutes and it has been possible to see that the conversion of methanol was almost complete. In the third day the concentration as been limited to 4000 ppm in order to have a value more comparable to other set employed.

7.3.5 Comparison of the results: effect of co-catalyst and morphology

7.3.5.1 *Comparison of the different graphenes*

Figure 7.18 shows the comparison of the performances of the different membranes produced with the one-step approach with the co-catalyst with different degree of graphene oxidation. As can be seen from the results a significant difference is present between the membranes comprising graphene and graphene oxide with respect to the membrane containing the rGO-TiO_2 nanocomposite. The latter present a remarkable high photoactivity which has been attributed to the effect of the different morphology shown by electron microscopy. As hypothesized from the TEM analysis the confinement of graphene inside the fibers can be considered as the main reason behind the poor results of the PAN/G+TiO_2 and PAN/GO+TiO_2 membranes. In these membranes the fibers have higher diameters and a more porous structure while for the PAN/rGO+TiO_2 membranes the lower deposition of the catalyst on the fibers leads to a more compact structures, a more exposition of the photocatalyst and co-catalyst towards the pollutant improving the photoactivity towards the methanol oxidation.

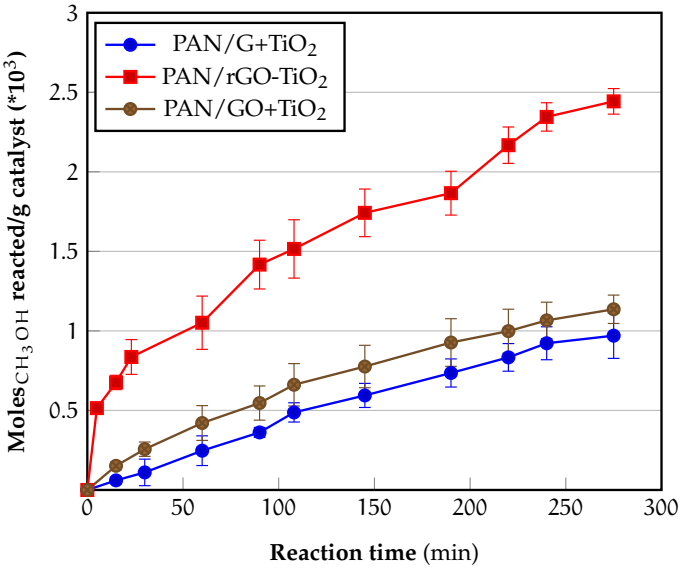

Figure 7.18: *Comparison of the moles reacted per gram of photocatalyst for the graphenes based membranes between the different types of graphenes employed*

7.3.5.2 *Comparison between the different morphologies*

A second comparison has been made in order to evaluate the possible advantages between the different morphologies employed in the study and the results are shown in Figure 7.19. Here different situations can be outlined according to the specific system

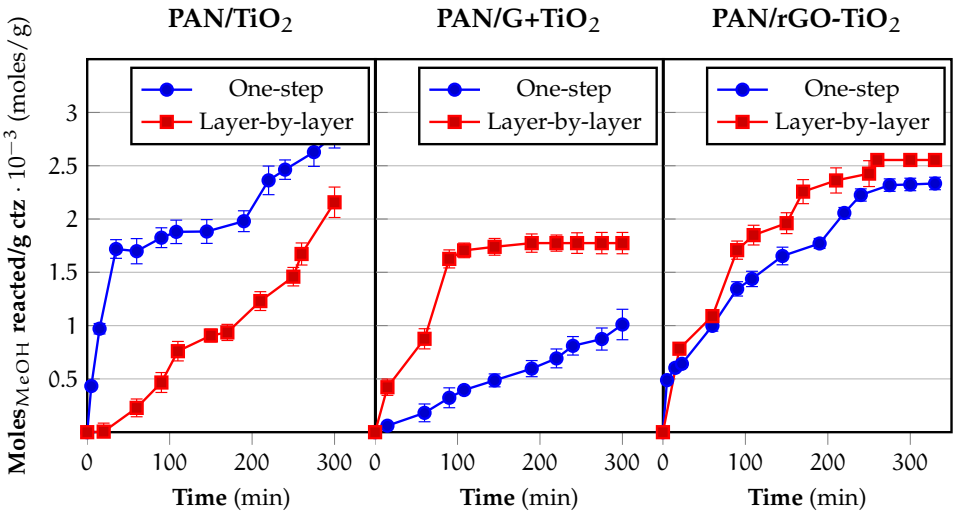

Figure 7.19: *Comparison of the moles reacted per gram of photocatalyst between the layer-by-layer and the one step approach for the different membranes employed*

taken in consideration. For the membranes employing only TiO_2 there is a clear advantage in the employment of the one-step approach. The amount of moles reacted increase rapidly and the kinetic of the reactions is much faster, probably thanks to the high surface area provided by the porous structure of the membranes.
For the membrane employing graphene and TiO_2 the situation is opposite and the best

performances are obtained by the layer-by-layer approach. Here the reason can be ascribed to the fact that when graphene is deposited on the fibers it acts as substrate to increase the adsorption of the pollutant and it is more efficiently in contact with TiO_2 to promote the charge separation and reducing the chances of their recombination.
In the last case the two different morphologies provide similar results and a slight improvement can be achieve by the layer-by-layer approach thanks to a better exploitation of the photocatalyst which is not partially blocked inside the fibers as in the other approach. However from the results of this last case it is clear that when a co-catalyst is employed in order to improve the photoactivity of TiO_2 it is necessary to provide proper exposition towards the pollutants. A clear advantage in the use of a morphology or the other is thus dependent by the presence of the co-catalyst and by the catalyst/co-catalyst couples taken into consideration. Preferential segregation of the co-catalyst is detrimental for the photoactivity even if in presence of an increase in active surface area of the photocatalyst. Besides further investigations are required to assess if the apparent increase in the surface area of the catalyst by the one step approach is capable to overcome the reduction of surface area provided by the confinement the co-catalyst which, in the layer-by-layer approach, is directly exposed to the atmosphere containing the pollutant.

7.4 CONCLUSIONS

Electrospun membranes have been produced by colloidal dispersion of solid particles of titania and different type of graphenes (graphene, graphene oxide and reduced graphene oxide coupled with TiO_2) to be tested for the photocatalytic abatement of methanol. The electrospinning of the membranes have analyzed by varying the catalyst/polymer ratio and a 70:30 ratio has been defined as optimal to obtain the complete coverage of polymeric support by the photocatalyst employed. Electron microscopy have shown that according to the different types of graphenes employed the final morphology can change as a result of the electrospinning process. Graphene and graphene oxide tend to be confined inside the fibers, leaving only TiO_2 exposed on outer surface and thus in contact with the pollutant. The rGO+TiO_2 once electrospun with the PAN solution provide less coverage of the fibers and tend to form agglomerates exposed on the external surface of the fibers. These differences in the morphologies have proved to determine a significant effect on the photocatalytic performances of the membranes. Both with graphene and graphene oxide the amount of moles of methanol reacted per gram of catalyst are significantly lower than the case of the rGO+TiO_2 composite. This results can be ascribed to the fact that the confinement induced on co-catalyst prevent the possibility of promoting an interaction with the main photocatalyst and the synergistic effect due to the coupling of the two materials. Same conclusions can be drawn from the comparison between the results of the different approaches followed for the deposition of the catalyst. In the case of TiO_2 the membranes obtained by the one-step approach have shown a significant higher photocatalytic activity as a consequence of the higher exploitation of the fibers surface. For the other systems employing graphene it has been seen that with pure graphene and titania mixing physically

the layer-by-layer approach is much more photoactive, while for the rGO+TiO_2 nanocomposite the performance are quite independent from one approach to the other. This last result can be ascribed to the fact that for rGO+TiO_2 system the final morphology of the deposition is not dissimilar and, thus, the better performances are obtained when graphene is more exposed on the surface of the fibers with the possibility to provide adsorption sites for the pollutant.

8 SYNTHESIS, ANALYSIS AND PERFORMANCE EVALUATION OF SILVER BASED NANOCOMPOSITE MEMBRANES FOR THE PHOTOCATALYTIC ABATEMENT OF METHANOL

8.1 RAW MATERIALS

On the basis of the results obtained in the first part of the study PAN (M_w = 150,000 Dalton, Sigma-Aldrich USA) was selected as polymeric support for the production of the electrospun membranes. TiO_2 nanoparticles (Aeroxide P25, Evonik Industries) was used as main photocatalyst, while graphene oxide (Sigma-Aldrich) was employed as co-catalysts. $AgNO_3$ (Sigma-Aldrich) and Na_2CO_3 (Normapur Prolabo) were employed for the synthesis of Ag_2CO_3.

8.2 CHARACTERIZATION

8.2.1 XRD

Wide Angle X-ray diffraction (WAXD) patterns were recorded in a 2θ angular range of 1.5° to 70° on a Philips X'Pert PRO diffractometer, working in reflection geometry and equipped with a graphite monochromator on the diffracted beam (CuKα radiation). The scanning step size was 0.02° with a measured uncertainty in terms of d-spacings of about 0.05 nm (2σ).

8.2.2 FTIR

FTIR spectra of the photocatalysts realized have been recorded in transmission mode with KBr tablets at 64 scans with a resolution of 4 cm^{-1} using a ThermoFisher Nicolet 670 spectrophotometer in transmission mode.

8.2.3 TGA

Thermogravimetric analyses were carried with a SDT Q600 (TA Instruments) TGA under air flux at a flow rate of 100 ml/min and at a constant heating rate of 20°C/min from room temperature up to 900°C.

8.2.4 UV-visible spectrophotometry

Diffuse reflactance UV-visible spectra were acquired with an UV-visible-NIR spectrophotometer (Cary 5000, Agilent Technologies) with an integrating sphere attachment, in the range of 200-800 nm. $BaSO_4$ was used as the reflectance standard material.

8.2.5 SEM

Scanning electron micrographs were collected with a JEOL 6490 SEM in conjunction with an energy dispersive X-ray spectra analyzer (EDAX)

8.2.6 TEM

Transmission electron microscopy (FEI Tecnai G12, 100KV with TVIPS Tietz F114 photocamera) were used for morphological analysis.

8.3 RESULTS AND DISCUSSION

8.3.1 Catalysts preparation

For each catalytic system prepared the common step has been the synthesis of silver carbonate by precipitation using the reaction between aqueous solutions of Na_2CO_3 and $AgNO_3$ according to the following chemical equation:

$$2AgNO_3 + Na_2CO_3 \rightarrow Ag_2CO_3 + 2NaNO_3 \tag{8.1}$$

Three different composites have been developed for further characterization:

- a binary composite containing TiO_2 and Ag_2CO_3 both by coupling (TiO_2 + Ag_2CO_3) and by simple mixing (TiO_2-Ag_2CO_3), with a relative composition of 70:30 on mass basis in order to obtain the same ratio of the two components as in the ternary composite
- a ternary composite containing TiO_2, Ag_2CO_3 and graphene oxide (TiO_2 + Ag_2CO_3 + GO) with the proportions 70:29.5:0.5 on mass basis to obtain a similar composition with respect to previous case and analyze the effect of the addition of graphene oxide

- a binary composite containing Ag_2CO_3 and graphene oxide (Ag_2CO_3 + GO) with a 2% content of graphene oxide on mass basis in order to obtain the same mass ratio of the two components as in the case of the ternary compound

For the preparation of the composites the recipes followed are the following:

- TiO_2/Ag_2CO_3 composites by coupling and by mixing: here two different procedures have been followed. In the first case the composite has been produced with the method developed by Feng *et al*. [367] in which TiO_2 has been dispersed in distilled water and mixed with a Na_2CO_3 solution to afford a a mixed suspension under sonication. In the resultant mixed suspension a $AgNO_3$ aqueous solution has been added dropwise under stirring to obtain the precipitation of Ag_2CO_3 directly in the TiO_2 suspension.
  In the second procedure the composite has been produced by simply adding the TiO_2 in the aqueous solution containing Ag_2CO_3 after its precipitation by reaction between $AgNO_3$ and Na_2CO_3.

- TiO_2+Ag_2CO_3+GO composite: firstly about 0.038 g of GO have been sonicated for one hour in 20 ml of distilled water in a glass container in order to obtain a homogeneous brown suspension. Subsequently 0.48 g of TiO_2 have been added to the suspension and the new dispersion have been mechanically stirred for an hour. After this step about 5 ml of a 0.1 M solution of Na_2CO_3 in distilled water have been added to the system which has subsequently sonicated for an hour. As a final step, 15 ml of a 0.1 M solution of $AgNO_3$ have been added to the suspension in order to produce silver carbonate. According to the relative amount of the components employed the final composition of the catalyst is: 70% TiO_2, 29.5% Ag_2CO_3

- Ag_2CO_3+GO composite: the last catalyst has been produced according to the procedure developed by Song *et al*. [368]. In this case the starting point is the dispersion of graphene oxide in deionized water (typically about 0.014 g in 20 ml) by sonication (30 minutes at 40% of instrument maximum amplitude). Subsequently $AgNO_3$ (0.849 g) is added to the suspension and a second sonication step is accomplished (15 minutes, at 40% of instrument maximum amplitude). 20 ml of Na_2CO_3 (0.125 M aqueous solution) are added dropwise to the mixture and the solution is kept under stirring for an hour. The precipitate is then filtered or centrifuged, washed several times with distilled water and ethanol to remove residual impurities and finally dried at 60°C for six hours. The final composite has a final mass content in graphene oxide of 2%.

For each type of nanocomposite realized the relative suspension has been left under stirring overnight and the precipitate formed has been subsequently filtered and washed several time with water and ethanol. The obtained product has been dried in oven at 50°C under vacuum until complete dryness. The catalysts have been ground to fine powder before processing for the preparation of the membranes by electrospinning. The recovered product after the removal of water has a pale gray color while after the drying process the material turned into a dark blue.

8.3.2 Photocatalysts characterization

The single and composites photocatalysts selected for the subsequent work have been analyzed by XRD and FT-IR techniques to identify their successful synthesis and coupling, analyzed by UV-visible diffuse reflectance spectroscopy to identify their light absorption characteristics and investigated by electron microscopy to evaluate their coupling and morphological features.

8.3.2.1 *XRD*

The WAXD pattern of Ag_2CO_3 (Figure 8.1) present the diffraction peaks at 2θ = 18.6°, 20.5°, 32.6°, 33.6°, 39.6°, 41.8° which can be indexed to crystallite planes of (020), (110),(-101), (-130), (200), (031), (220), (131) that correspond to monoclinic phase Ag_2CO_3 (JCPDS card No. 70-2184) [369] with lattice constant a = 4.84Å, b = 9.54Å, c = 3.24Å and β = 92.7°. No peaks from other impurities, such as metallic silver can be detected and the high diffraction intensity suggests that the sample has good cristallinity.

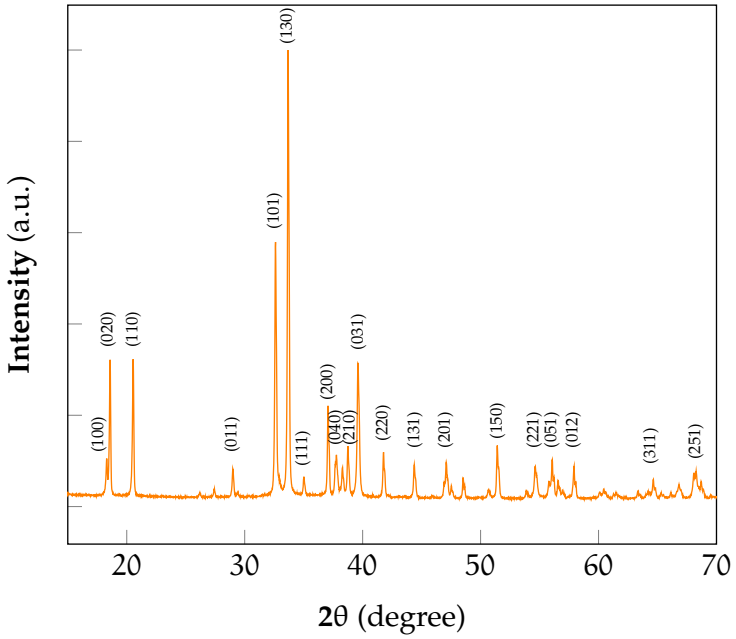

Figure 8.1: *XRD diffractogram of the synthesized Ag_2CO_3*

The complete list of peaks and related reflection planes are listed in Table 8.1 and have been identified by application of the Bragg law, with n = 1. From the calculated diffraction angle the reflection planes have been determined by comparison with the literature reference data [370] obtaining confirmation of the successful synthesis of the compound without detectable traces of impurities.

The WAXD pattern of the ternary compound (Figure 8.2) is more complex and the qualitative analysis shows the presence of different compounds. The identifiable peaks allows the identification of the two different crystalline form of titanium dioxide, rutile (27.4°, 36.1°, 41.2°) and anatase (25.3°, 37.8°, 48.0°, 53.9°, 55.1°, 62.7°, 68.8°, 70.3° and 75.0°) along with the characteristic peaks associable to the silver carbonate, without presence of

Table 8.1: *Diffraction data for the monoclinic structure of the synthesized Ag_2CO_3 (hkl = Miller indexes, d = interplanar distance,)*

hkl	2θ [degree]	d [Å]	Relative intensity [%]
100	18.3	4.85	10
020	18.5	4.78	10
110	20.5	4.32	32
011	29.0	3.08	32
101	32.7	2.74	58
130	33.7	2.66	100
111	35.0	2.56	7
200	37.1	2.42	22
040	37.8	2.39	11
210	38.3	2.35	9
121	37.8	2.38	13
031	39.7	2.27	31
220	41.8	2.16	12
131	44.4	2.04	9
201	48.5	1.875	6
150	51.4	1.777	13
221	54.7	1.678	9
051	56.1	1.639	10
012	57.9	1.591	9
311	66.8	1.4	5
251	68.2	1.3747	8

any type of impurity. Notably, besides the peaks of the two semiconductors a bump is detectable at $2\theta \sim 9°$. Such broad bump has a maximum corresponding to the characteristic diffraction peak of graphene oxide, but due to the low amount of the latter in the composite it can not be identified as proof its present in the final composite. Besides the same bump is clearly visible in the diffractogram of the TiO_2-Ag_2CO_3 composite and by taking a closer look to the results of the pure Ag_2CO_3 a small increase in the intensity above the baseline of the diffractogram can be identified. The higher intensity of the corresponding signal in the composites diffractograms can be ascribed to the derivation of the signal associated to titania which, as can be seen for the case of the pure compound, has non null slope between 5° and 20°. The broad nature of this bump can thus be ascribed to the presence of partial amorphous component in the structure of Ag_2CO_3.

The Scherrer equation was applied to estimate the average crystallite size of the sample (Table 8.2) using the FWHM of the XRD peak corresponding to the (130) plane [371] for Ag_2CO_3 and the (101) plane of anatase for TiO_2 diffractogram. The grain size of TiO_2 is in good accordance with the particles size reported by the manufacturer of the material of about 21 nm while the grain size of Ag_2CO_3 is two times higher suggesting the formation

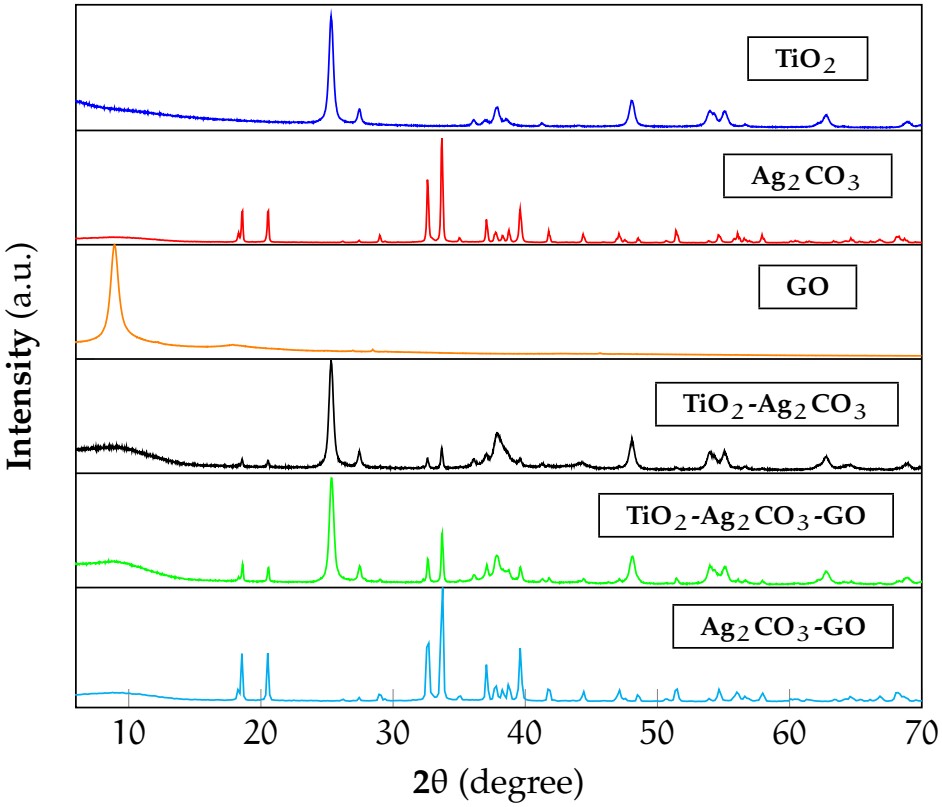

Figure 8.2: *WAXD spectra of TiO_2, Ag_2CO_3, GO, TiO_2-Ag_2CO_3 and TiO_2-Ag_2CO_3-GO, Ag_2CO_3-GO composites photocatalysts*

Table 8.2: *Average grain size of the samples calculated from XRD analysis*

Sample	Average grain size [nm]
Ag_2CO_3	58
TiO_2	22
Ag_2CO_3/GO	54
TiO_2/Ag_2CO_3	54
TiO_2/Ag_2CO_3/GO	54

of particles with higher dimensions, with slight decrease in the size related to the silver carbonate contained in the composites.

8.3.2.2 *FTIR*

A second characterization of the composites has been realized by the analysis of the infrared spectrum of the composites compared with that of pristine TiO_2, Ag_2CO_3 and graphene oxide. In the FTIR spectrum of Ag_2CO_3 it is possible to find the representative absorption bands at 1,448, 1,378, 883 and 705 cm^{-1} which can be associated to CO_3^{2-} [368], other peaks are located at 3386 and 3183 cm^{-1} (partially overlapped), and 1,659 cm^{-1}. In the Ag_2CO_3-GO composite a few changes are present in the infrared spectrum of the

composite with respect to the pure Ag_2CO_3. First the presence of new peaks at 1,476 cm^{-1} and 3,013 cm^{-1} (partially overlapped with that at 3,184 cm^{-1}) and the inversion on the relative intensity between the peaks at 705 and 669 cm^{-1} with a decrease in intensity of the latter with respect to the first.

The composites containing titania and silver carbonate presents the typical peaks at

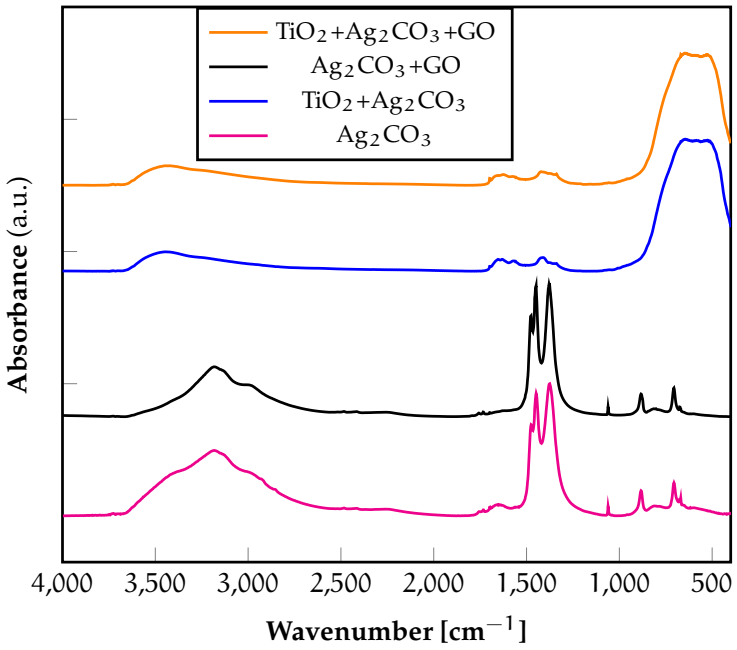

Figure 8.3: *Infrared spectra of Ag_2CO_3, TiO_2+Ag_2CO_3 and TiO_2+Ag_2CO_3+GO composites photocatalysts*

typical peaks at 505 cm^{-1} and 650 cm^{-1} of the O-Ti-O bonding in anatase morphology along with a tiny peak at 1,630 cm^{-1} and a broad absorption band with a maximum at 3,420 cm^{-1}, ascribed to the bending and vibration of surface-adsorbed water and hydroxyl groups. Besides also the characteristic peak of silver carbonate at 1,630 and 1,410 cm^{-1} are presented as further confirmation of the coupling of the two materials.

8.3.2.3 *TGA*

The analysis of the degradation of silver carbonate in air is important for the quantification of the content of catalyst on the electrospun membranes. Silver carbonate is known to be thermally instable above 200°C and can decompose by generating CO_2. Generally the thermal decomposition follows the subsequent scheme [372]:

$$Ag_2CO_3 \rightarrow Ag_2O + CO_2 \quad (\Delta m_1/m_0(Ag_2CO_3) = -15.96\%) \tag{8.2}$$

$$Ag_2O \rightarrow 2Ag + \frac{1}{2}O_2 \quad (\Delta m_2/m_0(Ag_2CO_3) = -5.80\%) \tag{8.3}$$

The thermal decomposition of Ag_2CO_3 is thus a multistep process and the extent of the different mass losses has been proved to be affected by the preparation conditions of the compound [373], presence of impurities [372], heating rate [374] and the decomposition

atmosphere [375]. Besides Yoshikawa *et al.* [374] have shown that the decomposition results from a competitive interaction of two physicochemical processes, i.e., sintering of the product particles in the surface product layer and the diffusional removal of the generated gases, during the thermal decomposition of Ag_2CO_3 and the intermediate compound Ag_2O. In this case the Ag_2CO_3 has been synthesized by an exchange reaction between $AgNO_3$ and Na_2CO_3. The analysis on the silver carbonate produced for the tests have

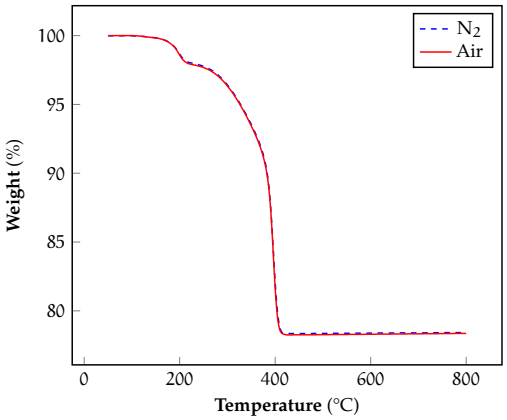

Figure 8.4: *TGA curves of Ag_2O and Ag_2CO_3*

been carried under nitrogen and under air to evaluate differences which could bu ascribed on the type of decomposition atmosphere, in the final residue. As can be seen from Figure 8.4 the two curves are perfectly overlapped, meaning that the transitions experience by the material during the decomposition are the same. The thermal degradation involves two steps and the final residue is 78.4% which is in agreement with the theoretical residue associated to the formation of metallic silver by generation of CO_2 and O_2.

8.3.2.4 *UV-visible diffuse reflectance spectroscopy*

Diffuse reflectance spectra have been collected with an integrating sphere on solid samples prepared by mixing $BaSO_4$ with a 5% by weight of the catalyst to be analyzed, analogously to the case of the graphene based photocatalysts. In this case, since two different semiconductors have been employed, DSR spectra can provide also information about the relative position of the conduction and valence of the two photocatalysts. For a compound, at the point of zero charge, the valence band (VB) position can been calculated by the following empirical formula [376]:

$$E_{VB} = X - E_e + 0.5 \cdot E_g \tag{8.4}$$

where X is the absolute electronegativity of the semiconductor [eV], which is defined as the geometric mean of the absolute electronegativity [eV] (Mulliken electronegativity) of the constituent atoms (defined as the arithmetic mean of the atomic electron affinity and first ionization energy), E_e is the energy of free electrons [eV] on the hydrogen scale (ca. 4.5 eV), E_{VB} is the VB edge potential [eV], and E_g is the band gap of the semiconductor.

The conduction band (CB) position can be deduced by the following relationship:

$$E_{CB} = E_{VB} - E_g \tag{8.5}$$

The values obtained are in the normal hydrogen electron (NHE) scale and can be converted in the absolute vacuum scale (AVS) by subtracting 4.5 from the NHE values:

$$E_{CB,AVS} = -4.5 - E_{CB,NHE} \tag{8.6}$$

$$E_{VB,AVS} = -4.5 - E_{VB,NHE} \tag{8.7}$$

Different are the values of the calculated band gap for Ag_2CO_3 reported in the scientific literature, ranging from 2.08 to 2.62 eV [350, 369, 377–380]. Despite this the common value for the adsorption edge of this compounds is generally recognized to be around 480 nm. The DRS spectra of Ag_2CO_3 along with those of the pure compounds employed for the realization of the different photocatalytic composites is depicted in Figure 8.5. As can be seen Ag_2CO_3 and GO present a lower absorption intensity compared to TiO_2, but a wider and narrower absorption range, respectively. All the DRS spectrum have been manipulated according to the Kubelka-Munk function with n=2 (indirect band gap).

Table 8.3: *Electronegativity properties of the atoms of the photocatalysts employed (E_{fi} = energy of first ionization, E_{aff} = electron affinity, X = absolute electronegativity)*

Atom	E_{fi} [kJ/mol]	E_{aff} [kJ/mol]	E_{abs} [kJ/mol]	X [eV]
Ag	731	126	428.5	4.44
C	1087	122	604.5	6.26
O	1314	141	727.5	7.54
Ti	659	8	333.5	3.46

Table 8.4: *Valence and conduction band position of the pure photocatalyst employed on the basis of the band gap energies calculated from DRS spectra*

Catalyst	Band gap (n = 1/2) [eV]	Abs. edge [nm]	X [eV]	E_{VB} [eV]	E_{CB} [eV]
TiO_2 (anatase)	3.21	388	5.81	2.92	-0.30
TiO_2 (rutile)	3.00	413	5.81	2.81	-0.19
Ag_2CO_3	2.15	545	6.13	2.71	0.56

The DRS spectra of the composites photocatalysts is shown in Figure 8.6. As can be seen the coupling of TiO_2 with Ag_2CO_3 induces an increase in the absorption in UV range and a red shifty towards higher wavelengths which is translated in an extension of the band gap of the material with respect to the reference TiO_2. Besides there is also absortpion in the visible range from 400-800 nm, similarly to what have been found with the case of the graphene based photocatalysts. While no differences are present in the UV range,

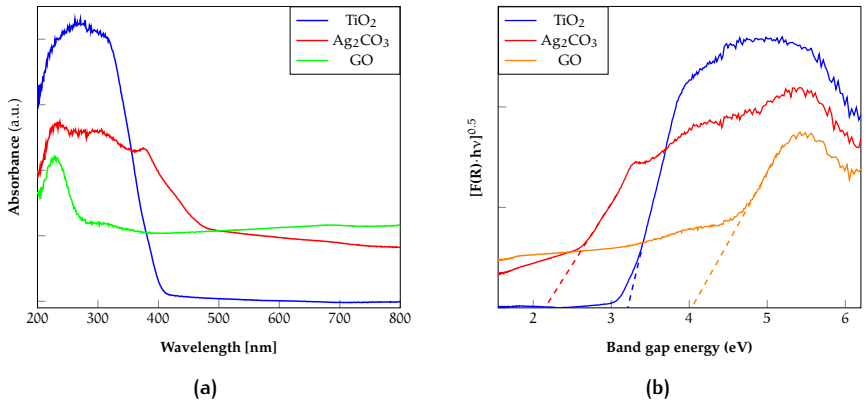

Figure 8.5: *(a) DRS spectra of pure components for the determination of the absorbance edge and (b) plot of $[F(R)\cdot h\nu]^{0.5}$ versus the energy for the determination of the band gap of the semiconductors*

between the two composites containing Ag_2CO_3, there is an higher absorption in visible range for sample comprising graphene oxide. For the Ag_2CO_3/GO generally the intensity of the absorption is lower than the other composites but the absence of TiO_2 produces a spectrum in which a band gap is not detectable.

This is accordance to the findings of previous studies [368, 381] on this composite pho-

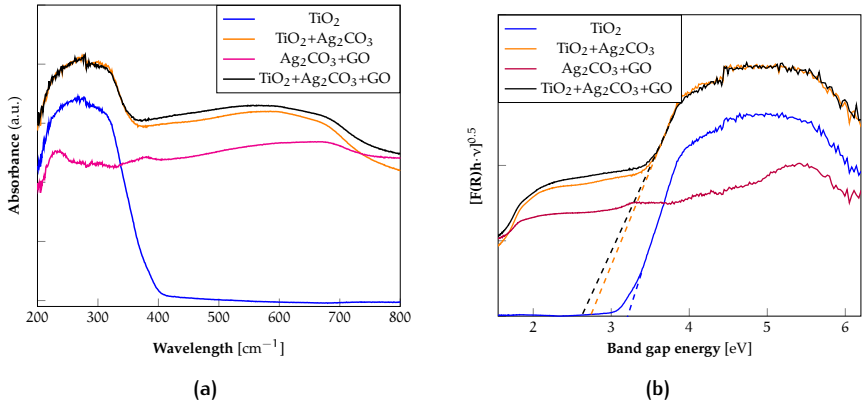

Figure 8.6: *(a) DRS spectra of composites catalytic systems and (b) plot of $[F(R)\cdot h\nu]^{0.5}$ versus the band gap energy in comparison with the reference TiO_2*

tocatalyst. Besides the high surface area of GO can improve the absorption of pollutants which in turn can provide benefits in the enhancement of the photocatalytic performance, while its superior electron conductivity can transfer photo-excited electrons (e^-) generated in Ag_2CO_3 to the surface of GO, thus enhancing the separation of the photo-generated electrons (e^-) and holes (h^+). Electron can react with adsorbed O_2 and transform to $O_2\cdot^-$ radicals. At the same time OH groups on the surface of catalyst can capture holes (h^+) to generate ·OH radicals. Table 8.5 shows the results of the calculation from the DRS spectra for the determination of the absorption edge and band gap. Notably the incorporation of silver carbonate produces an higher enhancement in absorption characteristic towards the

Table 8.5: *Band gap energy and absorbance edge values from DRS spectra of the different catalytic systems analyzed*

Catalyst	Band gap (n = 1/2) [eV]	Absorbance edge [nm]
TiO_2 (P25 Degussa)	3.21	387
Ag_2CO_3 (synthesized)	2.15	545
GO (Aldrich)	4.03	303
TiO_2+Ag_2CO_3 (70:30)	2.73	483
TiO_2+Ag_2CO_3+GO (70:29.5:0.5)	2.62	507
Ag_2CO_3+GO (98:2)	-	-

visible spectrum with respect to the graphene based photocatalysts of the previous part of the study; this means that this strategy could be more suitable for the preparation of visible responsive photocatalysts.

8.3.2.5 *SEM*

The synthesized particles of Ag_2CO_3 have been analyzed by electron microscopy to identify particles' dimensions and geometry. As can be seen from Figure 8.7 the Ag_2CO_3 is composed of microcuboids with a length of 0.5−2 μm.

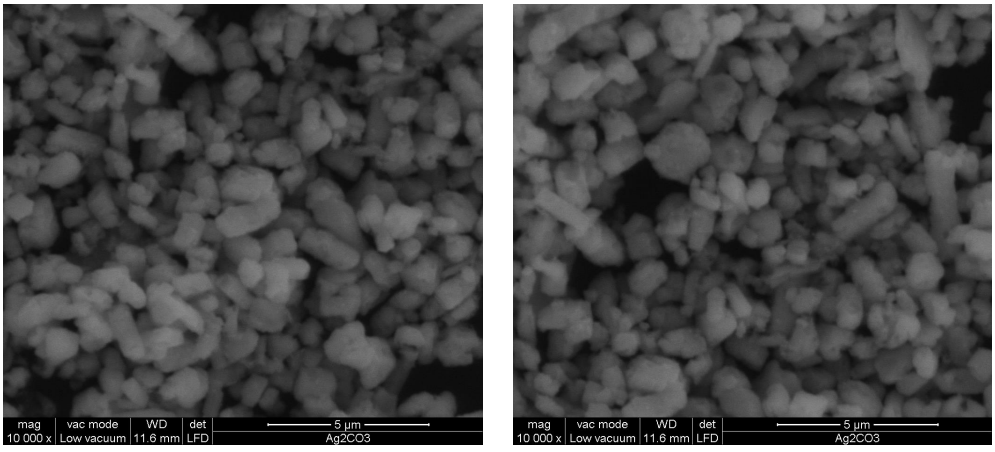

(a) (b)

Figure 8.7: *SEM micrographs of the synthesized particles of Ag_2CO_3*

8.3.2.6 *TEM*

A further characterization of the photocatalysts has been made by TEM on the powder dispersed in water by sonication. The Figure 8.8 presents the Ag_2CO_3+GO composites and shows a good deposition of the silver carbonate particles on the surface of the graphene oxide sheets. The particles are in contact between each other even after the sonication, meaning a good physical interaction between the two. Notably the dimension of the silver

particles are significantly reduced thus the presence of the dispersed graphene oxide in the solution in which the silver carbonate is produced by precipitation can have a significant impact in the reduction of the particles size.

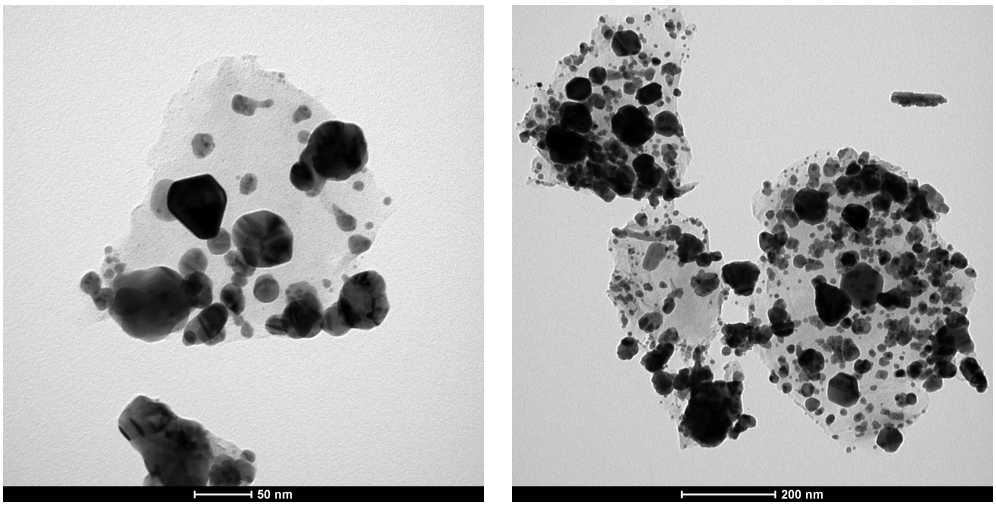

(a) (b)

Figure 8.8: *TEM micrographs of the Ag_2CO_3+GO catalyst particles*

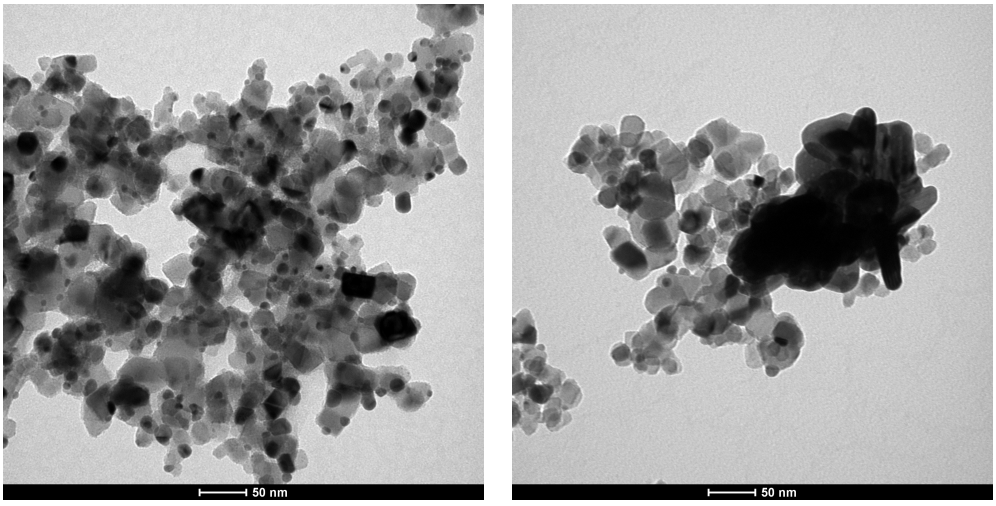

(a) (b)

Figure 8.9: *TEM micrographs of the TiO_2+Ag_2CO_3+GO catalyst particles*

Figure 8.9 shows the TEM micrograph of the TiO_2+Ag_2CO_3+GO sample. Even in this case a good coupling seems to be present between the two main components. The graphene oxide is of difficult identification and it is not detectable probably due to its low content (approximately 0.5%). Interesting to note is the fact that even in this case the dimension of the silver carbonate particles is lower than those of the pure compound obtained by precipitation in aqueous solution.

8.4 MEMBRANES PREPARATION BY ELECTROSPINNING

After the preparation of the catalysts the membranes have been produced by electrospinning starting from PAN/catalyst solutions in DMF. In each case the solution was prepared by using a catalyst/polymer ratio of 70:30 and a solution concentration of 5% by weight of PAN in DMF. The sequence for the preparation of the polymeric solution for the electrospinning required a first dispersion of the catalyst into DMF by mechanical stirring for an hour followed by the addition of the required quantity of polymer and subsequent stirring overnight to obtain an homogeneous solution. For completeness even the bare Ag_2CO_3 has electrospun with PAN in order to obtain the corresponding membranes.

- PAN/Ag_2CO_3: in this case three different ratios between the polymer and the photocatalyst have been added due to the difficulty in the deposition of the fibers, the electrospinning process has been carried using the conditions reported in Table 8.6:
  - 70/30 polymer-to-catalyst mass ratio: 1.22 g of DMF, 0.15 g of silver carbonate, 0.064 g of PAN (5% w/w with respect to the solvent quantity), 0.15 of Triton X-100 (50% w/w with respect to Ag_2CO_3)
  - 60/40 polymer-to-catalyst mass ratio: 1.27 g of DMF, 0.1 silver carbonate, 0.067 g of PAN (5% with respect to the solvent quantity)
  - 50/50 polymer-to-catalyst mass ratio: 9.44 g of DMF, 0.5 g of silver carbonate, 0.5 g of PAN (5% w/w with respect to the solvent quantity)

Table 8.6: *Electrospinning process parameters for the production of the PAN/Ag_2CO_3 composite membranes with different catalyst-to-polymer ratios*

Parameter	Value	Units
Flow-rate	0.900	ml/h
Voltage	15	kV
Tip-to-collector	20	cm
Needle (i.d)	0.413	mm
Relative humidity	< 30	%

Serious deposition problems have been encountered during the deposition of the fibers with the catalyst-to-polymer ratios of 70:30 and 60:40 and the production of a homogeneous membrane has been reached only in the 50:50 case for which the deposition time has been set at 80 minutes.

- PAN/Ag_2CO_3+GO: the electrospinning process has been carried using the conditions reported in Table 8.7. In this case the fibers experienced a complicated deposition which was not improved in any way by changing the process parameters.

- PAN/TiO_2+Ag_2CO_3: a typical solution for a production of an entire set of 5 membranes requires 7.22 g of DMF, 0.08 g of silver carbonate, 0.88 g of TiO_2 and 0.38 g of

Table 8.7: *Electrospinning process parameters for the production of the PAN/Ag_2CO_3+GO composite membranes with different catalyst-to-polymer ratios*

Parameter	Value	Units
Flow-rate	0.900	ml/h
Voltage	18	kV
Tip-to-collector	15	cm
Needle (i.d)	0.700	mm
Relative humidity	< 30	%
Deposition time	90	min

PAN (5% w/w with respect to the solvent quantity), the electrospinning process has been carried using the conditions reported in Table 8.8

Table 8.8: *Electrospinning process parameters for the production of the PAN/TiO_2+Ag_2CO_3 composite membranes with different catalyst-to-polymer ratios*

Parameter	Value	Units
Flow-rate	0.900	ml/h
Voltage	18	kV
Tip-to-collector	15	cm
Needle (i.d)	1.200	mm
Relative humidity	< 30	%

- PAN/TiO_2-Ag_2CO_3: a typical solution for the preparation of a 5 membranes set requires 5.66g of DMF, 0.7 g of composite, 0.3 g of PAN (5% w/w with respect to the solvent), the electrospinning process has been carried using the conditions reported in Table 8.9

Table 8.9: *Electrospinning process parameters for the production of the PAN/TiO_2-Ag_2CO_3 composite membranes with different catalyst-to-polymer ratios*

Parameter	Value	Units
Flow-rate	0.900	ml/h
Voltage	18	kV
Tip-to-collector	15	cm
Needle (i.d)	1.2	mm
Relative humidity	< 30	%
Deposition time	90	min

- PAN/TiO_2+Ag_2CO_3+GO: the electrospinning process has been carried using the conditions reported in Table 8.10. After this passage the polymer is added to the dispersion and the solution is stirred mechanically until reaching the complete dissolution of the polymer. The final membranes are gray and the deposition is quite straightforward.

Table 8.10: *Electrospinning process parameters for the production of the PAN-ternary (TiO_2/Ag_2CO_3/graphene oxide) composite membranes*

Parameter	Value	Units
Flow-rate	0.900	ml/h
Voltage	15	kV
Tip-to-collector	20	cm
Needle (i.d)	0.413	mm
Relative humidity	20	%
Deposition time	45	min

8.5 MEMBRANES CHARACTERIZATION

As done previously the electrospun membranes have been characterized electron microscopy for the evaluation of the final morphology of the fibers and indentification of the dispersion of catalysts and co-catalysts. The TGA analysis have been performed in order to determine the amount of catalyst deposited.

8.5.1 PAN/Ag_2CO_3 membranes

The first membranes analyzed have been those containing only Ag_2CO_3. Here different ratios between the catalyst and the polymer have been screened due to difficulties in the electrospinning of the final membranes. Generally the higher the ratio of catalyst to polymer the more difficult has been the electrospinning and the reason can be explained by looking at the morphology of the samples. Figure 8.10 shows the sample employing a catalyst/polymer ratio of 70/30. It is possible to observe that the low content in polymer prevent the formation of uniform covered fibers. Probably the higher dimension of the photocatalyst particles than the characteristic diameter of the polymeric nanofibers obtainable by the electrospinning process are such that with that ratio the particles are not capable to be spread along the fibers. The particles form big agglomerates which are connected by the polymer fibers. With a lower catalyst/polymer ratio of 60/40 (Figure 8.11)

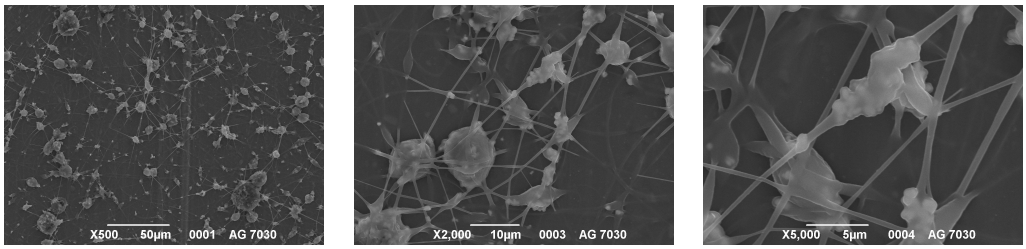

(a) (b) (c)

Figure 8.10: *SEM micrographs of PAN/Ag_2CO_3 electrospun nanofibers with a catalyst-to-polymer ratio of 70/30 at different magnifications*

the morphology changes and its was possible to obtain more uniform fibers. In this case

the surface of the fibers are quite rough and the final diameter is very high (~10 μm). Despite the more homogeneous morphology the ratio has provided to be not suitable to obtain a stable electrospinning process with problems of syringe tip clogging and very difficult homogeneous deposition.

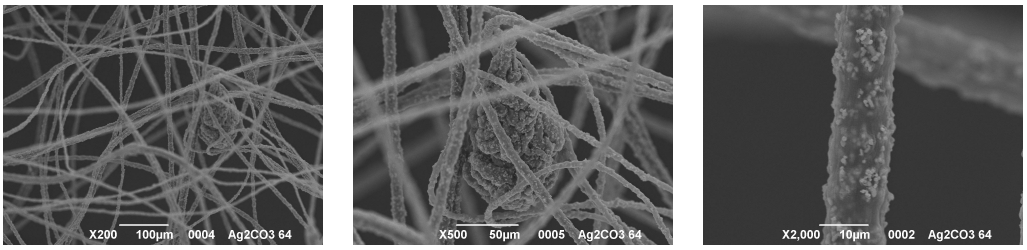

(a) (b) (c)

Figure 8.11: *SEM micrographs of PAN/Ag_2CO_3 electrospun nanofibers with a catalyst-to-polymer ratio of 60/40 at different magnifications*

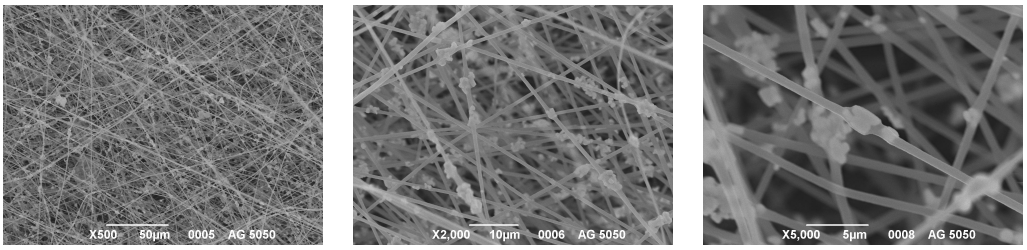

(a) (b) (c)

Figure 8.12: *SEM micrographs of PAN/Ag_2CO_3 electrospun nanofibers with a catalyst-to-polymer ratio of 50/50 at different magnifications*

In the case of the lower catalyst/polymer ratio (50:50) the deposition is more straightforward and it is possible to generate and deposit easily the nanofibers in order to obtain a testable membrane. However as can be seen from Figure 8.12 by lowering the ratio employed between the catalyst and the polymer the catalyst particles are no more uniformly distributed along the fibers and in most of the cases they are embedded inside the same fibers preventing to obtain they disposition on the outer surface of the membrane.
In this manner, although it is possible to obtain a protection from the phenomenon of photocorrosion [382], it is not possible to obtain photocatalytic activity of these membranes because the contact between the catalyst surface and the molecules of the organic pollutant is prevented. The TGA analysis are shown in Figure 8.13. The final residue is ~ 40% which is in accordance with the theoretical value associated to the removal of the organic component and the formation of metallic silver. Table 8.11 shows the amount of catalyst on the final membranes.

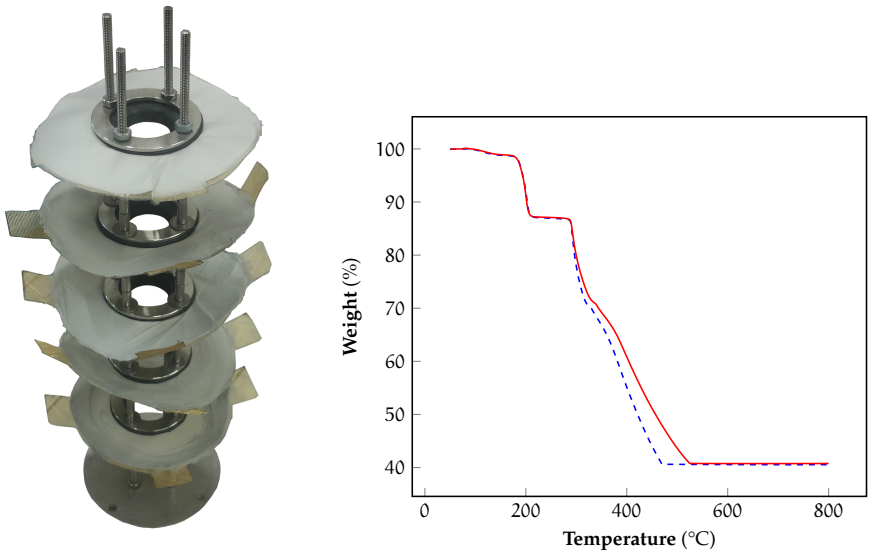

(a) (b)

Figure 8.13: *(a) membrane set-up and (b) TGA of the PAN/TiO_2+Ag_2CO_3 50:50 system*

Table 8.11: *Amount of catalyst as calculated from the gravimetric analysis residue for the PAN/Ag_2CO_3 membranes prepared*

Membrane sample	Catalyst for single membrane [mg]	Catalyst for a membrane set [mg]	Specific amount of catalyst [mg]
PAN/Ag_2CO_3	42.88 ± 3.1	214.4 ± 15.5	0.65 ± 0.03

8.5.2 PAN/Ag_2CO_3+GO

Figure 8.14 shows the images from SEM of the electrospun membranes for this type of membranes. The fibrous structure of all the sample is quite completely covered by the catalyst.

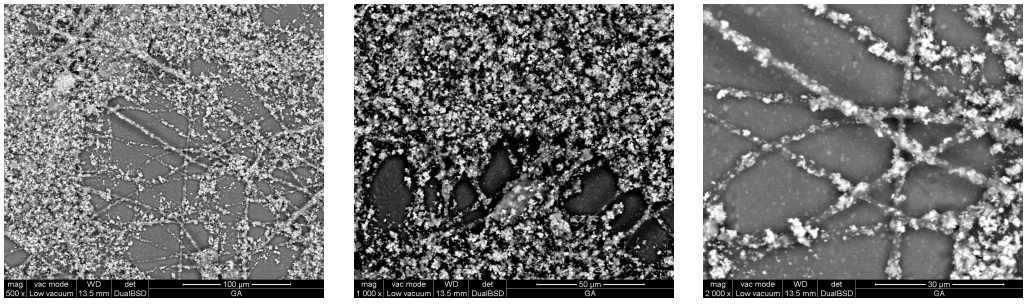

(a) (b) (c)

Figure 8.14: *SEM micrographs of PAN/Ag_2CO_3+GO electrospun nanofibers*

Even in this case the electrospinning process has been quite complicated and and it has not led to satisfactory results due to extreme difficulty in the deposition of the fibers produced. Due to the bad final morphology of the electrospun samples and the intrinsic

difficulty in the deposition of the fibers these kind of membranes have been discarded for further testing and thus TGA analysis has not been performed.

8.5.3 PAN/TiO_2+Ag_2CO_3

Here the comparison has been done on two different samples in order to define a possible difference due to the different ways by which the two photocatalyst have been coupled.

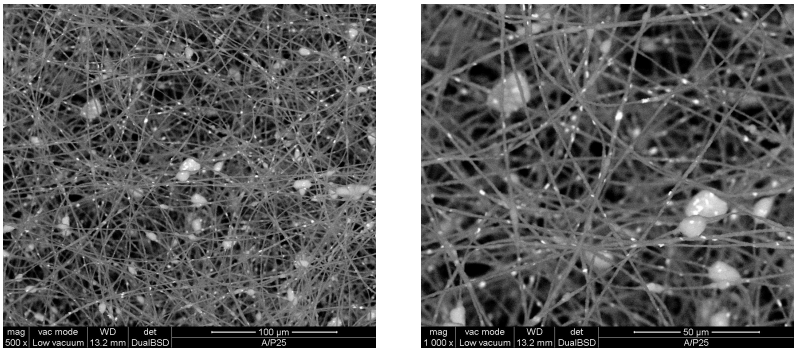

(a) (b)

Figure 8.15: *SEM micrographs at different magnifications of the nancomposite fibers of PAN with TiO_2+Ag_2CO_3 obtained by precipitation of Ag_2CO_3 in a colloidal dispersion of TiO_2*

Figure 8.15 and Figure 8.16 shows the fibers of the TiO_2-Ag_2CO_3 and TiO_2+Ag_2CO_3, respectively.

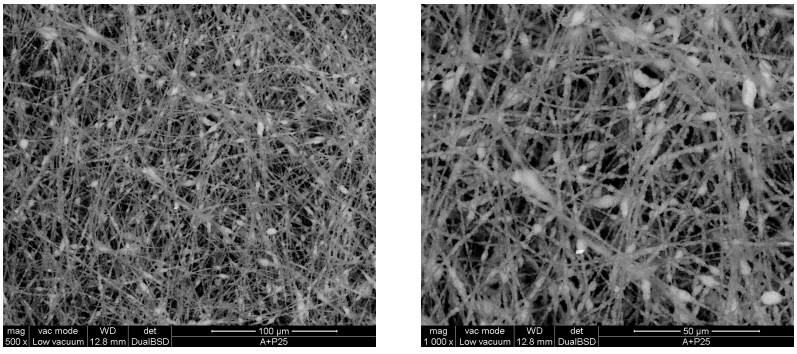

(a) (b)

Figure 8.16: *SEM micrographs at different magnifications of the nancomposite fibers of PAN with TiO_2+Ag_2CO_3 obtained by physical mixing*

As can be seen in the first case not only the fibers are more homogeneous and thin but the silver carbonate is exposed towards the external surface of the fibers as white spots among the titania layer. In the second case. although not visible by the micrographs, the presence of silver carbonate as been identified by EDAX semi-quantitative micro-analysis

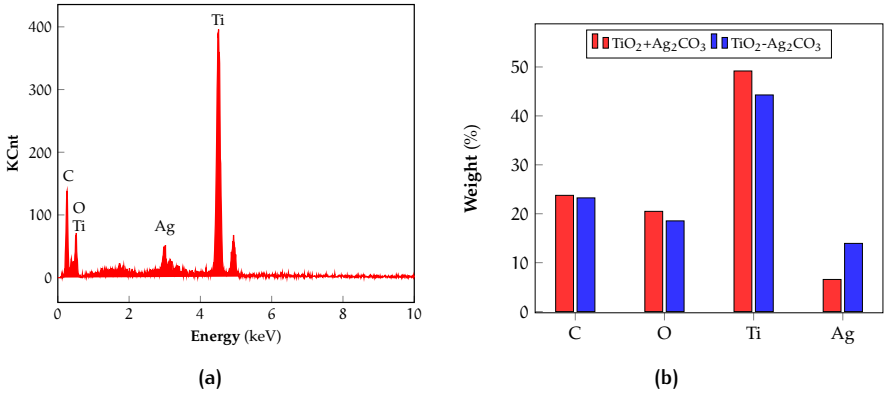

Figure 8.17: *(a) Micro-analysis of the PAN/TiO_2+Ag_2CO_3, (b) Comparison of the elements content from the microanalysis between the two different approaches for the production of the photocatalyst*

(Figure 8.17). Thus by physical mixing silver carbonate preferentially deposits on the inner part of the fibers. Since this last morphology has been considered as detrimental for the subsequent test only the first type of procedure has been selected for the production of the membranes and the TGA analysis. The TGA analysis and thermograms are resumed in

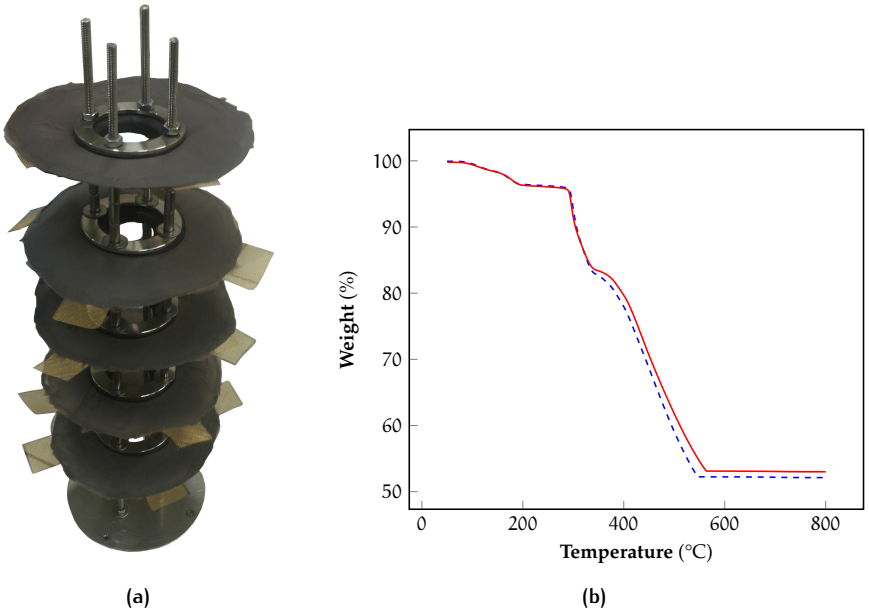

Figure 8.18: *(a) membrane set-up and (b) TGA of the PAN/TiO_2+Ag_2CO_3 system*

Figure 8.18 and Table 8.12.

8.5.4 PAN/TiO_2+Ag_2CO_3+GO

The ESEM micrograph of the membranes with the ternary photocatalytic system are shown in Figure 8.19. Even in the case the formation and deposition of the fibers is quite easy, thus the presence of titania can more easily allow the formation of homogeneously

Table 8.12: *Amount of catalyst as calculated from the gravimetric analysis residue for the membranes produced*

Membrane sample	Catalyst for single membrane [mg]	Catalyst for a membrane set [mg]	Specific amount of catalyst [mg]
PAN/TiO_2+Ag_2CO_3	55.54 ± 3.3	277.7 ± 16.6	0.84 ± 0.05

fibers in presence of silver carbonate. Both the two photocatalysts are exposed on the outer

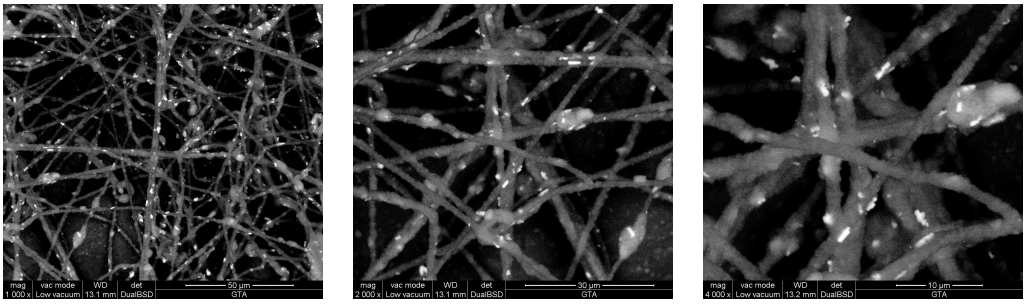

(a) (b) (c)

Figure 8.19: *SEM micrographs at different magnifications of the nancomposite fibers of PAN with the ternary catalyst of TiO_2+Ag_2CO_3+GO*

surface of the fibers and they can be in contact with the pollutant during the photocatalytic tests, while graphene oxide is not identifiable although its presence is justified by the color of the membranes which is darker than the previous type. The results of the TGA analysis and the amount of catalyst deposited along with the fibers are reported in Figure 8.20 and Table 8.13.

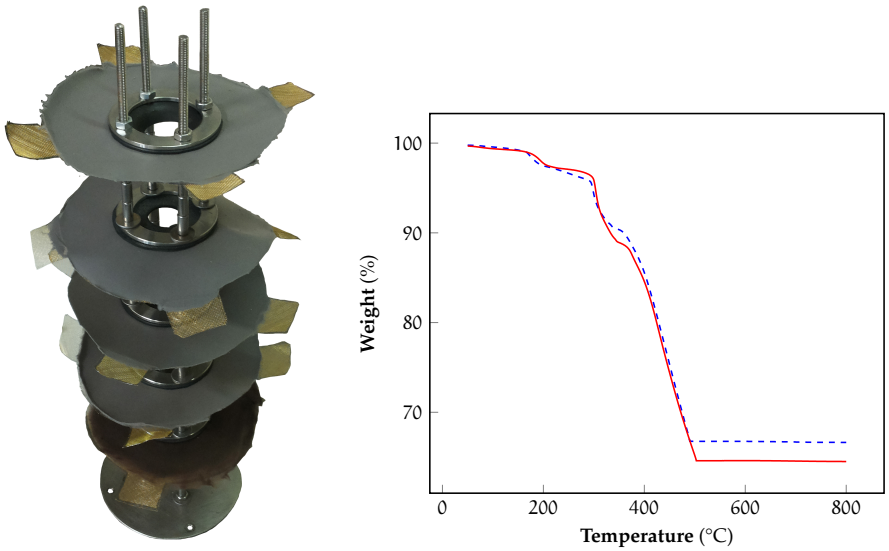

(a) (b)

Figure 8.20: *(a) membrane set-up and (b) TGA of the PAN/TiO_2+Ag_2CO_3+GO system*

Table 8.13: *Amount of catalyst as calculated from the gravimetric analysis residue for the PAN/TiO_2+Ag_2CO_3+GO membranes*

Membrane sample	Catalyst for single membrane [mg]	Catalyst for a membrane set [mg]	Specific amount of catalyst [mg]
PAN/TiO_2+Ag_2CO_3+GO	51.7 ± 2.6	230.75 ± 12.9	0.70 ± 0.04

8.6 PHOTOCATALYTIC EXPERIMENTS

The photocatalytic tests have been carried according to the same procedure followed in the previous chapters. In particular for these new photocatalysts comprising silver carbonate preliminary tests have been carried in full scan mode to evaluate the presence of possible new by-products as a consequence of modifications in the reaction scheme for the degradation of methanol. The results of such tests have proved that the main by-products of the photooxidation are still methyl formate as by-product and carbon dioxide as product of complete oxidation. For this reason the tests have been carried in SIR mode, selecting the ions corresponding to the identified chemical species.
The PAN/Ag_2CO_3 has been employed for photocatalytic tests but the results are not shown since they have proved to provide very little photocatalytic activity. The main reason can be found in the catalyst/polymer ratio of 50:50 which has been employed for the production of the membranes. With this low value the final membranes can be easily produced but the catalyst remain mainly confined inside the fibers and thus it can not provide adsorption of the pollutant and photocatalytic activity. Consequently only the results of the PAN/TiO_2+Ag_2CO_3 and PAN/TiO_2-Ag_2CO_3+GO are presented.

8.6.1 PAN/TiO_2-Ag_2CO_3

The results of the first type of membranes are shown in Figure 8.21 for which the starting concentrations over the days have been 2700, 3500 and 2800 ppm. As can be seen, commonly to the results of other type of membranes, the photocatalytic activity increases significantly after the first day of reaction. For the last two days of reaction the methanol is completely converted after 120 minutes of reaction and the conversion follows and exponential decay over time.

8.6.2 PAN/TiO_2-Ag_2CO_3-GO

For the second type of membranes a significant boost in the performances has been identified over the days and the tests have been carried for an additional fourth day at which the photocatalytic activity has stabilized. Here the starting concentrations have been 7000, 5350, 5900 and 4700 ppm. During the first day the starting concentration is quite high, but the final conversion of 77.5% can be considered quite satisfactory after 300 minutes of reaction. In the second day, thank to the lower initial concentration, the

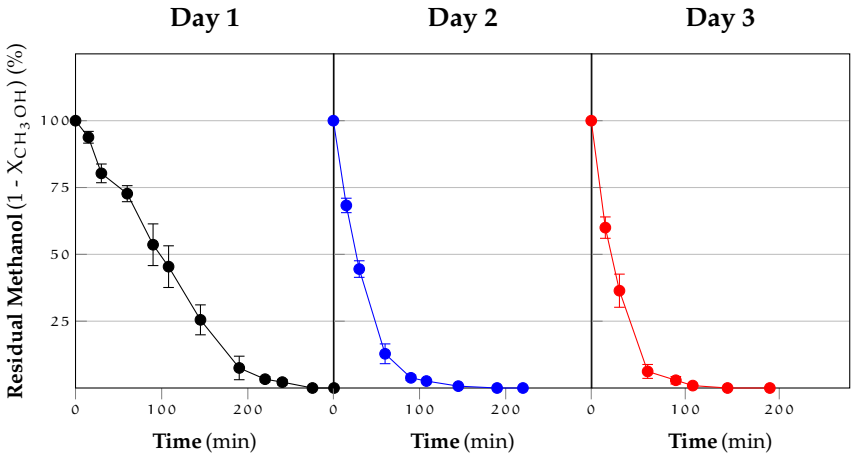

Figure 8.21: *Results of the photocatalytic abatement of methanol for the PAN/TiO_2+Ag_2CO_3 membranes during different subsequent experiments*

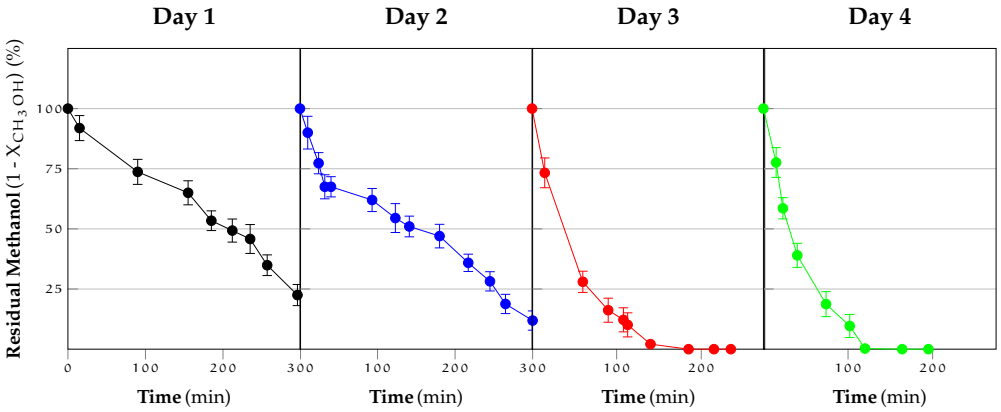

Figure 8.22: *Results of the photocatalytic abatement of methanol for the PAN/TiO_2+Ag_2CO_3+GO membranes during different subsequent experiments*

final conversion reached is 94% while in the last two days the complete conversion of the pollutant is reached after 120-150 minutes.

8.6.3 Comparison of the membranes performances and role of Ag_2CO_3

After the photocatalytic test a comparison of the performances of the different membranes has been performed with respect to the membranes which, in the previous part of the study, have shown the best performances, employing to the same approach (one-step). In order to obtain a fair comparison the evaluation between the different membranes have been realized on the basis of similar starting concentration of pollutant. Here the best membranes (PAN/TiO_2+Ag_2CO_3+GO) have been compared to the reference, PAN/TiO_2, and the PAN/rGO+TiO_2. The comparison has been realized on the basis of the moles reacted by taking into consideration the weight of the catalyst (Figure 8.23). The membranes with silver carbonate exhibit an higher photocatalytic activity compared to those

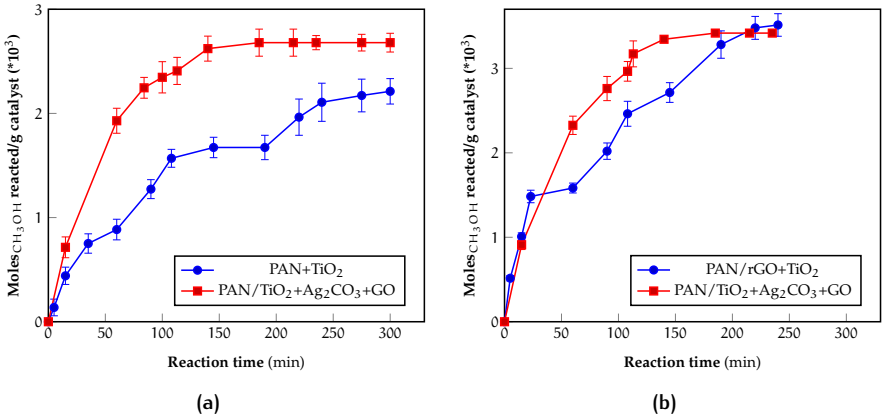

Figure 8.23: *Comparison between the performances of the different types of membranes: (a) PAN/TiO_2 vs. PAN/TiO_2+Ag_2CO_3+GO, (b) PAN/rGO+TiO_2 vs. PAN/TiO_2+Ag_2CO_3+GO*

containing only TiO_2. If compared to the membrane containing the rGO+TiO_2 composite the parformances are comparable but the kinetic of the reaction is improved in presence of the second photocatalyst.

The results of the tests can be explained by taking into consideration the structure of the final photocatalyst in presence of silver carbonate. Theoretically, when a p-type semiconductor and n-type semiconductor form a p-n junction, a strong inner electric field will be formed near the junction, pointing from n toward p, owing to the arrangement of the high concentrations of negatively and positively charged ions. The difference of the electric potential in the electric field can enhance the separation of photogenerated electrons and holes, increasing the quantum efficiency of the photocatalytic reactions. Ag_2CO_3 has been confirmed to exhibit a high photocatalytic activity for organic pollutant degradation, because the incorporation of a nonmetallic p-block carbon element into Ag_2O can broaden the band gap, which can enhance the redox ability [323]. At ambient temperatures, TiO_2 displays n-type semiconducting properties due to a tendency for oxygen deficiency which manifests itself in the formation of either oxygen vacancies or titanium interstitials; both of which are donor-type defects. Therefore, Ag_2CO_3, as a p-type semiconductor, can form a p-n heterojunction with TiO_2, which is an n-type semiconductor.

According to Yu *et al.* [383] the small difference in the VB position between Ag_2CO_3 and TiO_2 (2.71 eV and 2.92 as calculated from the DRS analyses) can lead to a negligible migration of holes from the CB of TiO_2 to that of Ag_2CO_3 under UV irradation. At the same time the high difference in the CB between the two compounds determines a migration of electrons in the CB of Ag_2CO_3; these electrons can react directly with the pollutant to generate $O_2^{\cdot -}$ radicals while the photogenerated hole can react with the OH groups producing $^{\cdot}OH$ radicals that in turn promote the degradation of methanol. The presence of graphene oxide can determine a further enhancement due to the possibility of the photogenerated electron to migrate on its surface, thus reducing the possible recombination with holes within the Ag_2CO_3 phase.

8.7 CONCLUSIONS

Electrospun membranes for the photocatalytic abatement of methanol employing composites of titania and silver carbonate have been produced and tested under UV light. Different photocatalytic composites have been produced and characterized. UV-visible spectroscopy has shown a remarkable improvement in the absorption and band gap narrowing of the photocatalysts comprising silver carbonate, thanks to its visible light harvesting capacity. Pristine silver carbonate has been difficult to electrospin with a colloidal solution comprising the polymer and the catalyst/polymer ratio has been changed to provide the formation of nanofibers. However the final morphology has lead to a confinement of the photocatalyst inside the fibers, determining the impossibility to employ the final membranes for photocatalytic tests. A similar problem as been found with the Ag_2CO_3/GO system for which the catalyst was completely deposited above the fibrous structure, reducing the active surface of the membranes. This reason and the extreme difficulty in the deposition of the fibers have led to discard their use for further testing. For these reason the only membranes tested have been those comprising silver carbonate and titania and a second set with a small addition of graphene oxide (0.5% of the total composition of the composite photocatalyst) to the previous mixture of compounds. Here the ratio of the two semiconductors hase been fixed 70:30 (TiO_2/Ag_2CO_3) in order to evaluate the potential improvement due to the presence of graphene oxide. The best photocatalytic performances have been shown by the the membranes obtained from the ternary system (PAN/TiO_2+Ag_2CO_3+GO), whose photoactivity is higher than those of the membranes with only TiO_2 and comparable to that of those employing the rGO+TiO_2 composite. The explanation of the high photoactivity can be inferred by the heterojunction formed between the Ag_2CO_3 and TiO_2 which can efficiently separate the charge carriers.

Part II.

Nanostructured membranes for PEM fuel cells

INTRODUCTION

Fuel cells are a promising technology for the efficient conversion of chemical energy into electrical energy by oxidation and reduction reactions, with low emission of pollutants. These devices are attracting a considerable attention as alternative energy conversion systems in relation to the emerging energy needs due to the increasing world population. Between the various type of fuel cells, proton exchange membranes fuel cells (PEMFC) have been considered so far promising for both portable and stationary applications thanks to their high power density and low operative temperatures. One of the key aspects for the commercialization of PEMFC is the necessity to provide membranes capable to combine high electrochemical performances with chemical and mechanical stability, with the minimum footprint possible. However the performances of actual commercial electrolyte membranes (e.g. Nafion) suffer from several drawbacks in terms of decrease in efficiency at high operating temperature and low humidity, low thermal stability, high price and high gas permeability. Between the different approaches followed to find alternative for the suitable replacement of these membranes, electrospinning has emerged in the last year as promising strategy for the design of nanofibers capable to provide very high specific surface to volume ratio, good pore interconnectivity and three dimensional networks which are suitable to improve the mechanical properties of composite membranes.
sPEEK is a sulfonated derivate of the poly(aryl ether ketone)'s family, which has been recognized as a promising candidate for the replacement of Nafion for proton exchange membranes (PEMs) due to its good conductivity and thermal stability. A mat of homogeneous electrospun sPEEK nanofibers can provide a suitable reinforcing conductive matrix, whose properties can be tailored according to its sulfonation degree. Besides a very thin fibrous morphology is desirable because it can promote dimensional stability and improve proton conductivity [112] or, in general, the electro-transport of ions through the alignment of the ionic groups along the fiber axis domain. However, despite this potential interest towards the application of such fibers, up to date only few literature works have reported the electrospinning of sPEEK [110, 123, 384, 385]. On the basis of these premises electrospinning has been employed for the preparation of composite proton exchange membranes based on a nanofibrous network of sPEEK. The starting material (PEEK) has been sulfonated and characterized while a specific optimization study has been carried to define optimal parameters for the electrospinning process. Two different approaches have been followed to produce the final composite membranes:

- electrospun sulfonated PEEK of different sulfonation degrees embedded in a proton conductive matrix by a casting procedure
- electrospun sulfonated PEEK of different sulfonation degrees embedded in a non proton conducting matrix by a dual electrospinning approach

The final membranes have been characterized and compared in order to evaluate their performances for practical applications as PEMs.

9 SULFONATION OF PEEK AND CHARACTERIZATION OF SPEEK

Electrophilic aromatic substitution reactions such as halogenation, nitration, sulfonation, Friedel-Crafts acylation and alkylation are of great preparative importance in the production of intermediates vital for the synthesis of many valuable industrial, pharmaceutical, and agrochemicals [386].
Polymer sulfonation is a frequently used process capable to modify the chemical structure of a given polymer in order to improve its expected properties in terms of: better wettability, higher water flux, higher antifouling capacity, better permaselectivity and increase solubility in solvents for processing. The most common approach for the development of proton conducting membrane based on aromatic conducting polymers is the sulfonation of pre-formed, commercially available, polymers. The choice of sulfonic acid groups as a source of protons is due to three reasons: they are easy to introduce into the aromatic rings, they dissociate more readily than typical carboxylic acids, resulting in a larger number of charge carriers, and, unlike phosphonic acids, they do not easily form anhydrides on dehydration, resulting in easy and quick rehydration of sulfonated polymers in contrast to phosponated ones [387].
Sulfonation reactions are typical electrophilic substitutions where more electronegative atoms of oxygen draw the electron density from the sulfur atom, which then becomes an electrophilic center. This electrophilic center can react with the delocalized π-electron system of an aromatic ring at the position with the highest electron density, which is controlled by the position and type of other groups located around the aromatic ring. Common sulfonating agent employed are compounds such as H_2SO_4, SO_3 and its complexes, such as acyl and alkyl sulfates and chlorosulfonic acid [388]. Sulfonation gives a better yield at elevated temperatures, especially in the case of sulfonation to high levels. In addition, the concentration of the sulfuric acid or oleum used as the sulfonating agent influences the course of the reaction. Sulfonation prefers high concentrations of sulfonating agents, while water formed as a side product in the sulfonation reaction reduces the rate of sulfonation [388]. The mechanism of sulfonation can be complex, as it is reversible in many cases, and the reaction rate depends significantly on:

- the nature of the electrophilic species, which may be derived from sulfuric acid or sulfur trioxide;

- the reactivity of the aromatic system under attack.

In this chapter PEEK is sulfonated in concentrated acid; the reaction is carried at different temperatures and the resulting material is analyzed at different reaction time to identify the final sulfonation degree, thermal properties and solubility for the subsequent production of sPEEK nanofibers by electrospinning.

9.1 MATERIALS

PEEK was purchased from Sigma-Aldrich (USA) in the form of pellets, with $\bar{M}_w \approx$ 20,800 and $\bar{M}_n \approx$ 10,300. The polymer was used without further treatment. 96% concentrated sulfuric acid (H_2SO_4) and pure methansulfonic acid (CH_3SO_3H) were purchased from Fluka, N,N-dimethylformamide (DMF), dimethylacetamide (DMAC), dimethyl sulfoxide (DMSO) and N-methyl pyrrolidone (NMP) were purchased from Aldrich (USA).

9.2 CHARACTERIZATION

9.2.1 Acid-base titration

Titration has been employed to evaluate the degree of sulfonation and ion-exchange capacity of sulfonated samples. Ion exchange capacity is important for proton exchange membranes since it is a measure of their ability for proton conduction. The procedure followed for all the samples requires about 0.1-0.2 g of sulfonated polymer soaked in 100 ml of 0.1 M NaCl solution for about 48 h with stirring. During this period of time the Na^+ ion has the possibility to substitute the H^+ ion present on the pendant sulfonic groups along the chain, in this manner the sPEEK-H is converted in its sodium salt form and H^+ ions are released increasing the acidity of the solution. The acid solution obtained has been back-titrated with a 0.01 M NaOH solution using phenolphtalein as indicator and evaluating the volume of the titrant poured until reaching the turning point of the indicator.
Accuracy: The experimental error for the evaluation of the sulfonation degree has been calculated with the error propagation method. The source of errors are: the accuracy of the mass determination with a precision balance ($\pm$ 0.0001 g) and that of the burette employed for adding the required amount of titrant volume to the solution for the back-titration procedure ($\pm$ 0.05 ml). The estimated has been calculated in the range of $\pm$ 2%.

9.2.2 Differential scanning calorimetry (DSC)

The thermal transition of the samples obtained by sulfonation and of the pristine PEEK were analyzed by TA Instruments DSC Q200 by applying a heat/cool/heat cycle procedure with a heating/cooling rate of 10°C/min under a constant flux of N_2 of 50 ml/min. The first heating run is necessary to erase the thermal history of the samples in order to obtain

the desired informations (first and/or second order transitions) from the two following cycles.

9.2.3 Fourier transform infra-red spectroscopy (FTIR)

FTIR spectra of the sulfonated samples and of the pristine PEEK were collected with an infrared spectrometer (ThermoFisher Nicolet 670) in transmission mode in the wavenumber range of 4,000-400 cm^{-1} (64 scans, 4 cm^{-1} resolution). Before the analysis a background spectrum was run, and samples spectra were normalized against it.

9.2.4 Solubility evaluation

The solubility of the sulfonated samples with different degrees of sulfonation were evaluated by preparing solutions of 5% by weight of polymer in different solvents. The solutions were kept for a day at ambient temperature and the solubility evaluation was done by checking the transparency of the solution and the presence of possible solids residues of polymer after 24 hours.

9.2.5 Thermo-gravimetric analysis (TGA)

The thermal and thermo-oxidative behavior of the samples obtained by sulfonation and of the pristine PEEK were analyzed by TA Instruments TGA Q600, usually with a heating rate of 10°C/min and a flux of about 100 ml/min of nitrogen (for the thermal stability evaluation) or air (for the thermo-oxidative evaluation). In both cases samples of about 9-10 mg were analyzed. Differential TG curves (DTGA) were obtained from the first derivative of TGA data.

9.3 RESULTS AND DISCUSSION

9.3.1 PEEK sulfonation

The sulfonation of PEEK was conducted by aromatic electrophilic substitution reaction in liquid phase in presence of concentrated sulfuric acid, according to the following formula (Figure 9.1):

$$PEEK + H_2SO_4 \rightarrow sPEEK + H_2O \tag{9.1}$$

PEEK is generally highly resistant to dissolution in most common solvents and for this reason its solubility is generally limited to harsh solvents, especially strong acids like H_2SO_4, CH_3SO_3H and HSO_3Cl. In this case two different routes have been evaluated in order to produce sulphonated PEEK. The first protocol is based on a more standard and

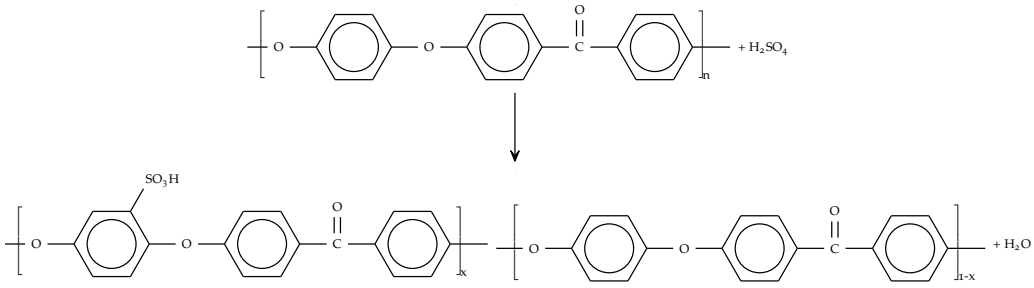

Figure 9.1: *Scheme of the sulfonation of PEEK with H_2SO_4*

recurring procedure commonly found in scientific literature and involves the reaction of PEEK with concentrated H_2SO_4, while the second method requires the dissolution of the polymer in CH_3SO_3H followed by addition of a proper quantity of H_2SO_4.

9.3.1.1 *Sulfonation of PEEK with H_2SO_4*

In this case a 96% sulfuric acid has been employed both for the dissolution and as sulfonating agent of the polymer. This is the common choice since in stronger acids like 100% H_2SO_4 and HSO_3Cl cross-linking has been observed due to the formation of sulfone links [389]. On the other hand in aqueous H_2SO_4 (low than 90%), due to the decrease of acid strength and associated protonating and sulfonating powers, the solubility of the polymer decreases dramatically [390]. For a more concentrated H_2SO_4 the sulfone formation is negligible because H_2O can decompose the postulated aryl pyrosulfonate intermediate which is required for sulfone formation [391, 392].
Previous studies have reported that the kinetics of PEEK sulfonation in concentrated sulfuric acid can be improved by mild heating above room temperature and for this reason the degree of sulfonation of the polymer was controlled by setting temperature and the time of reaction.
The protocol followed consisted in the dissolution of the polymer, after drying at 100°C overnight, in concentrated sulfuric acid at room temperature at a concentration of 5:95 w/v and with vigorous mechanical stirring in order to obtain an uniform mixture. The common procedure employed consisted in the dissolution about 12 g of polymer in 228 ml of H_2SO_4 inside a 500 ml five neck round bottom flask under N_2 atmosphere, in order to avoid moisture contamination. The temperature was measured with a bulb thermometer directly in contact with the reaction mixture while the flask was put into a water bath in order to provide the heat required for the reaction. The dissolution a few hours to be complete, however it has been demonstrated that at room temperature the sulfonation reaction has a very slow kinetics. Indeed for the case in analysis after dissolution a sample have been analyzed resulting in a DS medium value of 6%.
Several test were performed by varying the temperature from 45°C to 65°C and the time of reaction to an extent of 5 hours. In this manner the aim was to obtain samples with different but controllable degrees of sulfonation in order to characterize them. For every temperature a sample of about 30-40 ml of the reaction mixture was taken from the flask at every hour. The samples obtained were poured dropwise into iced deionized water un-

der vigorous stirring in order to precipitate the sulfonated polymer and block the reaction. After that the heterogeneous suspension was left to rest overnight. The recovered polymer was filtered and washed with deionized water in order to eliminate the acid residue. This procedure was iterated several times until the pH of the rinsed water was as close as possible to the neutral value. The product obtained was then heated at 40°C in order to eliminate the most abundant content of water and subsequently at 80°C under vacuum for a day. After the drying procedure the polymer changed its color from white to a brilliant yellow and then the color became darker by increasing the sulfonation degree until reaching an uniform red for sulfonation degrees above 60%.
The evaluation of the ion exchange capacity (IEC) has been carried according to the following equation:

$$IEC = \frac{V_{NaOH} \times C_{NaOH}}{W_{dry}} \ (meq/g) \tag{9.2}$$

where V_{NaOH} is the volume of NaOH solution consumed (ml), C_{NaOH} is the concentration of the NaOH solution (mol/l), W_{dry} is the dry weight of the sample (g) and meq is the milliequivalent, the thousandth part of the atomic mass of an ion, expressed in grams, divided by the number of electric charges present in the ion itself. The degree of sulfonation (DS), which quantify the extent of the functionalization of the polymer, has been evaluated by heterogeneous titration of the sulfonated samples according to the following formula:

$$DS = \frac{moles_{sPEEK}}{moles_{sPEEK} + moles_{PEEK}} \tag{9.3}$$

while the moles of sPEEK and PEEK in 1 g of sulfonated polymer can be expressed as [393]:

$$moles_{sPEEK} = \frac{IEC}{1000} \tag{9.4}$$

$$moles_{PEEK} = \frac{1 - 0.001 \times IEC \times 369}{288} \tag{9.5}$$

where 369 and 288 are the molecular weights of the repetitive unit of sPEEK and PEEK in Daltons, respectively. The results of tested carried at different temperatures in terms of sulfonation degree of the final samples are reported in Figure 9.2.

As can be seen the sulfonation degree follows a logarithmic behavior with time and the degree of sulfonation increase of about 10% by increasing the temperature by 10°C for the same value of the reaction time.

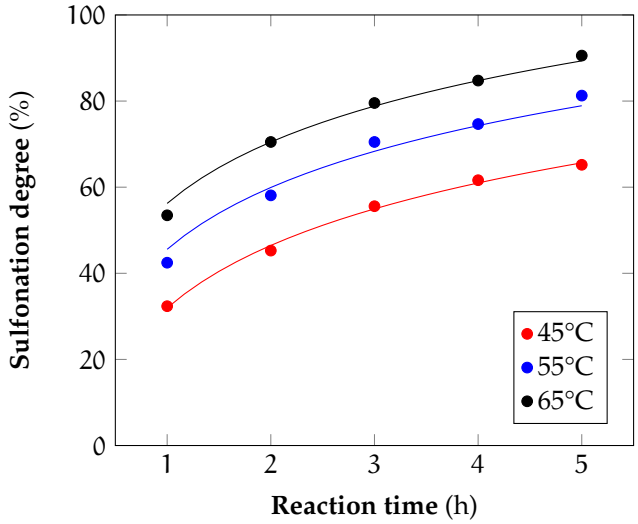

Figure 9.2: *Sulfonation degree as a function of time and reaction temperature for the sulfonated samples obtained*

9.3.1.2 *Kinetic modelling*

According to the scientific literature [392, 394] the most commonly used equation to express the aromatic sulfonation rate in aqueous sulfuric acid is the following:

$$-\frac{d[Ar]}{dt} = k[Ar]\frac{A^2_{H_2SO_4}}{A_w} \tag{9.6}$$

where [Ar] = concentration of the aromatic ring to be sulfonated, $[H_2SO_4]$ = concentration of sulfuric acid and A_W = activity of water which is proportional to the concentration of water in the system, k = reaction rate constant and t = reaction time. In this expression the rate is first order with respect to the substrate, the aromatic ring. The second order of the activity of the acid has been rationalized by a reaction of two H_2SO_4 molecules producing the sulfonation species.
Different kinetic models have been employed to describe the sulfonation of PEEK in concentrated sulfuric acid and the following section is devoted to the comparison of the two important ones.

9.3.1.2.1 KINETIC MODEL A

A first kinetic model has been evaluated according to analysis developed by Huang *et al.* [395]. They conducted an analysis by considering that the reaction can be modeled on the following assumptions:

1. substitution first takes place in one of the four sites of the aromatic ring between the two ether bridges
2. four sites have equal chance for the substitution
3. the first-type substitution is a second-order reaction

4. after the first type substitution is complete, further substitution (the second-type substitution) can happen in the other two identical aromatic rings
5. the reverse reaction is neglected for the high acid concentration
6. volume change during reaction is ignored

These assumptions allows to develop the following kinetic model for the reaction:

$$-\frac{dc}{dt} = k(a-c)(b-c) \tag{9.7}$$

where c = concentration of sPEEK and H_2O in the reaction mixture, a = initial concentration of PEEK in the reaction mixture, b = initial concentration of H_2SO_4 in the reaction mixture. The terms can be better understood by looking at the following table:

Table 9.1: *Scheme of the meaning for the terms in the kinetic model*

	PEEK	H_2SO_4	sPEEK	H_2O
Initial concentration	a	b	0	0
Concentration at time t	a-c	b-c	c	c

This differential equation can be simplified on the basis of the following assumption:

- the concentration of sulfuric acid is significantly higher than the concentration of sPEEK and water on molar basis (b-c $\approx$ b)

which leads to a simplified version of the previous equation:

$$-\frac{dc}{dt} = kb(a-c) \tag{9.8}$$

As the previous one this equation is a separable differential equation and its integration is straightforward:

$$-\frac{dc}{(a-c)} = kb\ dt \tag{9.9}$$

$$\int_0^c -\frac{dc}{(a-c)} = \int_0^t kb\ dt \tag{9.10}$$

$$\left[\ln(a-c)\right]_0^a = kbt \tag{9.11}$$

$$\ln(a) - \ln(a-c) = kbt \tag{9.12}$$

That gives:

$$-\ln\left(\frac{a-c}{a}\right) = kbt \tag{9.13}$$

Considering that c/a is the ratio between the units of sulfonated PEEK and the initial units of PEEK it is possible to equate this quantity to the degree of sulfonation:

$$-\ln(1-DS) = kbt \tag{9.14}$$

According to this equation if the reaction can be adequately described by this kinetic model the values of -$\ln(1-DS)/b$ versus time must lie along a straight line for the time range of the experiments.

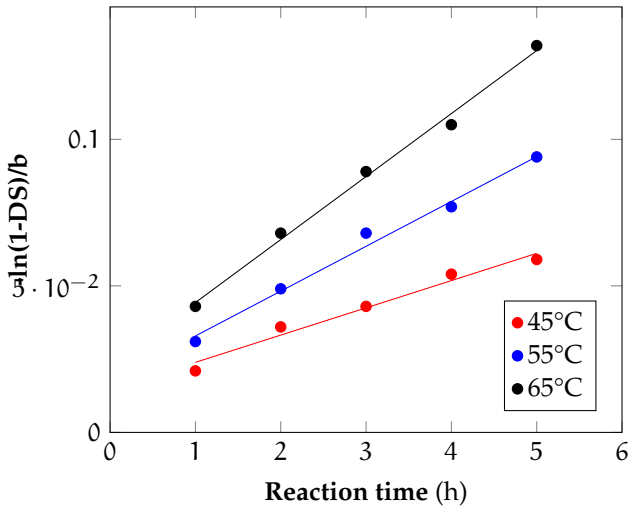

Figure 9.3: *Linearized plot of the sulfonation degree versus the reaction time for the samples sulfonated at different temperatures*

The data seem to fit quite well a straight line. Their intercept is not zero, which means that at the beginning of the reaction the sulfonation degree is different from zero, probably due to the fact that during the time interval necessary for the dissolution of the polymer at room temperature a mild sulfonation occurred. From the fitted values it is possible to evaluate the product kb at different temperatures, which is useful to determine values of the parameters of the kinetic constant and evaluate the goodness of the model for the experimental data fitting.
Since the expression for the kinetic constant is:

$$k = A\ exp\left(-\frac{E_a}{RT}\right) \tag{9.15}$$

Table 9.2: *Mean values of the parameters obtained by the experimental data for the kinetic model employed*

T [K]	**b** [mol/L]	**kb** [h^{-1}]	**k** [L/(mol*h)]
318.15	17.9	0.167	0.016
328.15	17.9	0.275	0.023
338.15	17.9	0.385	0.033

Thus by taking the logarithm:

$$\ln k = \ln A - \frac{E_a}{RT} \tag{9.16}$$

By collecting values of k at different temperatures it is possible to determine the pre-exponential (A) factor and the activation energy (E_a) using the Arrhenius plot (Figure 9.4)

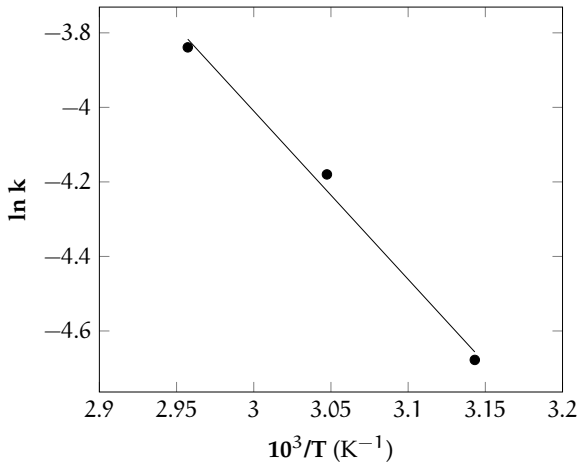

Figure 9.4: *Arrhenius plot for the evaluation of the activation energy and pre-exponential factor of the heterogeneous sulfonation reaction*

The data can be fitted with a straight line whose coefficient is the ratio E_a/R and the intercept is A. From this fitting the activation energy is estimated in about 7.35 kcal/mol and a pre-exponential factor of $1.38 \cdot 10^4$ L/(mol·h). However by taking these data to use the kinetic model in order to compare the predicted sulfonation degree versus the experimental results it is possible to observe a significant difference (Figure 9.5).

This result reflects an inconsistency of the model chosen for the kinetic description of the reaction, even though the linear relationship between -ln(1-DS) and t has been identified. A possible justification is related to the relatively small time interval chosen for the experiments that prevented to observe the behavior of the samples for higher degrees of sulfonation. On the other side the model predict that at the beginning of the reaction time the sulfonation degree is equal to zero, while the experiments showed that the time re-

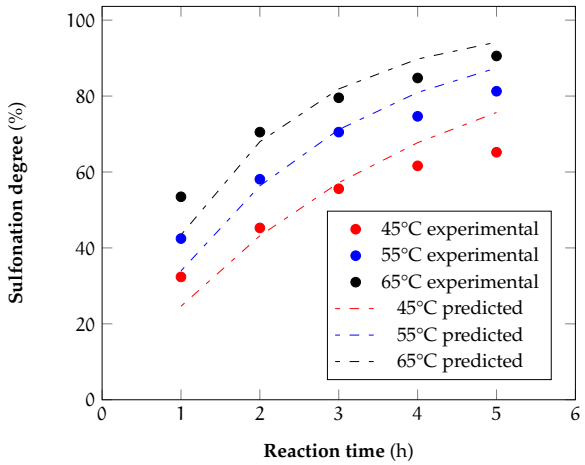

Figure 9.5: *Comparison between the experimental data and the kinetic model prediction*

quired for the dissolution of the polymer can determine a low sulfonation at the beginning of the reaction. The progressive decrease of the sulfonation rate with time can be explained from different points of view. First by increasing the sulfonation degree during the reaction the concentration of the sites for the first type substitution decrease and the second type requires to overcome an higher energy barrier due to the presence of the carbonyl group that has an high electron-attracting nature which decrease the electron density of the two aromatic rings attached to it. A second explanation can be attributed to a possible equilibrium condition that can be reached by the system due to the desulfonation reaction which occur in presence of water, main byproduct of the reaction. The experiments have been carried with an initial concentration of PEEK of about 53 g/L and the molar equivalent water produced in the hypothesis of a 100% sulfonation is equal to 3.3 g. This amount is not completely insignificant compared to the about 17 g of water presents in the 228 ml of acid employed in the experiments (assuming a mean acid concentration of about 96%). However this could led to a variation in the acid concentration from approximately 96 to 95.2%, which is not so high to judge the reverse reaction as particularly significant.

9.3.1.2.2 KINETIC MODEL B

In order to obtain a more precise description of the reaction kinetics a second model has been analyzed. Shibuya and Porter [389, 396] reported a different kinetic expression for the aromatic sulfonation by sulfuric acid based on the assumption of a negative effect of sulfonated aromatic ring on the rate expression. They proposed the following kinetic model:

$$-\frac{dc}{dt} = \frac{k_1 c}{k_d(c_0 - c)} \tag{9.17}$$

where c is the concentration of substrate at the time t, c_0 is the initial substrate concentration (at t = 0), k_1 is the rate constant of sulfonation, k_d is the constant for the negative effect of the product and c_0 - c is the product (sulfonated aromatic ring) concentration at

time t. This equation can be integrated from c_0 to c giving:

$$-\int_{c_0}^{c} \frac{c_0 - c}{c}\, dc = \frac{k_1}{k_d}\int_0^t dt \tag{9.18}$$

$$-\frac{c_0 - c}{c_0} - \ln\left(\frac{c}{c_0}\right) = \frac{k_1}{k_d}\frac{1}{c_0}t \tag{9.19}$$

now by considering that c = c_0(1-X) where X can be interpreted as the degree of sulfonation (DS) per repeating unit of the polymer it is possible to rewrite the previous equation obtaining the following one:

$$c_0[-\ln(1 - DS) - DS] = \frac{Kt}{c_0} \tag{9.20}$$

where $K = k_1/k_d$ is the equilibrium constant. Figure 9.6 shows the plot of c_0[-ln(1-DS)-DS] versus t, which shows a linear relationship.

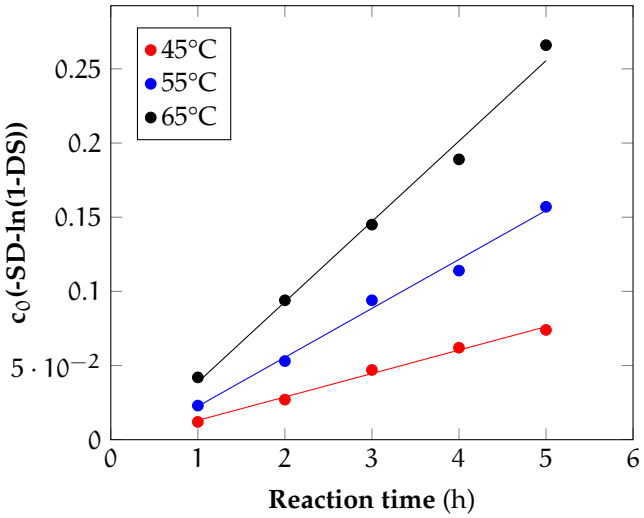

Figure 9.6: *Linearization of the kinetic expression for the sulfonation of PEEK in concentrated sulfuric acid*

This result support the hypothesis at the basis of the proposed kinetic model, thus it is reasonable to develop more in detail the analysis. From the plot obtained in Figure 9.7 it is possible to obtain the values of the equilibrium constant at the temperatures employed for the tests, which can be used to define the degree of sulfonation predicted by the model. These data can be compared with the measured values by titration to asses the goodness of the model. This comparison is shown in Figure 9.8:
The fit seems satisfactory so the second model can be taken in consideration as adequate for the description of the reaction. This means that the reaction can be modeled with a sort of equilibrium kinetics which incorporates a terms that slows the sulfonation due more to a negative effect of the aromatic ring than by the water produced and the H_2SO_4 consumed

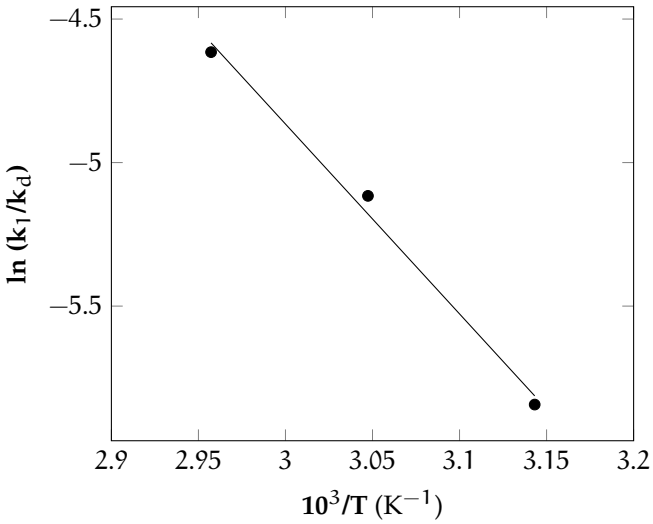

Figure 9.7: *Arrhenius plot for the evaluation of the activation energy and pre-exponential for the second kinetic model employed*

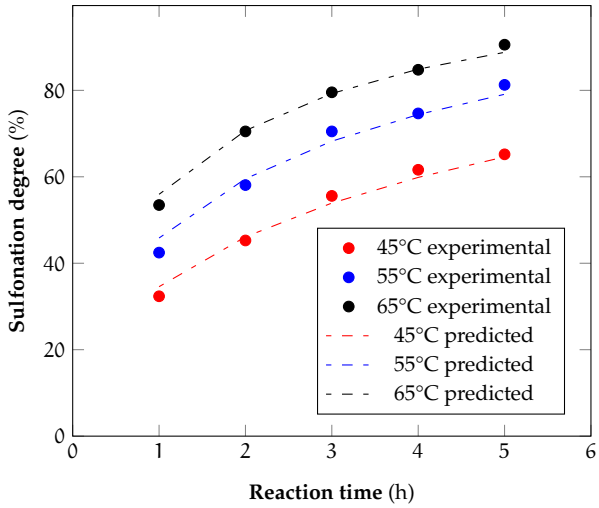

Figure 9.8: *Comparison between the experimental values and predicted values of the second kinetic model for value of the degree of sulfonation at different temperatures and over time of the samples treated*

during the reaction. According to Shibuya and Porter [396] this could be associated with desulfonation or a type of retardation on a reaction intermediate.

9.3.1.3 *Sulfonation of PEEK with H_2SO_4/CH_3OH*

The second protocol is a sulfonation conducted in a mixture of sulfuric and metansulfonic acid. In this case the first step is the complete dissolution of the polymer in MSA followed by addition of sulfuric acid. MSA is employed since it is capable to dissolve the polymer without starting the reaction [390] even if the mixture is leaved in this state for several days [397]. The subsequent addition of sulfuric acid starts the reaction allowing a more homogeneous sulfonation of the final product. However a major drawback for the

reaction is the low rate since the presence of MSA can affects the reaction mechanism in at least two ways [397]:

- dilution of the sulphonating species and their precursors
- solvation and reaction with part of the SO_3, further decreasing the concentration of active species

However the rate of the reaction is strictly dependent on the ratio between H_2SO_4 and MSA. With high ratios the rate is increased but this leads to a more diluted reaction mixture, with problems for recovering the polymer due to its high hydrophilic nature, so a balance between this two aspects is essential for developing an appropriate procedure.
A first test has been carried with a 10% w/v polymer/acid mixture, typically employing 5 g of PEEK dissolved in 50 ml of MSA inside of a 500 ml round bottom flask. After the dissolution of the polymer 250 ml of sulfuric acid have been added to the mixture (reaching a value of $r_{H_2SO_4/MSA} = 5$ on volumetric basis) which has been intensively stirred and prevented from moisture contamination.

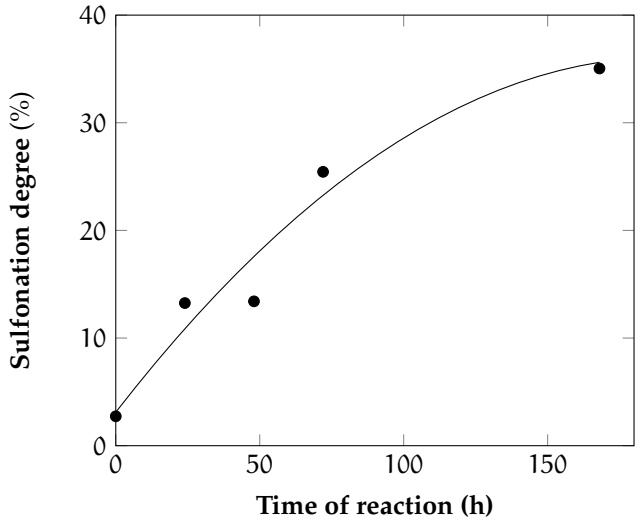

Figure 9.9: *Sulfonation degree as function of the reaction time for the second protocol with a 1:10 w/v PEEK/MSA solution and $r_{H_2SO_4/MSA} = 5$ on volumetric basis*

The reaction has been carried at room temperature for seven days taking some samples at different days of reaction to evaluate the sulfonation degree. These samples have been precipitated in iced deionized water to recover the polymer which has been filtered and washed several times in order to remove the acid residues until the pH of the rinsed water has been close as possible to the neutral value. With this new protocol that employs methansulfonic acid the polymer recovered after the washing and drying steps is generally dark red and brittle even for low sulfonation degrees and it becomes progressively stiffer by increasing the time of reaction.
The sulfonation degree has been evaluated by back-titration with a similar procedure for the case of the previous protocol, the results are shown in Figure 9.9.
In order to have a more accurate evaluation of the sulfonation degree the samples have

been analyzed by elemental analysis. The results are shown in Table 9.3 and compared with the results from titration. As can be seen pristine PEEK does not contain any trace of

Table 9.3: *Results of the elemental analysis for the samples obtained from the reaction at room temperature with a 1:10 w/v PEEK/MSA solution and* $r_{H_2SO_4/MSA} = 5$

Sample	%C	%H	%S	S/C	%DS	%DS titration
PEEK	78.21	4.35	0	0	0	-
0h	77.11	4.23	0.29	3.76e−3	2.7	-
24h	73.878	3.850	1.42	18.5e−3	13.25	
48h	70.38	4.28	1.32	1.87e−2	13.4	12.4
72h	69.71	4.81	2.48	3.56e−2	25.4	26.6
168h	62.75	4.022	3.08	4.91e−2	35.0	37.4

sulfur while the sample taken at the complete dissolution of the polymer show a very low sulfonation. The final sulfonation degree is about 35% after a week of reaction. This value is quite low for the purpose of obtaining samples that can be soluble in common organic solvents with a wide range of sulfonation degrees so a second test has been carried following the method of Kim *et al.* [398].

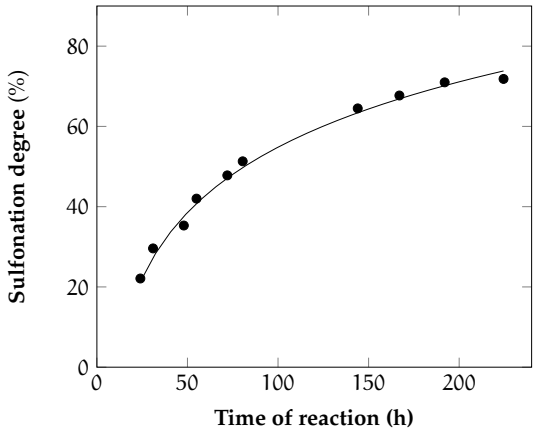

Figure 9.10: *Sulfonation degree as function of the reaction time for the second protocol with a 1:5 w/v PEEK/MSA solution and* $r_{H_2SO_4/MSA} = 8$ *on volumetric basis*

In this case a 20% w/v mixture of PEEK and MSA has been prepared by dissolving the polymer in methanesulfonic acid overnight and subsequently adding sulfuric acid in order to reach a value of $r_{H_2SO_4/MSA} = 8$ on volumetric basis and collecting several samples at different reaction times. Elemental analysis has been carried and even in this case the initial sulfonation degree after complete dissolution is low (3.2 ± 0.7) and can be considered negligible. The results of the reaction tests are shown in Figure 9.10.
For comparison with the results from the protocol that employs the heterogeneous sulfonation with sulfuric acids even for this second protocol some tests were realized employing different temperatures in order to investigate the effect on the kinetics of the reaction. In this case, due to the long time required, only the two higher temperatures (55 and 65°C) have been taken into consideration since they have been capable to provide adequate sul-

fonation degree within 10 hours. Figure 9.11 shows the results of these tests by taking a sample every two hours.

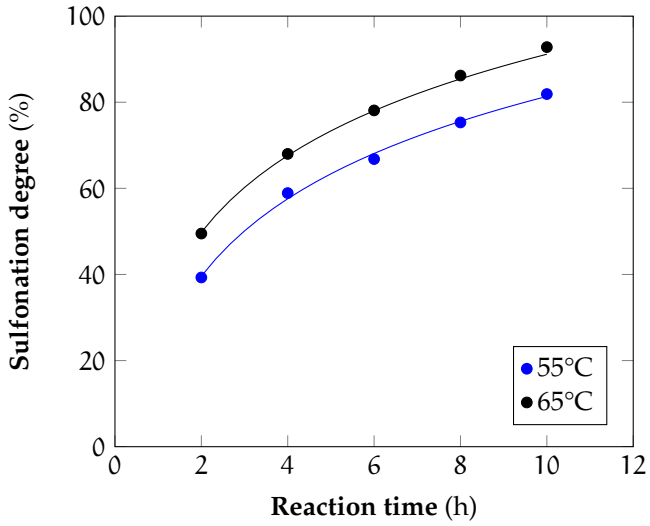

Figure 9.11: *Sulfonation degree as function of the reaction time for the second protocol with a 1:5 w/v PEEK/MSA solution and* $r_{H_2SO_4/MSA} = 8$ *on volumetric basis and different temperatures*

If compared with the results of the heterogeneous sulfonation it is possible to see that the same sulfonation degrees for a given temperatures between those employed can be achieved by doubling the reaction times.
In this case the kinetic analysis has been carried with the same second model employed for the case of the heterogeneous sulfonation of the polymer by taking into consideration the lower concentration of sulfuric acid employed. Here the kinetic constant are an order of magnitude lower than those with the procedure employing only sulfuric acid (Table 9.4), confirming the dilution provided by the presence of methanesulfonic acid in the reaction mixture.

Table 9.4: k_1/k_d *ratio obtained at different temperatures for the two different procedures*

Temperature [°C]	k_1/k_d (H_2SO_4) [mol/l·h]	k_1/k_d (MSA/H_2SO_4) [mol/l·h]
45	0.146	-
55	0.308	0.007
65	0.507	0.012

These results are thus important in order to define specific conditions (time and temperature) in order to obtain samples with desired sulfonation degree.

9.3.2 FTIR

Infra-red spectroscopy is a useful common technique which can be employed to evaluate qualitatively the extent of modification of the polymer and has been used to analyze characteristic bands corresponding to the sulfonated groups in different polymers, like sulfonated poly(arylene ether ketone)s [399, 400], polystyrene [401], polyester [402] , poly(phenylene sulfide) [403]. For the case in analysis a comparison can be made between the pristine polymer (PEEK) and the modified one in order to identify the appearance of new peaks or the modification in the shape or intensity of the existing ones. In general aromatic polymers such as PEEK are strongly absorbing in the mid IR region and past studies [404] were conducted to correlate the intensity of the IR spectra with the degree of crystallinity obtainable by WAXS analysis. The IR spectra of PEEK in Figure 9.12 shows some characteristic peaks that are common to all aromatic thermoplastic; these are the peak at 1490 cm^{-1} which can be associated to the absorption of the aromatic ring and the peaks at 863, 841 and 700 cm^{-1} which are characteristic deformation modes of the aromatic ring.

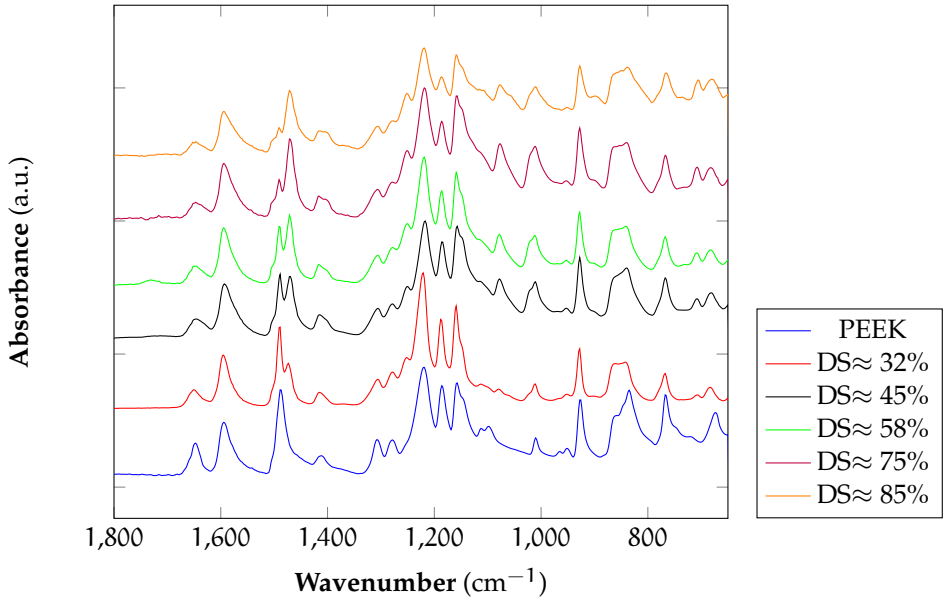

Figure 9.12: *FTIR spectra of sulfonated samples at different values of sulfonation degree*

In addition to those there is a strong absorption around 1650 cm^{-1} which is linked to the stretching of the carbonyl linkage present on the skeletal backbone of the polymer. On the other hand some distinguish features can be highlighted for the spectra of the sPEEK samples. Upon sulfonation there is the appearance of new peaks at 1300 cm^{-1} which can be attributed to the presence of the sulfone ester group, O=S=O [405], and new peaks at 1165, 1089 and 1025 cm^{-1} which can be attributed to the symmetric and asymmetric stretching of sulfonic acid groups. The intensity of these latter peaks changes with the degree of sulfonation so they can be used as indexes for a qualitative evaluation of the sulfonated samples.

An important feature of the sulfonated sample is the absorption at 1490 cm^{-1} the C-C

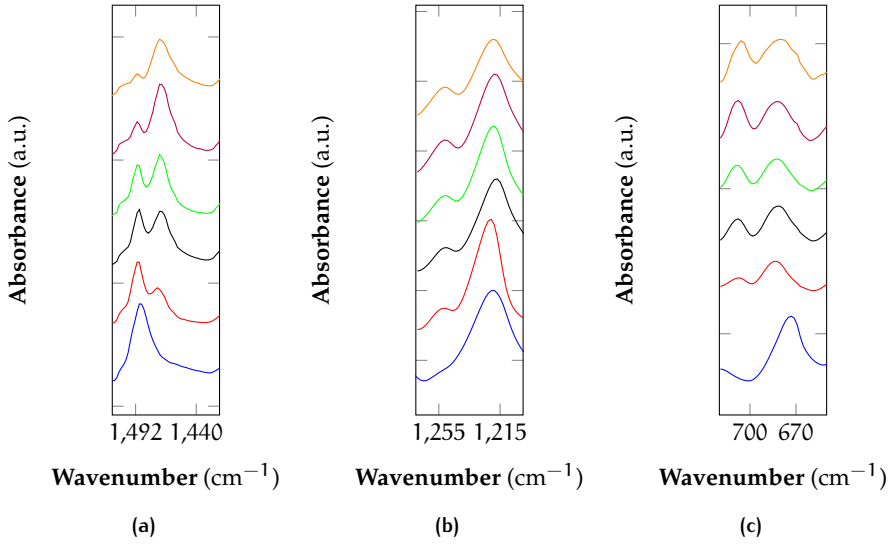

Figure 9.13: *Magnification of the wavenumber intervals of the FTIR spectra of sulfonated samples in order to highlight the new peaks due to presence of the sulfonic group in the aromatic ring: a) interval 1420-1512 cm^{-1}, b) interval 1200-1270, c) interval 650-720 cm^{-1}*

aromatic ring between the ether linkages in the PEEK, which refers to the 1,2,4-substitution aromatic ring. This peak decrease with increasing the sulfonation degree and then split into two new absorption bands at 1471 cm^{-1} and 1478 cm^{-1} that presented the aromatic ring. Jafar *et al.* [406] found that these two bands are increased as the concentration of sulfonic acid group in the sulfonated PEEK is increased and claimed that the significant shifting feature from the peak at 1490 cm^{-1} to these two new peaks implied that the sulfonic acid group is attached only to the 1,2,4-substitution aromatic ring between the ether linkages ring, meaning that only the substitution of the first type is involved. In addition a broad peak with a maximum at 3428 cm^{-1} is noticed and it's attributed to -OH vibration related to the hydrogen bonding formed between the -SO_3H groups and the molecules of absorbed water. Apart from the splitting of the peak related to the aromatic ring between the ether linkages it has been observed that with the progressive increase of the DS even the peak related to the stretching of the aromatic C-C starts to deform and give rise to a mild splitting that, however, is too low to be considered for a quantitative analysis. Another significant difference between the spectra is related to the two peaks at 865 and 836 cm^{-1} assigned to the bending of the aromatic hydrogens of the polymer chain. After sulfonation the peak at 836 cm^{-1} decreases its height reaching the level of the 865 cm^{-1} peak but without further changes with the increase of the DS. As a consequence of the chemical modification of the polymer there is also a broadening and an height increase of the peak at 1010 cm^{-1}. All these results confirm the sulfonation of the samples and the conclusion agree with the variation associable to the different sulfonation degrees of the samples analyzed.

9.3.3 DSC and XRD analysis

The glass transition temperature is a thermo-resistance indicator of the polymers. PEMFC and DMFC normally work at temperature ranging between 80-120°C and, therefore, T_g higher than these values indicate if the electrolyte polymer is temperature resistant and if any thermo-degradation takes place during the fuel cell operations [407]. DSC analysis were conducted on pristine PEEK and several samples at different sulfonation degree. The thermal transitions of PEEK are shown in Figure 9.14. As can be seen the PEEK employed is a semi-crystalline polymer with a melting peak around 345°C and a degree of crystallinity of about 38.8% (ΔH_m = 130 J/g [408]). The crystallization is visible from the sharp exothermic peak around 300 °C during the cooling cycle while the T_g, which is around, 144°C can be detectable only at high heating rates when the amount of crystalline phase can be limited during cooling.

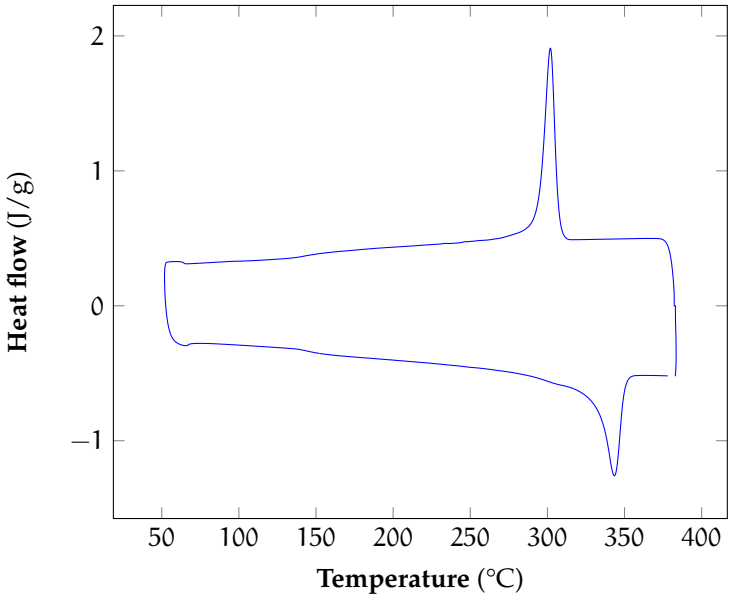

Figure 9.14: *DSC analysis for pristine PEEK: 2nd and 3rd heating cycles*

The semicrystalline nature of the polymer is considered the main limitations behind its solubility and justify the observed delay in its solubility also in the strong acids employed for its sulfonation. On the other side, after sulfonation, sPEEK present a random copolymer nature and the crystalline phase should disappear disappear. However for every sulfonated sample a sharp endothermic peak has been observed during the first heating run, which has disappeared during the following runs. The main peak temperature is significantly lower than that of the melting of pristine PEEK and the calculated areas increased with sulfonation degree (Figure 9.15a). In order to confirm the absence of any crystalline phase an evaluation was made by comparison of the wide angle X-ray diffraction patterns of the pristine PEEK and sPEEK samples at different degrees of sulfonation. As can be seen from Figure 9.16 pristine PEEK possess a crystalline phase evidenced by four distinct peaks at 2θ = 18.8°, 20.7°, 23° and 28.8° that are associated to the (110), (111), (200), (211)

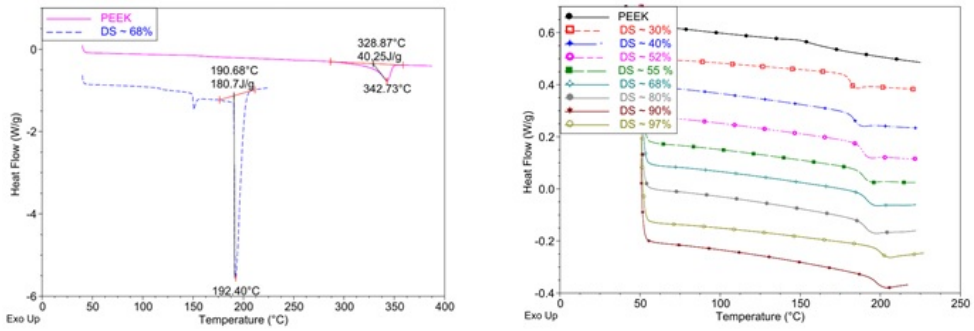

(a) (b)

Figure 9.15: *DSC thermograms for the analyzed samples: (a) comparison of the endothermic peaks, (b) progressive shifting of the glass transition temperature*

reflections respectively [409] and are common to all *para*-members of poly(aryl ether ketone)s family. As comparison four different sPEEK samples as been taken in consideration: a sample after the complete dissolution of the polymer in sulfuric acid and three samples at 33, 49 and 75% of sulfonation degree. The results show that with the complete dissolution of the polymer in the acid the crystalline peaks disappear leaving a broad principal amorphous peak with a maximum at $2\Theta = 20°$ and traces of tiny peaks probably associable to residual minor crystalline phases. For the other sulfonated samples the pattern is similar to the dissolved one. The intensity of the amorphous peak with respect to the baseline tends to decrease as the sulfonation increases and the residual crystalline peaks tends to disappear.

The possible explanation of the endothermic peaks observed has been attributed to struc-

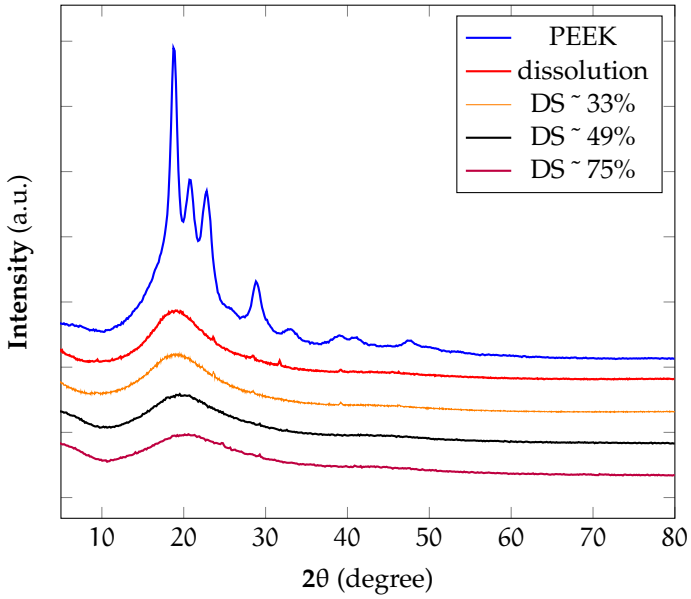

Figure 9.16: *XRD spectra of sPEEK and some sulfonated samples*

tural changes into ionic clusters formed during the polymer precipitations from the reac-

tion mixture and associated with the order destruction in these domains, similarly to what have been observed for other type of ionomers [132, 410–412]. The introduction of the group -SO_3H along the repeating unit of PEEK can lead to two effects:

- the increment of the intermolecular interactions by the pendant ions which is called ionomeric effect
- the increment of the molecular bulkiness which causes a significant steric hindrance

These effect have a direct reflection on the thermal properties of the sulfonated samples. Firstly there is usually an increment of the Tg values with the increase of the sulfonation level; this can be explained in terms both of the steric hindrance associated with the pendant sulfonic group and also with their ability to act as physical intra and inter-chain bridges forming strong hydrogen bonding with other sulphonic groups or with the ketonic groups of the polymer backbone, that produce a more rigid and resistant structure. These intermolecular forces make the internal rotation of sulphonated phenyl rings difficult compared to the non sulfonated PEEK [413]. The results obtained from the DSC analysis of the sulphonated samples are reported in Figure 9.15b and Figure 9.17. For the sulfonated

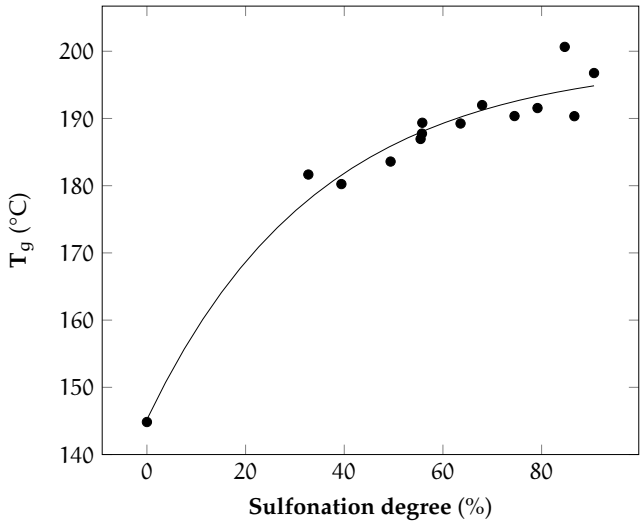

Figure 9.17: *Plot of the glass transition temperatures versus the sulfonation degree for sPEEK samples of different sulfonation degrees*

samples the final temperature of the analysis has been established around 230°C since it has been observed by TGA results, as can be seen later, that approximately around 250°C the decomposition of the samples begin. As can be seen there's effectively a monothonical increment in the Tg with the degree of sulfonation and there results are similar to those reported elsewhere [414].

9.3.4 TGA

The analysis of the thermal behavior of sPEEK is an important characterization to understand the performance of the polymer and it's stability in relation to its possible field

of employment. The incorporation of sulfonic group along the polymer chain leads to a decrease of the thermal stability of the material. In this case there are usually three main phenomena of mass loss during the heating of a sulfonated sample in air:

- a first mass loss at $\approx$ 100°C which is attributed to the evaporation of residual water in the material
- a desulfuration process at T > 200°C

$$4SO_3H \rightarrow 4SO_2 + 2H_2O + O_2 \tag{9.21}$$

- oxidative pyrolysis (formation of CO_2 and H_2O) at T $\approx$ 450°C

The degradation mechanism involved is radical and it is promoted by the presence of the sulfonic acid groups that, being less stable, act as weak points in the polymeric structure and allow the beginning of the radical decomposition. The sulfonated samples obtained

Table 9.5: *Bond dissociation energies between different atoms* [415]

Bond dissociation energy [kJ/mol]						
C=O	**S=O**	**C-S**	**O-C**	**C-C**	**C-H**	**C-C**
723	499	272	358	346	427	617

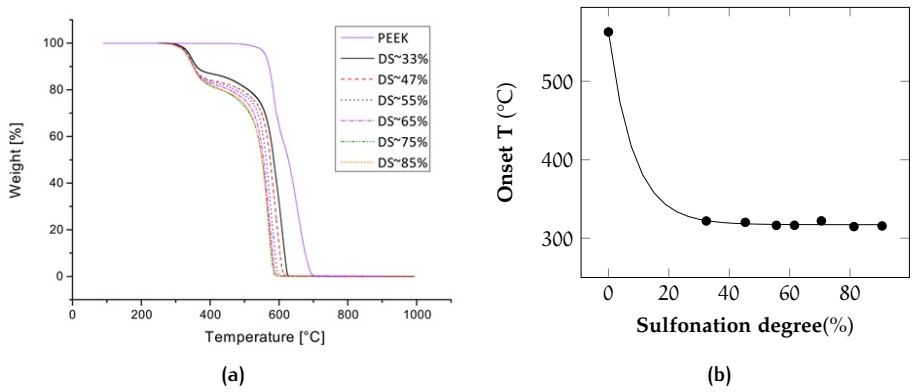

Figure 9.18: *(a) TGA thermograms and (b) onset temperature value for PEEK and sPEEK samples at different sulfonation degrees*

were analyzed in order to assess their thermal and thermo-oxidative behavior to comprehend if the stability of the polymer could be compromised if too high sulfonation degrees are achieved. The pristine PEEK has an high thermal stability, which is confirmed by the high onset temperature, and decomposes in two stages in oxidative atmosphere. The first degradation stage is completed at 590 °C with a mass loss of about 73.12% and a maximum decomposition rate at 584°C, while the subsequent stage has a maximum at 600°C and leads to the complete decomposition of the remaining mass of the samples. As expected the thermo-oxidative stability of the sulfonated samples is decreased significantly even from medium degrees of functionalization (Figure 9.18). The onset temperature of

the first degradation step for the sulfonated samples shows a plateau by increasing the degree of sulfonation. The main difference is related in the mass lost between the first and second degradation step. The amount of mass loss during the first degradation process is proportional to the amount of sulfonic groups in the polymer chains which create a proportional amount of sites to promote the subsequent degradation once removed during the desulfuration process.
However the final thermal properties are satisfactory for the final applications where the operative temperature are generally comprised between 80 and 120°C.

9.3.5 Solubility evaluation

Since pristine PEEK is insoluble in common organic solvents another important feature of the sulfonation process is to being able to increase the solubility of the polymer obtained. In this sense the effect of the reaction is double: on one side the sulfonation is capable to destroy the crystallinity of the polymer due to the random distribution of the sulfonic acid groups during the reaction, and, on the other, by attaching a sulfonic groups on the aromatic ring of the polymer, increasing the solubility of the material in polar aprotic solvents. A good solubility is necessary for electrospinning in order to have a stable

Table 9.6: *Solubility evaluation of different sPEEK samples in different organic solvents*

Sample	DMF	DMAc	DMSO	NMP	Acetone	THF	MEK	MeOH
DS ~ 33%	Sw.	Sw.	Sw.	+	-	-	-	-
DS ~ 45%	Sw.	Sw.	+	++	-	Sw.	-	-
DS ~ 50%	+	+	+	++	-	Sw.	-	-
DS ~ 55%	++	++	++	++	-	Sw.	-	Sw.
DS ~ 60%	++	++	++	++	-	Sw.	-	Sw.
DS ~ 70%	++	++	++	++	-	Sw.	-	++
DS ~ 80%	++	++	++	++	-	Sw.	-	++
DS ~ 90%	++	++	++	++	-	Sw.	-	++

solution during all the process for the production of the nanofibers. As can be seen from Table 9.6, to allow a complete solubility in the solvents employed a sulfonation degree of at least 55% is necessary but different behaviors can be identified. For example DMSO and NMP seem to be capable to interact more significantly with the polymer at low sulfonation degrees, probably due to their high polarity. Sulfonation degrees higher than 70%-75% are not considered suitable especially if the material has to be taken into consideration for DMFC applications.

9.4 CONCLUSIONS

Sulfonation of poly(ether ether ketone) has been accomplished as a preliminary phase for the production of electrospun nanofibers for potential applications in the energy field. The sPEEK samples have been characterized by different techniques in order to evaluate the extent of the sulfonation process and their thermal and solubility characteristics. Two different sulfonation procedures have been taken into consideration for the functionalization of the material to provide solubility and proton conducting characteristics to the material. Besides the reaction has been modeled with a suggested kinetic expression that takes into consideration a deflator effect of the sulfonated portion of the polymer, with a good fitting of the experimental data. The results have shown that the modified polymer can be completely solubilized in different organic aprotic solvents for medium degrees of sulfonation, defining a minimum sulfonation degree for conducting the electrospinning process. The thermal properties are satisfactory for the final applications but care must be taken to selected a proper interval for the sulfonation degree, which should be above 55% to allow solubility.

10 PROCESS OPTIMIZATION OF SPEEK NANOFIBERS BY RESPONSE SURFACE METHODOLOGY

An extensive scientific literature can be found regarding experimental studies concerning the optimization of the electrospinning process. Despite this the common approach is the so called "one-factor-at-a-time" in which the analysis is conducted by varying a single parameter each time, solution which is often incapable to face with the appropriate methodological in-depth analysis. The electrospinning process is characterized by a certain interaction between the parameters, that has to be properly evaluated case by case. Indeed an additional problem of this methodology is that different solvent/polymer systems can lead to different optimization solutions. Such variability is the main reason for which every single polymer/solution system requires a proper and specific optimization procedure. In this sense in the last years several studies has been conducted by using statistical analysis by the *Design of Experiments* (DoE) methodology, which allows to reduce the number of experimental run and is capable to provide statistical evidences on the results obtained in a way that is more efficient than a complete factorial experiments. The purpose of the following section is to provide a more deep insight regarding the applications of such approach (specifically with the employment of the *Response Surface Methodology*) for the optimization of sPEEK nanofibers production process by electrospinning.

10.1 ELECTROSPINNING SET-UP

The electrospinning experiments have been carried with a conventional apparatus, composed of a syringe pump, a variable DC power supply and a metal rotating collector in order to obtain an uniform distribution of the fibers. A common 6 ml plastic syringe (Terumo) was mounted on the syringe pump (Harvard 11 Pico Plus Syringe Pumps) and fitted with a 27G (Terumo, 0.4128 mm o.d, 0.21 mm i.d.) stainless steel hypodermic needle. A variable DC power supply (Gamma High Voltage, USA) was used to produce a potential difference in the range of 0-30 kV. The positive (anode) terminal was connected to the stainless steel needle using a steel spring-loaded clip with serrated jaws (alligator clip), while the ground (negative) terminal of the power supply (cathode) was attached to the rotating metal collector. The electrospinning apparatus was enclosed in a PMMA sealed chamber to electrically insulate the system, avoid air currents and maintain a stable environment. All the tests have been conducted in a monitored environment, where both temperature and humidity were measured constantly. The polymeric solutions were prepared by dis-

solving the samples overnight at room temperature in the selected solvents under intense stirring. The morphology of the electrospun samples was characterized by scanning electron microscopy (SEM) (JSM Jeol 6490) micrographs of gold sputtered samples deposited on aluminum foil. Fibers were measured by image analysis with ImageJ software (version 1.48), taking a total of 200 diameters for each sample from different photos.

10.2 SPEEK ELECTROSPINNING

Only few literature studies have dealt with the electrospinning of sPEEK (Table 10.1) or analogous poly (aryl ether ketone)s. The first attempt to produce nanofibers from a similar polymer is due to Li and coworkers [231] who tried to electrospun a synthesized sulfonated poly (ether ether ketone ketone) (sPEEKK) with a solution at 15 wt% in DMF. They employed a low voltage (12 kV) and a medium distance (15 cm) to obtain nanofibers. Li *et al*. [416] incorporated nanosilver particles in nanofibers and nanospheres of a synthesized sPEEK for potential catalytic applications, while Chakrabarty *et al*. [384] have fabricated electrospun sPEEK nanofibers for electro-dialytic separation of Na^+ from Mg^{2+} or Ca^{2+} for potable water production. In their study they used a 10% w/v solution of the polymer in DMAc, depositing very thin nanofibers on aluminum foil. Wang *et al*. [385] have synthesized a sulfonated poly(ether ether ketone) containing hexafluoropropylene moiety to produce core-shell nanofibers for gas sensing. However, due to the poor inherently electrospinnability of the polymer, they coupled it with polyacrylonitrile in a weight ratio equal to 1:10 to produce nanofibers. Lee *et al*. [417] electrospun a composite nanofiber mat of SiO_2/sPEEK for fuel cell applications, starting from a solution of sPEEK and SiO_2 gel. They used very low flowrate (0.08 ml/h) and low relative humidity (below 15%) in order to obtain nanofibers. Choi *et al*. [418] realized a highly performant composite PEM made of sPEEK and carbon nanotubes (CNTs) webs with a layer by layer deposition of such webs on ultrathin electrospun sPEEK nanofibers subsequently fused by solvent exposure.

Table 10.1: *Literature survey on the electrospinning of poly (aryl ether ketone)s*

Electrospun polyer	Ion-exchange capacity [meq/g]	Solvent	Solution concentration [wt %]	Voltage [kV]	Flow rate [ml/h]	Distance [cm]	Ref.
sPEEKK	2.01	DMF	15	12	n.a.	15	[231]
sPEEK	n.a.	DMF	15	14	n.a.	15	[416]
sPEEK	1.09	DMAc	10	12	0.2	12	[384]
sPEEK/PAN	1.68	DMF	20	15	n.a.	20	[385]
sPEEK/SiO_2	1.97	DMF	20	15	n.a.	10	[417]
sPEEK	n.a.	DMF	20	16	0.08	10	[418]
sPEK	2.9	DMF	25	25	0.1-0.2	15	[419]

Oroujzadeh *et al*. [419] realized a dual electrospinning process of a synthesized sulfonated poly (ether ketone) (sPEK) in DMF and poly (ether ketone) in DMF/THF as preliminary stage to realize a composite membrane by hot-pressing. The electrospinning of the sul-

fonated PEK has been realized by employing low flow-rates (0.1-0.2 ml/h), high voltage (25 kV) and intermediate distance of the tip from the needle (15 cm). From Table 10.1 it is possible to observe that usually low flow-rates and high concentration of the solutions are required for the electrospinning of such sulfonated polymers. DMF is the most commonly employed solvent, while no reports are available for the electrospinning with DMSO and NMP even though the polymer should be soluble in both of them. Despite other factors the choice of the solvent could be important since several studies have pointed out the relative importance of the type of solvent employed on the conductivity properties of casted sPEEK. These studies have shown that for the same degree of sulfonation the conductivity depends on the solvent employed, but the precise cause of the difference is not understood. Robertson *et al*. [420] have shown that the presence of residual DMF into casted sPEEK, which leads to strong hydrogen bonding with the sulfonic acids groups or formation of decomposition products responsible for the reduction of the protons available for proton transport, resulting in a decrease in membrane conductivity. In their study DMAc and NMP have proved to be better solvent for casting, but with different results according to the type of pretreatment employed. Low temperature pretreatments prevent complete removal of NMP while for high temperatures DMAc shows hydrogen bonding. Jun *et al*. [421] have shown, through evaluation of nitrogen amount by elemental analysis, that after the activation with H_2SO_4 the amount of residual solvent into casted sPEEK membrane significantly decreased with an increment in proton conductivity and best performances are achieved in the case of NMP as casted solvent.

10.3 SCREENING EXPERIMENTS FOR SPEEK ELECTROSPINNING

After the definition of the conditions for the appropriate solubility of sPEEK in some common organic solvent it has been possible to evaluate a first series of screening experiments regarding the electrospinning of the relative polymer solutions. To this end several solutions, with different polymer concentrations and solvents, have been realized. The polymer concentration has been varied from 20% to 30% by weight while the solvents chosen have been those employed in the solubility evaluation (DMF, DMAc, DMSO and NMP). This last choice is essentially related to the characteristics of these solvents which can be reflected on different spinning conditions and/or final morphology of the fibers for a given set of electrospinning parameters. All the solution were prepared at ambient conditions or by heating at a maximum temperature of 50 °C for low periods of time in order to avoid an excessive solvent evaporation that could lead to a change in the solutions concentration. This first screening activity was carried in order to identify the range of operative conditions and to have uniform and defects-free nanofibers.
The results of this screening showed that the different solvents have different impact on the resulting morphology of the samples for a fixed solution concentration (Figure 10.1). Generally speaking a concentration of at least 25% by weight of polymer in the solution is required for the formation of fibers, with the only exception for the solutions with NMP, for which the minimum concentration employable is 27% by weight. Below this values the

fibers are highly heterogeneous with the presence of beads or a bead-on-fibers morphology. On the other hand even a concentration of about 30% by weight is not recommended since the morphology changes leading to the formation of ribbons. This is true except for the case of NMP's solutions for which it results clear that the concentration interval for stable nanofibers is slightly higher than for the solutions of the other solvents. A possible explanation for this is related to the properties of the solvent. NMP possesses an high surface tension coupled an high boiling point, among the solvents chosen. This leads to a slower rate of solvent evaporation and the necessity to increase the polymer concentration to increase the viscosity of the solution. Indeed at a concentration of 25% the fibrous morphology is present but with an high concentration of defects. Moreover it can be clearly seen that some solvent residues led to the melting of bunches of fibers. However a slight increment in the concentration (27%) allowed the electrospinning of the solution at ambient temperature even for low distances between the tip and the collector, without the necessity to increase the temperature.
The results obtained are summarized in Table 10.2, in which the final morphologies of the samples are listed according to the concentration of polymer in the solution and the type of solvent employed.

Table 10.2: *Morphologies of the electrospun samples according to the different solution concentrations employed*

Solution	Solvent			
conc.	DMF	DMAc	DMSO	NMP
20% w/w	beads-on-fibers	fibers	beads-on-fibers	beads
25% w/w	fibers	fibers	fibers	beads-on-fibers
27% w/w	fibers	fibers	ribbons	fibers
30% w/w	fibers	ribbons	ribbons	fibers

Between the solvents chosen the solution with DMSO seems to provide the most difficult solutions to electrospun. Indeed, even if it can be used for obtaining fibers, the electrospinning process is unstable. One of the requirement for the process is the stability of the Taylor cone which is formed once that an equilibrium conditions is reached between the viscous forces and the surface tension of the solutions. For the DMSO solutions the Taylor cone is not stable and it has been noticed that after an initial stable condition it rapidly disappear due to the formation of a solution buildup at the tip of the syringe that, once reached a critical dimension, breaks into droplets. This phenomenon does not prevent the formation of fibers, which are collected on the metal plate, but alters the final structure of the mat. Indeed, as a result, this amount of solution is so high to not allow the complete evaporation of the solvent during the jet formation and leads to the deposition of solvent droplets that, once evaporated, leaves visible halos which can alter the random distribution of the fibers and damage the final mat Figure 10.2. A similar behavior has been found with NMP in relation to low tip-to-collector distances as a result of its high boiling point

and higher surface tension than the other solvents employed.

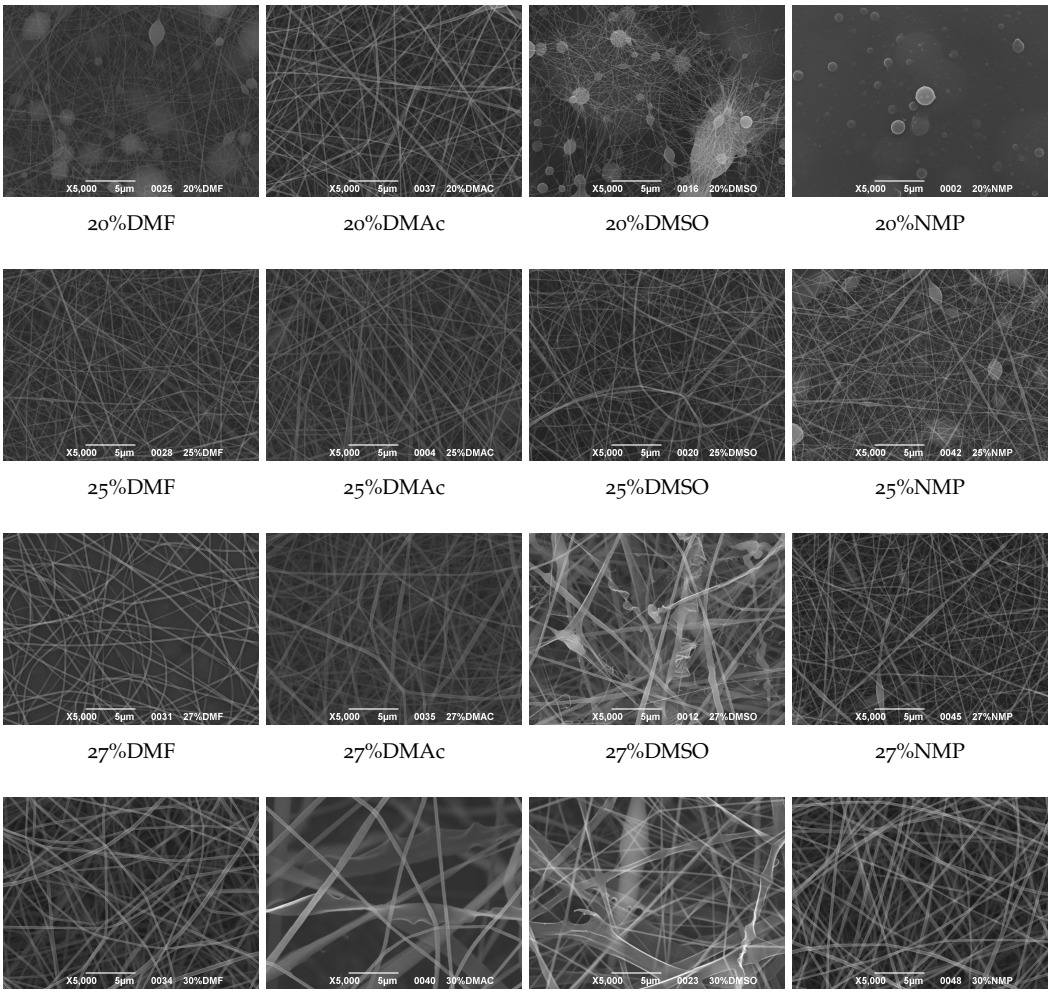

Figure 10.1: *Morphologies of the samples electrospun in different solvents with different solution concentrations*

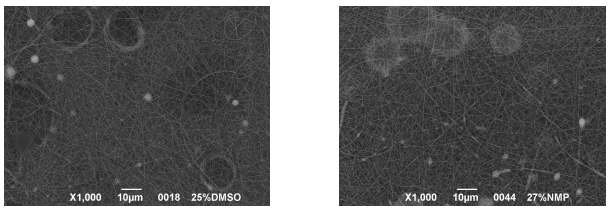

Figure 10.2: *Morphology of the a sample electrospun in DMSO*

Better results are obtained with DMF and DMAc. These solvents are commonly used for electrospinning and in the present case are capable to allow the formation of fibrous morphology of the electrospun samples in a wide range of polymer concentrations.

The optimal conditions for the electrospinning of a polymer solution can be identified both by matching the best process set-up conditions for the variables involved and by tuning the properties of the solution to be electrospun. Since it has been observed that a solution with a polymer concentration of about 27% w/w can be employed for most of the solvents chosen, some samples were realized with binary mixture of the solvent tested in a 50:50 weight ratio. The results of these tests are showed in Figure 10.3. As can be seen the best samples are those obtained by mixing DMF with DMAc and NMP with DMAc. In these cases the fibers are smooth and quite uniform. The samples electrospun with the DMF/NMP mixture presents a beads-on-fiber morphology that gives fibers highly non uniform. Despite the fact that at a 27% w/w concentration the solution with only DMSO as solvent produced ribbons instead of fibers, some samples of mixture with DMSO has been realized. The results in Figure 10.3 d) and e) show that by mixing DMSO with DMAc at the given concentration it is possible to produce fibers, even though the distribution of the fibers diameter seems irregular with significant variation along a single fiber. The DMSO/NMP samples present the worst morphology since there is the presence of both beads along fibers, branched jets in which smaller jets on the surface of primary jets and residual drops of solution which produce the formation of zones in which the fibers are fused together.

From this first screening activity it is possible to draw some preliminary conclusions regarding the operative conditions to employ in order to obtain a stable and uniform fibrous morphology of the electrospun solutions. First it is important to operate with low flow rates, usually with a maximum values of 0.2 ml/h. This is necessary in order to obtain the production of a uniform deposition of fibers since with high flow rates the process is not stable with a common range of voltage and it's likely to obtain the spraying of solution droplets from the tip of the syringe. In some cases, depending on the type of solvent employed, even higher flow rates (0.4 ml/h) are employable, but this seems not to be a good choice since, even if at the beginning the process is stable, once that a given amount of fibers are produced and a small layer of mat is deposited it probably acts as an insulating layer that decreases the potential difference between the two electrodes, with a final effect that is comparable to a decrease in the applied voltage. On the other hand even the voltage is an important parameter. A good choice is to use voltages that are not lower than 15 kV unless to employ very low tip-to-collector distance. This result can be ascribed to the high concentration of polymer required for the solution, which increase the viscosity and require high voltages to allow the stretching process to produce fibers. As maximum value it has been chosen a value of 30 kV, which is usually the full scale value for high voltage suppliers commonly employed for electrospinning, and for safety reasons.

The distances from the tip to the collector were chosen by considering the necessity to provide a sufficient time of flight of the jet in order to stretch and evaporate the solvent, and to be capable to reach the collector and to be subjected to a sufficient electric strength in order not to generate dripping. The conditions that satisfied this requisites where defined in terms of 10 cm for the lower value and 18 cm for the higher.

A very important aspect for the control of the process has been identified in the proper choice of the relative humidity in the electrospinning chamber. It has been observed that

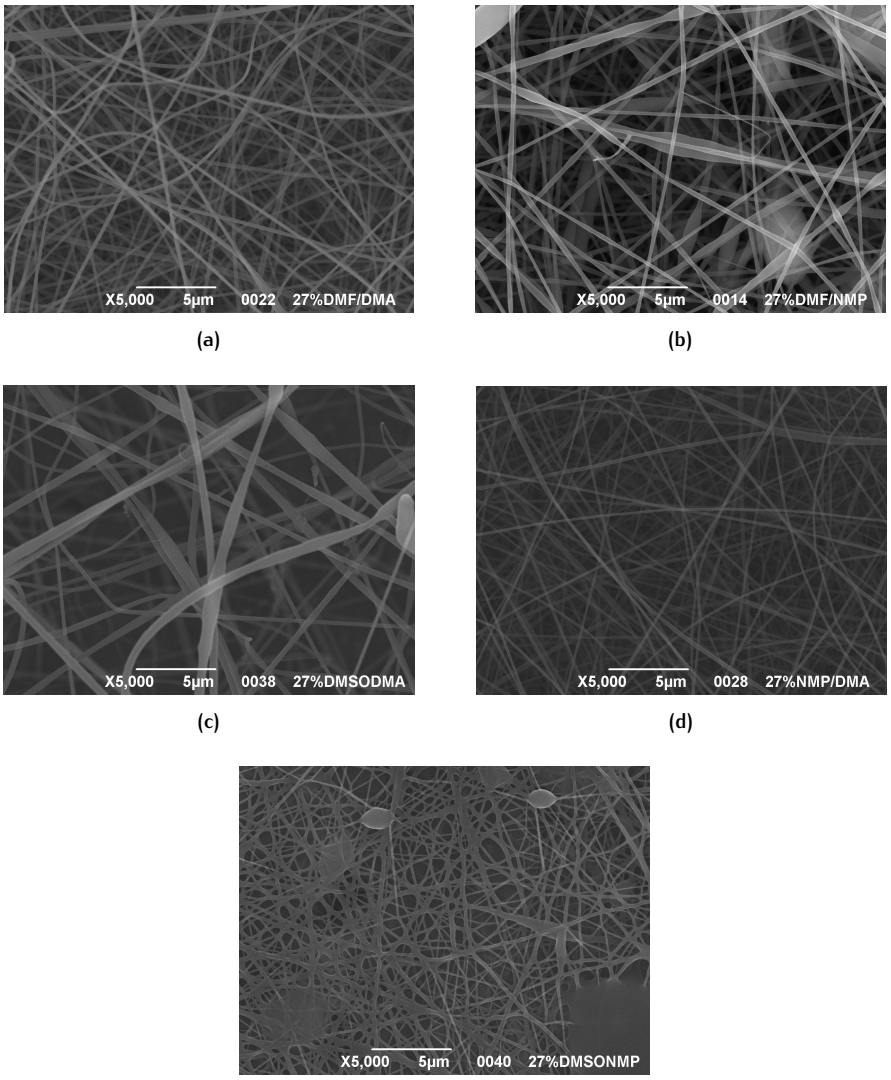

Figure 10.3: *Morphologies of electrospun samples from in different mixtures of solvents: a) 27% w/w in a 50:50 DMF/DMAc mixture, b) 27% w/w in a 50:50 DMF/NMP mixture, c) 27% w/w in a 50:50 DMSO/DMAc mixtures, d) 27% w/w in a 50:50 NMP/DMAc mixture, e) 27% w/w in a 50:50 DMSO/NMP mixture*

for a good and stable process low humidities are required. By increasing the relative humidity during the process the deposition of the fibers is problematic and the electrospun nanofibers tends to spontaneously form yarns on the surface of the metal collector Figure 10.4. A similar behavior has also described in relation to the electrospinning of other sulfonated polymer [422] and ionomers [223, 228]. According to these references the mechanism of the yarn formation is associated to the deposited precursor fibers discharge through polyelectrolyte chains to the grounded target, which prefers the subsequent deposition on the fibers so as to decrease the distance between the fibers and the needle. Once a yarn is formed by touching the adjacent fibers swinging under the instable jet, the following deposition may occur preferably on the yarn rather than on the individual

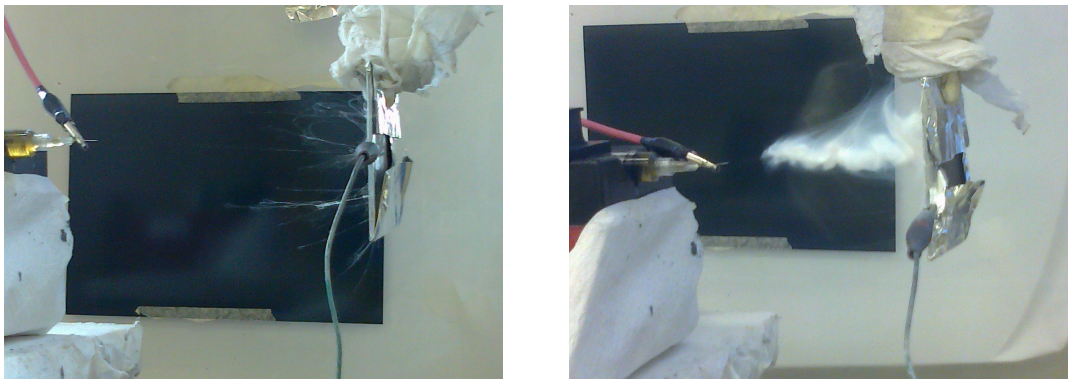

(a) (b)

Figure 10.4: *Spontaneous formation of yarn of electrospraying nanofibers under a conditions of high relative humidities (from 60 to 80%) for a solution of DMAc/DMF (50:50) at 27 % concentration: a) at the beginning of the process, b) after several minutes of electrospinning*

fibers. An electrostatic attractive force stretches the yarn vertically on the target electrode, leading to a successive upward growth of the yarn. This result has been observed also by Okuzaki *et al*. [423] with Poly(p-xylenetetrahydrothiophenium chloride), a precursor of Poly(p-phenylenevinylene), and in other studies concerning the electrospinning of cellulose, poly(vinyl pyrrolidone), chitosan/poly(2-acryloamido-2-methylpropanesulfonic acid) [424–426], in presence of low molecular weight salts (e.g. $CaCl_2$, NaCl, LiCl, $Fe(NO_3)_3$). The aforementioned phenomenon is thought to happen only for polymer solutions with high electrical conductivity since their conductive nature plays a key role in the formation of nanofiber yarns. Finally, the choice of the solvent to be employed is an important aspect to define. The experimental tests have shown that the better solution is to employ DMF and DMAc, or a combination of the two, for the possibility of having a lower values of concentration to use, lower surface tensions and boiling points. Since these two solvents have very similar properties maybe the choice of a mixture of the two can't have a significant impact on the final morphologic and geometric properties of the fibers, thus a choice can be made between the two.

Table 10.3: *Conditions for electrospraying electrospinning*

Solvent	Solution conc. [%]	Flow rate [ml/h]	Distance [cm]	Voltage [kV]	UR [%]
DMAc	20-27	0.05-0.2	10-18	20-30	<20
DMF	25-30	0.05-0.2	10-18	20-30	<20

The final conditions identified for a possible optimization of the electrospraying electrospinning are reported in Table 10.3. This conditions will be analyzed in depth with a

statistical approach based on the design of experiments (DoE) approach in order to better identify which conditions can be employed for obtaining high quality fibers.

10.4 ANALYSIS AND OPTIMIZATION OF SPEEK NANOFIBERS PRODUCTION BY ELECTROSPINNING

10.4.1 Response Surface Methodology

Response Surface Methodology (RSM) is a collection of statistical and mathematical techniques capable to allow the construction of an approximating model for the description of the relationship between a response and a set of predictor variables, on the basis of empirical data obtained by an appropriate experimental design. With RSM it is possible to carry out a simultaneous investigation the effect of the single variables and their mutual interaction, with the possibility to define quantitatively optimized conditions to apply to a given process.

10.4.2 Variables and design selection

After the preliminary screening activity stable operative conditions to have a stable electrospinning process and a uniform fiber morphology have been defined in terms of a proper solvent choice, polymer concentration and definition a suitable range for the other variables considered. Once that those conditions were identified the second part of the study has been characterized by an experimental campaign based on a Box-Behnken Design (BBD). In this case to approximate the relationship between the response and the different variables selected, a second-order linear model has been built according to the following general equation [427]:

$$y = \beta_0 + \sum_{i=1}^{k} \beta_i x_i + \sum_{i=1}^{k} \beta_{ii} x_{ii}^2 + \sum \sum_{i<j}^{k} \beta_{ij} x_i x_j + \epsilon_{ij} \tag{10.1}$$

where y is the response of the design, x_i and x_j are the components of the vectors corresponding to the different coded levels of the variables selected, k is the number of variables, β_i and β_{ii} are the coefficients associated to the linear and quadratic levels of the single variables while β_{ij} is the coefficient associated to the interaction between pairs of variables. The term ϵ_{ij} represents the statistical error associated to the model, assumed to be an independent and identically distributed random variable. The previous expression makes use of coded levels of the variables which can be obtained by a simple transformation, using the minimum and maximum values of the natural variables (z_i) selected [428]:

$$x_i = \frac{z_i - \frac{(max(z_i) + min(z_i))}{2}}{\frac{(max(z_i) - min(z_i))}{2}} \tag{10.2}$$

This coding procedure is widely used for the fitting of linear regression models because all the xis become dimensionless and their values fall between -1 and +1, allowing a better comparison between the relevance of variables that, in their natural state, have different orders of magnitude and units of measure. The present study is based on 4-variables-3-level BBD for the evaluation of the effect of the following four variables: voltage, flow-rate, tip- to-collector distance and sulfonation degree. The choice of these variables has been done in order to evaluate the effect of the process parameters, which could be specific for a given polymer/solvent system, and the effect of the sulfonation degree on the final morphology and dimension of the nanofibers. The influence of the solution concentration has not been screened in depth because it can be predominant over other factors and its effect on the final morphology of the fibers is generally accepted and widely reported in the scientific literature [54, 429, 430]. In this regard the choice has been to select a concentration value capable to produce good and uniform nanofibers and keep it constant at that specific value.

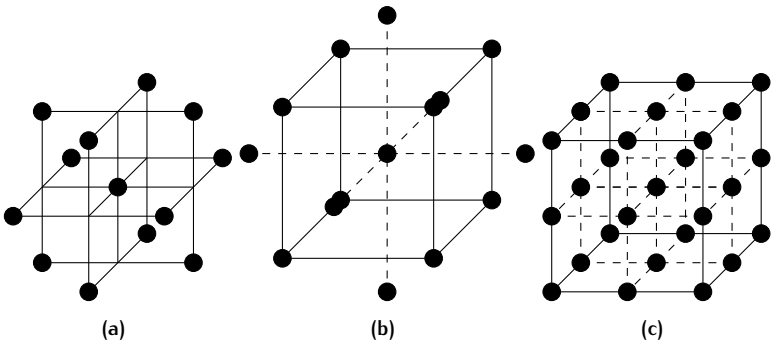

Figure 10.5: *Representation of the different experimental approach for a 3-variables-3-levels design: a) Box-Behnken design (BBD), b) Central Composite design (CCD), c) full factorial design*

For this number of factors and levels taken into consideration the choice of a BBD is more convenient, since it possesses features very similar to a classic Central Composite Design but requires a lower number of runs, avoiding the employment of axial runs and with the possibility of using only three evenly spaced levels of the variables (Figure 10.5). The statistical analysis of the experimental data has been conducted by employing Design Expert software (trial version 9.0.2, Stat-Ease), using the fibers mean diameter and their standard deviation as response variables. The statistical tests for the diagnostic of the developed model have been carried with R (The R Foundation for Statistical Computing, version 3.1.2).

10.4.3 The Box-Behnken design

Once identified the conditions to allow a stable electrospinning process of the polymer, the following step has been the determination of the variables influence on the fiber dimension by the employment of a 4-variables-3-levels BBD. The solvent selected was DMAc, while the solution concentration was fixed at the value of 26 wt%, since it has been identified as the lower value capable to produce fibers without defects. The choice of the factors involved has included three process variables and one material property, namely the current voltage (kV), the tip-to-collector distance (cm), the solution flow rate (ml/h) and the sulfonation degree (%) respectively. Each run has been carried under controlled environmental conditions, with a relative humidity below 30% and 21.3 $\pm$ 0.5°C of temperature. The values of the other variables are reported in Table 10.4. The experimental design consisted in 29 runs with 5 repetitions in the center point Table 10.4. The sequence of the runs

Table 10.4: *Variables chosen for the designed experiment*

Variable	Symbol	Lower value	Center value	Upper value
DS [%]	X_1	60	70	80
Voltage [kV]	X_2	20	25	30
Distance [cm]	X_3	10	14	18
Flow rate [ml/h]	X_4	0.050	0.125	0.200
Coded value	/	-1	0	+1

were randomly defined by the software in order to highlight possible external influences not taken into consideration in the design. The results of the image analysis, summarized in Table 10.5, have shown that the variation of the variables selected produced fibers mean diameters ranging from about 165 to 235 nm and standard deviations ranging from 25 to 60 nm. This result, although seems not to show an high variability of the selected response, is reasonable due to the choice to exclude the polymer concentration from the parameters explored.

10.4.4 Analysis of the model

The first step in the evaluation of the response of the design has been carried by conducting an analysis of variance (ANOVA) Table 10.6, as preliminary phase in the construction of a second-order model to describe the response surface for the fitting of the experimental data. With this approach the statistical significance of each variable selected and the possible interactions between them were evaluated with a backward elimination method by retaining only those terms with a p-value $\leqslant 0.05$ to reduce the complexity of the polynomial expression. The estimation of the coefficients of the linear regression model was determined by a least square minimization.
The final refined model excluded the presence of the interaction terms AB and BC, leading

Table 10.5: *Design matrix for the employed BBD design with the experimental responses at different factors levels in coded form*

Run #	DS (%)	Voltage (kV)	Distance (cm)	Flow rate (ml/h)	Mean diameter (nm)	Std. dev. (nm)
1	-1	-1	0	0	181	32
2	1	0	-1	0	166	35
3	0	0	0	0	164	29
4	0	-1	0	1	167	35
5	1	0	0	1	205	50
6	1	0	0	-1	192	32
7	-1	0	-1	0	218	50
8	0	1	0	-1	182	36
9	0	0	0	0	167	25
10	0	0	0	0	171	28
11	0	-1	1	0	179	38
12	0	-1	0	-1	189	34
13	-1	0	0	1	193	27
14	0	1	1	0	190	45
15	0	0	0	0	167	25
16	0	0	-1	1	184	40
17	-1	0	1	0	199	33
18	-1	1	0	0	187	32
19	0	0	1	-1	225	40
20	0	0	0	-1	201	55
21	1	0	1	0	222	54
22	0	0	1	1	216	60
23	0	1	-1	0	172	38
24	0	0	0	0	170	29
25	0	1	0	1	182	35
26	1	-1	0	0	170	31
27	1	1	0	0	171	31
28	0	1	-1	0	173	37
29	-1	0	0	-1	233	46

Table 10.6: *ANOVA for Response Surface Reduced Quadratic Model of the mean fibers diameter*

Source	SS	Df	MS	F-value	p-value
Model	11782.88	11	1071.17	140.13	< 0.0001
A-DS	720.75	1	720.75	94.29	< 0.0001
B-Voltage	133.33	1	133.33	17.44	0.0006
C-Distance	1102.08	1	1102.08	144.17	< 0.0001
D-Flow rate	481.33	1	481.33	62.97	< 0.0001
AC	1369.00	1	1369.00	179.09	< 0.0001
AD	784.00	1	784.00	102.56	< 0.0001
BD	121.00	1	121.00	15.83	0.0023
A^2	1891.17	1	1891.17	247.40	<0.0001
B^2	502.31	1	502.31	65.71	< 0.0001
C^2	2003.55	1	2003.55	262.10	< 0.0001
D^2	3125.21	1	3125.21	408.84	< 0.0001
Residual	129.95	17	7.64		
Lack of fit	96.75	13	7.44	0.90	0.6090
Pure error	33.20	4	8.30		

to the following final equation in terms of coded factors:

$$\begin{aligned} Md =& 167.60 - 7.75 * DS + 3.33 * Voltage + 9.58 * Distance - 6.33 * Flowrate \\ &+ 18.50 * DS * Distance + 14.00 * DS * Flowrate + 5.50 * Voltage * Flowrate \\ &+ 17.07 * DS^2 - 8.80 * Voltage^2 + 17.58 * Distance^2 + 21.95 * Flowrate^2 \end{aligned}$$

The adequacy of the regression model chosen for the description of the experimental results has been confirmed by the value of 0.98 for the determination coefficient (R^2) and the not significant lack of fit (p-value = 0.6) with respect to the pure error. The obtained ratio of 40.062 for the adequate precision, which measures the signal-to-noise ratio, is greater than 4 and indicates that the model can be used to navigate in the design space. All the factors selected for the design have proven to be important in the description of the variability in the data, although with different extents. Indeed, from the analysis of the relative important of the different regressors on the determination coefficient Figure 10.6, voltage has been identified as the factor that has less relevance with respect to the other terms of the model for both its first-order, interaction and quadratic terms. A similar result has been previously noted for the electrospinning of *Bombyx mori* silk [431] and PAN [432] in relation to the employment of solutions with an high polymer concentration although the opposite result has been found for the electrospinning of Poly(D,L-lactide) [433], probably due to a low tip-to-collector distance [432]. Between the terms of different order the quadratic component is the most significant for the prediction of the data, with a total con-

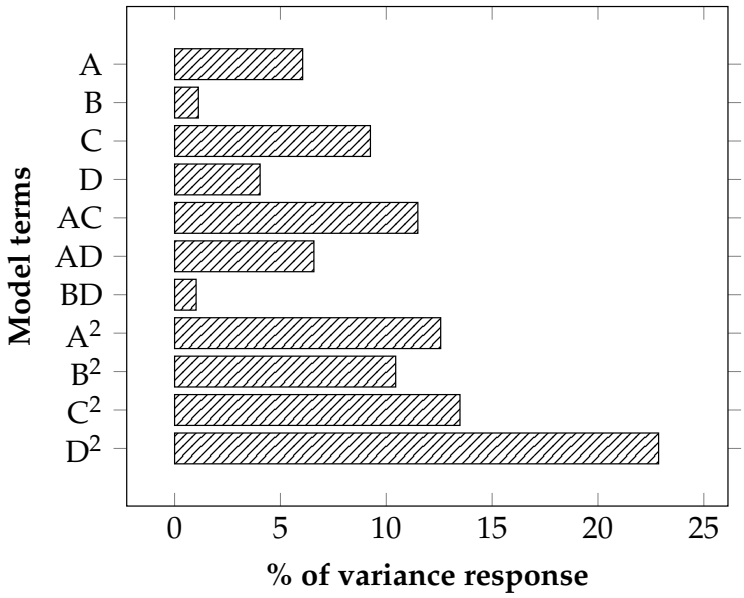

Figure 10.6: *Proportionate contribution of each term of the quadratic model to the R^2 statistic*

tribution of about 60%. This result indicates the presence of strong curvature and optimal conditions probably not far from the center of the design space, in agreement with the assumptions on which the BBD is based.

10.4.5 Model diagnostic

After the model building phase it is necessary to assess the validity of the assumptions that are behind the construction of the response surface by a diagnostic analysis. This phase has been accomplished by looking at:

- Normal probability plot of the studentized residuals to check if they are distributed normally;
- Studentized residuals versus predicted values plot in order to check for constant error;
- Externally studentized residuals to look for outliers (i.e., influential observations).

The normal probability plot (Figure 10.7 b) of the residuals seems to fit a straight line in a quite satisfactory manner. A more reliable way to have a statistical indication of this assumption has been found with the application of the Anderson-Darling test (ADT) [434].
This test can be used to quantify the deviation of a set of residuals from a given distribution. In this case it has been used to test the null hypothesis that the normal distribution adequately describe the residuals, using the comparison of the calculated statistics with a critical value at a 5% level of significance. For the present sample size of 29 residuals the obtained p-value of 0.75 is higher than the cut-off value of 0.05, confirming the conclusion drawn from the visual inspection of the normal probability plot.

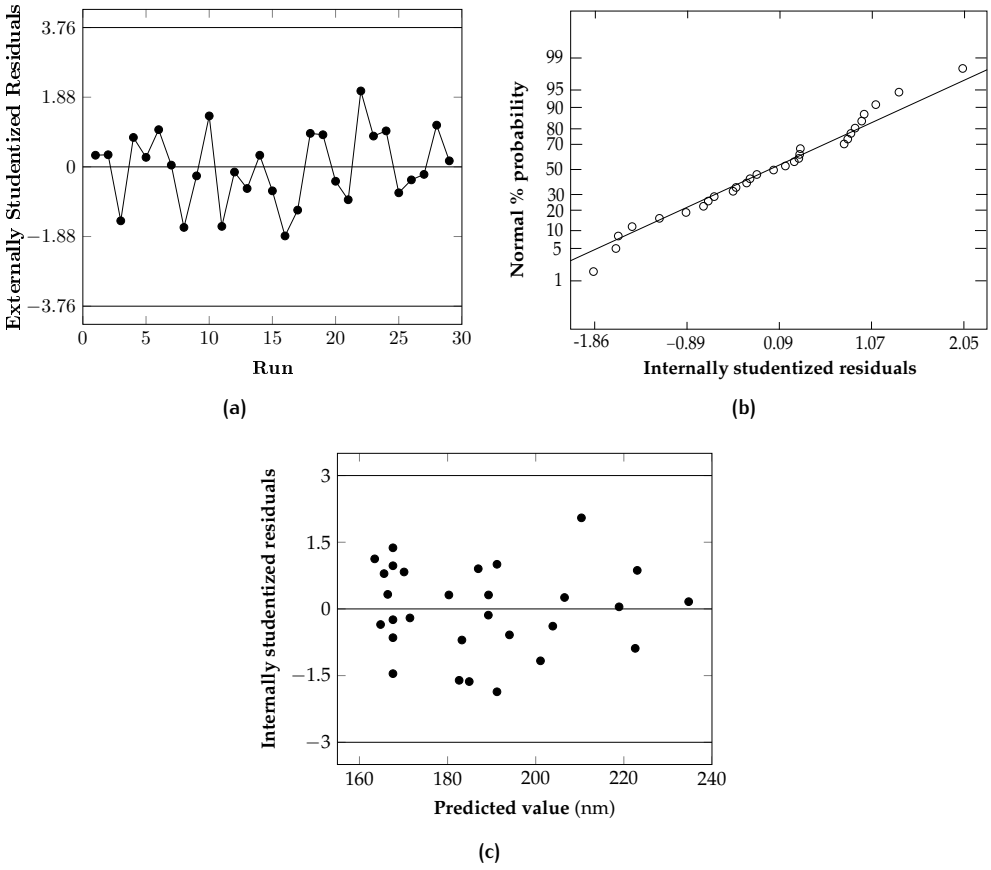

Figure 10.7: *Diagnostic plots for the check of the consistency of the model developed: (a) Residuals versus run for the check of the presence of time-related variable lurking in the background, (b) Normal probability plot for the check of the normal distribution of the residuals, (c) Residual versus predicted values plot for the check of the assumption of constant variance of the residuals.*

The assessment of the presence of autocorrelation in the residuals obtained from the linear regression was realized with the Durbin-Watson test [435, 436]. In this case the statistics is used to evaluate the null hypothesis that the residuals are not negatively nor positively correlated, at a 5% level of confidence. According to the formula, the value of the statistics always falls between 0 and 4 and a value of 2 indicates no presence of autocorrelation. In the present case the test gave a value of 1.99 which is very close to 2 and indicates not significant autocorrelation [436]. A second control can be done, visually, from the plot of the residuals versus the runs which shows no increasing or decreasing distinct pattern over time (Figure 10.7 b). The plot of the residuals versus the predicted values (Figure 10.7 c), for the assumption of the constant variance, does not seem to present a specific increasing or decreasing funnel pattern so the final model has been used without specific transformation of the data. In any case a statistical evaluation of the homoscedasticity condition has been carried with the Levene's test [437] both for the residuals versus the predicted values and for the comparison of the residuals variances at the different levels of each regressor. In the first case the violation of this condition should provide a different spreading of the

residuals along the predicted value axis and to evaluate this the interval has been divided into three parts of equal extension and the residuals of each interval have been grouped and their variances tested against each other.

Table 10.7: *Summary of the Levene's test for the analysis of the homoscedasticity conditions of the residuals of the different levels of the model regressors*

Regressor	Levene's statistic	p-value
Sulfonation degree	4.907	0.086
Voltage	0.152	0.927
Distance	3.057	0.217
Flow-rate	0.603	0.740

The resulting statistics gives a value of 1.79 and a p-value of 0.4077 (higher than the threshold value of 0.05) according to which it is not possible to reject the null hypothesis of equal variances. In the second case the test was applied by grouping the residuals according to the three different levels of the regressors and the corresponding variances tested between each other. The results of the test Table 10.7 reported a p-value higher than 0.05 for each of the regressors, excluding the possibility to reject the null hypothesis of equal variances.

10.4.6 Analysis of the response surface

From the polynomial model developed through the previous analysis it has been possible to construct the response surface to analyze the effect of the different variables on the final mean diameter of the nanofibers.

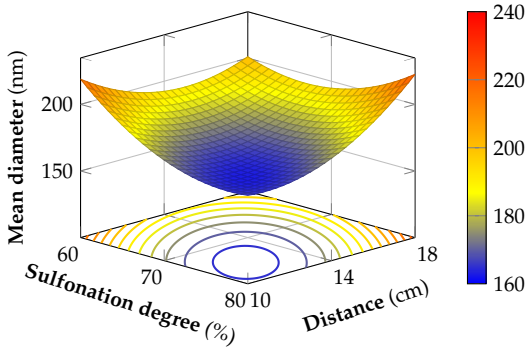

Figure 10.8: *3D response surface of the mean diameter for the sulfonation degree versus distance at an applied voltage of 25 kV and a flow-rate of 0.125 ml/h*

The relationship between the DS and the tip-to-collector distance in Figure 10.8 shows that a decrease of the mean diameter is accomplished by a combination between high sulfonation degrees and low distances, independently from the different levels of the voltage employed because of the statistical insignificance of the interaction terms AB and BC. For low sulfonation degrees a possible improvement can be achieved at medium distances

but the final dimension of the fibers are generally greater than those at high sulfonation degree for the same conditions of the other factors. However this condition is verified for low-medium values of the flow-rate because for the highest level the minimum of the response surface shift towards the center of the design space, with a concurrent increment in the final fibers mean diameter. A possible explanation can be related to the fact that an increase of the sulfonation degree of the material is capable to provide an increase in the conductivity of the solution in a similar way to the addition of a salt [231], leading to the formation of thinner fibers.

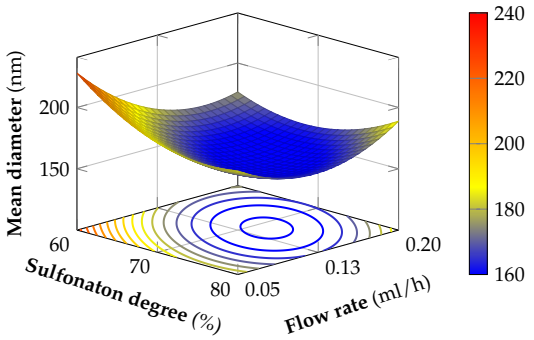

Figure 10.9: *3D response surface of the mean diameter for the sulfonation degree versus flow-rate at an applied voltage of 20 kV and at a distance of 14 cm*

Figure 10.9 presents the interaction between the sulfonation degree and the flow-rate. In this second case better and more stable conditions are achieved by employing a low voltage coupled with low-medium distances since the curvature of the response surface is less significant and it is possible to obtain lower mean fibers diameters for a wider range of flow rates and sulfonation degrees, with an higher flexibility of the process. This result can be ascribed to the fact that in this condition an optimal balance between electric field strength, solvent evaporation rate and polymer jet stretching is achieved. For low flow rates the mean diameter increases probably due to a non-equilibrium condition between the flow rate and the jet removal from the tip which prevents the formation of a visible Taylor cone, with a more marked effect for low sulfonation degrees where the solution conductivity is lower. For higher distances the response surface is flatter and the mean diameter increases above the 200 nm. In the latter case this effect is predominant on the different levels of the other variables involved, determining non optimal conditions for the production of thin fibers.

The relationship between the voltage and the flow-rate, when the other variables at their medium values, is reported in Figure 10.10 from which it is possible to observe a saddle shape of the response surface.

In this situation it is not possible to define univocally a specific optimal condition, but the contour plot of the response surface seems to suggest that for a given flow rate lower mean diameters could be obtained by operating with the lowest voltage value. The presence of a saddle shape of the response is not uncommon during the analysis of the relationship between these two factors [197] and several aspects needs to be pointed out in the explanation of such behavior. An increment in the applied voltage, when all the other variables

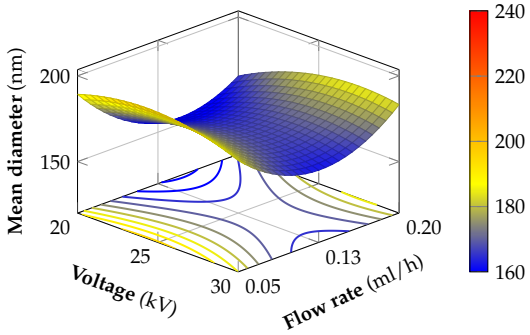

Figure 10.10: *3D response surface of the mean diameter for the voltage versus flow rate at a sulfonation degree of ~70% and a distance of 14 cm from the tip to the needle*

are held constant, is traduced in an increment in the mass flow rate ejected from the tip of the needle and an higher charge density. This induces an increment of the instability and stretching of the jet which could produce smaller fiber diameters. However discrepancies between the experimental results of several scientific works on the effect of the applied voltage for different polymer/solvent systems could suggest the necessity to include a concurrent effect of other variables, like feed rate and tip-to-collector distance, in the evaluation of such effect [438]. For the case in analysis the interaction shows more significant variation when the flow rate is changed for a fixed voltage, rather than the opposite case, stated the poor relevance of the voltage contribution term with respect to the flow rate, on the developed model.

10.4.7 Model validation

Once analyzed the behavior of the approximated response surface in relation to the different levels of the variables involved in the design, the final step has been the validation of the obtained model. The objective of this validation has been to define constrained optimization conditions in order to obtain uniform and thin sPEEK nanofibers for samples at a given sulfonation degree and comparing the results from the values predicted by the software both in terms of mean diameter and standard deviation. In order to define optimal conditions for the standard deviation of the analyzed samples a response surface was built based on a specific model developed for the data collected from the image analysis. The combined analysis of the mean diameter and standard deviation of the fibers shows the presence of a positive correlation (correlation coefficient = 0.718) between the two responses, providing a good chance to obtain similar conditions for the combined optimization. To this end both the two responses have been minimized by employing a desirability function, defined as:

$$D = \left[\prod_{i=1}^{N} d_i^{r_i} \right]^{1/\sum r_i} \tag{10.3}$$

where N is the number of responses, r_i is the value of the importance attributed to the

selected response and d_i is the partial desirability function for specific responses. For the case in analysis the relative importance selected was a value of 3 on a maximum value of 5, in order to set the optimization of the process by define an equal importance for both the two responses. The numerical optimization has been carried via a penalty function approach using the downhill simplex method (Nelder-Mead method [439]) for multidimensional minimization. By this procedure the numerical optimization allows the determination of the conditions that maximize the desirability function. Three samples with different sulfonation degrees were selected within the range defined during the RSM analysis, and the relative optimized conditions were set for the electrospinning experiments (Table 10.8).

Table 10.8: *Predicted optimized conditions and relative desirability function values for three samples at different sulfonation degrees*

Sample	DS [%]	Voltage [kV]	Distance [cm]	Flow rate [ml/h]	Desirability
1	62	20	14.5	0.163	0.954
2	65	21	14.5	0.143	0.971
3	73	21	13.5	0.114	0.962

These conditions were defined for the electrospinning process in order to produce the corresponding nanofibers. The sample produced according to these optimized conditions were analyzed by SEM for the calculation of the mean diameter and standard deviation of the nanofibers, analogously to previous analysis. The comparison between the measured values and the predicted values by the model are presented in Figure 10.11.

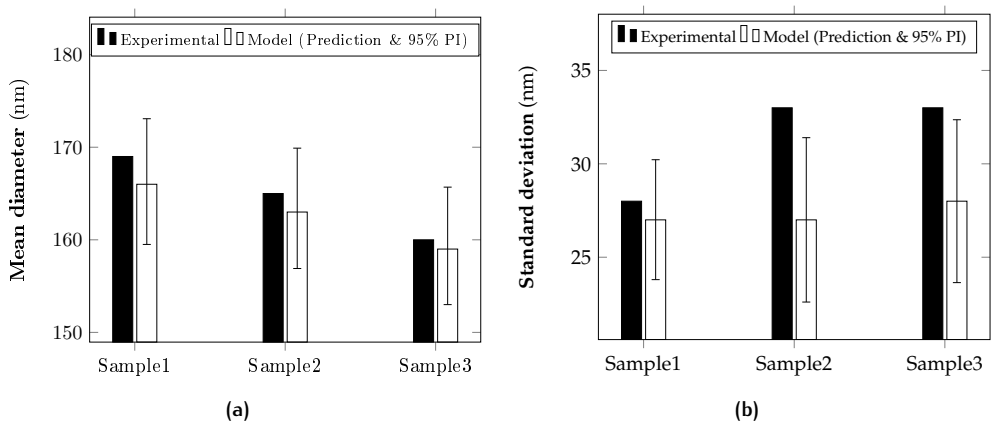

Figure 10.11: *Comparison between the experimental results and the model prediction (prediction and 95% prediction interval) for: (a) the mean diameters and (b) the standard deviation of electrospun nanofibers*

The comparison has been made between the expected values taking into consideration the 95% prediction interval provided by the model. The results have shown an acceptable accordance with the model prediction for the mean diameter and, to a less extent, for the

standard deviation, probably due to the low value (0.88) of the predicted R^2 of the relative model. The final discrepancy on the standard deviation is considered acceptable, thus the combined optimization has been taken into consideration for the definition of the optimal conditions for the production of sPEEK nanofibers employed in the subsequent part of the study.

10.5 CONCLUSIONS

A first screening activity has been carried to select the proper set of variables for the electrospinning of sPEEK nanofibers in solutions of polar aprotic solvents. After the selection of the proper solvent and polymer concentration a subsequent, more careful, analysis and optimization for the production of thin and uniform nanofibers has been realized using a DoEs' approach with the employment of Response Surface Methodology. The general conditions for the electrospinning of the material require high polymer concentrations, medium-high voltages, low flow-rates and low relative humidity to allow a proper collection of the nanofibers. A more detailed analysis has been carried to develop a model for the description of the response surface of the mean fibers' diameter using a BBD in which both process (voltage, tip-to-collector distance, flow-rate) and material (sulfonation degree) factors has been taken into consideration. The developed model has shown a good descriptive capability of the observed data, the presence of interaction between sulfonation degree and both the flow rate and the distance parameters while voltage has proved to have little or no effect on the final fibers dimensions. The model showed a good capability in the description of the selected response changes in the design space and it has been validated, in combination with a second model employed for the description of the standard deviation, using optimized conditions for samples at different sulfonation degrees. Good results have been obtained for the description of the first response while the standard deviation showed less accordance to the predicted values. In this manner it has been possible to define optimized conditions in order to minimize the final mean diameter and standard deviation of the fibers according to the different values of the sulfonation degree in the range analyzed.

11 COMPOSITE MEMBRANES BASED ON ELECTROSPUN SPEEK NANOFIBERS INTO A CONDUCTIVE MATRIX

On the basis of the results of the previous experimental activity the following step is based on the realization of composite membranes based on electrospun sulfonated PEEK at different sulfonation degrees embedded in a proton conductive matrix by a casting procedure. Since sulfonated aromatic hydrocarbons generally suffers of low conductivity than reference PEMs material the choice has been to couple sPEEK with a short-side chain perfluorosulfonic acid. Solvay Specialty Polymers has developed a short side chain perfluorosulfonic membrane with the trade name Aquivion®. This polymer is characterized by both larger crystallinity and higher glass transition temperature than long side chain polymers at a given equivalent weight, combining higher proton conductivity than Nafion®. Composite membranes of electrospun sPEEK and Aquivion have been produced by dipping the mat into the casted solution of the ionomers and the obtained membranes have been characterized in terms of proton conductivity, water uptake, swelling and mechanical tests. The aim is to evaluate the effect of the sulfonation degree and analyze the performances of the final membrane in terms both of conductivity and durability of the same. In this sense good mechanical properties could lead to the realization of thinner membranes, reducing the internal ionic resistance or realize membranes with higher durability.

11.1 RAW MATERIALS

For this part of the study sPEEK samples at different sulfonation degree have been prepared by reaction in acid. sPEEK mat have been embedded in a ionomeric matrix of a commercial grade short side chain Aquivion (D83-24B, Solvay Solexis, EW = 810-850 meq/g).

11.2 CHARACTERIZATION

11.2.1 Elemental analysis

Samples of about 15 mg were analyzed by combustion with an Elementar Vario Micro Cube analyzer. The weight % content of the mass of elemental carbon, hydrogen and sulfur

were recorded twice for each sample, taking the mean value of the two measurements as reference.

11.2.2 Proton nuclear magnetic resonance (H-NMR)

Solution at 3% by weight of SPEEK samples at different sulfonation degrees were prepared by dissolution in d_6-DMSO for NMR analysis using a Bruker Avance spectrometer (Bruker BioSpin Co.). The NMR spectra were collected acquiring 64 scans at a working frequency of 300 MHz, at room temperature. The chemical shift of tetramethylsilane was used as internal reference.

11.2.3 Scanning Electron Microscopy (SEM)

The morphology of the electrospun samples were characterized by SEM (Hitachi S-2600N) micrographs of gold sputtered samples cutted from the membranes. The cross-sections have been analyzed on freeze-fractured samples soaked in liquid nitrogen.

11.2.4 Proton conductivity tests

In-plane proton conductivity of the membranes have been measured by a BekkTech conductivity test cell using a four probe arrangement. Strip of known size and thickness have been placed in a controlled temperature/humidity chamber and fixed onto a Teflon fixture in contact with four platinum electrode. Conductivity tests have been performed at 80°C and 110°C and 50-90% relative humidity.

11.2.5 Swelling measurement

Membranes have been soaked into deionized water for 15 hours and subsequently rapidly dried with a cloth and weighted. After this measurement they have been re-hydrated in water for 1-2 hours and then the samples have been measured in the wet state. Finally the membranes have been dried in oven at 120°C for 3 hours and than measured and weighted again. The water uptake (WU) has been calculated as:

$$WU = 100 \times \frac{W_{wet} - W_{dry}}{W_{dry}} \tag{11.1}$$

where W_{wet} and W_{dry} are the weights of the wet and dry membranes, respectively.
The swelling has been measured according to the following equation:

$$\% \text{ swelling} = 100 \times \frac{X_{wet} - X_{dry}}{X_{dry}} \tag{11.2}$$

where X can be the membranes volume or area.

11.2.6 Mechanical tests

Stress–strain mechanical tests were carried out by a Zwick Roell Z1.0 testing machine, with a 200 N static load cell. Young's modulus (the slope of the stress–strain curve in the elastic deformation region), yield stress (maximum stress that can be developed without causing plastic deformation) and elongation at break (the percentage increase in length that occurs before the sample breaks) were measured on rectangle shaped film stripes, length and width of which were 100 and 5 mm.

11.3 RESULTS AND DISCUSSION

11.3.1 Synthesis and electrospinning of sPEEK at different sulfonation degrees

The first step in the realization of the membranes has been the sulfonation of the PEEK and three different sulfonation degrees have been taken into consideration from the previous part of the study §9.3.1. Due to constraints in terms of polymer solubility and dimensional stability in high humid environment the interval of sulfonation degrees employable is quite narrow. Generally speaking the sulfonation degree of sPEEK for PEMS should be between 40% and 70% [440], however, due to the solubility constraints in relation to the high polymer concentration in the solutions required for the electrospinnig, in this case the selected interval has been defined in the range between 60 and 70%. Three different batches have been realized by sulfonating PEEK in a mixture of MSA/H_2SO_4 (§9.3.1.3) in a MSA/H_2SO_4 mixture. In order to have a reliable estimation of the degree of functionalization, two techniques have been employed to estimate the sulfonation degree: liquid H-NMR and elemental analysis. The evaluation of the sulfonation degree by elemental analysis has been realized by evaluating the ratio between the carbon and the sulfur content of the samples while the evaluation by proton spectra has been carried by using the following formulas [395]:

$$\frac{n}{12-2n} = \frac{Area_{H_A}}{(Area_{H_{B,C,D,D',E,E'}})} \quad (0 \leqslant n \leqslant 1) \tag{11.3}$$

$$DS = n \times 100\% \tag{11.4}$$

The interpretation of the formula can be given by referring to Figure 11.1. Liquid H-NMR spectra of SPEEK the presence of a sulfonic acid group causes a significant 0.25 ppm downfield shift of the hydrogen H_A signal compared with H_B or H_C in the hydroquinone ring, resulting in a distinct signal for protons at the A position. The H_A signal intensity may be used for estimation of the H_A content which is equivalent to the SO_3H group concentration or the degree of sulfonation per repeat unit. The DS can be derived from the ratio between the peak area of the H_A signal (A_{H_A}), and the integrated peak area of the signals

corresponding to all the other aromatic hydrogens (Figure 11.2).

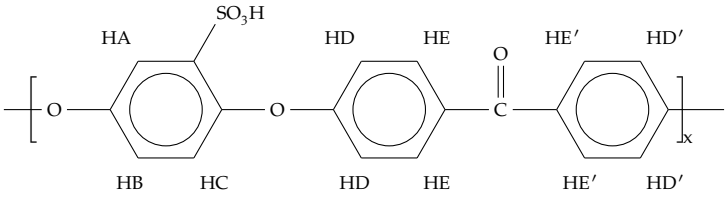

Figure 11.1: *Nomenclature of the aromatic protons for the SPEEK repeat unit*

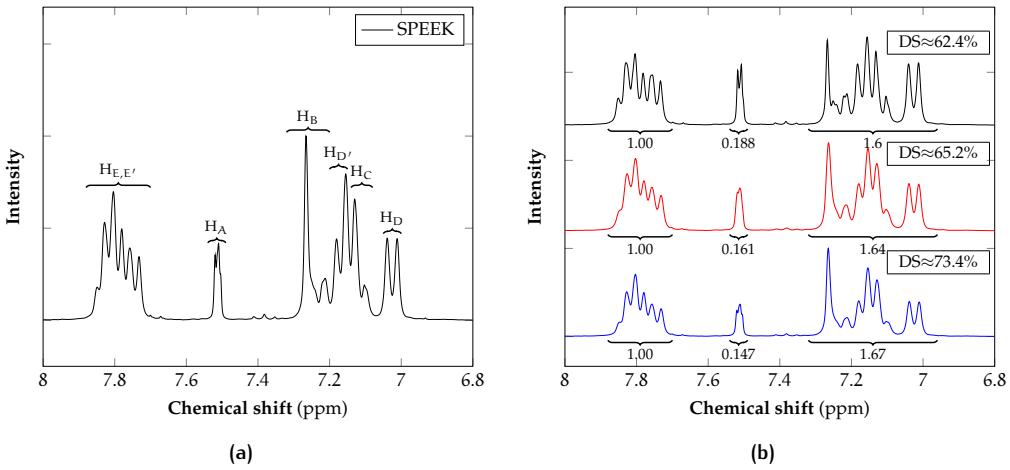

Figure 11.2: *A typical H-NMR spectra of sPEEK in DMSO-d_6*

Table 11.1: *Results of elemental analysis of the sulfonated samples and comparison with the sulfonation degree provided by H-NMR*

Sample	%C	%S	S/C	DS [%]	DS from NMR [%]
Batch 1	62.74	5.48	0.0874	62.4 ± 0.4	60.3 ± 0.8
Batch 2	60.15	5.50	0.0914	65.3 ± 1.9	66.9 ± 1.6
Batch 3	59.84	6.15	0.1028	73.4 ± 1.9	76.3 ± 0.5

As can be seen from Table 11.1 the data shows a good accordance between the two techniques of analysis employed, proving the reliability of the results attained. However the results from the elemental analysis have considered more reliable and have been taken into consideration as the real values of sulfonation for the different samples realized. Besides, since the sulfonation degree should be sensibly different to appreciate differences in the final membranes, for the subsequent phase of testing only the samples at the lower and higher sulfonation degree have been employed.

All the electrospinning tests have been carried by using a roto-traslating drum, rotating at a velocity of 800 rpm with a translational motion of 10 mm/s, enclosed into a plastic chamber. Humidity was controlled in order not to overcome a threshold value, but not set to a specific values. The electrospinning conditions were defined accordingly to optimal

parameters individuated during the optimization process while the time for the deposition of the nanofibers has been defined in order to obtain a uniform mat with an average thickness of 20 μm ± 2.

11.3.2 Mat impregnation

The composite membrane has been realized by solution casting of the ionomer dispersion in water followed by immersion of the sPEEK mats. The target has been to embed the nanofibrous support inside the final membrane and to allow its expansion along the cross section of the final membrane to act as mechanical reinforcement.
The dispersion of Aquivion has been diluted from the initial value of 24% to 12% by weight by addition of distilled water. The casting has been conducted on glass plate using a casting blade of 200 μm with a first layer of solution, deposition of the electrospun mat of sPEEK and subsequent casting of a second layer of Aquivion dispersion. The obtained films have been dried overnight to allow the evaporation of the water and subsequently thermally annealed at 160°C in oven for 1 hour in order to crystallize the ionomer for improving its mechanical strength and preventing its dissolution in water (Figure 11.3). To ensure membrane protonation the samples have been acidified for 24 hours in 1M solution of HCl and rinsed with distilled water until the pH of the washing solution was neutral. The final membranes obtained are shown in Figure 11.4. The samples produced have been

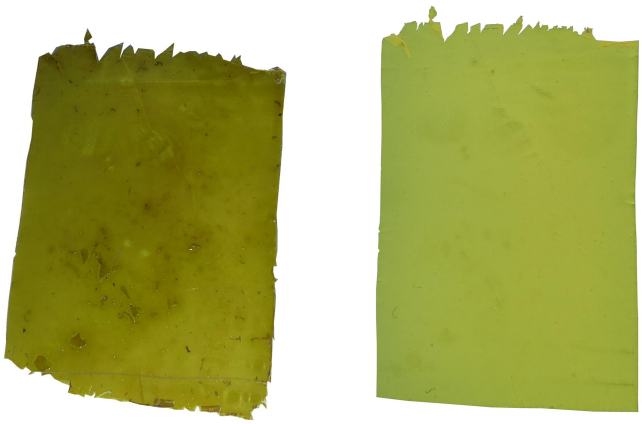

Figure 11.3: *Aquivion/electrospun SPEEK composite membranes after drying and before removal from glass plate a) with electrospun sPEEK at 62% of sulfonation degree and (b) with electrospun sPEEK at 73% of sulfonation degree*

analyzed by SEM in order to identify the presence of the nanofibers in the cross-section of the membrane and evaluation of their distribution inside the membranes. In order to better identify the presence of the nanofibers the comparison has been made with an Aquivion casted membrane which has been subsequently employed as reference for the characterization of the membranes properties. A first comparison is shown in Figure 11.5 where a composite membrane is compared with the reference casted Aquivion membrane. In the

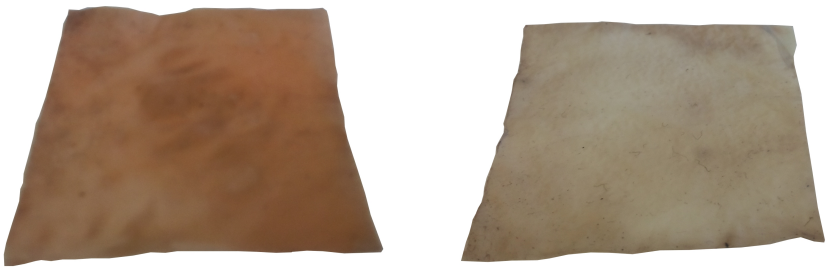

(a) (b)

Figure 11.4: *Aquivion/electrospun SPEEK composite membranes: (a) with electrospun sPEEK at 62% of sulfonation degree and (b) with electrospun sPEEK at 73% of sulfonation degree after removal from glass plate with a 1M solution of HCl*

latter case the membrane is homogeneous all along the section while for the composite membrane the fibers are presents all along the cross-section of the membrane. However their the density distribution of the fibers is not high and this is probably due to the expansion effect of the mat itself into the perfluorosulfonated matrix.
High resolution SEM images have allowed a better identification of the presence and distribution of the nanofibers in the composite membrane. As can be seen from Figure 11.6 and Figure 11.7 although in both cases the nanofibers are distributed all along the section of the membrane a clear distinction is identifiable.

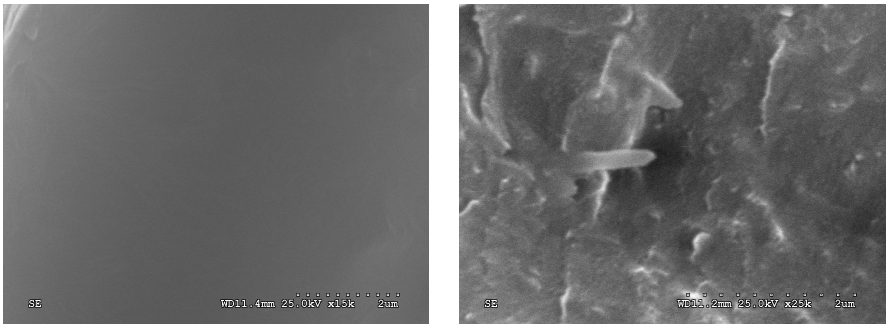

(a) (b)

Figure 11.5: *SEM micrographs of the cross-section: (a) casted Aquivion membrane, (b) composite Aquivion/sPEEK membrane*

At lower sulfonation degree the nanofibers tend to form clusters on a micron scale while for at higher sulfonation degree this phenomenon is no longer present and the final morphology is very homogeneous. To explain this behavior a possible explanation can be found in the processing for the preparation of the final membranes. sPEEK present a more pronounced hydrophilicity at higher sulfonation degrees; since the casting of Aquivion is realized from water dispersion the higher interaction with water molecules which can be obtained for the sample at higher sulfonation degree is capable to provide an higher expansion of the nanofibers in the final membrane.

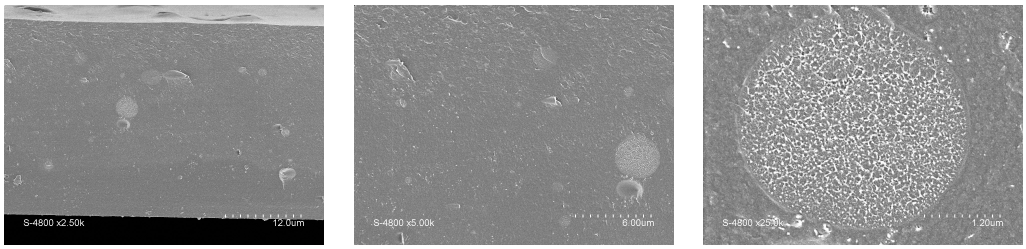

Figure 11.6: *SEM micrographs of the cross-section of the Aquivion/sPEEK (sulfonation degree ~62%) composite membrane at different magnifications*

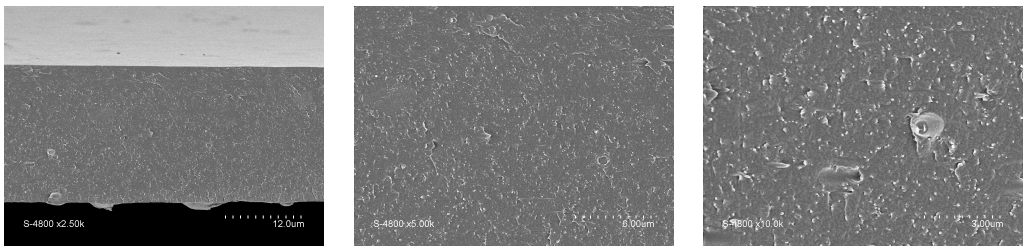

Figure 11.7: *SEM micrographs of the cross-section of the Aquivion/sPEEK (sulfonation degree ~73%) composite membrane at different magnifications*

11.3.3 Membranes characterization

Proton conductivity measurement are presented in Figure 11.8. The measurement have been conducted at two different temperatures under different relative humidities and the results have been compared to the reference of a casted Aquivion membranes. Generally the proton conductivity of all the membranes tested have shown higher values at 110°C than 80°C, a typical Arrhenius behavior for proton conduction [441, 442].

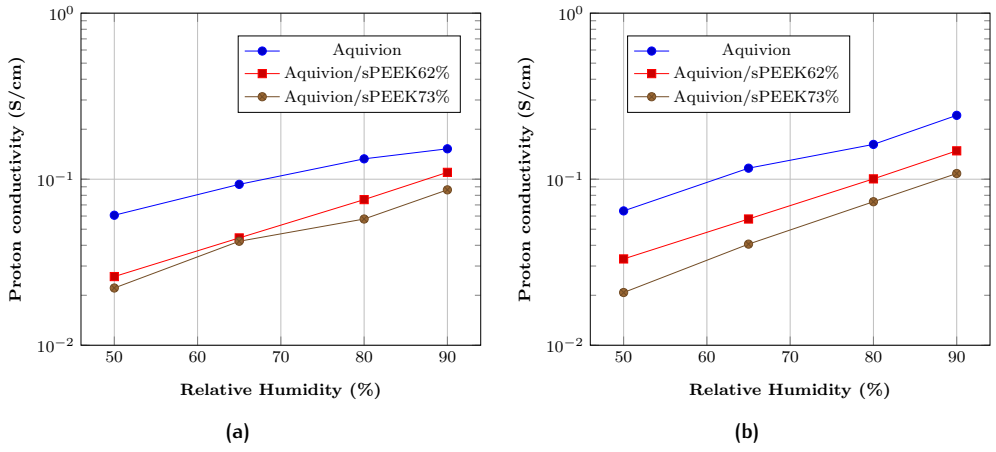

Figure 11.8: *Proton conductivity of the membranes under different humidities and at two different temperatures: (a) 80°C, (b) 110°C*

The proton conductivity of the composite membranes has been lower than the reference.

This can be ascribed in part from the characteristic lower proton conductivity of sulfonated polymer with respect to perfluorosulfonic acid ionomers[443] and partially to the specific morphology of the reinforce. Indeed a first comparison has also been made between densified electrospun mat of sPEEK (applied pressure of 10 kPa) at the two different sulfonation degrees. At 80°C and 90% of relative humidity the proton conductivity are 6 and 13 mS/cm. Under the same conditions the values obtained are comparable but lower to the relative values for casted membrane of the same polymer at the same sulfonation degree. This behavior as been previously reported by Won *et al*. [444] and can be attributed to the limited volume reduction of the mat (~ 42%) upon compression at room temperature since, for this type of morphology it has been demonstrated that the proton conductivity is proportional to the volume fraction of polymer electrolyte fibers [225, 445]. A particular results can be found in the higher proton conductivity shown by the membrane containing the sPEEK at lower sulfonation degree than that employing the higher value. A possible explanation can be related to fact that the proton conduction characteristic of the porous reinforcement becomes preminent with high sulfonation degree. In this case, as it will be shown from the swelling measurement, the higher hydrophilicity of sPEEK can preferentially absorb more water than the corresponding ionomeric matrix of the composite membrane at a given relative humidity. In this manner, since the proton conductivity is general strongly dependent on humidity, the proton transport is more influenced by the porous reinforcement which cause a decrease on the performance of the composite membrane with respect to the reference material. However, for all the range of humidity tested, the final conductivites of the membranes are higher than 10^{-2} S/cm, considered the lower limit for practical applications [446].
The results of the swelling measurements are presented in Table 11.2. As can be noted the membranes containing the sPEEK with the higher sulfonation degree lead to the complete disruption of the membrane as a consequence of the excessive swelling in water, preventing any type of measurement. In this case the choice of the selected sulfonation degree has revealed to be detrimental and in combination with the results of proton conductivity it is possible to conclude that the limitation of the hydrophilicity of the proton conductive reinforcement is of vital importance for the performances and durability of the composite membrane. Such high sulfonation degrees can be possibly employed by introducing crosslinking of the polymer chain to limit swelling or by solvent exposure to promote interfiber welding. The swelling behavior of the neat Aquivion and Aquivion/sPEEK(62%) are quite similar. However the composite membranes exhibits an higher water uptake as a consequence of the higher hydrophilicity of the sPEEK components compared to that of Aquivion (IEC of versus 1.15 meq/g, respectively). This result is quite interesting; since the amount of water absorbed is higher the similar values are a result of lower expansion induced by the nanofibrous membrane. However such non-isotropic behavior of the swelling is desirable for fuel cells applications [447].

The results of the mechanical test performed are presented in Table 11.3 and Figure 11.9 which shows the stress–strain curves of the composite membranes, together with those of the neat ionomer. The reference membrane exhibits a typical ductile behavior: after reaching the yield point, the stress first drops slightly and then gradually increases with

Table 11.2: *Results of the water uptake and water swelling measurements*

Sample	Water uptake [%]	Area swelling [%]	Thickness swelling [%]	Volume swelling [%]
Aquivion	74	80	19	114
Aquivion/sPEEK(62%)	96	85	18	118
Aquivion/sPEEK(73%)	-	-	-	-

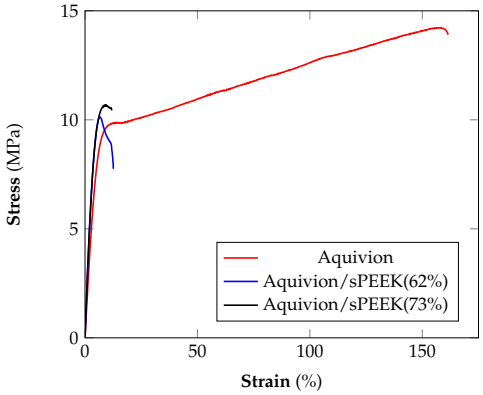

Figure 11.9: *Stress-strain curves for the membranes tested*

Table 11.3: *Mechanical properties of the membranes as determined from the stress-strain curves*

Sample	Young modulus [MPa]	Yield stress point [MPa]	Elongation at break [%]
Aquivion	183.9 ± 4.2	9.71 ± 0.2	167.1 ± 8.0
Aquivion/sPEEK(62%)	279.9 ± 5	10.3 ± 0.1	7.8 ± 4
Aquivion/sPEEK(73%)	267.5 ± 0.4	10.7 ± 0.1	10.4 ± 2

strain (strain hardening) until fracture occurs. The slope of the curve in the elastic region is higher for the composites than for the neat ionomer. Correspondingly, a reduction of the elongation at break is generally observed, thus indicating that the composites are less ductile than the neat polymer, typical behavior of polymeric composites membranes. For the nanofiber composite membranes it is observed that the Young's modulus is significantly higher for both the two different sulfonation degree, specifically an increase of +52% and +45% for the lower and higher sulfonation degree. This is attributed to the sPEEK in the fibrous structure which acts as a reinforcing non-woven network. A little improvement is also observed in the yield stress as a consequence of the aforementioned reason.

11.4 CONCLUSIONS

Composite nanofibrous membranes based on electrospun sPEEK mat with different sulfonation degree embedded in a perfluorosulfonated matrix (Aquivion) have been realized

by a two step procedure. Firstly electrospun sPEEK mats have been produced and subsequently soaked into casted solution of Aquivion, obtaining the final dense membranes after solvent evaporation. The final samples have shown dispersion of the nanofibers along the section of the membranes but to different extent according to the sulfonation degree of the sPEEK nanofibers. At the lower sulfonation degree the nanofibers are more segregated an form clusters while at the higher sulfonation degree the higher interaction between the two polymers favored a more homogeneous dispersion of the two. The composite membranes showed lower proton conductivity than the reference but still quite satisfactory for the final application. The swelling test have shown a good dimensional stability of the composite membrane comprising the lower sulfonated sPEEK compared to the relative amount of water uptake, with an non isotropic swelling. The membranes with the higher sulfonation degree are too much hydrophilic (due to the polar nature of the sulfonic acid group) and have led to excessive swelling with membrane failure. Mechanical test have also determined an increase of the mechanical strength upon incorporation of the porous reinforcement, which restrict the elasticity of the final membrane in comparison to the reference material.

12 COMPOSITE MEMBRANES BASED ON ELECTROSPUN SPEEK NANOFIBERS INTO A NON CONDUCTIVE MATRIX

A second route followed during the experimental activity has been to introduce a non-proton conductive matrix in the nanofibrous mat of sPEEK. Two different fluorinated polymers, poly(vinylidene fluoride) (PVDF) and poly(vinylidene-co-hexafluoropropylene) (PVDF-co-HFP), have been selected as structural components for their excellent thermal stability, mechanical strength and their hydrophofobicity which can help in reducing the swelling of the final membranes [448, 449]. The choice has also been determined due to the solubility of the sulfonated polymer which imparts several limitations on the employable polymers to realize composite membranes based on a nanofibrous network. The successful solution has been the dual electrospinning of PVDF and sPEEK followed by the densification of the membranes by melting of the PVDF to obtain a final compact membrane. Two different mass ratios between the two polymers and two different sulfonation degree of sPEEK have been evaluated for the test with a comparison with the same type of membranes produced by casting. The obtained membranes have been characterized in terms of proton conductivity, water uptake, swelling and mechanical tests.

12.1 RAW MATERIALS

sPEEK at two different sulfonation degrees (~ 60% and ~ 70%) have been employed from the same batches realized in the first part of the study. PVDF-co-HFP pellets (melt viscosity = 20-25 kpoise (230 °C)(100 sec^{-1})) were purchased from Sigma-Aldrich while PVDF Kynar 500 (melt viscosity = 34-40 kpoise (230°C)(100 sec^{-1})) was purchased from Arkema.

12.2 CHARACTERIZATION

12.2.1 SEM

The morphology of the electrospun samples were characterized by SEM (Jeol 6490) micrographs of gold sputtered samples cutted from the membranes. Both the surface of the

membranes and the cross-sections have been analyzed and in the latter case the analyses have been conducted on freeze-fractured samples soaked in liquid nitrogen.

12.2.2 DSC

The thermal transition of the composite membranes and of the pristine PVDF were analyzed by TA Instruments DSC Q200 by applying a heat/cool/heat cycle procedure with a heating/cooling rate of 10°C/min under a constant flux of N_2 of 50 ml/min. The first heating run is necessary to erase the thermal history of the samples in order to obtain the desired informations (first and/or second order transitions) from the two following cycles.

12.2.3 Proton conductivity

An impedance/gain phase spectroscopy analyzer Solartron 1260 (AC amplitude 10 mV; initial frequency 10 MHz, final frequency 1 Hz) was used to measure membrane resistance to, proton transport; the results were elaborated by the Zplot software (Scribner Associates, Inc., USA). The impedance data were corrected for the contribution of the empty and the short-circuit cell. A membrane disc (diameter 9 mm) was placed in a home made two-compartment conductivity measurement cell already described [450]. The membrane was clamped between two carbon paper electrodes in the membrane compartment under a pressure of 13 bar. The relative humidity (RH) was controlled by a second compartment containing water kept at temperatures equal to, or lower than, the first compartment by using a tubular furnace. The samples were tested from lower to higher relative humidity at a fixed temperature of 80±1°C. The conductivity of the membrane samples in the transverse direction was calculated from the impedance data,

12.2.4 Swelling and water uptake tests

The water uptake of the pristine polymers and their blends by dual-electrospinning (followed by PVDF melting and densification) and casting have been evaluated according to the ASTM D 570-81 standard. The membranes have been dried in oven for 24 hours at 50°C, cooled in a desiccator and immediately weighed to the nearest 0.001 g. Subsequently they have been soaked in deionized water for 24h then removed from water, wiped free of water with a tissue paper and then immediately weighted. Water uptake and swelling have been determined according to Equation 11.1 and Equation 11.2, respectively.

12.2.5 Mechanical testing

Stress-strain curves of the membranes at 30°C and approximately 50% of relative humidity were obtained using a Dynamic Mechanical Analyzer (DMA Q800, TA Instruments) operating in tension mode. Before the measure the membranes have been conditioned for

24h at 30°Cat 50% of relative humidity. The measures have been conducted with a ramp of force of 0.1 N/min until sample yielding. Young modulus, yield stress, strain at break and proportional limit stress have been determined from the obtained curves.

12.3 RESULTS AND DISCUSSION

12.3.1 Membranes preparation

As in the first of the study, as first approach in the development of composite membranes employing a non-proton conductive matrix has been followed by soaking electrospun sPEEK mat is casted solution of a second polymer. However, due to the high solubility of sPEEK in common organic solvents for membrane casting the choice of a suitable fluorinated non-conductive matrix is not easy. In this case PVDF is unsuitable since it is soluble in the same solvents of sPEEK, creating problems for membrane casting. Other solvents (e.g. acetone) are cited in literature [451] but they can be considered as latent solvents, in which the polymer doesn't dissolve completely or swells. A partial improvement towards these solvents can be achieved by employing a PVDF copolymer: poly (vinylidene fluoride-co-hexafluoropropylene). In this case the addition of the HFP unit allows the solubilization of the polymer in less strong polar solvents (acetone, ethyl acetate, methyl ethyl ketone, tetrahydrofuran). However it is important to know that the solubility of the polymer in such solvents is strictly dependent both on the ratio between the two monomers present in the structure (Figure 12.1) of the copolymer and on the molecular weight. In

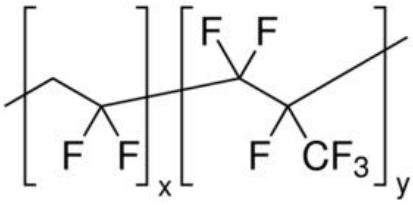

Figure 12.1: *Repetitive unit of PDVF-co-HFP*

order to evaluate the extent of the solubility of the polymer some tests have been carried with the previously cited solvents for two different types of PVDF-co-HFP with 10% w/w solutions.
As can be seen from Table 12.1 a stable solution at a concentration suitable for solvent casting is obtained only for the case of dissolution in acetone. A second possibility is also to employ ethyl acetate by dissolving the polymer at about 50°C under stirring, followed by a progressive decrease to room temperature. In this case, however, the solution is not stable for long time and once reached room temperature it is necessary to realize the casting quickly because, otherwise, the solution starts to become a gel. The second type of PVDF-co-HFP is essentially not soluble even upon heating probably because of the high molecular weight and the higher melting temperature of the polymer which is an index of the lower content of the hexafluoropropylene unit in the copolymer, that is responsible

Table 12.1: My caption

PVDF-co-HFP sample	Melting temperature [°C]	Solvent	Note
1	135-140	acetone	soluble
		ethyl acetate	strong swelling
		methyl ethyl ketone	strong swelling
		tetrahydrofuran	strong swelling
2	155-160	acetone	not soluble
		ethyl acetate	not soluble
		methyl ethyl ketone	not soluble
		tetrahydrofuran	low swelling

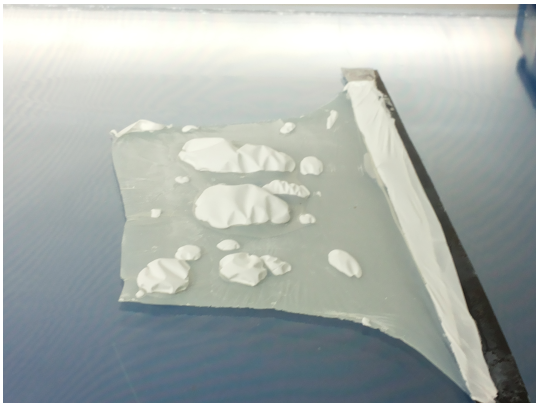

Figure 12.2: *Deposition of sPEEK mat on casted solution of PVDF-co-HFP in acetone: effect of mat shrinking during its deposition on the casted polymer solution*

for the increase of solubility in the solvents considered. On the basis of these results the following step has been the realization of the composite membrane by casting the first type of PVDF-co-HFP with the two solutions realized. A first test has been conducted with a solution of PVDF-co-HFP in acetone casted on glass plate with a 200 μm casting blade. A first attempt has been made by depositing the mat on the casted solution but a significant drawback has been found due to a fast shrinking of the mat when in contact to the solution, leading to a decrease of the final membrane size and presence of heterogeneities due to lack of contact between the solution and the surface of the mat. Unfortunately no significant improvement has been found in trying to fix the edges of the mat to a solid support. A possible explanation can be related to the fast evaporation of the acetone which prevents a stable deposition of the mat on the solution. As can be seen from Figure 12.2 this leads also to a lack of complete deposition of the mat on the surface of the solution, which is responsible for the formation of air bubbles between the mat and the casted solution. An alternative approach has been tried by reversing the procedure for the realization of the composite membranes so that the mat is first deposited on the glass plate and subsequently the polymeric solution is deposited on top of it. In this second case even though the deposition seems initially fine without the formation of surface heterogeneities as in the previous case, a few seconds after the deposition of the layer of casted solution the mat starts to shrink symmetrically, significantly decreasing its initial size. Despite the difficulty

to obtain a final membrane some SEM micrographs have been realized on the cross-section of the sample obtained from the first procedure (Figure 12.3), in correspondence to a point where the impregnation seemed to be homogeneous on a macroscopic scale. As can be seen, although the final membrane is dense, no fibrous morphology is present and a clear two distinct layers can be identified. The upper layer is much more heterogeneous and it is likely to represents the part in which the shrunk nanofibrous mat is present. Due to the

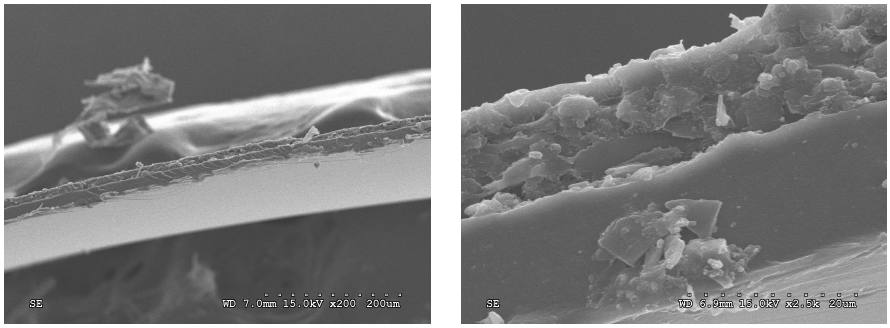

Figure 12.3: *SEM micrographs of the cross-section of composite membrane of casted PVDF-co-HFP in acetone with sPEEK mat at different magnifications*

lack of improvement on both the two strategies adopted to realize the final membrane, a second series of tests has been done by using ethyl acetate as casting solvent of PVDF-co-HFP. The use of such solvent prevent the phenomenon of the shrinking of the mat thanks to its higher boiling point, however the impregnation of the mat is not uniform.

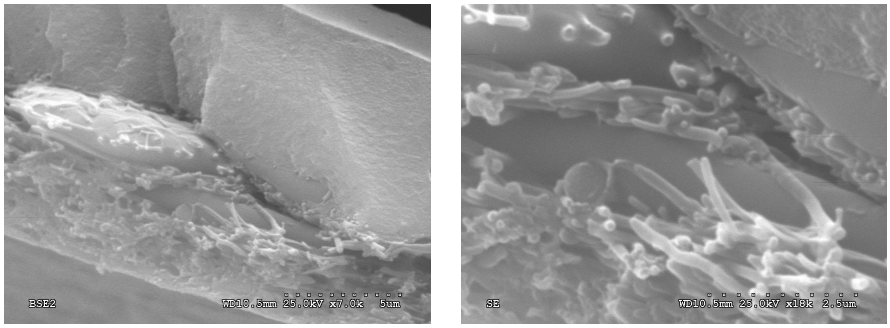

Figure 12.4: *Cross-section of composite membrane of casted PVDF-co-HFP in ethyl acetate with sPEEK mat at different magnifications*

As can be seen from the SEM micrographs in Figure 12.4, even in correspondence to the side of the membrane which appeared to be fully impregnated there is a neat separation between the mat and the casted part of the membrane. Such situation is not improved by forcing the casting of the solution over the mat and the possible cause can be ascribed to the different chemical nature of the two polymers involved. PVDF-co-HFP is essentially an hydrophobic polymer, with some similarity to PVDF, while sPEEK is highly hydrophilic and such conditions prevent the complete expansion of the mat inside the casted solution and the final result is a segregation of the mat one side of the membrane.
An alternative strategy to solve the problem can be found in using a dual electrospinning

approach. In this case it is possible to use PVDF, which has better thermal and mechanical properties than PVDF-co-HFP, and carrying a simultaneous electrospinning process with sPEEK. In this manner PVDF can be embedded in the form of nanofibers inside the mat and subsequently act as matrix of the membrane with fibers melting by hot pressing [230], avoiding the complex issues related to the solution casting method. In this case both PVDF and sPEEK have been electrospun simultaneously to realize a mat of the two polymers and subsequently the mat has been thermally treated under pressure to melt the fibers of PVDF and realize a dense membrane. For the electrospinning step PVDF has been solubilized in a DMAc/acetone solution (composition of 2:1 on mass basis) at a concentration of 15% w/w using standard conditions (15 kV of voltage, 12 cm of tip-to-collector distance and low relative humidity) defined from a thesis work [452]. Two different membranes were produced by electrospinning with a composition of, respectively, 50:50 and 30:70 of PVDF and sPEEK on mass basis. This procedure has been repeated for two different sulfonation degrees in order to evaluate its effect, leading to the production of four different membranes. The relative amount of the two polymers has been defined by adjusting the flow-rate of the PVDF solution, on the basis of the density of the two solution and their polymer content on mass basis. The electrospun membranes have been subsequently densified by using a mechanical pressing machine (Collin P200) operating at 170°C(above the melting point of PVDF), with an applied pressure of 250 ± 2 bar for 180 seconds. For comparison membranes employing the same two polymers and with the same composition have been produced from a single casted solution containing the same two polymers. The solutions were prepared in DMAc with a concentration of 10% by weight.

All the membranes for testing, both casted or electrospun and densified, have been soaked into a 3M H_2SO_4 overnight at room temperature to ensure protonation, and subsequently washed repeatedly with deionized until the pH of the rinsed water was as close as possible to neutrality.

Figure 12.5 shows the cross-section of the casted membranes obtained from solutions at different compositions. The final membranes are quite homogeneous and the two polymeric components are distributed all along the section of the membrane, without visible macrosegregation due to their different chemical nature.

Figure 12.6 and Figure 12.7 present a series of SEM micrographs relative to the analysis of the surface and cross section of the densified membranes after the thermal treatment under pressure. This evaluation has been necessary to ensure the homogeneous distribution of the nanofibers along the membranes cross section and to verify the compaction of the membrane surface by pore filling thanks to the melting of the PVDF phase. For the conditions employed it is possible to observe that at the lower sulfonation degree the compaction has been realized successfully providing a uniform dense membrane independently by the final composition. On the other side with the higher sulfonation degree, although the section seems quite dense, the membrane surface is not homogeneous and the fibrous morphology is still evident. This is more visible with an higher content of sPEEK and represents an undesirable characteristic because it determines an higher porosity in the final membrane and can lead to an inefficient contact with the electrode during proton exchange measurements, determining higher gas permeability and low proton con-

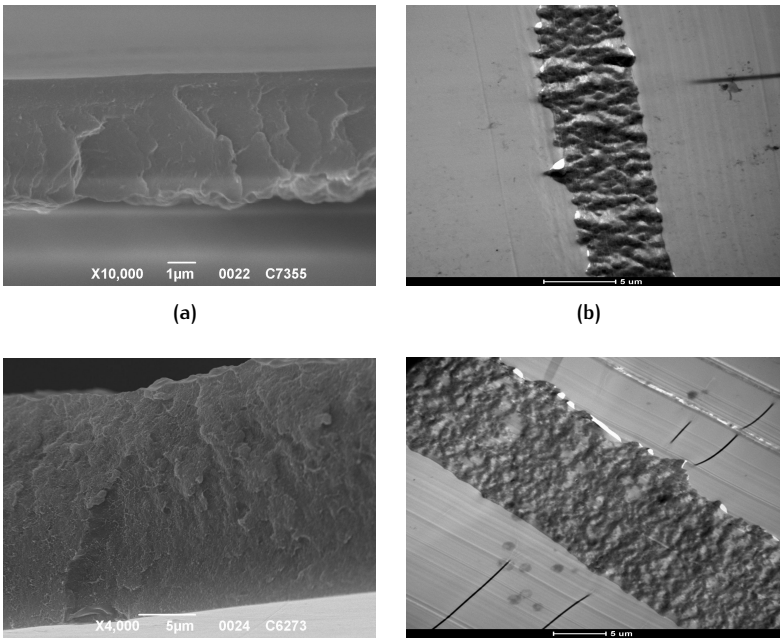

(a) (b)

(c) (d)

Figure 12.5: *(a) SEM and (b) TEM cross sections of sPEEK/PVDF membranes at 50:50 composition; (c) SEM and (d) TEM cross sections of sPEEK/PVDF membranes at 70:30 composition*

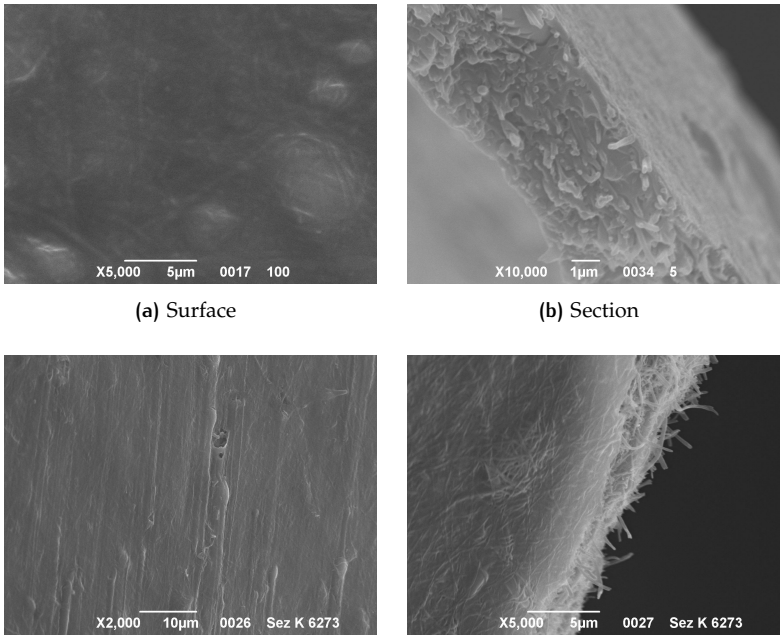

(a) Surface **(b)** Section

(c) Surface **(d)** Section

Figure 12.6: *Cross section and surface of the sPEEK/PVDF membranes at different composition (sPEEK sulfonation degree ≈ 62%)*

ductivity.

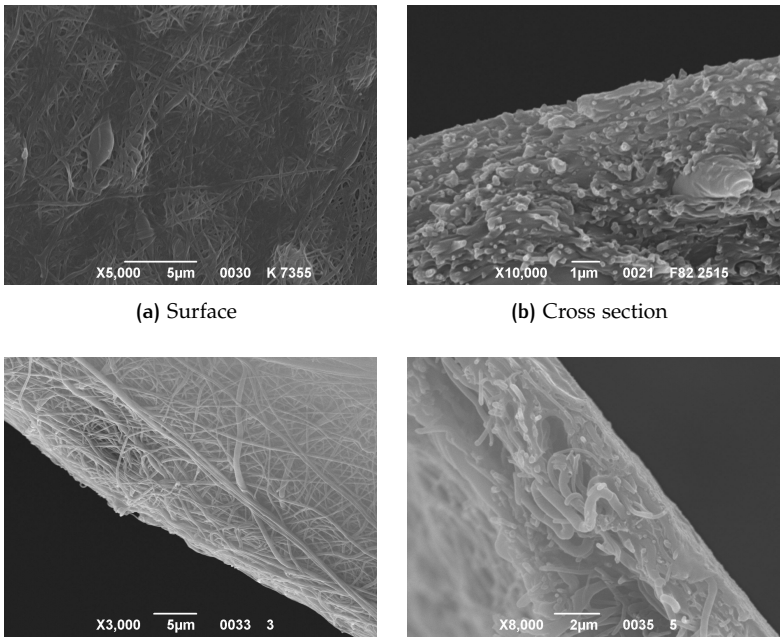

(a) Surface **(b)** Cross section

(c) Surface **(d)** Cross section

Figure 12.7: *Cross section and surface of the sPEEK/PVDF membranes at different composition (sPEEK sulfonation degree ≈ 73%)*

The final morphology can be considered as a consequence of the high glass temperature of the highly sulfonated samples (above the 170°C employed during the compaction procedure) which imparts processing limitations due to problems of thermal degradation when employing higher temperatures. For these reason the membranes employing the sPEEK at the higher sulfonation degree were discarded for the subsequent analysis.

12.3.2 Membranes characterization

A first characterization of the membranes has been performed by DSC analysis as an indirect method for the evaluation of the PVDF content into the final membrane. PVDF is a semicrystalline polymer while sPEEK, as previously determined, is amorphous as a consequence of its random copolymer nature. Thus by the evaluation of the endothermic peak associated to the melting of the PVDF it is possible to obtain a quantification of its presence. The results are shown in Table 12.2 and Figure 12.8 The casted membranes present a composition in accordance to the composition required while the membranes produced by dual electrospinning present a lower content and an higher standard deviation in the final composition as a result of the random nature of the process deposition of the nanofibers.
The mechanical test conducted on the membranes are presented in Figure 12.9 and the main mechanical properties are summarized in Table 12.3. The two neat polymers present quite different mechanical properties. sPEEK presents a significant higher elastic modulus and yield stress point as a result of its polymaromatic structure which is capable to

Table 12.2: *Results of the DSC measurements*

Sample	Peak area [J/g]	PVDF content [%]
PVDF	41.4 ± 0.1	100
PVDF/sPEEK (50:50) dual	18.1 ± 1.4	44 ± 3
PVDF/sPEEK (30:70) dual	11.2 ± 2.8	27 ± 4
PVDF/sPEEK (50:50) cast	20.2 ± 0.2	49 ± 0.3
PVDF/sPEEK (30:70) cast	13.3 ± 0.7	32 ± 2

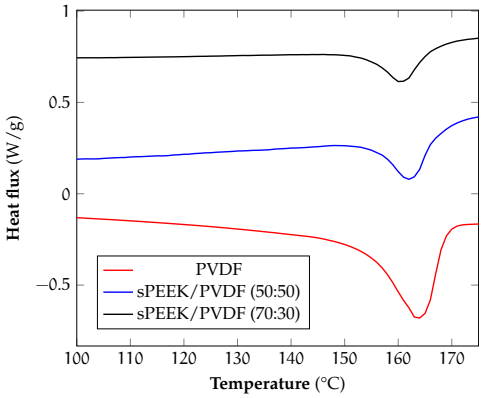

Figure 12.8: *Comparison of the DSC analysis of PVDF with two composites membranes*

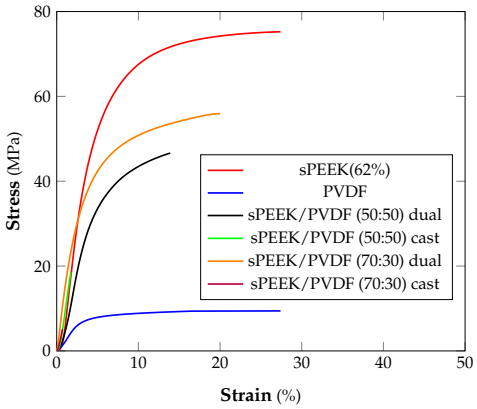

Figure 12.9: *Stress strain curves of the membranes*

provide high strength and toughness to the final membrane. The composite membranes are influenced by the presence of PVDF and show properties which are intermediate between the two neat polymer. However a significant different in the properties has been found in relation to the methodology employed for the membranes preparation. All the membranes prepared by casting exhibited a very fragile behavior which has determined a very low yield stress point possibly due to the incompatibility between the two polymeric phases. Better results have been obtained with the composite membranes obtained by dual electrospinning, confirming as the composite morphology obtained is capable to provide a better compatibility between the two polymers. In this case not only the membranes have

Table 12.3: *Mechanical properties of the membranes as determined from the stress-strain curves*

Sample	Young modulus [MPa]	Yield stress point [MPa]	Elongation at break [%]	Proportional limit stress [MPa]
sPEEK	1694 ± 17	72 ± 10	18 ± 8	69 ± 12
PVDF	208 ± 69	7 ± 2	28 ± 6	7 ± 2
PVDF/sPEEK (50:50) dual	1023 ± 143	53 ± 5	15 ± 2	49 ± 7
PVDF/sPEEK (30:70) dual	1517 ± 145	56 ± 1	24 ± 6	52 ± 3
PVDF/sPEEK (50:50) cast	816 ± 200	8 ± 1	2 ± 0.5	-
PVDF/sPEEK (30:70) cast	1007 ± 59	17 ± 4	2 ± 0.3	-

higher elasticity but generally present higher elastic modulus with respect to their casted counterparts. These values present a slightly non-additive behavior as a consequence of the higher reinforcement of the nanofibrous network. Similar behavior has been found for the yield stress and proportional limit stress as a confirmation of the good mechanical properties of the final membranes. Water uptake and swelling measurements conducted

Table 12.4: *Results of the water uptake and water swelling measurements*

Sample	Water uptake [%]	Area swelling [%]	Thickness swelling [%]	Volume swelling [%]
sPEEK (62%)	29	6.5	8.6	15.6
PVDF/sPEEK (50:50) dual	5	< 5	< 5	< 5
PVDF/sPEEK (30:70) dual	11	5.2	< 5	7.4
PVDF/sPEEK (50:50) cast	7	< 5	< 5	< 5
PVDF/sPEEK (30:70) cast	18	6	7.3	11.1

on the membranes are summarized in Table 12.4. The addition of the hydrophobic PVDF component in the structures of the membranes has generally produced a decrease in the amount of water adsorbed by the samples with respect to a casted membrane of sPEEK, accordingly to the amount of PVDF present in the membranes. The comparison of the different composite membranes has shown that for the same final composition the membranes with fibrous reinforcement are capable to provide a lower water uptake. This result in reflected in the lower swelling exhibited by those membranes which is an important aspect to provide mechanical stability under operating conditions in a fuel cell. The main reason of this behavior can be ascribed to the fact that the fibers of the proton conductive reinforcement are subjected to a more restricted movement in the PVDF matrix and can allocate less amount of water molecules in their structures with respect to a continuous non fibrous morphology. On the other side this can be detrimental in terms of proton conductivity since water is essential to provide dissociation of ion pair, increasing the concentration of charge carriers and the solvation of both anions and protons.

The results of proton conductivity are shown in Figure 12.10. For these measurement the proton conductivity of the composite membranes obtained by casting could not be performed due lack of mechanical stability during the measurements.

As can be seen the proton conductivity of the composite membranes are lower than the reference due to the incorporation of the non conductive matrix and quite unsatisfactory.

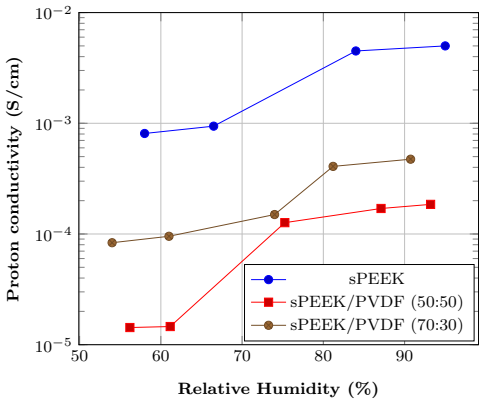

Figure 12.10: *Proton conductivity of the membranes under different humidities and at 80°C*

In this sense better results are provided by the composite containing the higher amount of sPEEK which not only increase the amount of proton conductive component but also determine an higher exposition of that component on the surface of the membrane where the measurement are realized. Better results could be obtained by creating interconnecting protonic pathways by sPEEK fibers welding through solvent exposure because when the density of sulfonic groups is low, the hydrophilic sulfonic groups form isolated ionic clusters in the continuous hydrophobic phase. When the density of sulfonic groups increases up to a certain value, the isolated ionic clusters form crosslinked channels with good connectivity and protons can be transported faster in these channels [453]. However also this strategy can be challenging due to limitations induced by the same solubility characteristics of the two polymeric components and increasing the content of the proton conducting component can prevent the complete densification of the final membranes.

12.4 CONCLUSIONS

Composite nanofibrous membranes sPEEK mat with different sulfonation degree embedded in a non proton conductive matrix (PVDF) have been realized at different composition ratios. A first attempt with a two step approach (electrospinning of sPEEK mat and soaking into casted solution of a second polymer) has been discarded due to incompatibility between the two polymers to be coupled while a dual electrospinning process followed by densification by thermal treatment has revealed to be successful in obtaining final dense membranes. However high sulfonation degrees prevented the complete filling of the microporous mat after the melting of the PVDF component limiting the amount of samples to be tested. For comparison also casted membranes with similar composition have been realized from a single solution comprising the two polymers. Results of the measurements revealed good mechanical properties of the final membranes obtained by dual electrospinning with a remarkable improvement in the stability with respect of their casted counterparts. Swelling measurement revealed a lower water uptake for all the composite membranes as a result of the incorporation of the hydrophobic PVDF components

with lower values for the membranes obtained by dual electrospinning. This results determined a lower swelling, proving the higher stability of the final membranes which, however, displayed lower proton conductivity than pure sPEEK. In these sense further studies are required in order to overcome this limitation by changing the non proton conductive matrix and enhance the proton conductivity by interfiber welding.

CONCLUSIONS

This work explored the experimental investigation and development of nanostructured membranes produced by electrohydrodynamic techniques (electrospinning/electrospraying) for evaluation of their performances in relation to energy and environmental applications.

The first part of the activity has been devoted to the realization of composite membranes comprising a polymeric matrix for the deposition of composite photocatalysts in order to produce nanostructured filters for the photo-oxidation of methanol under UV irradiation. Different approaches have been taken into consideration for the realization of the photocatalysts, by either coupling TiO_2 with graphenes co-catalysts or coupling TiO_2 with silver carbonate as second photocatalyst, and their deposition. For the latter aspect the deposition has been realized comparing a two-step (layer-by-layer) approach with the electrospinning of the polymeric matrix and subsequent electrospraying of the photocatalysts, with a one-step procedure in which the desired membranes have been produced by electrospinning of a single colloidal solution comprising both the photocatalyst and the polymer. For all the membranes PAN has been employed as polymeric structure thanks to its high resistance to UV light which, on the other side, determined photo-oxidative degradation and loss of mechanical properties in the case of PSU employment.

A first series of photocatalytic membranes have been prepared using pristine TiO_2 and composites with graphene and TiO_2 obtained by physical mixing (G+TiO_2 composite) or deposition by hydrothermal treatment (rGO-TiO_2 composite), comparing the different deposition strategies employed and the role of graphene on the photocatalytic activity. The employed graphene-based composite photocatalysts have shown a synergistic effect due to the coupling between the titania with the graphenes at different degrees of reduction, providing more strong absorption of light and reduction of the characteristic band gap of TiO_2. With the layer-by-layer approach the best performances are provided by the G+TiO_2 thanks to the high mobility of free electrons on the surface of graphene and reduced recombination of the electron-hole couple generated in the photocatalyst. The rGO+TiO_2 shows better result than bare titania but not as good as in the case of G+TiO_2, probably because of the structural defects which determine lower electron mobility and in turn lower efficient charge separation. In the one-step approach, by a proper selection of the catalyst/polymer ratio, it has been possible to obtain the complete coverage of polymeric support by the photocatalyst employed. However the final morphology of the fibers has been dependent on the type of graphene employed. In presence of a co-catalyst the complete coverage of the fibers is detrimental for the photocatalytic activity due to a segregation effect which confine the co-catalyst inside the fibers. For this morphology best results are obtained employing only TiO_2 as a consequence of the higher exploitation of the nanofibers surface, while for the G+TiO_2 system the layer-by-layer approach is much more photoactive. The rGO+TiO_2 once electrospun with the PAN solution provide less coverage of the fibers and

tend to form agglomerates exposed on the external surface of the fibers and the final morphology of the deposition is not dissimilar form the layer-by-layer approach. On the basis of this results it has been possible to conclude that in presence of graphenes co-catalyst the extent of the interaction with titania in composite photocatalysts influence the photocatalytic activity as a result of the different deposition approaches followed and generally a layer-by-layer deposition is preferred due to the possibility to obtain more exposition of the co-catalyst on the surface of the fibers with the possibility to provide adsorption sites for the pollutant and an efficient reduction of the charge carrier recombination.
On the other side the one step approach can be suitable for the production of composite membrane comprising a single photocatalyst or composites of different photocatalyst but the effect is dependent on the size of the solid particles. The nanosized structure of the TiO_2 particles is suitable for this task and allow an easy production of the membranes while the micron size of the Ag_2CO_3 particle creates problem for the electrospinning process, requiring a lower catalyst/polymer ratio and leading to the particles confinement into the fibers. However the combination of the two different photocatalysts has led to the production of fully covered fibers in which Ag_2CO_3 is adequately dispersed into TiO_2. In this manner it has been possible to take advantage of the high absorption features of this composites which exhibited a significant narrowing of the band gap of TiO_2 compared to the results of the graphene-based composites photocatalysts. The best photocatalytic performances have been shown by the the membranes obtained from the ternary system (PAN/TiO_2+Ag_2CO_3+GO), whose photoactivity is higher than those of the membranes with only TiO_2 and comparable to that of those employing the rGO+TiO_2 composite. This result is ascribed to the heterojunction formed between the Ag_2CO_3 and TiO_2 which can efficiently separate the charge carriers, promoted by the contact between the photocatalysts thanks to the morphology obtained.
In the second part of the work composite membranes based on electrospun sPEEK mats at different sulfonation degrees have been prepared by two different approaches: incorporation of the mats into a conductive matrix, to provide good proton conductivity and improve mechanical properties, and in a non conductive matrix, to reduce swelling and promote higher dimensional stability. As a preliminary phase to this study the starting non functionalized material (PEEK) has been sulfonated and a kinetic analysis has been carried to control the final sulfonation degree. The sulfonated material exhibited solubility in polar aprotic starting from medium sulfonation degree, with a proportional increase in the glass transition temperature with the degree of functionalization. The electrospinning of sPEEK has been analyzed by a first screening activity concerning the evaluation of solvent and concentration choice and suitable operative window of the process parameters to obtain a stable electrospinning process. The general conditions for the electrospinning of the material require high polymer concentrations, medium-high voltages, low flow-rates and low relative humidity to allow a proper collection of the nanofibers. On the basis of this conclusion a subsequent optimization has been realized by the employment of the Response Surface Methodology, employing a Box-Behnken design in order to obtain uniform thin nanofibers. Both solution and material properties were taken into consideration to analyze their effect on the final fibers dimension, defining an operative window between

60 and 80% for the final sulfonation degree. The model demonstrated as voltage is the factor which less influences the final diameter which, however, depends on mutual influence of sulfonation degree, distance and voltage. The good capability of description provided by the model have been employed to define optimal conditions for the production of the electrospun sPEEK mats.

On the basis of these premises the first type of composite membranes realized have comprised the employment of a short side chain perfluorsulfonated ionomer (Aquivion®) in which sPEEK mats have been embedded by impregnation on a casted solution of the ionomer. The final membranes have shown a good dispersion of the nanofibers into the membranes matrix, but differences have been noted according to the different sulfonation degrees of the sPEEK component; this has determined a more homogeneity with higher sulfonated samples probably by an higher expansion of the mat thanks to a better interaction with the solvent employed during the casting procedure. The composite membranes showed lower proton conductivity than the reference but still quite satisfactory for the final application. The swelling test have shown a good dimensional stability of the composite membrane comprising the lower sulfonated sPEEK compared to the relative amount of water uptake, with an non isotropic swelling. The membranes with the higher sulfonation degree are too much hydrophilic probably due to the polar nature of the sulfonic acid group and have led to excessive swelling with membrane failure. Mechanical test have also determined an increase of the mechanical strength upon incorporation of the porous reinforcement, which restrict the elasticity of the final membrane in comparison to the reference material.

For the second type of composite membranes a different strategy has been followed employing a dual electrospinning approach to overcome the limitations imparted by the similar solubility of sPEEK and PDVF, selected as non proton conductive component. In this case the two polymers have been simultaneously electrospun and membranes at different compositions have been prepared by proper choice of the flow-rates during the deposition process. The final membranes have been densified by hot pressing to obtain the melting of the PVDF nanofibers. Limitations have been imparted by the more sulfonated sPEEK which prevented the complete filling of the microporous mat probably as a consequence of its high glass transition temperature and by the constaint to avoid membrane thermal degradation. For comparison also casted membranes with similar composition have been realized from a single solution comprising the two polymers. The characterization of the obtained samples revealed good mechanical properties of the final membranes obtained by dual electrospinning with a remarkable improvement in the stability and improved compatibility between the two different polymer, compared to their casted counterparts. Swelling measurements revealed a lower water uptake for all the composite membranes as a result of the incorporation of the hydrophobic PVDF components with lower values for the membranes obtained by dual electrospinning. This results determined a lower swelling, proving the higher stability of the final membranes which, however, displayed lower proton conductivity than the reference material (sPEEK). Possible improvements could be achieved by changing the non proton conductive matrix to avoid solubility con-

traints in order to promote interfiber welding and create a more interconnected network and will be the aim of a future work.

APPENDIX

RESPONSE SURFACE METHODOLOGY (RSM)

The *Response surface methodology* (RSM) is a collection of mathematical and statistical techniques based on the fit of a polynomial equation to the experimental data, which must describe the behavior of a data set with the objective of making statistical previsions. It can be well applied when a response or a set of responses of interest are influenced by several variables. The objective is to simultaneously optimize the levels of these variables to attain the best system performance. The starting point is a response variable y which depends on a set of controllable variables $x_1, x_2, ..., x_n$; the RSM technique is based on the assumption that it is possible to describe the response by an approximating function of the true response and that the differences between the data and the RS are due to uncorrelated, normally distributed random noise of magnitude ϵ in the experiments.

$$y = f(x_1, x_2, ..., x_n) + \epsilon \tag{12.1}$$

The regression coefficients are determined with the method of least squares:

$$L = \sum_{i=1}^{n} \epsilon_i^2 = \sum_{i=1}^{n} \left(y_i - \beta_0 \sum_{j=1}^{k} \beta_j x_{ij}\right) \tag{12.2}$$

This method allows the selection of the coefficients in order to minimize the sum of the squares of the errors, ϵ_i. The function L must be minimized with respect to the regression coefficients. This requires that the least squares estimators must satisfy:

$$\frac{\partial L}{\partial \beta_0}\Big|_{b_0, b_1, ..., b_k} = -2 \sum_{i=1}^{n} \left(y_i - b_0 - \sum_{j=1}^{n} b_j x_{ij}\right) = 0 \tag{12.3}$$

and

$$\frac{\partial L}{\partial \beta_j}\Big|_{b_0, b_1, ..., b_k} = -2 \sum_{i=1}^{n} \left(y_i - b_0 - \sum_{j=1}^{n} b_j x_{ij}\right) x_{ij} = 0 \tag{12.4}$$

The same equation can be written in compact form by recurring to a matrix notation. Assuming that the relationship between the response variable and the controllable variables is linear with the respect to the regression coefficients the model can be written as:

$$\mathbf{y} = \mathbf{X}\boldsymbol{\beta} + \boldsymbol{\epsilon} \tag{12.5}$$

In general, $\mathbf{y}$ is an $n \times 1$ vector of the observations, $\mathbf{X}$ is an $\mathbf{n} \times \mathbf{p}$ model matrix consisting

of the levels of the independent variables expanded to model form, $\boldsymbol{\beta}$ is a $\mathbf{p} \times \mathbf{1}$ vector of the regression coefficients, and $\boldsymbol{\epsilon}$ is an $\mathbf{n} \times \mathbf{1}$ vector of random errors. The objective is to find the vector $\mathbf{b}$ that minimizes:

$$L = \sum_{i=1}^{n} \epsilon_i^2 = \boldsymbol{\epsilon}'\boldsymbol{\epsilon} = (\mathbf{y} - \mathbf{X}\boldsymbol{\beta})'(\mathbf{y} - \mathbf{X}\boldsymbol{\beta}) \tag{12.6}$$

$$= \mathbf{y}'\mathbf{y} - 2\boldsymbol{\beta}'\mathbf{X}'\mathbf{y} + \boldsymbol{\beta}'\mathbf{X}'\mathbf{X}'\boldsymbol{\beta} \tag{12.7}$$

Thus:

$$\left.\frac{\partial L}{\partial \boldsymbol{\beta}}\right|_{\mathbf{b}} = -2\mathbf{X}'\mathbf{y} + 2\mathbf{X}'\mathbf{X}\mathbf{b} = \mathbf{0} \tag{12.8}$$

that leads to the least squares estimators of $\boldsymbol{\beta}$:

$$\mathbf{b} = (\mathbf{X}'\mathbf{X})^{-1}\mathbf{X}'\mathbf{y} \tag{12.9}$$

The fitted regression model is:

$$\hat{\mathbf{y}} = \mathbf{X}\mathbf{b} \tag{12.10}$$

that in scalar notation can be expressed as:

$$\hat{y}_i = b_o + \sum_{j=1}^{k} b_j x_{ij} \quad i = 1,2...,n \tag{12.11}$$

The difference between the observation y_i and the fitted value $\hat{y}_i$ is the residual e_i:

$$\mathbf{e} = \mathbf{y} - \hat{\mathbf{y}} \tag{12.12}$$

Analysis of variance (ANOVA)

The *Analysis of variance* (ANOVA) is a collection of statistical models used to analyze the differences between group means and their associated procedures. ANOVA is employed to evaluate the significance of the regression coefficients of the RS model in order to determine if there is a linear relationship between the variable y and a subset of the regressor variables x_1,x_2,...,x_k. The appropriate hypotheses are:

$$H_0 : \beta_1 = \beta_2 = ... = \beta_k \tag{12.13}$$

$$H_1 : \beta_j \neq 0 \quad \text{for at least one j} \tag{12.14}$$

Rejection of β_0 implies that at least one of the regressor variables x_1,x_2,...,x_k contributes significantly to the model. The test procedure involves partitioning the total sum of squares (SS_T) into a sum of squares due to the model (or to regression) and a sum of squares due to the residual:

$$SS_T = SS_R + SS_E \tag{12.15}$$

with:

$$SS_T = \sum_{i=1}^{n} (y_i - \bar{y})^2 \tag{12.16}$$

$$SS_E = \sum_{i=1}^{n} (y_i - \hat{y}_i)^2 = \sum_{i=1}^{n} e_i^2 = \mathbf{e'e} \tag{12.17}$$

If the null hypothesis H_0 is true, then SS_R/σ^2 (where σ^2 = SS_E/(n-p)) is distributed as χ^2_k, where the number of degrees of freedom for χ^2 is equal to the number of regressor variables in the model. The test procedure for H_0 is to compute:

$$F_0 = \frac{SS_R/k}{SS_E/(n-k-1)} = \frac{MS_R}{MS_E} \tag{12.18}$$

and to reject H_0 if F_0 exceeds $F_{\alpha,k,n-k-1}$. Alternatively, its is possible to use the p-value approach to hypothesis testing and reject H_0 if the p-value for the statistic F_0 is less than α.
The total sum of squares is then:

$$SS_T = y'y - \frac{\sum_{i=1}^{n}(y_i)^2}{n} = \sum_{i=1}^{n}(y_i)^2 - \frac{\sum_{i=1}^{n}(y_i)^2}{n} \tag{12.19}$$

Then the coefficient of multiple determination R^2 is defined as:

$$R^2 = 1 - \frac{SS_E}{SS_T} \tag{12.20}$$

R^2 is a measure of the amount of reduction in the variability of y obtained by using the regressor variables x_1,x_2,...,x_k in the model.
Because R^2 always increases as we add terms to the model, some regression model builders prefers to use an adjusted R^2 statistic defined as:

$$R^2_{adj} = 1 - \frac{SS_E/(n-p)}{SS_T/(n-1)} = 1 - \frac{n-i}{n-p}(1-R^2) \tag{12.21}$$

which is general will not always increase as variables are added to the model. In fact, if unnecessary terms are added to the model, the value of R^2_{adj} will often decrease. When R^2 and R^2_{adj} differ dramatically, there is a good chance that non significant terms have been included in the model.

ABBREVIATIONS AND ACRONYMS

AC alternate current

AOP Advanced oxidation process

cBPPO crosslinked bromomethylated poly(2,6-dimethyl-1,4-phenlyene oxide)

CB conduction band

C-PAMPS crosslinked poly(2-acrylamido-2-meathylpropane-sulfonic acid)

DC direct current

DMAc dimethylacetamide

DMF dimethylformamide

DMSO dimethyl sulfoxide

MSA methanesulfonic acid

NMP N-methyl pyrrolidone

PAA poly(acrylic acid)

PAM polyacrylamide

PAN poly(acrylonitrile)

PBI poly(benzoimidazole)

PBSS poly(benzyl sulfonic acid)siloxane

PBz poly(benzoxazine)

PCO photocatalytic oxidation

PDMS poly(dimethyl siloxane)

PEI polyetheleneimine

PEO poly(ethylene oxide)

PES poly(ether sulfone)

PFSA perfluorosulfonic acid

PFZ polyphosphazenes

PLGA poly(lactic-co-glycolic acid)

PPBP poly(4phenoxybenzoyl-1,4-phenylene)

PS polystryene

PSSA-g-PVDF poly(styrene sulfonic acid)-grafted poly(vinylidene fluoride)

PSU polysulfone

PU polyurethane

PVA poly(vinyl alcohol)

PVDF poly(vinylidene fluoride)

PVDF-co-HFP poly(vinylidene fluoride-co-hexafluoropropylene)

PWA phosphotungstic acid

RSM response surface methodology

sPAES sulfonated poly(arylene ether sulfone)

sPEEKK sulfonated poly(ether ether ketone ketone)

sPES sulfonated (poly ether sulfone)

sPEEK sulfonated poly(ether ether ketone)

sPPEK poly(phthalazinone ether ketone)

SPFEK sulfonated poly(fuorenyl ether ketone)

sPI sulfonated polyimide

sPPO sulfonated poly(phenylene oxide)

sPS sulfonated polystyrene

sPSU sulfonated polysulfone

VB valence band

VOC volatile organic compounds

$Zr(OPr)_4$/PVP zirconium propoxide/poly(vinylpirrolidone)

ACKNOWLEDGMENTS

I would like to express my profound gratitude to my supervisor Prof. Michele Modesti for the opportunity given me with this experience, for his support and encouragement throughout my activity in his research group.
I am truly thankful to Prof. Lorenzetti, Dr. Martina Roso, Dr. Denis Hrelja and Dr. Stefano Besco for their support, their precious advices during my daily work in the laboratory and their unvaluable friendship.
I would like to express special thanks to Dr. Sara Cavaliere of the Laboratory for Aggregates, Interfaces and Materials for Energy of the Charles Gerhardt Institute for Molecular Chemistry and Materials in Montpellier, for her support and extreme kindness during my research period in France.
I want to thank Dr. Stefano Giancola, Dr. Rakhi Sood and Dr. Anna Donnadio for their help, encouragement and support in the testing of the membranes. I also want to thank Dr. Enrica Fontananova for the proton conduction measurements, Dr. Maria Pelizzo and Dr. Alain Corso for the UV-vis diffuse reflectance spectroscopy measurements.
As lab-mate it worths to mention all the people with whom I shared these years during development of my research activity: Nicola Pozzan, Davide Zulian, Andrea Bruschetta, Marco Pasetto, Annamaria Lauria (especially), Francesca Piovesan and last, but not least, my lab technician (and life coach) Romeo Rabachin.
Finally, thanks to my family for always supporting and believing in me and for all the sacrifices made for me during all these years.

BIBLIOGRAPHY

[1] S. Ramakrishna, K. Fujihara, W. E. Teo, T. C. Lim, and Z. Ma, *An introduction to electrospinning and nanofibers*. World Scientific Publishing Company, 2005.

[2] T. Ondarçuhu and C. Joachim *Europhys. Lett.*, vol. 42, no. 2, p. 215, 1998.

[3] C. R. Martin *Chem. Mater*, vol. 8, no. 8, pp. 1739–1746, 1996.

[4] J. Klein, R. H. II, D. Palmer, M. J. Sailor, C. J. Brumlik, and C. R. Martin *Chem. Mater*, vol. 5, no. 7, pp. 902–904, 1993.

[5] P. X. Ma and R. Zhang *J. Biomed. Mater. Res.*, vol. 46, no. 1, 1999.

[6] G. Whitesides and B. Grzybowski *Science*, vol. 295, no. 5564, pp. 2418–2421, 2002.

[7] C. J. Ellison, A. Phatak, D. W. Giles, C. W. Macosko, and F. S. Bates *Polymer*, vol. 48, no. 11, pp. 3306 – 3316, 2007.

[8] D. Li and Y. Xia *Adv. Mater.*, vol. 16, no. 14, pp. 1151–1170, 2004.

[9] Y. Dai, W. Liu, E. Formo, Y. Sun, and Y. Xia *Polymer. Adv. Tech.*, vol. 22, no. 3, pp. 326–338, 2011.

[10] Z. M. Huang, Y. Zhang, M. Kotaki, and S. Ramakrishna *Compos. Sci. Technol.*, vol. 63, no. 15, pp. 2223–2253, 2003.

[11] H. Wu, W. Pan, D. Lin, and H. Li *J. Adv. Ceram.*, vol. 1, no. 1, pp. 2–23, 2012.

[12] R. Sahay, P. S. Kumar, R. Sridhar, J. Sundaramurthy, J. Venugopal, S. G. Mhaisalkar, and S. Ramakrishna.

[13] M. Bognitzki, M. Becker, M. Graeser, W. Massa, J. H. Wendorff, A. Schaper, D. Weber, A. Beyer, A. Gölzhäuser, and A. Greiner *Adv. Mater.*, vol. 18, no. 18, pp. 2384–2386, 2006.

[14] A. Greiner and J. Wendorff *Angew. Chem. Int. Ed.*, vol. 46, no. 30, pp. 5670–5703, 2007.

[15] H. Wu, R. Zhang, X. Liu, D. Lin, and W. Pan *Chem Mater*, vol. 19, no. 14, pp. 3506–3511, 2007.

[16] G. Bose, *Recherches sur la cause et sur la véritable théorie de l'électricité*. 1745.

[17] L. Rayleigh *Philos. Mag. 5*, vol. 14, no. 87, pp. 184–186, 1882.

[18] J. F. Cooley, Feb. 4 1902. US Patent 692,631.

[19] W. Morton, July 29 1902. US Patent 705,691.

[20] J. Zeleny *Phys. Rev.*, vol. 3, no. 2, pp. 69–91, 1914.

[21] J. Zeleny *Phys. Rev.*, vol. 10, no. 1, pp. 1–6, 1917.

[22] B. Vonnegut and R. L. Neubauer *J. Colloid Interface Sci.*, vol. 7, no. 6, pp. 616–622, 1952.

[23] V. G. Drozin *J. Colloid. Interface Sci.*, vol. 10, no. 2, pp. 158–164, 1955.

[24] G. I. Taylor *Proceedings of the Royal Society of London*, vol. 313, no. 1515, pp. 453–475, 1969.

[25] H. L. Simons, 1966. US Patent 3,280,229.

[26] T. Subbiah, G. S. Bhat, R. W. Tock, S. Parameswaran, and S. S. Ramkumar *J. Appl. Polym. Sci.*, vol. 96, no. 2, pp. 557–569, 2005.

[27] P. K. Baumgarten *J. Colloid Interface Sci.*, vol. 36, pp. 71–79, 5 1971.

[28] G. Martin, I. Cockshott, and F. Fildes, Aug. 30 1977. US Patent 4,044,404.

[29] L. Larrondo and R. S. J. Manley *J. Polym. Sci. Part B Polym. Phys.*, vol. 19, no. 6, pp. 921–932, 1981.

[30] G. Srinivasan and D. H. Reneker *Polym. Int.*, vol. 36, no. 2, pp. 195–201, 1995.

[31] N. Bhardwaj and S. C. Kundu *Biotechnol. Adv.*, vol. 28, no. 3, pp. 325–347, 2010.

[32] S. Ramakrishna, K. Fujihara, W. Teo, T. Yong, Z. Ma, and R. Ramaseshan *Mater. Today*, vol. 9, no. 3, pp. 40–50, 2006.

[33] G. C. Rutledge and S. V. Fridrikh *Adv. Drug Deliv. Rev.*, vol. 59, no. 14, pp. 1384–1391, 2007.

[34] D. H. Reneker and H. Fong, *Structure Formation in Polymeric Fibers*. 2001.

[35] G. Taylor *P. Roy. Soc. Lond. A. Mat.*, vol. 280, no. 1382, pp. 383–397, 1964.

[36] A. Buer, S. C. Ugbolue, and S. B. Warner *Text. Res. J.*, vol. 71, no. 4, pp. 323–328, 2001.

[37] D. H. Reneker, A. L. Yarin, H. Fong, and S. Koombhongse *J. Appl. Phys.*, vol. 87, no. 9, pp. 4531–4547, 2000.

[38] A. L. Yarin, S. Koombhongse, and D. H. Reneker *J. Appl. Phys.*, vol. 90, no. 9, pp. 4836–4846, 2001.

[39] A. L. Yarin, S. Koombhongse, and D. H. Reneker *J. Appl. Phys.*, vol. 89, no. 5, pp. 3018–3026, 2001.

[40] A. F. Spivak, Y. A. Dzenis, and D. H. Reneker *Mech. Res. Commun.*, vol. 27, no. 1, pp. 37–42, 2000.

[41] S. Koombhongse, W. Liu, and D. Reneker *J. Polym. Sci. Part B Polym. Phys.*, vol. 39, no. 21, pp. 2598–2606, 2001.

[42] R. Kessick and G. Tepper *Appl. Phys. Lett.*, vol. 84, no. 23, pp. 4807–4809, 2004.

[43] H. Qi and A. W. P. Hu, J. Xu *Biomacromolecules*, vol. 7, no. 8, pp. 2327–2330, 2006.

[44] E. H. Sanders, R. Kloefkorn, G. L. Bowlin, D. G. Simpson, and G. E. Wnek *Macromolecules*, vol. 36, no. 11, pp. 3803–3805, 2003.

[45] P. Gupta and G. L. Wilkes *Polymer*, vol. 44, no. 20, pp. 6353 – 6359, 2003.

[46] Z. Sun, E. Zussman, A. Yarin, J. Wendorff, and A. Greiner *Adv. Mater.*, vol. 15, no. 22, pp. 1929–1932, 2003.

[47] P. Gibson, H. Schreuder-Gibson, and D. Rivin *Colloids Surf., A*, vol. 187–188, pp. 469 – 481, 2001.

[48] S. Choi, Y. S. Lee, C. W. Joo, S. G. Lee, J. K. Park, and K. Han *Electrochim. Acta*, vol. 50, no. 2–3, pp. 339 – 343, 2004.

[49] E. D. Boland, G. E. Wnek, D. G. Simpson, K. J. Pawlowski, and G. L. Bowlin *J. Macromol. Sci. A.*, vol. 38, no. 12, pp. 1231–1243, 2001.

[50] M. Peng, D. Li, L. Shen, Y. Chen, Q. Zheng, and H. Wang *Langmuir*, vol. 22, no. 22, pp. 9368–9374, 2006.

[51] Y. Jian and G. Rutledge, *Electrospinning*. John Wiley & Sons, Inc., 2002.

[52] Q. P. Pham, U. Sharma, and A. G. Mikos *Tissue Eng.*, vol. 12, no. 5, pp. 1197–1211, 2006.

[53] C. Luo, M. Nangrejo, and M. Edirisinghe *Polymer*, vol. 51, no. 7, pp. 1654 – 1662, 2010.

[54] H. Fong, I. Chun, and D. Reneker *Polymer*, vol. 40, no. 16, pp. 4585 – 4592, 1999.

[55] C. J. Luo, M. Nangrejo, and M. Edirisinghe *Polymer*, vol. 51, no. 7, pp. 1654–1662, 2010.

[56] X. Zong, K. Kim, D. Fang, S. Ran, B. S. Hsiao, and B. Chu *Polymer*, vol. 43, no. 16, pp. 4403–4412, 2002.

[57] Mituppatham, C., Nithitanakul, M., and P. Supaphol *Macromol. Chem. Phys.*, vol. 205, no. 17, pp. 2327–2338, 2004.

[58] T. Lin, H. Wang, H. Wang, and X. Wang *Nanotechnology*, vol. 15, no. 9, p. 1375, 2004.

[59] J. S. Choi, S. W. Lee, L. Jeong, S. Bae, B. C. Min, J. H. Youk, and W. H. Park *Int. J. Biol. Macromol.*, vol. 34, no. 4, pp. 249 – 256, 2004.

[60] S. J. Kim, C. K. Lee, and S. I. Kim *J. Appl. Polym. Sci.*, vol. 96, no. 4, pp. 1388–1393, 2005.

[61] X. Zong, K. Kim, D. Fang, S. Ran, B. S. Hsiao, and B. Chu *Polymer*, vol. 43, no. 16, pp. 4403 – 4412, 2002.

[62] C. J. Angammana and S. H. Jayaram *IEEE Trans. Ind. Appl.*, vol. 47, no. 3, pp. 1109–1117, 2011.

[63] *Eur. Polym. J.*, vol. 41, no. 3, pp. 409 – 421, 2005.

[64] L. Wannatong, A. Sirivat, and P. Supaphol *Polym. Int.*, vol. 53, no. 11, pp. 1851–1859, 2004.

[65] W. K. Son, J. H. Youk, T. S. Lee, and W. H. Park *Polymer*, vol. 45, no. 9, pp. 2959 – 2966, 2004.

[66] Z. Sun, J. M. Deitzel, J. Knopf, X. Chen, and J. W. Gillespie *J. Appl. Polym. Sci.*, vol. 125, no. 4, pp. 2585–2594, 2012.

[67] J. Doshi and D. H. Reneker *J. Electrostat.*, vol. 35, no. 2–3, pp. 151–160, 1995.

[68] D. H. Reneker and I. Chun *Nanotechnology*, vol. 7, no. 3, pp. 216–223, 1996.

[69] S. R. Coles, D. K. Jacobs, J. O. Meredith, G. Barker, A. J. Clark, K. Kirwan, J. Stanger, and N. Tucker *J. Appl. Polym. Sci.*, vol. 117, no. 4, pp. 2251–2257, 2010.

[70] M. Demir, I. Yilgor, E. Yilgor, and B. Erman *Polymer*, vol. 43, no. 11, pp. 3303 – 3309, 2002.

[71] S. Megelski, J. S. Stephens, D. B. Chase, and J. F. Rabolt *Macromolecules*, vol. 35, no. 22, pp. 8456–8466, 2002.

[72] C. J. Buchko, L. C. Chen, Y. Shen, and D. C. Martin *Polymer*, vol. 40, no. 26, pp. 7397 – 7407, 1999.

[73] R. Kessick, J. Fenn, and G. Tepper *Polymer*, vol. 45, no. 9, pp. 2981 – 2984, 2004.

[74] H. Liu and Y. Hsieh *J. Polym. Sci. Part B Polym. Phys.*, vol. 40, no. 18, pp. 2119–2129, 2002.

[75] N. Li, J. Xiong, and H. X. Hua *Polym. Eng. Sci.*, vol. 51, no. 11, pp. 2178–2183, 2011.

[76] D. Katti, K. Robinson, F. Ko, and C. Laurencin *J. Biomed. Mater. Res. B*, vol. 70B, no. 2, pp. 286–296, 2004.

[77] C. Wang, H. Chien, C. Hsu, Y. Wang, C. Wang, and H. Lu *Macromolecules*, vol. 40, no. 22, pp. 7973–7983, 2007.

[78] S. D. Vrieze, T. V. Camp, A. Nelvig, B. Hagstrom, P. Westbroek, and K. D. Clerck *J. Mater. Sci.*, vol. 44, no. 5, pp. 1357–1362, 2009.

[79] L. Huang, N. Bui, S. S. Manickam, and J. R. McCutcheon *J. Polym. Sci. Part B Polym. Phys.*, vol. 49, no. 24, pp. 1734–1744, 2011.

[80] M. Bognitzki, W. Czado, T. Frese, A. Schaper, M. Hellwig, M. Steinhart, A. Greiner, and J. H. Wendorff *Adv. Mater.*, vol. 13, no. 1, pp. 70–72, 2001.

[81] R. S. Carson, C. D. Hendricks, J. Hogan, and J. M. Schneider *AIAA J.*, vol. 2, pp. 733–737, 08/01; 2014/04 1964.

[82] J. Feng *Phys. Fluids*, vol. 14, no. 11, pp. 3912–3926, 2002.

[83] L. Persano, A. Camposeo, C. Tekmen, and D. Pisignano *Macromol. Mater. Eng.*, vol. 298, no. 5, pp. 504–520, 2013.

[84] S. Agarwal, J. H. Wendorff, and A. Greiner *Polymer*, vol. 49, no. 26, pp. 5603–5621, 2008.

[85] T. J. Sill and H. A. von Recum *Biomaterials*, vol. 29, no. 13, pp. 1989–2006, 2008.

[86] R. Jayakumar and S. Nair, *Biomedical Applications of Polymeric Nanofibers*. Springer Berlin Heidelberg, 2012.

[87] N. G. Rim, C. S. Shin, and H. Shin *Biotechnol. Adv.*, vol. 8, no. 1, p. 014102, 2013.

[88] N. Ashammakhi, A. Ndreu, Y. Yang, H. Ylikauppila, and L. Nikkola *Eur J Plast Surg*, vol. 35, no. 2, pp. 135–149, 2012.

[89] M. Zamani, M. P. Prabhakaran, and S. Ramakrishna *Int. J. Nanomedicine*, vol. 8, p. 2997—3017, 2013.

[90] Z. L. W. K. Yu, D. and C. Branford-White vol. 1, 2009.

[91] P. Zahedi, I. Rezaeian, S. Ranaei-Siadat, S. Jafari, and P. Supaphol *Polymer. Adv. Tech.*, vol. 21, no. 2, pp. 77–95, 2010.

[92] R. S. Barhate and S. Ramakrishna *J Membrane Sci*, vol. 296, no. 1–2, pp. 1–8, 2007.

[93] V. Thavasi, G. Singh, and S. Ramakrishna *Energy Environ.Sci.*, vol. 1, no. 2, pp. 205–221, 2008.

[94] S. Homaeigohar and M. Elbahri *Materials*, vol. 7, no. 2, p. 1017, 2014.

[95] C. T. de Kwaadsteniet and K. B. Gule NP, *Electrospun nanofibrous membranes for water treatment applications*. IWA Publishing, London, 2013.

[96] C. Feng, K. C. Khulbe, and S. Tabe *Desalination*, vol. 287, pp. 98–102, 2012.

[97] C. Shin, G. G. Chase, and D. H. Reneker *Colloids Surf., A*, vol. 262, no. 1–3, pp. 211–215, 2005.

[98] K. Yoon, K. Kim, X. Wang, D. Fang, B. S. Hsiao, and B. Chu *Polymer*, vol. 47, no. 7, pp. 2434–2441, 2006.

[99] M. W. Lee, S. An, S. S. Latthe, C. Lee, S. Hong, and S. S. Yoon *ACS Appl. Mater. Interfaces*, vol. 5, no. 21, pp. 10597–10604, 2013.

[100] G. Viswanadam and G. G. Chase *Sep. Purif. Technol.*, vol. 104, pp. 81–88, 2013.

[101] X. Wang, X. Chen, K. Yoon, D. Fang, B. S. Hsiao, and B. Chu *Environ. Sci. Technol.*, vol. 39, no. 19, pp. 7684–7691, 2005.

[102] H. Ma, B. S. Hsiao, and B. Chu *J Membrane Sci*, vol. 452, pp. 446–452, 2014.

[103] P. Kampalanonwat and P. Supaphol *ACS Appl. Mater. Interfaces*, vol. 2, no. 12, pp. 3619–3627, 2010.

[104] Y. Lin, W. Cai, X. Tian, X. Liu, G. Wang, and C. Liang *J.Mater.Chem.*, vol. 21, no. 4, pp. 991–997, 2011.

[105] A. Mahapatra, B. G. Mishra, and G. Hota *Ind. Eng. Chem. Res.*, vol. 52, no. 4, pp. 1554–1561, 2013.

[106] C. Lee, C. Chiang, and S. Liu *Sep. Purif. Technol.*, vol. 118, pp. 737–743, 2013.

[107] J. Wu, H. Lee, J. You, Y. Kau, and S. Liu *J. Colloid Interface Sci.*, vol. 420, pp. 145–151, 2014.

[108] S. A. A. N. Nasreen, S. Sundarrajan, S. A. S. Nizar, R. Balamurugan, and S. Ramakrishna *Membranes*, vol. 3, no. 4, p. 266, 2013.

[109] S. Homaeigohar and M. Elbahri *Materials*, vol. 7, no. 2, pp. 1017–1045, 2014.

[110] B. Dong, L. Gwee, D. S. de la Cruz, K. I. Winey, and Y. A. Elabd *Nano Lett.*, vol. 10, no. 9, pp. 3785–3790, 2010.

[111] S. Cavaliere, S. Subianto, I. Savych, D. J. Jones, and J. Roziere *Energy Environ Sci*, vol. 4, no. 12, pp. 4761–4785, 2011.

[112] R. Wycisk, P. N. Pintauro, and J. W. Park *Curr. Opin. Chem. Eng.*, vol. 4, pp. 71–78, 2014.

[113] K. M. Lee, J. Choi, R. Wycisk, P. N. Pintauro, and P. Mather *ECS Transactions*, vol. 25, no. 1, pp. 1451–1458, 2009.

[114] J. Choi, K. M. Lee, R. Wycisk, P. N. Pintauro, and P. T. Mather *J. Mater. Chem.*, vol. 20, no. 30, pp. 6282–6290, 2010.

[115] J. B. Ballengee and P. N. Pintauro *J Membrane Sci*, vol. 442, pp. 187–195, 2013.

[116] S. Wang and H. Lin *J. Power Sources*, vol. 257, pp. 254–263, 2014.

[117] H. Li and Y. Liu *J.Mater.Chem.A*, vol. 2, no. 11, pp. 3783–3793, 2014.

[118] D. M. Yu, S. Yoon, T. Kim, J. Y. Lee, J. Lee, and Y. T. Hong *J Membrane Sci*, vol. 446, pp. 212–219, 2013.

[119] C. Subramanian, R. A. Weiss, and M. T. Shaw *Ind. Eng. Chem. Res.*, vol. 52, no. 43, pp. 15088–15093, 2013.

[120] J. Choi, K. M. Lee, R. Wycisk, P. N. Pintauro, and P. T. Mather *J. Electrochem. Soc.*, vol. 157, no. 6, pp. B914–B919, 2010.

[121] J. Choi, R. Wycisk, W. Zhang, P. N. Pintauro, K. M. Lee, and P. T. Mather *ChemSusChem*, vol. 3, no. 11, pp. 1245–1248, 2010.

[122] J. R. Lee, N.-Y. Kim, M.-S. Lee, and S.-Y. Lee *J Membrane Sci*, vol. 367, no. 1–2, pp. 265–272, 2011.

[123] C. Lee, S. Jo, J. Choi, K. Baek, Y. Truong, I. Kyratzis, and Y. G. Shul *J. Mater. Sci.*, vol. 48, no. 10, pp. 3665–3671, 2013.

[124] W. Qi, C. Lu, P. Chen, L. Han, Q. Yu, and R. Xu *Mater. Lett.*, vol. 66, no. 1, pp. 239–241, 2012.

[125] S. Wang and H. Lin *J. Power Sources*, vol. 257, pp. 254 – 263, 2014.

[126] A. I. Gopalan, K. Lee, K. M. Manesh, and P. Santhosh *J Membrane Sci*, vol. 318, no. 1–2, pp. 422 – 428, 2008.

[127] A. I. Gopalan, P. Santhosh, K. M. Manesh, J. H. Nho, S. H. Kim, C. Hwang, and K. Lee *J Membrane Sci*, vol. 325, no. 2, pp. 683 – 690, 2008.

[128] B. Ding and J. Yu, *Electrospun Nanofibers for Energy and Environmental Applications*. Nanostructure Science and Technology, Springer-Verlag Berlin Heidelberg, 2014.

[129] Gibson, P. W., Schreuder-Gibson, H. L., and D. Rivin *AIChE J.*, vol. 45, no. 1, pp. 190–195, 1999.

[130] A. Jaworek and A. Sobczyk *J. Electrostat.*, vol. 66, no. 3–4, pp. 197 – 219, 2008.

[131] M. Cloupeau and B. Prunet-Foch *J. Aerosol. Sci.*, vol. 25, no. 6, pp. 1021 – 1036, 1994.

[132] A. Jaworek and A. Krupa *Exp. Fluids*, vol. 27, no. 1, pp. 43–52.

[133] A. Jaworek and A. Krupa *J. Aerosol. Sci.*, vol. 30, no. 7, pp. 873 – 893, 1999.

[134] A. Jaworek *Powder Technol.*, vol. 176, no. 1, pp. 18 – 35, 2007.

[135] M. A. Henderson and J. S. McIndoe *Chem. Commun.*, no. 27, pp. 2872–2874, 2006.

[136] M. Davis, D. Stahl, K. Swiderek, and T. Lee *Methods*, vol. 6, no. 3, pp. 304 – 314, 1994.

[137] P. A. M. Eagles, A. N. Qureshi, S. N. Jayasinghe, and S. N. *Biochem. J.*, vol. 394, no. 2, pp. 375–378, 2006.

[138] U. E. P. Agency, *Why is the environment indoors important to us?* 2000.

[139] N. R. Council, *Indoor Pollutants*. The National Academies Press, 1981.

[140] "Indoor air quality." `http://www.epa.gov/indoor-air-quality-iaq`.

[141] J. M. Seltzer *J. Allergy Clin. Immunol.*, vol. 94, pp. 351–361, 1994.

[142] M. Cheng and S. Brown in *Proceedings of National Clean Air Conference*, pp. 23–27.

[143] J. Namieśnik, T. Górecki, B. K.-Z. ła, and J. Łukasiak *Build. Environ.*, vol. 27, no. 3, pp. 339 – 356, 1992.

[144] C. E. P. A. (CalEPA), "Air toxics hot spots program risk assessment guidelines: Part iii. technical support document for the determination of noncancer chronic reference exposure levels," srp draft, Office of Environmental Health Hazard Assessment, Berkeley, CA, 1999.

[145] "Advanced oxidation processes," in *Treatise on Water Science* (P. Wilderer, ed.), pp. 377 – 408, Oxford: Elsevier, 2011.

[146] G. Palmisano, V. Augugliaro, M. Pagliaro, and L. Palmisano *Chem. Commun.*, pp. 3425–3437, 2007.

[147] J. Herrmann, C. Duchamp, M. Karkmaz, B. T. Hoai, H. Lachheb, E. Puzenat, and C. Guillard *J. Hazard. Mater.*, vol. 146, no. 3, pp. 624 – 629, 2007.

[148] S. Banerjee, S. C. Pillai, P. Falaras, K. E. O'Shea, J. A. Byrne, and D. D. Dionysiou *J. Phys. Chem. Lett.*, vol. 5, no. 15, pp. 2543–2554, 2014.

[149] M. Pelaez, N. T. Nolan, S. C. Pillai, M. K. Seery, P. Falaras, A. G. Kontos, P. S. Dunlop, J. W. Hamilton, J. A. Byrne, K. O'Shea, M. H. Entezari, and D. D. Dionysiou *Appl Catal B: Environ*, vol. 125, pp. 331 – 349, 2012.

[150] A. L. Linsebigler, G. Lu, and J. T. Yates *Chem. Rev.*, vol. 95, no. 3, pp. 735–758, 1995.

[151] T. Inoue, A. Fujishima, S. Konishi, and K. Honda *Nature*, vol. 227, no. 5698, pp. 637–638, 1979.

[152] M. Fukuda, *Optical Semiconductor Devices*. A Wiley Interscience publication, Wiley, 1999.

[153] J. Peral, X. Domènech, and D. F. Ollis *J. Chem. Technol. Biotechnol.*, vol. 70, no. 2, pp. 117–140, 1997.

[154] J. Mo, Y. Zhang, Q. Xu, J. J. Lamson, and R. Zhao *Atmos. Environ.*, vol. 43, no. 14, pp. 2229 – 2246, 2009.

[155] D. F. Ollis, E. Pelizzetti, and N. Serpone *Environ. Sci. Technol.*, vol. 25, no. 9, pp. 1522–1529, 1991.

[156] J. Bolton, A. Safarzdadeh-Amiri, and S. R. Carter, *The detoxification of waste water streams using solar and artificial UV light sources*. Taylor & Francis, 1994.

[157] R. Yang, Y. Zhang, Q. Xu, and J. Mo *Atmos. Environ.*, vol. 41, no. 6, pp. 1221 – 1229, 2007.

[158] M. Salaices, B. Serrano, and H. de Lasa *Ind. Eng. Chem. Res.*, vol. 40, no. 23, pp. 5455–5464, 2001.

[159] J.-M. Herrmann *Catal. Today*, vol. 53, no. 1, pp. 115 – 129, 1999.

[160] C. Ao and S. Lee *J. Photochem. Photobiol., A*, vol. 161, no. 2–3, pp. 131 – 140, 2004.

[161] C. Chang, J. Chen, and M. Lu *J. Environ. Sci. Health., Part A*, vol. 38, no. 6, pp. 1131–1143, 2003.

[162] T. N. Obee and S. O. Hay *Environ. Sci. Technol.*, vol. 31, no. 7, pp. 2034–2038, 1997.

[163] S. Morales-Torres, L. M. Pastrana-Martinez, J. L. Figueiredo, J. L. Faria, and A. M. T. Silva *Environ. Sci. Pollut. R.*, vol. 19, no. 9, pp. 3676–3687, 2012.

[164] R. Vinu and G. Madras *J Indian Inst Sci*, vol. 30, no. 2, pp. 189–230, 2010.

[165] G. L. Chiarello, D. Ferri, and E. Selli *J. Catal.*, vol. 280, no. 2, pp. 168 – 177, 2011.

[166] S. B. Sadale, K. Noda, K. Kobayashi, H. Yamada, and K. Matsushige *Thin Solid Films*, vol. 520, no. 10, pp. 3847 – 3851, 2012.

[167] Y. Yeom, , and H. Frei *J. Phys. Chem. A*, vol. 105, no. 22, pp. 5334–5339, 2001.

[168] H. Kominami, H. Sugahara, and K. Hashimoto *Catal. Commun.*, vol. 11, no. 5, pp. 426 – 429, 2010.

[169] J. Lichtenberger, D. Lee, and E. Iglesia *Phys. Chem. Chem. Phys.*, vol. 9, pp. 4902–4906, 2007.

[170] H. Jia, G. Zhu, B. Vugrinovich, W. Kataphinan, D. H. Reneker, and P. Wang *Biotechnol. Prog.*, vol. 18, no. 5, pp. 1027–1032, 2002.

[171] X. Zhang, S. Xu, and G. Han *Mater. Lett.*, vol. 63, no. 21, pp. 1761 – 1763, 2009.

[172] Q. Li, D. Sun, and H. Kim *Mater. Res. Bull.*, vol. 46, no. 11, pp. 2094 – 2099, 2011.

[173] K. N. T. O. T. M. A. F. SH. Liu, BS. LLiu *J Nanomater*, no. 491927, pp. 1–5, 2012.

[174] H. Liu, J. Yang, J. Liang, Y. Huang, and C. Tang *J. Am. Ceram. Soc.*, vol. 91, no. 4, pp. 1287–1291, 2008.

[175] C. Pan, L. Dong, and J. Qiu *Chem. J. Chin. Univ.*, vol. 33, no. 5, pp. 1031–1035, 2012.

[176] Y. Qiu and J. Yu *Solid State Commun.*, vol. 148, no. 11–12, pp. 556 – 558, 2008.

[177] X. Xia, S. Li, X. Wang, J. Liu, Q. Wei, and X. Zhang *J. Mater. Sci.*, vol. 48, no. 9, pp. 3378–3385, 2013.

[178] X. Wang, H. Fan, and P. Ren *Catal. Commun.*, vol. 31, pp. 37 – 41, 2013.

[179] C. Pan, R. Ding, Y. Hu, and G. Yang *Physica E*, vol. 54, pp. 138 – 143, 2013.

[180] C. Srisitthiratkul, W. Yaipimai, and V. Intasanta *Appl Surf Sci*, vol. 259, pp. 349 – 355, 2012.

[181] M. Kanjwal, N. Barakat, F. Sheikh, W. Baek, M. Khil, and H. Kim *Fiber Polym*, vol. 11, no. 5, pp. 700–709, 2010.

[182] C. Srisitthiratkul, V. Pongsorrarith, and N. Intasanta *Appl Surf Sci*, vol. 257, no. 21, pp. 8850 – 8856, 2011.

[183] C. Su, L. Liu, M. Zhang, Y. Zhang, and C. Shao *CrystEngComm*, vol. 14, pp. 3989–3999, 2012.

[184] C. Pan and L. Dong *J. Macromol. Sci. Phy.*, vol. 48, no. 5, pp. 919–926, 2009.

[185] N. A. Barakat, M. A. Kanjwal, I. S. Chronakis, and H. Y. Kim *J. Mol. Catal. A: Chem*, vol. 366, pp. 333 – 340, 2013.

[186] D. Lin, H. Wu, R. Zhang, and W. Pan *Chem. Mater*, vol. 21, no. 15, pp. 3479–3484, 2009.

[187] X. Liu, Y. Hu, R. Chen, Z. Chen, and H. Han *Synth. React. Inorg. M.*, vol. 44, no. 3, pp. 449–453, 2014.

[188] Z. Liu, D. D. Sun, P. Guo, and J. O. Leckie *Nano Lett.*, vol. 7, no. 4, pp. 1081–1085, 2007.

[189] X. Peng, A. C. Santulli, E. Sutter, and S. S. Wong *Chem. Sci.*, vol. 3, pp. 1262–1272, 2012.

[190] C. Wang, C. Shao, X. Zhang, and Y. Liu *Inorg. Chem.*, vol. 48, no. 15, pp. 7261–7268, 2009.

[191] L. Zhu, M. Hong, and G. Wei Ho vol. 5, no. 11609.

[192] Z. Zhang, C. Shao, X. Li, L. Zhang, H. Xue, C. Wang, and Y. Liu *J. Phys. Chem. C*, vol. 114, no. 17, pp. 7920–7925, 2010.

[193] Y. Wang, J. Zhang, L. Liu, C. Zhu, X. Liu, and Q. Su *Mater. Lett.*, vol. 75, pp. 95 – 98, 2012.

[194] C. Zhu, Y. Li, Q. Su, B. Lu, J. Pan, J. Zhang, E. Xie, and W. Lan *J. Alloy Compd.*, vol. 575, pp. 333 – 338, 2013.

[195] D. D. Camillo, F. Ruggieri, S. Santucci, and L. Lozzi *J. Phys. Chem. C*, vol. 116, no. 34, pp. 18427–18431, 2012.

[196] H. Li, W. Zhang, S. Huang, and W. Pan *Nanoscale*, vol. 4, pp. 801–806, 2012.

[197] M. Modesti, M. Roso, C. Boaretti, S. Besco, D. Hrelja, P. Sgarbossa, and A. Lorenzetti *Appl Catal B: Environ*, vol. 144, pp. 216 – 222, 2014.

[198] S. Ramasundaram, A. Son, M. G. Seid, S. Shim, S. H. Lee, Y. C. Chung, C. Lee, J. Lee, and S. W. Hong *J. Hazard. Mater.*, vol. 285, pp. 267 – 276, 2015.

[199] H. R. Pant, D. R. Pandeya, K. T. Nam, W. Baek, S. T. Hong, and H. Y. Kim *J. Hazard. Mater.*, vol. 189, no. 1–2, pp. 465 – 471, 2011.

[200] F. Kayaci, C. Ozgit-Akgun, I. Donmez, N. Biyikli, and T. Uyar *ACS Appl. Mater. Interfaces*, vol. 4, no. 11, pp. 6185–6194, 2012.

[201] M. W. and R. J. Brodd *Chem. Rev.*, vol. 104, no. 10, pp. 4245–4270, 2004.

[202] H. L. MacLean and L. B. Lave *Prog. Energ. Combust.*, vol. 29, no. 1, pp. 1 – 69, 2003.

[203] S. Zaidi and M. A. Rauf, *Research Trends in Polymer Electrolyte Membranes for PEMFC*. John Wiley & Sons, Inc., 2002.

[204] K. A. Mauritz and R. B. Moore. *Chem. Rev.*, vol. 104, no. 10, pp. 4535–4586, 2004.

[205] K. Kreuer *Solid State Ionics*, vol. 97, no. 1–4, pp. 1 – 15, 1997.

[206] T. D. Gierke, G. E. Munn, and F. C. Wilson *J. Polym. Sci. Part B Polym. Phys.*, vol. 19, no. 11, pp. 1687–1704, 1981.

[207] M. Eikerling, A. A. Kornyshev, and U. Stimming *J. Phys. Chem. B*, vol. 101, no. 50, pp. 10807–10820, 1997.

[208] M. Rikukawa and K. Sanui *Prog. Polym. Sci.*, vol. 25, no. 10, pp. 1463 – 1502, 2000.

[209] F. Wang, M. Hickner, Y. S. Kim, T. A. Zawodzinski, and J. E. McGrath *J Membrane Sci*, vol. 197, no. 1–2, pp. 231 – 242, 2002.

[210] Y. A. Elabd and M. A. Hickner *Macromolecules*, vol. 44, no. 1, pp. 1–11, 2011.

[211] G. Alberti and M. Casciola, "Basic aspects in proton-conducting membranes for fuel cells," in *Comprehensive Membrane Science and Engineering* (E. Drioli and L. Giorno, eds.), pp. 431 – 465, Oxford: Elsevier, 2010.

[212] Y. S. Kim, M. A. Hickner, L. Dong, B. S. Pivovar, and J. E. McGrath *J Membrane Sci*, vol. 243, no. 1–2, pp. 317 – 326, 2004.

[213] W. J. Hogarth, J. D. da Costa, and G. Lu *J. Power Sources*, vol. 142, no. 1–2, pp. 223 – 237, 2005.

[214] J. L. Malers, M. Sweikart, J. L. Horan, J. A. Turner, and A. M. Herring *J. Power Sources*, vol. 172, no. 1, pp. 83 – 88, 2007.

[215] B. P. Ladewig, R. B. Knott, A. J. Hill, J. D. Riches, J. W. White, D. J. Martin, J. C. D. da Costa, and G. Q. Lu *Chem. Mater*, vol. 19, no. 9, pp. 2372–2381, 2007.

[216] H. Zhang and P. K. Shen *Chem. Soc. Rev.*, vol. 41, pp. 2382–2394, 2012.

[217] R. Wycisk, P. N. Pintauro, and J. W. Park *Curr. Opin. Chem. Eng.*, vol. 4, no. 0, pp. 71 – 78, 2014.

[218] S. Cavaliere, S. Subianto, I. Savych, D. J. Jones, and J. Roziere *Energy Environ. Sci.*, vol. 4, no. 12, pp. 4761–4785, 2011.

[219] J. Choi, K. M. Lee, R. Wycisk, P. N. Pintauro, and P. T. Mather *Macromolecules*, vol. 41, no. 13, pp. 4569–4572, 2008.

[220] H. Chen, J. D. Snyder, and Y. A. Elabd *Macromolecules*, vol. 41, no. 1, pp. 128–135, 2008.

[221] B. Loppinet, G. Gebel, and C. E. Williams *J. Phys. Chem. B*, vol. 101, no. 10, pp. 1884–1892, 1997.

[222] E. Szajdzinska-Pietek, S. Schlick, and A. Plonka *Langmuir*, vol. 10, no. 4, pp. 1101–1109, 1994.

[223] A. Laforgue, L. Robitaille, A. Mokrini, and A. Ajji *Macromol. Mater. Eng.*, vol. 292, no. 12, pp. 1229–1236, 2007.

[224] C. Pan, H. Wu, C. Wang, B. Wang, L. Zhang, Z. Cheng, P. Hu, W. Pan, Z. Zhou, X. Yang, and J. Zhu *Adv. Mater.*, vol. 20, no. 9, pp. 1644–1648, 2008.

[225] J. B. Ballengee and P. N. Pintauro *J. Electrochem. Soc.*, vol. 158, no. 5, pp. B568–B572, 2011.

[226] R. Bajon, S. Balaji, and S. Guo *J. Fuel Cell. Sci. Tech.*, vol. 6, no. 3, pp. 031004–031006, 2009.

[227] J. Choi, K. M. Lee, R. Wycisk, P. N. Pintauro, and P. T. Mather *J. Mater. Chem.*, vol. 20, pp. 6282–6290, 2010.

[228] S. Subianto, S. Cavaliere, D. J. Jones, and J. Rozière *J. Polym. Sci. A Polym. Chem.*, vol. 51, no. 1, pp. 118–128, 2013.

[229] S. Cavaliere, *Electrospinning for Advanced Energy and Environmental Applications*. CRC Press, 2015.

[230] J. B. Ballengee and P. N. Pintauro *Macromolecules*, vol. 44, no. 18, pp. 7307–7314, 2011.

[231] X. Li, X. Hao, D. Xu, G. Zhang, S. Zhong, H. Na, and D. Wang *J Membrane Sci*, vol. 281, no. 1–2, pp. 1 – 6, 2006.

[232] T. Tamura and H. Kawakami *Nano Lett.*, vol. 10, no. 4, pp. 1324–1328, 2010.

[233] Z. Hongwei, Y. Fei, and Z. Danying *J. Appl. Polym. Sci.*, vol. 130, no. 6, pp. 4581–4586, 2013.

[234] R. Takemori, G. Ito, M. Tanaka, and H. Kawakami *RSC Adv.*, vol. 4, pp. 20005–20009, 2014.

[235] R. Takemori and H. Kawakami *J. Power Sources*, vol. 195, no. 18, pp. 5957 – 5961, 2010.

[236] T. Tamura, R. Takemori, and H. Kawakami *J. Power Sources*, vol. 217, pp. 135 – 141, 2012.

[237] Y. Yao, L. Ji, Z. Lin, Y. Li, M. Alcoutlabi, H. Hamouda, and X. Zhang *ACS Appl. Mater. Interfaces*, vol. 3, no. 9, pp. 3732–3737, 2011.

[238] H. Li, Y. Lee, J. Lai, and Y. Liu *J Membrane Sci*, vol. 466, no. 0, pp. 238 – 245, 2014.

[239] H. Lin and S. Wang *J Membrane Sci*, vol. 452, no. 0, pp. 253 – 262, 2014.

[240] S. Mollá and V. Compañ *J Membrane Sci*, vol. 372, no. 1–2, pp. 191 – 200, 2011.

[241] H. Lin, S. Wang, C. Chiu, T. L. Yu, L. Chen, C. Huang, T. Cheng, and J. Lin *J Membrane Sci*, vol. 365, no. 1–2, pp. 114 – 122, 2010.

[242] H. Li and Y. Liu *J. Mater. Chem. A*, vol. 2, pp. 3783–3793, 2014.

[243] C. Lee, S. Jo, J. Choi, K.-Y. Baek, Y. Truong, I. Kyratzis, and Y.-G. Shul *J. Mater. Sci.*, vol. 48, no. 10, pp. 3665–3671, 2013.

[244] S. Yun, J. Woo, S. Seo, L. Wu, D. Wu, T. Xu, and S. Moon *J Membrane Sci*, vol. 367, no. 1–2, pp. 296 – 305, 2011.

[245] L. Wang, J. Zhu, J. Zheng, S. Zhang, and L. Dou *RSC Adv.*, vol. 4, pp. 25195–25200, 2014.

[246] H. Li and Y. Liu *J. Mater. Chem. A*, vol. 1, pp. 1171–1178, 2013.

[247] Z. Wang, H. Tang, J. Li, A. Jin, Z. Wang, H. Zhang, and M. Pan *Int. J. Hydrogen Energy*, vol. 38, no. 11, pp. 4725 – 4733, 2013.

[248] Y. Yao, B. Guo, L. Ji, K. Jung, Z. Lin, M. Alcoutlabi, H. Hamouda, and X. Zhang *Electrochem. Commun.*, vol. 13, no. 9, pp. 1005 – 1008, 2011.

[249] D. M. Yu, S. Yoon, T. Kim, J. Y. Lee, J. L., and Y. T. Hong *J Membrane Sci*, vol. 446, no. 0, pp. 212 – 219, 2013.

[250] J. Choi, K. M. Lee, R. Wycisk, P. N. Pintauro, and P. T. Mather vol. 157, no. 6, pp. B914–B919, 2010.

[251] W. Liu, S. Wang, M. Xiao, D. Han, and Y. Meng *Chem. Commun.*, vol. 48, pp. 3415–3417, 2012.

[252] M. V. Kakade, S. Givens, K. Gardner, K. H. Lee, D. B. Chase, and J. F. Rabolt *J. Am. Chem. Soc.*, vol. 129, no. 10, pp. 2777–2782, 2007.

[253] S. F. Fennessey and R. J. Farris *Polymer*, vol. 45, no. 12, pp. 4217 – 4225, 2004.

[254] Clagett, D., and R. Narr, *Engineering Plastics*. John Wiley & Sons, Inc., 2000.

[255] H. Kricheldorf, O. Nuyken, and G. Swift, *Handbook of Polymer Synthesis: Second Edition*. Plastics Engineering, CRC Press, 2004.

[256] D. Parker, J. Bussink, H. T. van de Grampel, G. W. Wheatley, E. Dorf, E. Ostlinning, K. Reinking, F. Schubert, O. Jünger, and R. Wagener, *Polymers, High-Temperature*. Wiley-VCH Verlag GmbH & Co. KGaA, 2000.

[257] A. K. Geim and K. S. Novoselov *Nat. Mater.*, vol. 6, pp. 183–191, 2007.

[258] O. V. Prezhdo *Surf. Sci.*, vol. 605, no. 17–18, pp. 1607 – 1610, 2011.

[259] K. S. Novoselov, A. K. Geim, S. V. Morozov, D. Jiang, Y. Zhang, S. V. Dubonos, I. V. Grigorieva, and A. A. Firsov *Science*, vol. 306, no. 5696, pp. 666–669, 2004.

[260] V. Sridhar, J.-H. Jeon, and I.-K. Oh *Carbon*, vol. 48, no. 10, pp. 2953 – 2957, 2010.

[261] A. K. Geim *Science*, vol. 324, no. 5934, pp. 1530–1534, 2009.

[262] A. Ismach, C. Druzgalski, S. Penwell, A. Schwartzberg, M. Zheng, A. Javey, J. Bokor, and Y. Zhang *Nano Lett.*, vol. 10, no. 5, pp. 1542–1548, 2010.

[263] W. S. H. Jr. and R. E. Offeman *J. Am. Chem. Soc.*, vol. 80, no. 6, pp. 1339–1339, 1958.

[264] M. J. Allen, V. C. Tung, and R. B. Kaner *Chem. Rev.*, vol. 110, no. 1, pp. 132–145, 2010.

[265] W. Gao, L. B. Alemany, L. Ci, and P. M. Ajayan *Nat. Chem.*, vol. 1, pp. 403 – 409, 2009.

[266] Y. Hernandez, V. Nicolosi, M. Lotya, F. M. Blighe, Z. Sun, S. De, M. T., B. Holland, M. Byrne, Y. K. Gun'Ko, J. J. Boland, P. Niraj, G. Duesberg, S. Krishnamurthy, R. Goodhue, J. Hutchison, V. Scardaci, A. C. Ferrari, and J. N. Coleman *Nat Nano*, vol. 3, no. 9, pp. 563–568, 2008.

[267] U. Khan, A. O'Neill, M. Lotya, S. De, and J. N. Coleman *Small*, vol. 6, no. 7, pp. 864–871, 2010.

[268] F. Schedin, A. K. Geim, S. V. Morozov, E. W. Hill, P. Blake, M. I. Katsnelson, and K. S. Novoselov *Nat Mater*, vol. 6, no. 9, pp. 652–655, 2007.

[269] K. S. Novoselov, D. Jiang, F. Schedin, T. J. Booth, V. V. Khotkevich, S. V. Morozov, and A. K. Geim vol. 102, no. 30, pp. 10451–10453, 2005.

[270] K. S. Novoselov, A. K. Geim, S. V. Morozov, D. Jiang, M. I. Katsnelson, I. V. Grigorieva, S. V. Dubonos, and A. A. Firsov *Nature*, vol. 438, no. 7065, pp. 197–200, 2005.

[271] C. Lee, X. Wei, Q. Li, R. Carpick, J. W. Kysar, and J. Hone *Phys. Status Solidi B*, vol. 246, no. 11-12, pp. 2562–2567, 2009.

[272] C. Lee, X. Wei, J. W. Kysar, and J. Hone *Science*, vol. 321, no. 5887, pp. 385–388, 2008.

[273] J.-W. Jiang, J.-S. Wang, and B. Li *Phys. Rev. B*, vol. 80, p. 113405, 2009.

[274] A. R. Ranjbartoreh, B. Wang, X. Shen, and G. Wang *J. Appl. Phys.*, vol. 109, no. 1, p. 014306, 2011.

[275] J. H. Seol, I. Jo, A. L. Moore, L. Lindsay, Z. H. Aitken, M. T. Pettes, X. Li, Z. Yao, R. Huang, D. Broido, N. Mingo, R. S. Ruoff, and L. Shi *Science*, vol. 328, no. 5975, pp. 213–216, 2010.

[276] Y. Zhu, S. Murali, W. Cai, X. Li, J. W. Suk, J. R. Potts, and R. S. Ruoff *Adv. Mater.*, vol. 22, no. 35, pp. 3906–3924, 2010.

[277] K. Saito, J. Nakamura, and A. Natori *Phys. Rev. B*, vol. 76, p. 115409, 2007.

[278] U. Stafford, K. A. Gray, P. V. Kamat, and A. Varma *Chem. Phys. Lett.*, vol. 205, no. 1, pp. 55 – 61.

[279] G. Riegel and J. R. Bolton *J. Phys. Chem. Lett.*, vol. 99, no. 12, pp. 4215–4224, 1995.

[280] D. C. Hurum, A. G. Agrios, , K. A. Gray, T. Rajh, , and M. C. Thurnauer *J. Phys. Chem. B*, vol. 107, no. 19, pp. 4545–4549, 2003.

[281] P. Ehrenfest *Proc. Roy. Acad. Amsterdam*, vol. 36, pp. 153–157, 1933.

[282] C. Hammond, *The Basics of Crystallography and Diffraction*. International Union of Crystallography texts on crystallography, OUP Oxford, 2009.

[283] U. Holzwarth and N. Gibson *Nat Nano*, vol. 6, no. 9, p. 534, 2011.

[284] W. W. Leung, C. Hung, and P. Yuen *Sep Purif Technol*, vol. 71, no. 1, pp. 30 – 37, 2010.

[285] M. J. McAllister, J. Li, D. H. Adamson, H. C. Schniepp, A. A. Abdala, J. Liu, M. Herrera-Alonso, D. L. Milius, R. Car, R. K. Prud'homme, , and I. A. Aksay *Chem. Mater*, vol. 19, no. 18, pp. 4396–4404, 2007.

[286] R. R. Nair, P. Blake, A. N. Grigorenko, K. S. Novoselov, T. J. Booth, T. Stauber, N. M. R. Peres, and A. K. Geim *Science*, vol. 320, no. 5881, pp. 1308–1308, 2008.

[287] H. Zhang, X. Lv, Y. Li, Y. Wang, and J. Li *ACS Nano*, vol. 4, no. 1, pp. 380–386, 2010.

[288] N. Khalid, E. Ahmed, Z. Hong, L. Sana., and M. Ahmed *Curr. Appl. Phys.*, vol. 13, no. 4, pp. 659 – 663, 2013.

[289] T. Nguyen-Phan, V. H. Pham, E. W. Shin, H. Pham, S. K., J. S. Chung, E. J. Kim, and S. H. Hur *Chem. Eng. J.*, vol. 170, no. 1, pp. 226 – 232, 2011.

[290] G. Jiang, Z. Lin, C. Chen, L. Zhu, Q. Chang, N. Wang, W. Wei, and H. Tang *Carbon*, vol. 49, no. 8, pp. 2693 – 2701, 2011.

[291] D. Yoo, T. V. Cuong, V. H. Pham, J. S. Chung, N. T. Khoa, E. J. Kim, and S. H. Hahn *Curr. Appl. Phys.*, vol. 11, no. 3, pp. 805 – 808, 2011.

[292] F. Wang and K. Zhang *J. Mol. Catal. A: Chem*, vol. 345, no. 1–2, pp. 101 – 107, 2011.

[293] E. Lee, J. Hong, H. Kang, and J. Jang *J. Hazard. Mater.*, vol. 219–220, pp. 13 – 18, 2012.

[294] Y. Min, K. Zhang, W. Zhao, F. Zheng, Y. Chen, and Y. Zhang *Chem. Eng. J.*, vol. 193–194, pp. 203 – 210, 2012.

[295] D. Wang, X. Li, J. Chen, and X. Tao *Chem. Eng. J.*, vol. 198–199, pp. 547 – 554, 2012.

[296] Z. Qianqian, B. Tang, and H. Guoxin *J. Hazard. Mater.*, vol. 198, pp. 78 – 86, 2011.

[297] N. S. Andryushina and O. L. Stroyuk *Appl Catal B: Environ*, vol. 148–149, pp. 543 – 549, 2014.

[298] W. Jo and H. Kang *Powder Technol.*, vol. 250, pp. 115 – 121, 2013.

[299] Y. Zhang, Z. Tang, X. Fu, and Y. Xu *ACS Nano*, vol. 4, no. 12, pp. 7303–7314, 2010.

[300] Y. Liu, G. Griffin, S. Chan, and I. Wachs *J. Catal.*, vol. 94, no. 1, pp. 108 – 119, 1985.

[301] R. M. Alberici and W. F. Jardim *Appl Catal. B.- Environ*, vol. 14, no. 1–2, pp. 55 – 68, 1997.

[302] D. S. Muggli, M. J. Odland, and L. R. Schmidt *J. Catal.*, vol. 203, no. 1, pp. 51 – 63, 2001.

[303] C.-C. Chuang, C.-C. Chen, , and J.-L. Lin *J. Phys. Chem. B*, vol. 103, no. 13, pp. 2439–2444, 1999.

[304] C. Zhang and H. He *Catal. Today*, vol. 126, no. 3–4, pp. 345 – 350, 2007.

[305] G. Liu, L. Wang, H. G. Yang, H.-M. Cheng, and G. Q. (Max) Lu *J. Mater. Chem.*, vol. 20, pp. 831–843, 2010.

[306] A. Zaleska, "Doped-tio2: A review," *Recent Patents on Engineering*, vol. 2, no. 3, pp. 157–164, 2008.

[307] M. V. Dozzi and E. Selli *J. Photochem. Photobiol. C*, vol. 14, pp. 13 – 28, 2013.

[308] L. G. Devi and R. Kavitha *Appl Catal. B.- Environ*, vol. 140–141, pp. 559 – 587, 2013.

[309] J. Yang, D. Wang, H. Han, and C. Li *Acc. Chem. Res.*, vol. 46, no. 8, pp. 1900–1909, 2013.

[310] C. Yu, W. Zhou, J. C. Yu, H. Liu, and L. Wei *Chin. J. Catal.*, vol. 35, no. 10, pp. 1609 – 1618, 2014.

[311] H. Wang, L. Zhang, Z. Chen, J. Hu, S. Li, Z. Wang, J. Liu, and X. Wang *Chem. Soc. Rev.*, vol. 43, pp. 5234–5244, 2014.

[312] P. Wang, B. Huang, X. Qin, X. Zhang, Y. Dai, J. Wei, and M.-H. Whangbo *Angew. Chem. Int. Ed.*, vol. 47, no. 41, pp. 7931–7933, 2008.

[313] P. Wang, B. Huang, X. Zhang, X. Qin, H. Jin, Y. Dai, Z. Wang, J. Wei, J. Zhan, S. Wang, J. Wang, and M.-H. Whangbo *Chem.–Eur. J.*, vol. 15, no. 8, pp. 1821–1824, 2009.

[314] C. An, J. Liu, S. Wang, J. Zhang, Z. Wang, R. Long, and Y. Sun *Nano Energy*, vol. 9, pp. 204 – 211, 2014.

[315] X. Wang, S. Li, H. Yu, J. Yu, and S. Liu *Chem.–Eur. J.*, vol. 17, no. 28, pp. 7777–7780, 2011.

[316] H. Xu, C. Wang, Y. Song, J. Zhu, Y. Xu, J. Yan, Y. Song, and H. Li *Chem. Eng. J.*, vol. 241, pp. 35 – 42, 2014.

[317] J. Liu, X. Li, F. Liu, L. Lu, L. Xu, L. Liu, W. Chen, L. Duan, and Z. Liu *Catal. Commun.*, vol. 46, pp. 138 – 141, 2014.

[318] X. Hu and C. Hu *J. Solid State Chem.*, vol. 180, no. 2, pp. 725 – 732, 2007.

[319] H. Dong, G. Chen, J. Sun, C. Li, Y. Yu, and D. Chen *Appl Catal. B.- Environ*, vol. 134–135, pp. 46 – 54, 2013.

[320] C. Yu, G. Li, S. Kumar, K. Yang, and R. Jin *Adv. Mater.*, vol. 26, no. 6, pp. 892–898, 2014.

[321] C. Yu, L. Wei, W. Zhou, J. Chen, Q. Fan, and H. Liu *Appl. Surf. Sci.*, vol. 319, pp. 312 – 318, 2014.

[322] H. Dong, G. Chen, J. Sun, Y. Feng, C. Li, G. Xiong, and C. Lv *Dalton Trans.*, vol. 43, pp. 7282–7289, 2014.

[323] H. Xu, J. Zhu, Y. Song, W. Zhao, Y. Xu, Y. Song, H. Ji, and H. Li *RSC Adv.*, vol. 4, pp. 9139–9147, 2014.

[324] C. Dong, K.-L. Wu, X.-W. Wei, X.-Z. Li, L. Liu, T.-H. Ding, J. Wang, and Y. Ye *CrystEngComm*, vol. 16, pp. 730–736, 2014.

[325] Y. Li, L. Fang, R. Jin, Y. Yang, X. Fang, Y. Xing, and S. Song *Nanoscale*, vol. 7, pp. 758–764, 2015.

[326] J. Hodkiewicz, "Characterizing carbon materials with raman spectroscopy," application note: 51901, Thermo Fisher Scientific, 2010.

[327] A. C. Ferrari, J. C. Meyer, V. Scardaci, C. Casiraghi, M. Lazzeri, F. Mauri, S. Piscanec, D. Jiang, K. S. Novoselov, S. Roth, and A. K. Geim *Phys. Rev. Lett.*, vol. 97, p. 187401, 2006.

[328] A. C. Ferrari *Solid State Commun.*, vol. 143, no. 1–2, pp. 47 – 57, 2007.

[329] D. Graf, F. Molitor, K. Ensslin, C. Stampfer, A. Jungen, C. Hierold, and L. Wirtz *Nano Lett.*, vol. 7, no. 2, pp. 238–242, 2007.

[330] M. A. Pimenta, G. Dresselhaus, M. S. Dresselhaus, L. G. Cancado, A. Jorio, and R. Saito *Phys. Chem. Chem. Phys.*, vol. 9, pp. 1276–1290, 2007.

[331] F. Hardcastle *J. Ark. Acad. Sci.*, vol. 65, pp. 43–48, 2011.

[332] T. Szabó, O. Berkesi, P. Forgó, K. Josepovits, Y. Sanakis, D. Petridis, and I. Dékány *Chem. Mater.*, vol. 18, no. 11, pp. 2740–2749, 2006.

[333] K. S. Novoselov, A. K. Geim, S. V. Morozov, D. Jiang, Y. Zhang, S. Dubonos, I. V. Grigorieva, and A. A. Firsov *Science*, vol. 306, no. 5696, pp. 666 – 669, 2004.

[334] A. Gupta, G. Chen, P. Joshi, S. Tadigadapa, and P. Eklund *Nano Lett.*, vol. 6, no. 12, pp. 2667–2673, 2006.

[335] A. N. Sidorov, M. M. Yazdanpanah, R. Jalilian, P. J. Ouseph, R. W. Cohn, and G. U. Sumanasekera *Nanotechnology*, vol. 18, no. 13, p. 135301, 2007.

[336] F. Giannazzo, S. Sonde, V. Raineri, G. Patanè, G. Compagnini, F. Aliotta, R. Ponterio, and E. Rimini *physica status solidi (c)*, vol. 7, no. 3-4, pp. 1251–1255, 2010.

[337] P. Nemes-Incze, Z. Osváth, K. Kamarás, and L. Biró *Carbon*, vol. 46, no. 11, pp. 1435 – 1442, 2008.

[338] H. R. Pant, C. H. Park, P. Pokharel, L. D. Tijing, D. S. Lee, and C. S. Kim *Powder Technol.*, vol. 235, pp. 853 – 858, 2013.

[339] T. Zhang, D. Zhang, and M. Shen *Mater. Lett.*, vol. 63, no. 23, pp. 2051 – 2054, 2009.

[340] G. J. de A. A. Soler-Illia, A. Louis, , and C. Sanchez *Chem. Mater.*, vol. 14, no. 2, pp. 750–759, 2002.

[341] J. C. Yu, L. Zhang, Z. Zheng, and J. Zhao *Chem. Mater.*, vol. 15, no. 11, pp. 2280–2286, 2003.

[342] G. Williams, B. Seger, and P. V. Kamat *ACS Nano*, vol. 2, no. 7, pp. 1487–1491, 2008.

[343] R. A. Spurr and H. Myers *Anal. Chem.*, vol. 29, no. 5, pp. 760–762, 1957.

[344] K. Krishnamoorthy, M. Veerapandian, K. Yun, and S. Kim *Carbon*, vol. 53, pp. 38 – 49, 2013.

[345] A. L. Patterson *Phys. Rev.*, vol. 56, pp. 978–982, 1939.

[346] J. Liu, H. Bai, Y. Wang, Z. Liu, X. Zhang, and D. D. Sun *Adv. Funct. Mater.*, vol. 20, no. 23, pp. 4175–4181, 2010.

[347] A. Lerf, H. He, M. Forster, and J. Klinowski *J. Phys. Chem. B*, vol. 102, no. 23, pp. 4477–4482, 1998.

[348] M. A. Butler *J. Appl. Phys.*, vol. 48, no. 5, pp. 1914–1920, 1977.

[349] R. Lopez and R. Gomez *J. Sol-Gel Sci. Technol.*, vol. 61, no. 1, pp. 1–7, 2011.

[350] C. Xu, Y. Liu, B. Huang, H. Li, X. Qin, X. Zhang, and Y. Dai *Appl. Surf. Sci.*, vol. 257, no. 20, pp. 8732–8736, 2011.

[351] J. Tauc, R. Grigorovici, and A. Vancu *Phys. Status Solidi B*, vol. 15, no. 2, pp. 627–637, 1966.

[352] M. E. Achaby, F. Arrakhiz, S. Vaudreuil, E. Essassi, and A. Qaiss *Appl. Surf. Sci.*, vol. 258, no. 19, pp. 7668 – 7677, 2012.

[353] S. Thakur and N. Karak *Carbon*, vol. 50, no. 14, pp. 5331 – 5339, 2012.

[354] X. Zhao, Q. Zhang, D. Chen, and P. Lu *Macromolecules*, vol. 43, no. 5, pp. 2357–2363, 2010.

[355] L. K. Putri, W.-J. Ong, W. S. Chang, and S.-P. Chai *Appl. Surf. Sci.*, vol. 358, Part A, pp. 2–14, 2015.

[356] K. M. Reddy, S. V. Manorama, and A. R. Reddy *Mater. Chem. Phys.*, vol. 78, no. 1, pp. 239 – 245, 2003.

[357] K. Woan, G. Pyrgiotakis, and W. Sigmund *Adv. Mater.*, vol. 21, no. 21, pp. 2233–2239, 2009.

[358] Y. Yu, J. C. Yu, C.-Y. Chan, Y.-K. Che, J.-C. Zhao, L. Ding, W.-K. Ge, and P.-K. Wong *Appl Catal. B.- Environ*, vol. 61, no. 1–2, pp. 1 – 11, 2005.

[359] M. Roso, S. Sundarrajan, D. Pliszka, S. Ramakrishna, and M. Modesti *Nanotechnology*, vol. 19, no. 28, p. 285707, 2008.

[360] M. Folli, "Progettazione e sviluppo di nuove membrane nanostrutturate per applicazioni ambientali," master thesis, University of Padova, 2011.

[361] "Photon irradiance." `http://goldbook.iupac.org/P04637.html`.

[362] T. N. K. Van Krevelen, D.W., *Chemical Degradation*, pp. 779–786. Elsevier, Amsterdam, 2009.

[363] A. Rivaton and J. Gardette *Polym. Degrad. Stabil.*, vol. 66, no. 3, pp. 385 – 403, 1999.

[364] R. Leary and A. Westwood *Carbon*, vol. 49, no. 3, pp. 741 – 772, 2011.

[365] S. Krishnamurthy, I. V. Lightcap, and P. V. Kamat *J. Photochem. Photobiol., A*, vol. 221, no. 2–3, pp. 214 – 219, 2011.

[366] N. A. Barakat, M. Abadir, F. A. Sheikh, M. A. Kanjwal, S. J. Park, and H. Y. Kim *Chem. Eng. J.*, vol. 156, no. 2, pp. 487 – 495, 2010.

[367] C. Feng, G. Li, P. Ren, Y. Wang, X. Huang, and D. Li *Appl Catal. B.- Environ*, vol. 158-159, pp. 224–232, 2014.

[368] Y. Song, J. Zhu, H. Xu, C. Wang, Y. Xu, H. Ji, K. Wang, Q. Zhang, and H. Li *J. Alloy Compd.*, vol. 592, pp. 258–265, 2014.

[369] C. Yu, L. Wei, J. Chen, Y. Xie, W. Zhou, and Q. Fan, 2014.

[370] H. Swanson, M. Morris, R. Stinchfield, and S. EH, "Standard x-ray diffraction powder pattern," 1962.

[371] C. Yu, L. Wei, W. Zhou, J. Chen, Q. Fan, and H. Liu *Appl. Surf. Sci.*, vol. 319, pp. 312–318, 2014.

[372] N. Koga, S. Yamada, and T. Kimura *J. Phys. Chem. C*, vol. 117, no. 1, pp. 326–336, 2013.

[373] P. Barnes and F. Stone *Thermochim. Acta*, vol. 4, no. 2, pp. 105 – 115, 1972.

[374] M. Yoshikawa, S. Yamada, and N. Koga *J. Phys. Chem. C*, vol. 118, no. 15, pp. 8059–8070, 2014.

[375] P. Norby, R. Dinnebier, and A. N. Fitch *Inorg. Chem.*, vol. 41, no. 14, pp. 3628–3637, 2002.

[376] X. Zhang, L. Zhang, T. Xie, and D. Wang, 2009.

[377] C. Dong, B.-B. Jiang, K.-L. Wu, Y. Hu, S.-H. Xia, and X.-W. Wei *Mater. Lett.*, vol. 146, pp. 37–39, 2015.

[378] J. Y. Gaopeng Dai and G. Liu *J. Phys. Chem. C*, vol. 116, no. 29, pp. 15519–15524.

[379] J. Li, L. Wei, C. Yu, W. Fang, Y. Xie, W. Zhou, and L. Zhu *Appl. Surf. Sci.*, vol. 358, Part A, pp. 168–174, 2015.

[380] W. Fa, P. Wang, B. Yue, F. Yang, D. Li, and Z. Zheng *Chin. J. Catal.*, vol. 36, no. 12, pp. 2186–2193, 2015.

[381] J. Li, L. Wei, C. Yu, W. Fang, Y. Xie, W. Zhou, and L. Zhu *Appl. Surf. Sci.*, vol. 358, Part A, pp. 168 – 174, 2015.

[382] G. Panthi, S.-J. Park, T.-W. Kim, H.-J. Chung, S.-T. Hong, M. Park, and H.-Y. Kim *J. Mater. Sci.*, vol. 50, no. 13, pp. 4477–4485, 2015.

[383] C. Yu, L. Wei, J. Chen, Y. Xie, W. Zhou, and Q. Fan *Ind. Eng. Chem. Res.*, vol. 53, no. 14, pp. 5759–5766, 2014.

[384] T. Chakrabarty, M. Kumar, K. Rajesh, V. K. Shahi, and T. Natarajan *Sep. Purif. Technol.*, vol. 75, no. 2, pp. 174 – 182, 2010.

[385] W. Wang, Z. Li, T. Jiang, Z. Zhao, Y. Li, Z. Wang, and C. Wang *ACS Appl. Mater. Interfaces*, vol. 4, no. 11, pp. 6080–6084, 2012.

[386] A. R. Katritzky, M. S. Kim, D. Fedoseyenko, K. Widyan, M. Siskin, and M. Francisco *Tetrahedron*, vol. 65, no. 6, pp. 1111–1114, 2009.

[387] G. Maier and J. Meier-Haack, "Sulfonated aromatic polymers for fuel cell membranes," in *Fuel Cells II* (G. G. Scherer, ed.), vol. 216 of *Advances in Polymer Science*, pp. 1–62, Springer Berlin Heidelberg, 2008.

[388] F. Kucera and J. Jancar *Polym. Eng. Sci.*, vol. 38, no. 5, pp. 783–792, 1998.

[389] N. Shibuya and R. S. Porter *Macromolecules*, vol. 25, no. 24, pp. 6495–6499, 1992.

[390] M. T. Bishop, F. E. Karasz, P. S. Russo, and K. H. Langley *Macromolecules*, vol. 18, no. 1, pp. 86–93, 1985.

[391] E. Gilbert, *Sulfonation and Related Reactions*. Interscience monographs on chemistry, Interscience Publishers, 1965.

[392] H. Cerfontain, *Mechanistic aspects in aromatic sulfonation and desulfonation*. Interscience monographs on organic chemistry, Interscience Publishers, 1968.

[393] R. Jiang, H. R. Kunz, and J. M. Fenton *J. Power Sources*, vol. 150, pp. 120 – 128, 2005.

[394] R. Compton, C. Bamford, and C. Tipper, *Reactions of Aromatic Compounds*. Comprehensive Chemical Kinetics, Elsevier Science, 1972.

[395] R. Y. M. Huang, P. Shao, C. M. Burns, and X. Feng *J. Appl. Polym. Sci.*, vol. 82, no. 11, pp. 2651–2660, 2001.

[396] N. Shibuya and R. S. Porter *Macromolecules*, vol. 27, no. 22, pp. 6267–6271, 1994.

[397] C. Bailly, D. J. Williams, F. E. Karasz, and W. J. MacKnight *Polymer*, vol. 28, no. 6, pp. 1009 – 1016, 1987.

[398] D. Kim, N. Do, and E. Cho, 2009. US Patent App. 12/247,599.

[399] F. Wang, J. Li, T. Chen, and J. Xu *Polymer*, vol. 40, no. 3, pp. 795 – 799, 1999.

[400] F. Wang, T. Chen, and J. Xu *Macromol. Chem. Phys.*, vol. 199, no. 7, pp. 1421–1426, 1998.

[401] K. Sakurai, E. Douglas, and W. J. MacKnight *Macromolecules*, vol. 26, no. 1, pp. 208–212, 1993.

[402] Y. Xue and M. Hara *Macromolecules*, vol. 30, no. 13, pp. 3803–3812, 1997.

[403] K. Miyatake, H. Iyotani, K. Yamamoto, and E. Tsuchida *Macromolecules*, vol. 29, no. 21, pp. 6969–6971, 1996.

[404] J. Chalmers, W. Gaskin, and M. Mackenzie *Polym. Bull.*, vol. 11, no. 5, pp. 433–435, 1984.

[405] X. Ling, C. Jia, J. Liu, and C. Yan *J Membrane Sci*, vol. 415–416, no. 0, pp. 306 – 312, 2012.

[406] J. Jaafar, A. Ismail, and A. Mustafa *Mat. Sci. Eng. A-Struct.*, vol. 460–461, no. 0, pp. 475 – 484, 2007.

[407] L. Vasquez, *Fuel Cell Research Trends*. Nova Science Publishers, 2007.

[408] "Thermal applications note 48." `http://www.tainstruments.com/library_download.aspx?file=TN048.pdf`.

[409] R.-M. Ho, S. Z. D. Cheng, B. S. Hsiao, and K. H. Gardner *Macromolecules*, vol. 27, no. 8, pp. 2136–2140, 1994.

[410] K. Tadano, E. Hirasawa, H. Yamamoto, and S. Yano *Macromolecules*, vol. 22, no. 1, pp. 226–233, 1989.

[411] E. Hirasawa, Y. Yamamoto, K. Tadano, and S. Yano *Macromolecules*, vol. 22, no. 6, pp. 2776–2780, 1989.

[412] H. Tachino, H. Hara, E. Hirasawa, S. Kutsumizu, and S. Yano *J. Appl. Polym. Sci.*, vol. 55, no. 1, pp. 131–138, 1995.

[413] A. Carbone, R. Pedicini, G. Portale, A. Longo, L. D'Ilario, and E. Passalacqua *J. Power Sources*, vol. 163, no. 1, pp. 18 – 26, 2006.

[414] S. Zaidi, S. Mikhailenko, G. Robertson, M. Guiver, and S. Kaliaguine *J. Membrane Sci.*, vol. 173, no. 1, pp. 17 – 34, 2000.

[415] D. Marani, M. L. Di Vona, E. Traversa, S. Licoccia, I. Beurroies, P. L. Llewellyn, and P. Knauth *J. Phys. Chem. B*, vol. 110, no. 32, pp. 15817–15823, 2006.

[416] X. Li, X. Hao, and H. Na *Mater. Lett.*, vol. 61, no. 2, pp. 421 – 426, 2007.

[417] C. Lee, S. M. Jo, J. Choi, K.-Y. Baek, Y. B. Truong, I. L. Kyratzis, and Y.-G. Shul *J. Mater. Sci.*, vol. 48, no. 10, pp. 3665–3671, 2013.

[418] J. Choi, C. Lee, S. C. Hawkins, C. P. Huynh, J. Park, Y. Jeon, Y. B. Truong, I. L. Kyratzis, Y.-G. Shul, and R. A. Caruso *RSC Adv.*, vol. 4, pp. 32787–32790, 2014.

[419] M. Oroujzadeh, S. Mehdipour-Ataei, and M. Esfandeh *Chem. Eng. J.*, vol. 269, pp. 212 – 220, 2015.

[420] G. P. Robertson, S. D. Mikhailenko, K. Wang, P. Xing, M. D. Guiver, and S. Kaliaguine *J Membrane Sci*, vol. 219, no. 1–2, pp. 113 – 121, 2003.

[421] M.-S. Jun, Y.-W. Choi, and J.-D. Kim *J Membrane Sci*, vol. 396, pp. 32 – 37, 2012.

[422] C. Subramanian, R. Weiss, and M. T. Shaw *Polymer*, vol. 51, no. 9, pp. 1983 – 1989, 2010.

[423] H. Okuzaki, T. Takahashi, N. Miyajima, Y. Suzuki, , and T. Kuwabara *Macromolecules*, vol. 39, no. 13, pp. 4276–4278, 2006.

[424] A. Frenot, M. W. Henriksson, and P. Walkenström *J. Appl. Polym. Sci.*, vol. 103, no. 3, pp. 1473–1482, 2007.

[425] M. M. Li and Y. Z. Long *Mater. Sci. Forum*, vol. 688, pp. 95–101, 2011.

[426] D. Paneva, N. Manolova, I. Rashkova, H. Pencheva, M. Mihai, and E. S. Dragan *Dig. J. Nanomater. Bios.*, vol. 5, no. 4, pp. 811–819, 2010.

[427] G. Box and N. Draper, *Empirical model-building and response surfaces*. Wiley series in probability and mathematical statistics: Applied probability and statistics, Wiley, 1987.

[428] R. Myers, D. Montgomery, and C. Anderson-Cook, *Response Surface Methodology: Process and Product Optimization Using Designed Experiments*. Wiley Series in Probability and Statistics, Wiley, 2011.

[429] J. Deitzel, J. Kleinmeyer, D. Harris, and N. B. Tan *Polymer*, vol. 42, no. 1, pp. 261 – 272, 2001.

[430] K. Lee, H. Kim, H. Bang, Y. Jung, and S. Lee *Polymer*, vol. 44, no. 14, pp. 4029 – 4034, 2003.

[431] S. Sukigara, M. Gandhi, J. Ayutsede, M. Micklus, and F. Ko *Polymer*, vol. 45, no. 11, pp. 3701 – 3708, 2004.

[432] O. Yordem, M. Papila, and Y. Menceloglu *Materials & Design*, vol. 29, no. 1, pp. 34 – 44, 2008.

[433] S.-Y. Gu and J. Ren *Macromol. Mater. Eng.*, vol. 290, no. 11, pp. 1097–1105, 2005.

[434] T. W. Anderson and D. A. Darling *Ann. Math. Stat.*, vol. 23, no. 2, pp. 193–212, 1952.

[435] J. Durbin and G. S. Watson *Biometrika*, vol. 37, no. 3/4, pp. 409–428, 1950.

[436] J. Durbin and G. S. Watson *Biometrika*, vol. 38, no. 1/2, pp. 159–177, 1951.

[437] M. Brown and A. Forsythe vol. 69, no. 346, pp. 364–367, 1974.

[438] A. Andrady, *Science and Technology of Polymer Nanofibers*. Wiley, Hoboken, NJ (USA), 2008.

[439] W. Press, *Numerical Recipes in Pascal (First Edition): The Art of Scientific Computing*. No. v. 1, Cambridge University Press, 1989.

[440] X. Jin, M. T. Bishop, T. S. Ellis, and F. E. Karasz *Brit. Polym. J.*, vol. 17, no. 1, pp. 4–10, 1985.

[441] M. Cappadonia, J. Erning, S. M. Niaki, and U. Stimming *Solid State Ionics*, vol. 77, pp. 65 – 69, 1995.

[442] R. W. Kopitzke, C. A. Linkous, H. R. Anderson, and G. L. Nelson *J. Electrochem. Soc.*, vol. 147, no. 5, pp. 1677–1681, 2000.

[443] N. Li, A. Fane, W. Ho, and T. Matsuura, *Advanced Membrane Technology and Applications*. Wiley, 2011.

[444] J.-H. Won, H.-J. Lee, J.-M. Lim, J.-H. Kim, Y. T. Hong, and S.-Y. Lee *Journal of Membrane Science*, vol. 450, pp. 235 – 241, 2014.

[445] J. Choi, K. M. Lee, R. Wycisk, P. N. Pintauro, and P. T. Mather *Macromolecules*, vol. 41, pp. 4569–4572, 07/01 2008.

[446] N. E. W. P. Ramaswamy and G. K. H. Shimizu *Chem. Soc. Rev*, vol. 43, pp. 5913–5932, 2014.

[447] K. M. Lee, J. Choi, R. Wycisk, P. N. Pintauro, and P. Mather *ECS Trans.*, vol. 25, no. 1, pp. 1451–1458, 2009.

[448] S. Ren, G. Sun, C. Li, Z. Wu, W. Jin, W. Chen, Q. Xin, and X. Yang *Mater. Lett.*, vol. 60, no. 1, pp. 44 – 47, 2006.

[449] T. Y. Inan, H. Doğan, E. E. Unveren, and E. Eker *Int. J. Hydrogen Energy*, vol. 35, no. 21, pp. 12038 – 12053, 2010.

[450] A. Regina, E. Fontananova, E. Drioli, M. Casciola, M. Sganappa, and F. Trotta *J. Power Sources*, vol. 160, no. 1, pp. 139 – 147, 2006.

[451] Y. J. Park, Y. S. Kang, and C. Park *Eur. Polym. J.*, vol. 41, no. 5, pp. 1002 – 1012, 2005.

[452] S. Zanderigo, "Ottimizzazione del processo di electtrofilatura per modifica di sistemi filtranti," master thesis, University of Padova, 2011.

[453] Y. Gao, G. P. Robertson, M. D. Guiver, X. Jian, S. D. Mikhailenko, K. Wang, and S. Kaliaguine *J. Polym. Sci. Part A: Polym. Chem.*, vol. 41, no. 17, pp. 2731–2742, 2003.